SHEAR BANDING IN COARSE SANDS

UNDER COMBINED STRESSES

by

THOMAS J. MOON JR.

Submitted in partial fulfillment of the requirements

for the degree of Master of Science

Thesis Advisor: Dr. Adel S. Saada

Department of Civil Engineering

CASE WESTERN RESERVE UNIVERSITY

May, 1998

Shear Banding in Coarse Sands Under Combined Stresses

Abstract
by
Thomas Moon

The phenomenon of shear banding in soils has been studied over the last few years at Case Western Reserve University. Prior research was performed on cohesive and fine-grain, angular soils. To complete the study, a coarse-grain sand was used to determine the effect grain size has on the propagation of shear bands. Many state-of-the-art techniques were used to collect the necessary data; these include digital imaging programs and constant mean stress testing devices.

Several different variables were examined to determine the effect they have on the development and propagation of the shear band. Some of these parameters include relative density, stress path, and confining pressure. The genesis of the slip plane and the eventual direction of the shear band was monitored using video cameras. At regular times during the testing process, "snapshots" from these cameras were taken and stored as VGA images on a computer. The images were then digitally traced using specifically designed software packages. With the images digitally recorded, a great deal of information could then be calculated; such as the angle of the slip plane and the strains in and around the shear band.

With the final phase of this ongoing project now completed, a comparative analysis between the different types of media was performed. This information is summarized and several theories attempting to predict the angle of failure are evaluated in this report.

Acknowledgments

The author wishes to, first and foremost, thank his advisor and mentor, Dr. Adel S. Saada, for his patience and guidance on this thesis. His knowledge on the subject of Soil Mechanics has been a tremendous asset to myself and to Case Western Reserve University. This project was sponsored by a research grant provided by the United States Air Force Office of Scientific Research and their support is appreciated.

The author wishes to acknowledge the countless hours of work contributed by Dr. Liqun Liang. Much of the new technology used on this project was conceived by Dr. Liang and his support was invaluable. Dr. J. Ludwig Figueroa, C. Tucker Cope, and Carol Dietz provided much appreciated advice throughout the duration of this research.

On a more personal note, the author would like to thank his family and friends for their unwavering support over the past two years. My parents, Thomas and Judy Moon, and my sister, Nancy Tofil, have always stood beside me and encouraged me to better myself as a student and person. Finally, the author would like to extend his gratitude to Scott Castelli for being an excellent colleague, roommate, and friend.

Table of Contents

List of Figures

List of Tables

Chapter One

Introduction

1.1 History of Research On Shear Banding

The shear banding phenomenon has been studied for well over two centuries. Coulomb first reported his findings on the subject back in 18th century. His famous equation predicting the angle of shear banding was the recognized standard for many decades. Roscoe attempted to improve upon this classical solution by substituting the angle of dilation for the angle of friction. In the last 25 years, since these two theories were presented, there has been a concerted effort to further understand the onset and propagation of shear bands. The following section will highlight some of the major discoveries and their importance.

In 1967, Morgenstern and Tchalenko noticed shear bands were influenced by boundary conditions. They used a direct shear device to study cohesive materials. In this study, clay was infused with carbowax to instigate the onset of a shear band. Nearly a decade later in 1976, Balasubramaniam used X-rays to investigate the deformation of clays. He noticed that the local and global strains were in excellent agreement up to approximately 75% of the peak value. In 1977, Arthur et al. introduced the idea that the angle of shear banding could be more accurately predicted by taking an average of the theories presented by Coulomb and Roscoe. In this theory, both the angles of friction and dilation were taken into account. Vardoulakis (1980) further supported this claim of a geometrical average of the two classical solutions. Houlsby and Wroth (1980) stated that for the case of plastic deformation in plane strain, it was not necessary that a velocity discontinuity be a line of zero extension, contrary to prior beliefs. They also separated

kinematic discontinuities into multiple categories. In 1982, Arthur & Dunstan used radiography to study granular non-cohesive sands. They noted that the previously determined average of the Coulomb and Roscoe theories still gave the best prediction of the rupture zone angle, but the particle size of a particular media would effect this inclination. It was also found that shear bands tended to fully form at failure. This was true when the sample was under conditions of homogeneous stresses with fixed principal stress directions. Radiography was also used by Scarpelli & Wood in 1982. They investigated the inclination of shear bands found in simple shear devices. The findings from that study showed that the degree of constraint imposed on the sample effected the shear band angle. For highly restrained samples, the angle would approach the Coulomb solution and the line of zero extension. Otherwise, the angle would be more consistent with the inclination predicted by the Arthur-Vardoulakis theory.

In 1990, Koenders et al. came upon the same conclusion as Arthur & Dunstan. It was suggested that the shear band inclination was dependent upon the average grain size of the sand used. Vermeer (1990) tended to agree with the notion that the particle size effected the shear band inclination but attributed this, in part, to the width of the shear band. Fine-grained sands typically have thinner shear bands and thus have a smaller influence. Coarse-grained sands have thicker bands and these tend to be more affected by boundary conditions. For this reason, the finer sands have a tendency to yield shear band angles consistent with the Coulomb solution. The general findings from this study, Vermeer contended, showed that most sands would exhibit Coulomb-type inclinations if there were small effects from boundary conditions.

Saada, Bianchini & Liang (1994) performed numerous tests on clay using a hollow cylinder testing device. These tests indicated that clays, when tested under undrained conditions, acted like a frictional material to which Coulomb's theory applied. Cope (1997) used the same hollow cylinder device to analyze fine-grained soils. By using a new visual/digital analysis method, he determined that the Arthur-Vardoulakis theory gave the most accurate predictions of shear band angles.

With all the research on shear bands, much debate still exists on several issues. This thesis attempts to clarify some of those questions. Additional information on the subject is presented by analyzing a coarse-grained sand in a hollow cylinder device using the same testing regiment used by Cope. In this manner, definitive conclusions can be drawn about the effect of grain size.

1.2 Phenomenon of Shear Bands

1.2.1 The Definition and Mechanism of Shear Banding

Shear bands are defined as the localization of plastic deformation at areas of discontinuity in soil. A shear band can be compared to a tear in a piece of paper. Once a fissure forms, it will continue to propagate along a given path but the rest of the paper will remain relatively unaffected. In a soil specimen, a shear band starts at an area of high local stress, typically at a weakness or discontinuity. Sand behaves as an elasto-plastic material and slip surfaces are generated as soon as nonrecoverable deformations take place. At a stress level close to the peak, slip surfaces coalesce in areas of high stress concentrations giving birth to a shear band that propagates until total failure is reached. Shear banding is associated with a high local deformation and only regions

relatively near the shear band are affected. Therefore, after a shear band has fully developed, the two halves of a specimen, separated by the band, will act as two independent blocks. The only permanent deformation that will take place after shear banding has occurred will be along the shear band itself. It is important to note that, after failure, the majority of the sample will be relatively unaffected by continued loading.

1.2.2 Parameters Thought to Affect Shear Banding

Several factors have been thought to affect the formation and propagation of shear bands; they include:

- confining pressure
- relative density
- applied stress path
- type of soil (sands vs. clays)
- grain size distribution
- boundary conditions

Several of these factors will be analyzed to determine their effect on shear banding. With so many parameters to study, this research will attempt to determine the most significant. The effect of grain size distribution is of particular interest in this investigation.

1.2.3 Initial Formation of Shear Bands

Slip lines, as previously mentioned, begin to form the instant plastic deformations occur in sand. To further explore the onset and propagation of shear bands, a plain strain model will be examined. This will be achieved by using a hollow cylinder testing apparatus. A paper entitled "Shear Banding in Sands Observed in Plain Strain

Compression" (T. Yoshida et al., 1994) suggests that slip lines form early on when a soil is subjected to stress. (Cope) and current studies tend to agree with this notion. Proof of this can be seen in figures 1.1 to 1.6. A shear band cannot be seen at it's initiation, however. This is because shear banding is an observation and only after sufficient deformation has occurred can one be perceived. In general, the term shear band is used to describe the rupture surface that has developed at approximately the same time as the maximum shear stress, hence the term "slip line" is used to define the smaller lines which may or may not evolve into the main shear band.
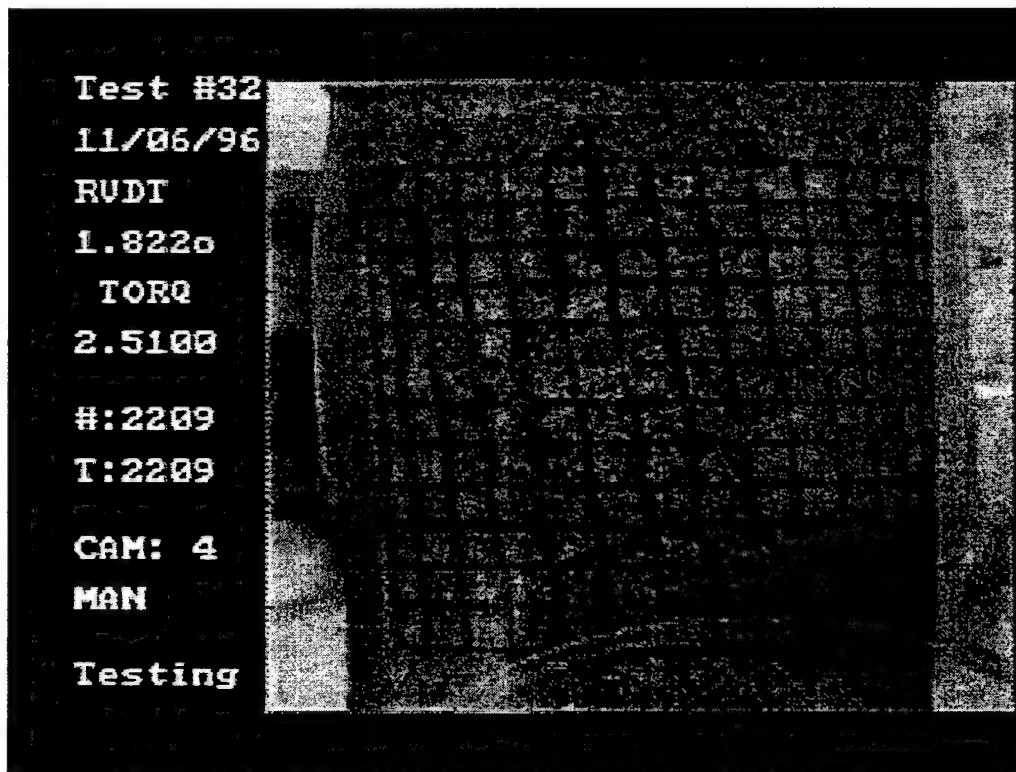
Figure 1.1 Multiple Slip Lines (Cope: Test #32, Time 2209 sec.)
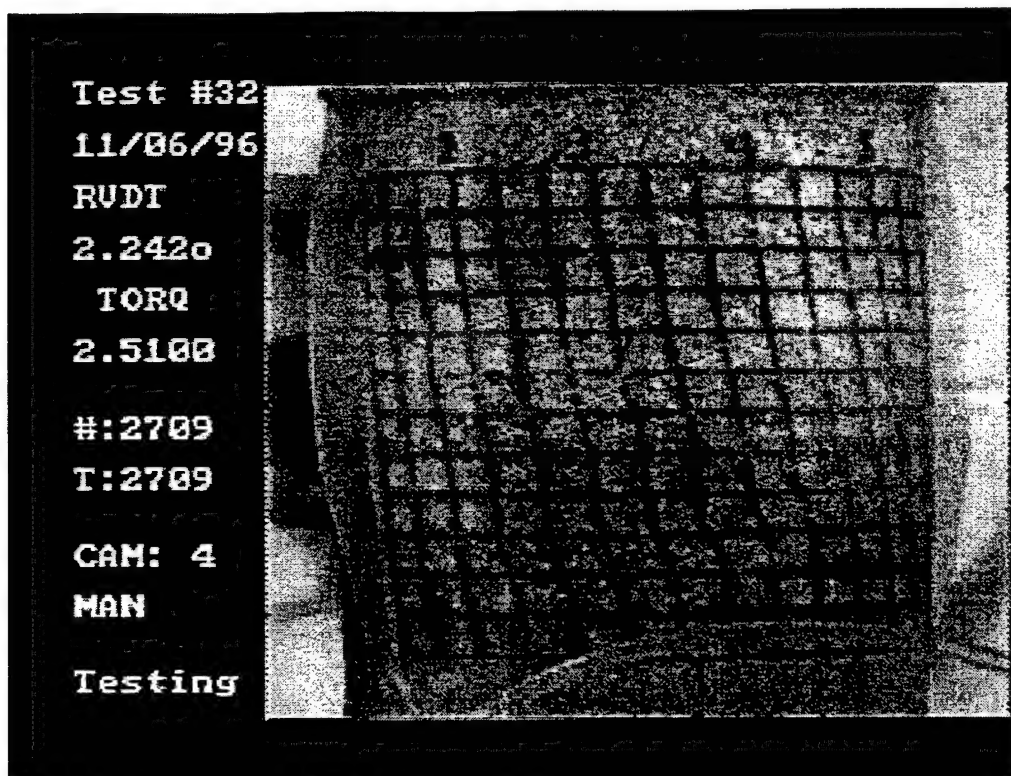
Figure 1.2 Multiple Slip Lines (Cope: Test #32, Time 2709 sec.)
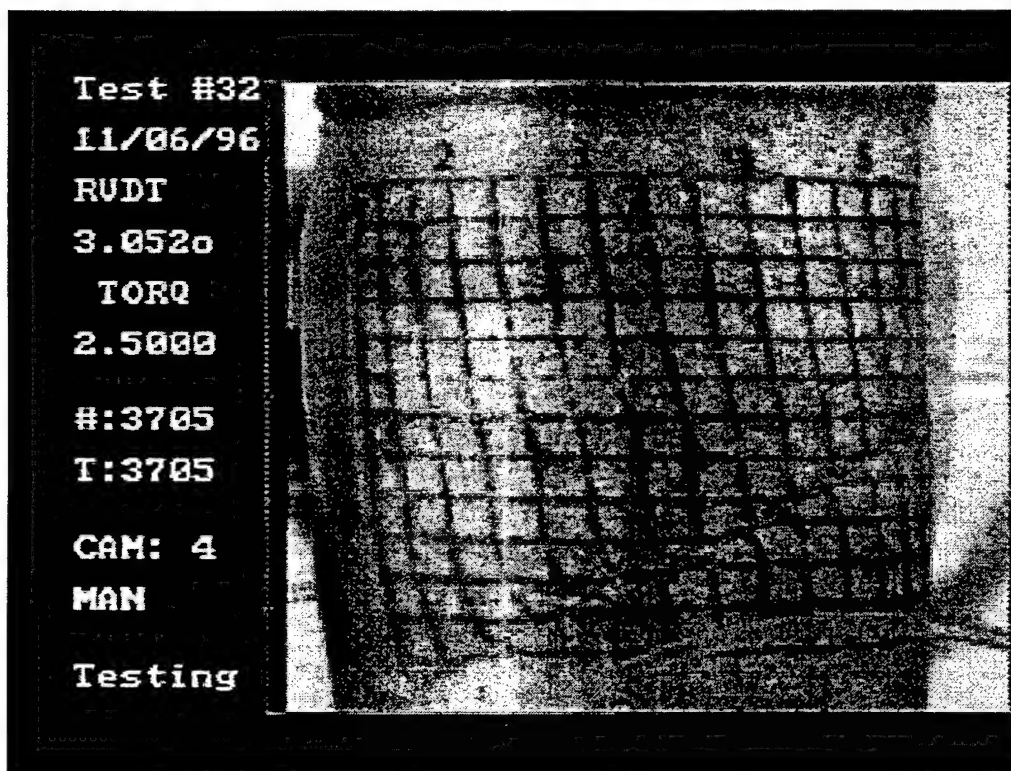
Figure 1.3 Dominant Shear Band (Cope: Test #32, Time 3705 sec)
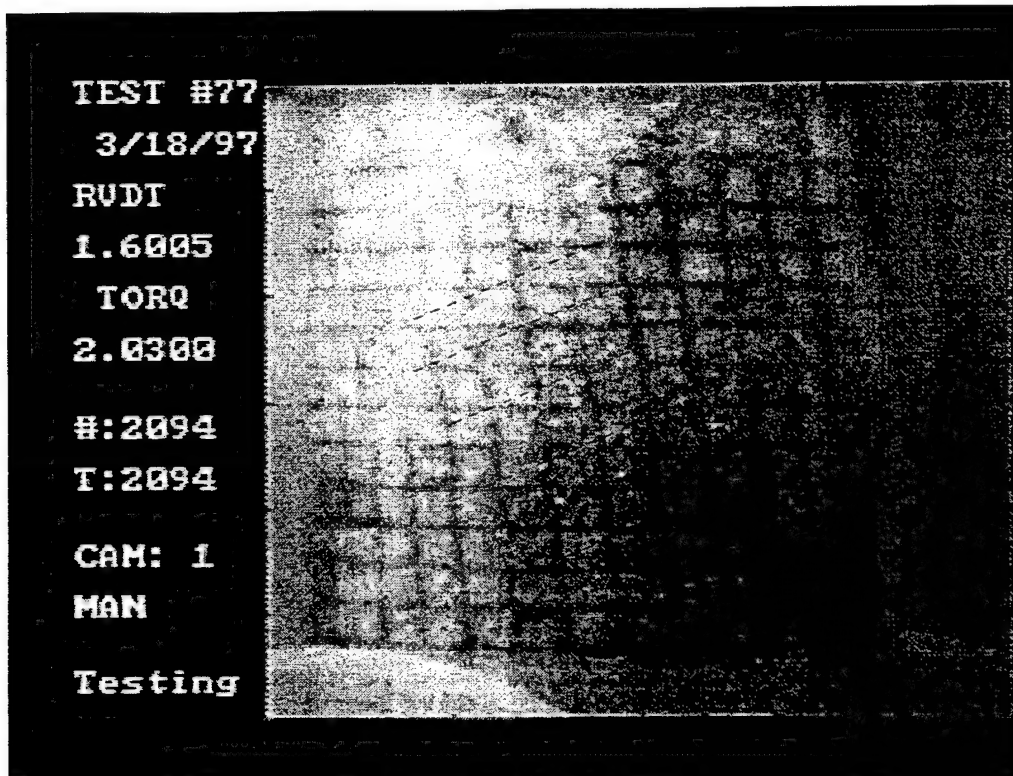
Figure 1.4 Multiple Slip Lines (Moon: Test #77, Time 2094 sec.)
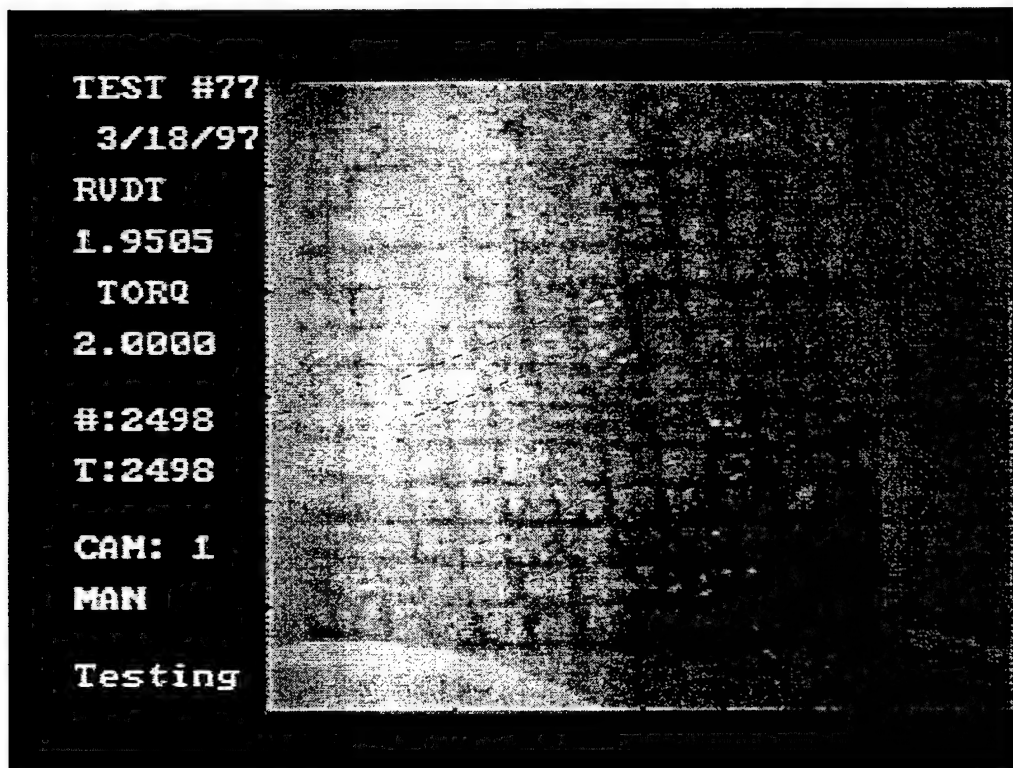
Figure 1.5 Multiple Slip Lines (Moon: Test #77, Time 2498 sec.)
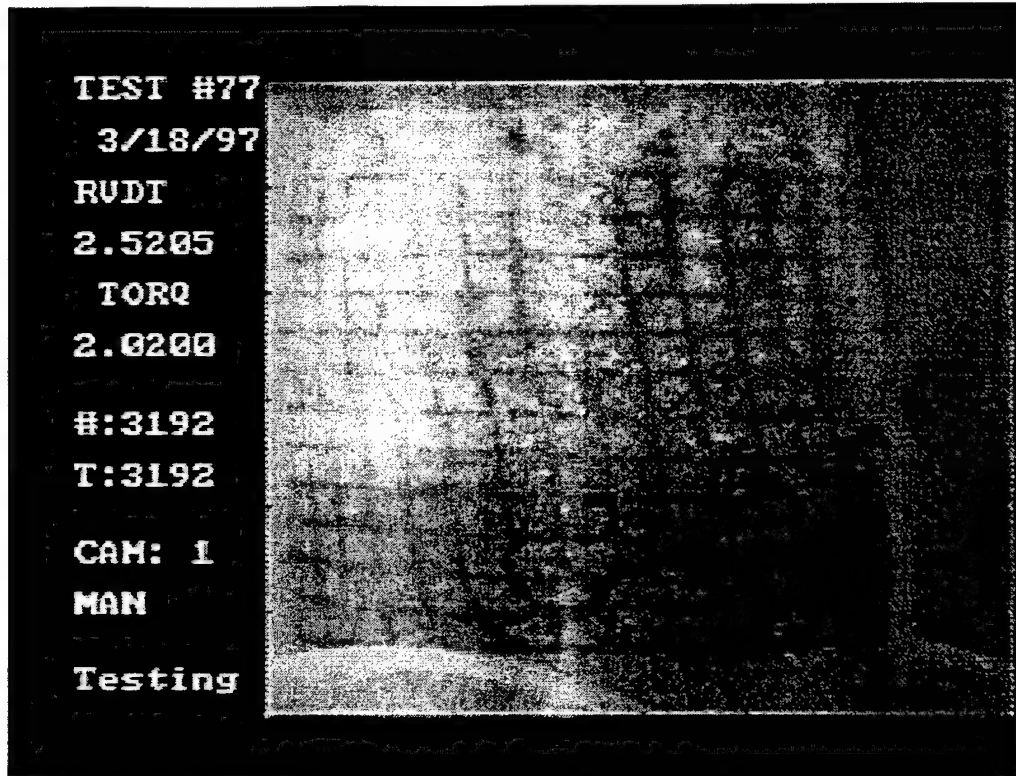
Figure 1.6 Dominant Shear Band (Moon: Test #77, Time 3192 sec.)

Since sand behaves as an elasto-plastic material, a small degree of rebounding will occur with the formation of a shear band. The smaller slip lines may become less noticeable as a result. Examples of this can be seen in figures 1.1 to 1.6 also.

1.3 Previous Theories Predicting Angle of Shear Banding

Coulomb predicted that failure in sands would form at an angle of $(\pi/4 - \phi'/2)$ from the principal stress direction. In this theory, ϕ' represents the effective angle of friction.

$$\pi/4 - \phi'/2$$
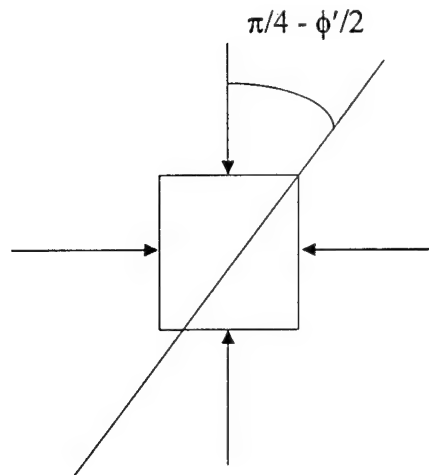
Figure 1.7 Coulomb's Theory

In 1970, Roscoe published a paper entitled "The Influence of Strains in Soil Mechanics". In this paper, Roscoe noticed that Coulomb's theory tended to overestimate the angle of shear banding. For this reason, he suggested that the angle of dilation (Ψ) be used instead of the angle of friction (ϕ'). The angle of dilation is consistently smaller then the angle of friction. Thus, Roscoe's theory states that the shear band will form at an angle of ($\pi/4 - \Psi/2$) from the principal stress direction.

$$\pi/4 - \psi/2$$
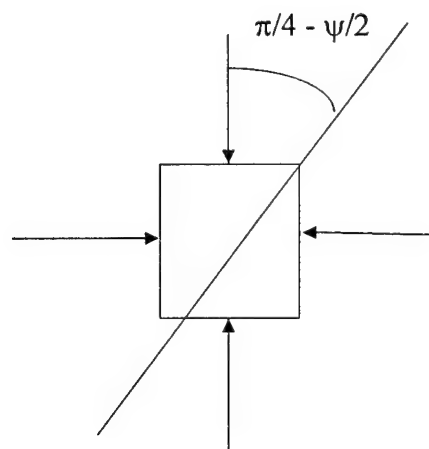
Figure 1.8 Roscoe's Theory

The angle of dilation is a quantity used to describe the expansion of a sand when subjected to shearing. A direct shear test can best be used to explain this idea. In this test, a sample is sheared but a line of zero extension is maintained. As the sand is sheared, it will tend to expand. Figure 1.9 shows how the angle of dilation is determined.
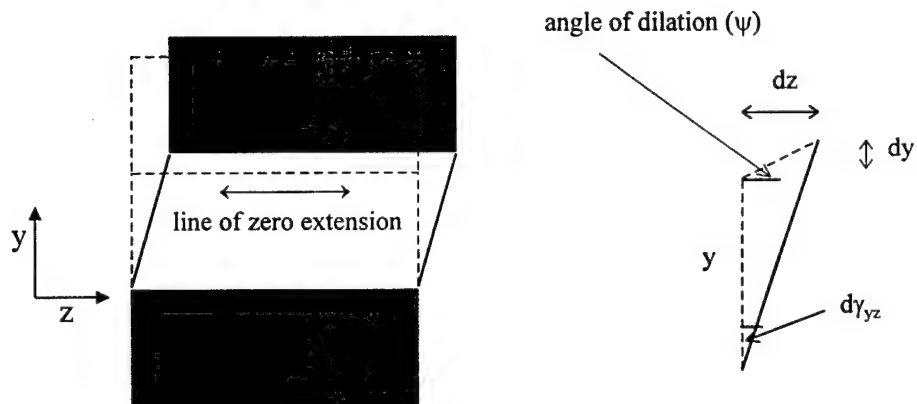
Figure 1.9 Angle of Dilation (ψ) -Direct Shear
(Bolton, 1986)

It is generally recognized that the maximum rate of dilation $(-d\varepsilon_v / d\varepsilon_1)_{max}$ occurs simultaneously with the maximum stress. Figure 1.10 demonstrates this point. It is necessary to note that σ_1 and σ_3 are the two principal stress values of concern (σ_1 being the major principal stress), ε_v is the volumetric strain and ε_1 is the major principal strain. Both the stresses and strains are positive in compression.
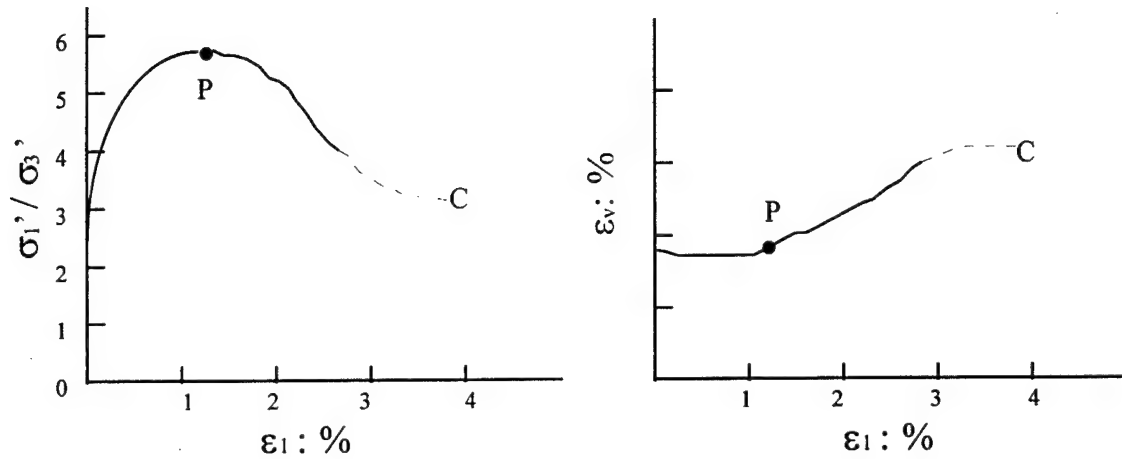
Figure 1.10 Stress-Strain Behavior of Dense Sand
(Bolton, 1986)

Mohr's circle is used to determine the value of Ψ. Figure 1.11 shows Mohr's circle with the principal strain differences needed to calculate Ψ. This assumes a plain strain condition. There are several equations that can be used to compute Ψ from Mohr's circle (see equations 1.1 a,b,c). However, equation 1.1c is used most often for this research. This formula requires only one quantity $(d\varepsilon_1/d\varepsilon_3)_{max}$.
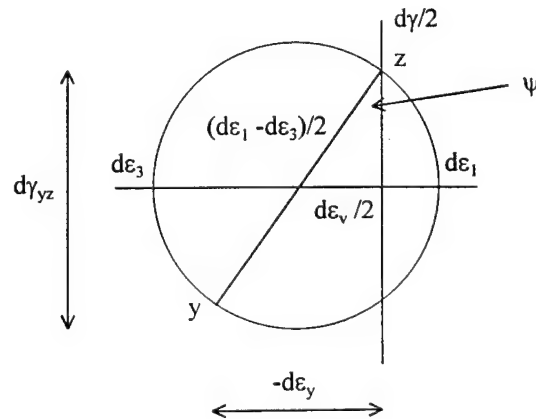
Figure 1.11 Angle of Dilation (Ψ) -Mohr Circle

(Bolton, 1986)

$$\sin \psi_{max} = \left[-\frac{d\varepsilon v / 2}{(d\varepsilon 1 - d\varepsilon 3) / 2} \right] \tag{1.1a}$$

$$\sin \psi_{max} = \left[-\frac{(d\varepsilon 1 + d\varepsilon 3) / 2}{(d\varepsilon 1 - d\varepsilon 3) / 2} \right] \tag{1.1b}$$

$$\sin \psi_{max} = \left[-\frac{(d\varepsilon 1 / d\varepsilon 3)_{max} + 1}{(d\varepsilon 1 / d\varepsilon 3)_{max} - 1} \right] \tag{1.1c}$$

Schantz and Vermeer (1996) noticed that the angle of dilation can be computed from a standard triaxial compression test by using equation 1.2.

$$\sin \psi_{max} = \left[-\frac{(d\varepsilon v / d\varepsilon 1)_{min}}{2 - (d\varepsilon v / d\varepsilon 1)_{min}} \right] \tag{1.2}$$

This equation reduces to equation 1.1c when replacing the volumetric strain term (ε_v) with the equivalent term of $\varepsilon_1 + \varepsilon_3$. This is true since ε_2 drops out of the equation for a plain strain case, as is the condition of this testing. Zitouni (1988) introduced a third method for computing the angle of dilation. In this method, he uses the formula

$$\sin \psi = \left[-\frac{1 + (d\varepsilon 3 / d\varepsilon 1)}{1 - (d\varepsilon 3 / d\varepsilon 1)} \right] = \left[-\frac{1 - \tan\theta}{1 + \tan\theta} \right] = \tan[\theta - \Pi / 4] \tag{1.3}$$

Where θ is the angle found from a plot of ε_1 versus ε_3 (figure 1.12)
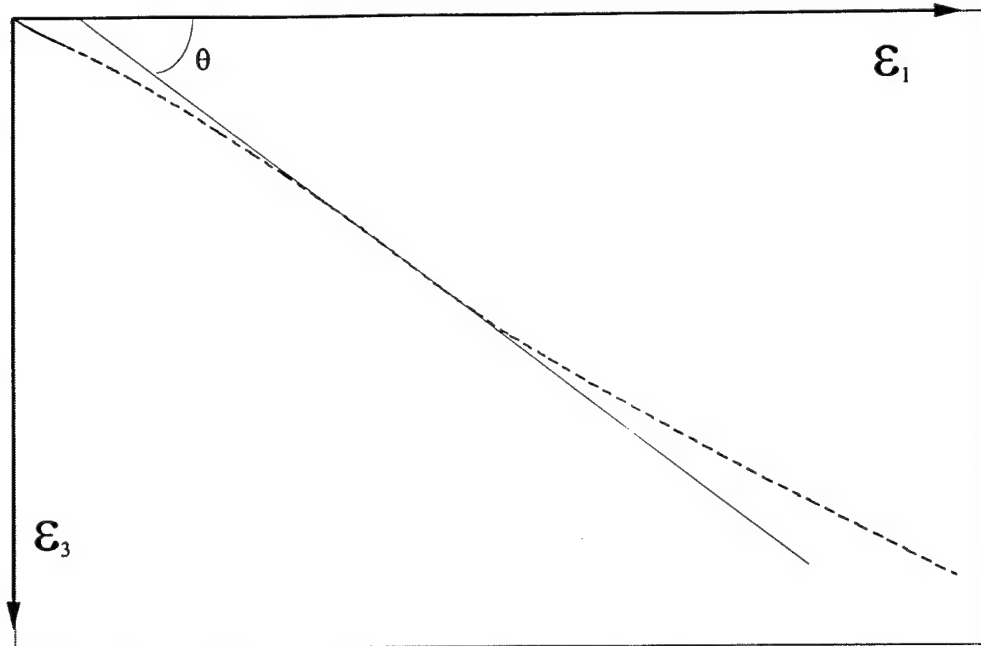
Figure 1.12 Zitouni's Method for Determining Ψ

Arthur et al. (1977) and Vardoulakis (1980) suggested that since Coulomb's theory overestimated the shear band angle and Roscoe's theory underestimated it, that a combination of these two theories should result in greater accuracy. This hypothesis stated that the angle of failure will occur at an angle of ($\pi/4 - (\psi+\phi')/4$) with the major principal direction.
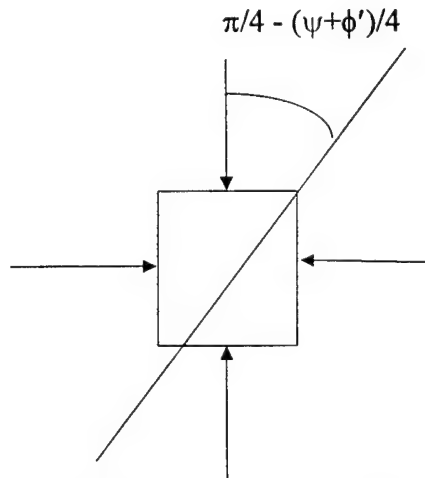
Figure 1.13 Arthur-Vardoulakis Theory

Still further research proposed that Coulomb's, Roscoe's, and Arthur-Vardoulakis' formulas were each valid depending on the particle sizes of the soil. Koenders, Arthur & Dunstan (1990) stated that the average grain size (D_{50}) was the determining factor when deciding on the most applicable formula. It was proposed that for sands with "small" grain sizes ($D_{50} \leq 0.65$ mm), Coulomb's theory would prove to be the most accurate. Conversely, for "large" grained sands ($D_{50} \geq 0.77$ mm), Roscoe's theory would give the best prediction. For the intermediate range, Arthur-Vardoulakis' theory should be used. Table 1.1 demonstrates this principle.

Table 1.1 Shear Band Equations as a Function of Average Grain Size (Koender et. al., 1990)

	Shear Band Inclination		
Coulomb	$(\pi/4 - \phi'/2)$		
Arth.-Vard.		$(\pi/4 - (\psi+\phi')/4)$	
Roscoe			$(\pi/4 - \psi/2)$
	$D_{50} \leq 0.65$	$0.65 > D_{50} > 0.77$	$D_{50} \geq 0.77$

Average Grain Size (mm) (D_{50})

1.4 Extent of Research

1.4.1 Selected Method of Study

The goal of this thesis is to expand the current understanding of the shear banding phenomenon. Recent research at Case Western Reserve used a fine-grained sand (Cope, 1997). The results from that study would not be complete without a comparable study

using a coarse-grained sand. This paper presents the findings of the testing done on that sand and compares the results with the previous studies.

A wide variety of tests were conducted to monitor the onset and propagation of the bifurcation process. A torsional hollow cylinder device was chosen to investigate the influence of a wide array of stress combinations and loading conditions. These tests exactly match the conditions selected for Cope's research. The methods of monitoring the shear band formation remain the same. These procedures are discussed in greater detail in subsequent chapters.

1.4.2 Research Objectives

The systematic approach of this research makes it possible to determine:

- The effect of various testing conditions on shear banding including: stress path, confining pressure, relative density, and direct vs. generalized testing.
- The angle of dilation (Ψ) for each test.
- The theory that best predicts the shear band inclination.
- The effect of grain size on shear banding.

1.5 Thesis Outline

- **Chapter 2** gives an explicit description of the specific testing schedule. It also gives a detailed summary on how a test is set up and conducted.
- **Chapter 3** presents the method by which the shear bands are monitored and analyzed, including specific information on the digitization process.

- **Chapter 4** summarizes the results obtained from the testing program. In this chapter, the angles of dilation from each test are listed.

- **Chapter 5** tabulates the failure angles as well as lists the angles predicted by each of the theories mentioned. The effect of each parameter on the shear band angle are also discussed.

- **Chapter 6** gives the results and conclusions of this program of study. This section presents suggestions for any future studies which might extend this research.

- **Appendix B** presents the results from the digital image analysis. This information includes data on the shear band inclination, strains in and around the shear band, and the width of the shear band.

Chapter Two

Experimental Program

2.1 Introduction

To complete our research on shear banding, the previously established testing method used for the last phase of the project was implemented for this stage (Cope,1997). While the method remained the same, the particular sand used was varied. For this section, as in the previous one, a non-cohesive, angular sand was tested. The major difference between the two media was the grain size distribution. Loire sand was chosen for this phase due to its average grain size in comparison to the previous LSI 30 sand. The Loire sand had significantly larger particle diameters versus the LSI 30, which could be described as a fine-grain sand. Figure 2.1 gives the grain size distribution curves for both sands. With the medium and the testing process determined, all the same parameters involved were researched. These include variations in the stress paths, relative density, effective confining pressure and the type of loading control (generalized versus direct testing). Each of the mentioned parameters are explained thoroughly in the following sections.

2.2 Testing Material

The sand used for this research was named Loire sand after the region in France from where it was collected. This sand was selected due to the desired particle sizes it possessed. To thoroughly complete the testing process, several ASTM standard tests were conducted on the Loire sand. These tests were needed to accurately describe and classify the sand. The tests performed included the determination of the void ratio

Grain Size Distribution
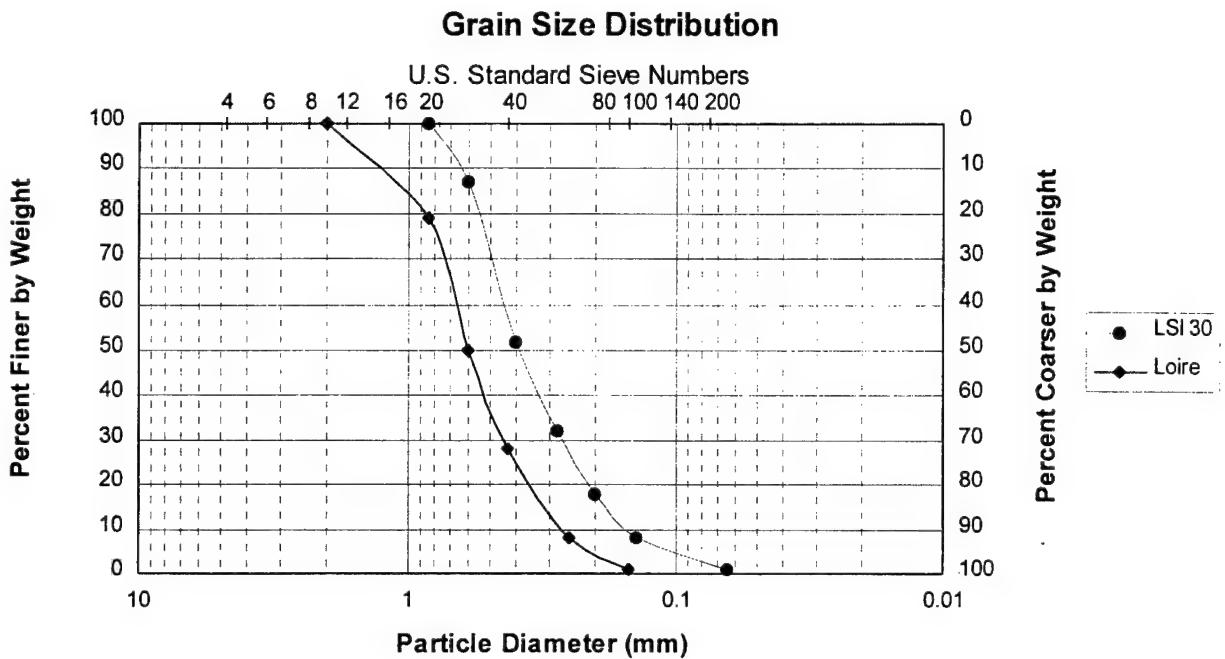
Figure 2.1 Grain Size Distribution of Loire versus LSI 30 Sand (Liang, 1995)

Table 2.1 Index Properties and Classification of Loire versus LSI 30 Sand (Liang, 1995)

Sand Name	Loire	LSI 30
USCS Group	SP	SP
Specific Gravity	2.64	2.66
Maximum Void Ratio	0.76	0.83
Minimum Void Ratio	0.49	0.52
D_{50}	0.60 mm, 0.023 in	0.39 mm, 0.015 in

(maximum and minimum), the relative density, and the particle size distribution. The information collected from these tests is summarized and compared to the corresponding data from the LSI 30 sand in Table 2.1

2.3 Experimental Investigation

2.3.1 Variation of Parameters

The variables thought to influence the propagation of the shear band were the confining pressure, the relative density, the mean stress, and the inclination of the major principal stress with respect to the vertical axis. These parameters were systematically varied to determine their individual influence on the angle of the shear band. As a result, a total of 35 separate tests were conducted. These tests were broken down into sets of five. Each set was subjected to the same conditions with the exception of the inclination of the principal stress.

Of the seven sets of tests run, three were on loose samples and four were on dense samples. The initial relative density of these samples were chosen to be 50% and 80%, respectively. The relative density of a sand is typically one of the most influential variables in the behavior of sand. For this reason, the accuracy of the initial density was carefully calculated for each test. Only samples showing an actual density within plus or minus three percent of the desired density were kept; and therefore, repeatable accuracy was extremely important. Table 2.4 lists the averaged initial relative densities.

Two types of tests were conducted; generalized and direct. In a generalized test, both the axial and cell pressures were changed throughout the test such that the mean stress remained constant. In a direct test, the axial stress was changed but the cell

pressure remained constant. Torsional stresses have no effect on the mean stress. Only one set of direct tests was run to see if the variation in the mean stress during a given test affected the angle of shear banding. The other six sets were all generalized.

There were three different initial confining pressures chosen, namely 40 psi (276 kPa), 60 psi (414 kPa), and 80 psi (552 kPa). However, since a backpressure of 10 psi (69 kPa) was used on all tests, the effective confining pressures were reduced to 30 psi (207 kPa), 50 psi (345 kPa), and 70 psi (483 kPa). Since strength depends on effective stresses, these values were the ones worthy of note. These values were chosen to maintain consistency with the previous tests conducted on fine sand.

Table 2.2 Inclination of Principal Stresses
(Cope, 1997)

Inclination of Principal Stresses (β)	0°	30°	45°	60°	90°
Description	Pure Compression	Compression Torsion	Pure Torsion	Extension Torsion	Pure Extension

Finally, the last parameter studied was the inclination of the principal stress with respect to the vertical axis of symmetry. This was the most important parameter studied because each of the three theories predicts the shear band inclination from this reference angle. Five different angles were chosen. Table 2.2 shows these angles and the type of test needed to produce such an inclination. Most, if not all, theories predicting the angle of shear banding include a term describing the stress path. This was the reason why all of the seven sets of tests were grouped into subsets of five.

By systematically varying the type of test conducted and analyzing the resultant

shear band angle produced, all the proposed variables and their effects were studied. In addition to this, several theories predicting the angle of the shear band were analyzed to determine the most accurate. Many of these theories incorporate the angle of dilation in their prediction. For this reason, all the tests conducted were drained since the volume change was an essential component in the dilation angle's computation.

2.3.2 Case Data Base Adopted Nomenclature

Several years ago at Case Western Reserve University, a data base was developed to systematically catalog all testing done on soil samples (Saada, 1993). The results of many years of research and testing were recorded using this program. To maintain consistency, the same system of notation was adopted to uniquely identify each test. The test identifier code is a string of six characters to describe the type of test, the relative density, the initial confining pressure... etc. The first character is either a G or D to denote a general or direct test. The second space is to describe the relative density of the specimen. Here, an L represents a loose sample of 50% while an N is for the dense sample of 80%. The next two characters are used to indicate the initial confining pressure and the inclination of the of the principal stress, respectively. The fifth space is used to describe the shape of the sample. Some possible shapes include the standard triaxial form or cube. However, since all of the conducted for this project were of the hollow cylinder, dog-bone form, every test uses the character T. Finally, the last space refers to the level of saturation for each test. A P indicates partial saturation while an F denotes complete or full saturation. Table 2.3 demonstrates this nomenclature while Table 2.4 lists the entire array of tests.

Table 2.3 Test Nomenclature
(Saada et. al., 1993)

Test Identification Format : ABXYCD	
A = Type of Test	A = G ⇒ Generalized A = D ⇒ Direct
B = Relative Density	B = L ⇒ D_r = 50% (Initial) B = N ⇒ D_r = 80% (Initial)
X = Initial Confining Pressure	X = 1 ⇒ σ'_c = 30 psi X = 2 ⇒ σ'_c = 50 psi X = 3 ⇒ σ'_c = 70 psi
Y = Inclination of Principle Stress	Y = 0 ⇒ β = 0° Y = 2 ⇒ β = 30° Y = 4 ⇒ β = 45° Y = 6 ⇒ β = 60° Y = 8 ⇒ β = 90°
C = Shape of Specimen	C = T ⇒ Dog Bone
D = Amount of Saturation	D = P ⇒ Partial D = F ⇒ Full

Table 2.4 Complete List of Testing Program

Hollow Cylinder Tests (Dogbone) 1/50 motor speed or 0.012 in/min, static Drained specimen						
Test #	Name	β/b	σ_c' (psi)	D_r Target	D_r Avg. Actual	Test Type
71	GL10TF	0°/0.00	30	50	53.2	Generalized
72	GL12TF	30°/0.25	30	50	53.2	Generalized
73	GL14TF	45°/0.50	30	50	53.2	Generalized
74b	GL16TF	60°/0.75	30	50	53.2	Generalized
75	GL18TF	90°/1.00	30	50	53.2	Generalized
76a	GL20TF	0°/0.00	50	50	53.2	Generalized
77	GL22TF	30°/0.25	50	50	53.2	Generalized
78a	GL24TF	45°/0.50	50	50	53.2	Generalized
79	GL26aTF	60°/0.75	50	50	53.2	Generalized
80	GL28TF	90°/1.00	50	50	53.2	Generalized

81b	GL30TF	0°/0.00	70	50	53.2	Generalized
82	GL32TF	30°/0.25	70	50	53.2	Generalized
83a	GL34TF	45°/0.50	70	50	53.2	Generalized
84a	GL36TF	60°/0.75	70	50	53.2	Generalized
85	DL38TF	90°/1.00	70	50	53.2	Direct
86a	GN10TP	0°/0.00	30	80	79.4	Generalized
87a	GN12TP	30°/0.25	30	80	79.4	Generalized
88	GN14TP	45°/0.50	30	80	79.4	Generalized
89	GN16TP	60°/0.75	30	80	79.4	Generalized
90	GN18TP	90°/1.00	30	80	79.4	Generalized
91a	GN20TP	0°/0.00	50	80	79.4	Generalized
92	GN22TP	30°/0.25	50	80	79.4	Generalized
93a	GN24TP	45°/0.50	50	80	79.4	Generalized
94d	GN26TP	60°/0.75	50	80	79.4	Generalized
95	GN28TP	90°/1.00	50	80	79.4	Generalized
96	GN30TP	0°/0.00	70	80	79.4	Generalized
97a	GN32TP	30°/0.25	70	80	79.4	Generalized
98	GN34TP	45°/0.50	70	80	79.4	Generalized
99c	GN36TP	60°/0.75	70	80	79.4	Generalized
100a	DN38TP	90°/1.00	70	80	79.4	Direct
101a	DN10TP	0°/0.00	30	80	79.4	Direct
102	DN12TP	30°/0.25	30	80	79.4	Direct
103	DN14TP	45°/0.50	30	80	79.4	Direct
104	DN16TP	60°/0.75	30	80	79.4	Direct
105	DN18TP	90°/1.00	30	80	79.4	Direct

2.4 Specimen Preparation

2.4.1 Specimen Shape

For this particular study, a "dog-bone", hollow cylinder specimen shape was selected. There were several reasons for this decision. This shape leads to the formation of the shear band in the middle of the sample due to its thicker ends, as well as minimizes complications due to boundary constraints. In addition, the thin wall shape helps to obtain a more uniform torsional stress. It allows for easy determination of torsional and

axial stresses, which were crucial in providing feedback to maintain constant mean

stresses. The paper "Hollow Cylinder Torsional Devices: Their Advantages and

Limitations" (Saada, 1988), further illustrates the rationale behind the selection of this

shape. Every effort was made to prepare identical samples. Table 2.5 gives typical

dimensions:

Table 2.5 Typical Specimen Dimensions

Outside Diameter (ends)	2.77 in	7.03 cm
Outside Diameter (middle)	2.60 in	6.60 cm
Inside Diameter	2.0 in	5.08 cm
Height of Middle Section	4.1 in	10.41 cm
Height of Overall Specimen	5.1 in	12.95 cm
Volume	11.80 in^3	193.40 cm^3

2.4.2 Specimen Preparation

Since the approximate volume of the sample and the properties of the soil being

used were known, the weight of the soil to be used could be measured. For these

experiments, two different soil sample weights were used. These corresponded to the

50% and 80% relative densities. After the soil weight was determined, the following

steps were taken to build the specimen:

1. Select two membranes (outer and inner) and check each for any leaks. Each

membrane must be intact. Trim the ends off to obtain the desired length and

measure the thickness of each membrane.

2. Affix both membranes to the bottom cap using two concentric rubber bands and
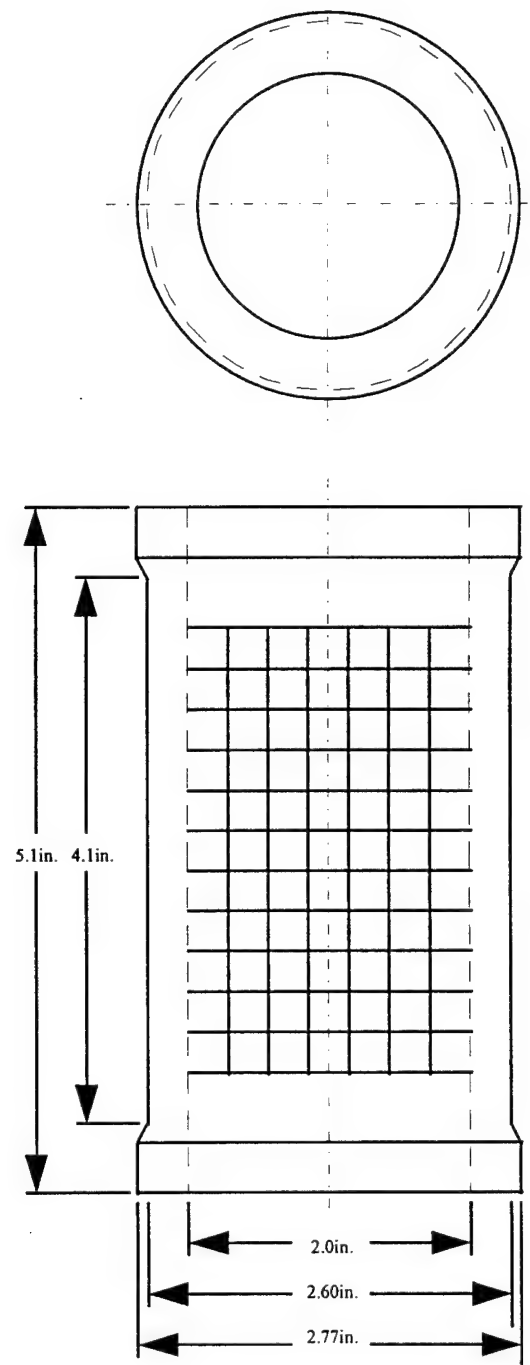
Figure 2.2 "Dog Bone" Shaped Specimen

a hose clamp. Place the outer mold on the bottom cap and around the outer membrane.

3. Apply a vacuum to the outer mold to pull the membrane taut. Slide the inner mold inside the smaller membrane and tighten the fastener to fix it into place.

4. Place the sand between the two membranes and tamp the sides to obtain the pre-selected relative density.

5. Affix the top cap over the existing specimen and fasten it to the sample, again using rubber bands and a ring clamp. Figure 2.3 gives a profile view of the sample as it look at this point.

6. Draw water into the sample to roughly fill the void spaces using a vacuum. Place the specimen sample in the freezer for at least two hours to freeze the water.

7. Take the outer mold off the sample and roll down the membrane down, exposing the surface of the sample. Thaw the outer layer of ice off the sample to create a dry surface onto which an ink grid is stamped.

8. Pull the membrane up over the sample and apply a vacuum to the specimen to adhere both membranes to their respected surfaces. Measure the dimensions of the sample by taking several measurements and finding their average. For instance, four height measurements are taken for each sample and their values are averaged to obtain the best value. The same procedure is used for both the outside and inside diameters. All of the measurements are then used to determine the sample's actual volume and the corresponding relative density.

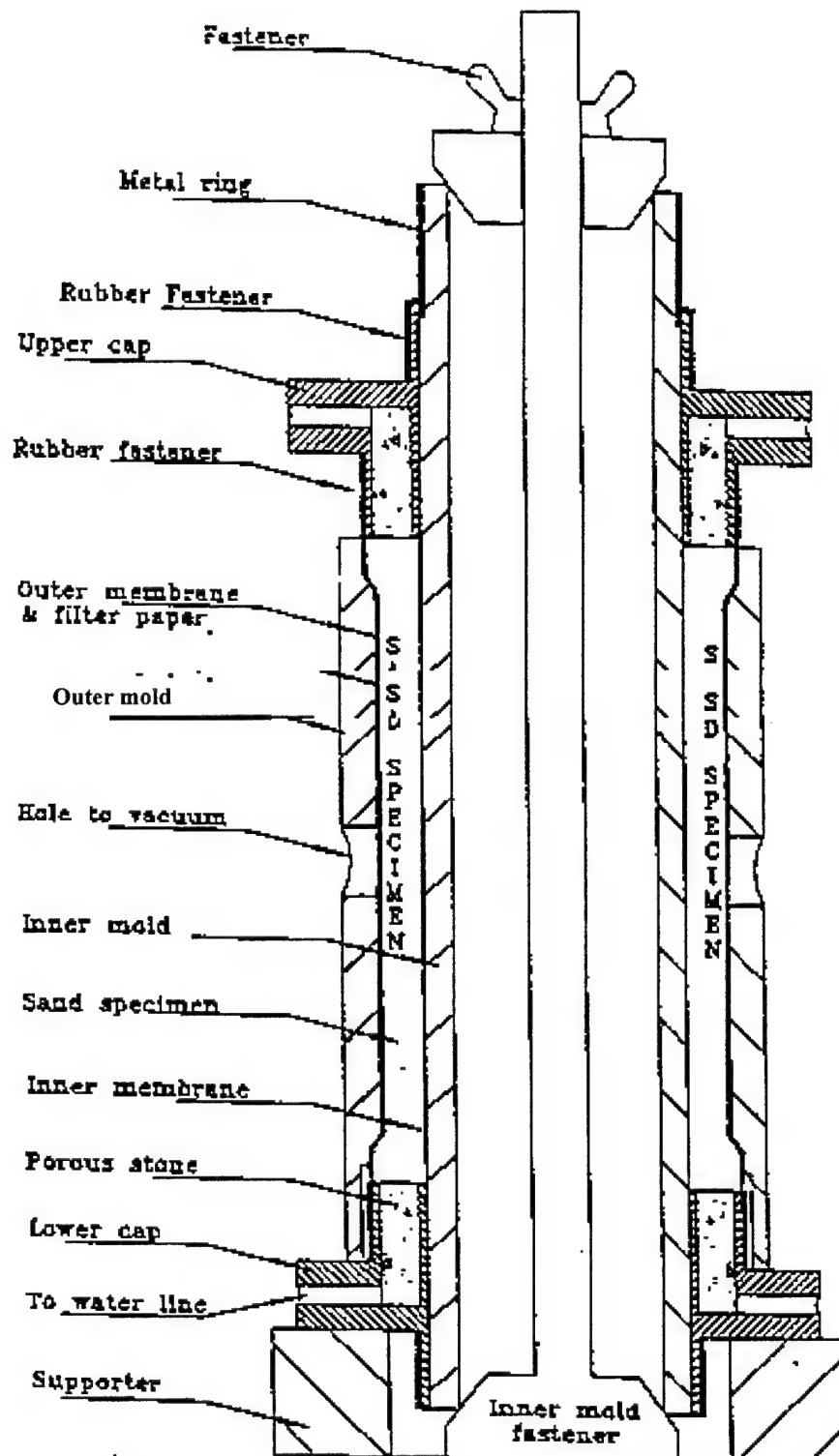9. Secure the specimen to the cell and place a capped plexiglass cylinder over the

Fastener

Metal ring

Rubber Fastener

Upper cap

Rubber fastener

Outer membrane
& filter paper

Outer mold

Hole to vacuum

Inner mold

Sand specimen

Inner membrane

Porous stone

Lower cap

To water line

Supporter

Inner mold
fastener

Figure 2.3 Profile of Specimen and Preparation Mold Configuration

entire setup to seal the sample inside.

10. Pressurize the cell slightly to support the now thawed sample and flood the cylinder with silicon oil. The oil will magnify the grid on the specimen, making it easier for the cameras to capture images. The sample is now ready for saturation.

2.4.3 Sample Saturation Procedure

For the volume change of the sample to be accurately measured, the specimen needed to be completely saturated with distilled water. The following procedure was used to fulfill this requirement.

1. Connect a line to the sample to supply carbon dioxide. The source of the gas was at a pressure of just over atmospheric, namely 1 psi gauge. Carbon dioxide was used to force all the air from the specimen.

2. The carbon dioxide was fed to sample via the same inlet hose but the outlet was varied between the other three hoses. Each of the three outlets were open for at least 10 minutes to allow for sufficient gaseous saturation.

3. The gas line was then replaced with a deaired water line. Again, as with the carbon dioxide, the inlet hose remained the same but the outlet varied. For the water line, at least 40 milliliters of water was passed through each hose. This cycle was repeated twice with the water pressure at 1 psi.

4. After the water was fed into the specimen with the initial cell pressure at 5 psi, the cell pressure was increased to 15 psi and a back pressure on the water line was brought up to 10 psi. This was done in small increments to keep the sample at the

same approximate effective pressure (cell pressure minus back pressure).

5. As with the previous step, water was passed through each hose. This time, however, only 20 milliliters of water was passed through each outlet hose but the cycle was still repeated twice.

6. The specimen then sat under these conditions to allow for all of the remaining carbon dioxide to dissolve into the water. Usually this was done overnight but at least for three hours.

7. Just before the application of the deviator stress, water was passed through each line again to remove any remaining gas.

8. Finally, one of the drainage lines was connected to a pressure transducer to measure the volume change by reading the water level in a vertical pipette.

2.4.4 Consolidation of Specimen

At this stage of preparation, the cell pressure was 15 psi (103.43 kPa) above atmospheric. This pressure was raised to reach the 30 psi (207 kPa), 50 psi (345 kPa), or 70 psi (483 kPa) effective initial confining pressure, depending on the test specifications. The effect of this increase tended to consolidate the specimen. Since the volume change was measured, the influence of the effective mean stress on relative density and strength can be determined.

2.5 Testing Procedure

2.5.1 Testing Equipment

The capabilities of the testing device made it possible to accurately measure seven channels of information. These included axial displacement both inside and outside the

cell, axial force and torque, rotational displacement, cell pressure and volume change. By incorporating the use of LVDT's, RVDT's, strain gages...etc., all of this information was converted to corresponding voltages and fed into a control computer. The computer was also connected to a pneumatic control panel that regulated the axial force and cell pressure accordingly to maintain a constant mean stress.

2.5.2 Data Acquisition

For the specific purposes of these experiments, a program entitled ACQ_MENU.EXE was developed. The capabilities of this program are as follows:

- To print specific experimentation information including: test date, conductor, effective initial confining pressure, back pressure, and loading control.
- To list material properties including: sample name and type (I.E. Loire sand), USCS classification, maximum and minimum void ratios, and specific gravity.
- To print the measured sample dimensions including: height, inner and outer diameters, and post-consolidation height and volume changes.
- To give input control information including: data input rate and duration, scan upper and lower bound limits, channel names, calibration coefficients, and maximum and minimum voltage limits.
- To give visual data information including: real time plot of all seven channels as they are received from the testing device.

The testing process produced a data file containing somewhere between 1200 and 3600 data points for each channel, depending on the type of test run. This data file contained all the information needed to analyze the test. However, back up acquisition

recorders were used to collect redundant data to ensure that the testing information was still gathered in the event of a computer malfunction. There were four separate graphic plotters to collect all seven channels of data.

In addition to digital and plotter data, video images were recorded as well. For all torsion tests, digital cameras were set up to capture the sample from four different views. When spliced together, these images gave a complete depiction of the sample. At predetermined times during the testing procedure, "snapshots" of the camera images were taken. These pictures were the ones that would later be digitized to complete the analysis process. In addition to the captured images, a VCR was used to record the slow progression of shear banding in case a picture turned out poorly.

2.6 Data Analysis and Parameter Calculation

Several computer programs aided in the processing of raw test data and determination of key parameters. Since testing was done on samples with two different relative densities, namely 50% and 80%, the weight of the sand used in each case needed to be known. This was calculated by the same program used to determine the relative density. Also, the raw data received from testing often contained small variations commonly referred to as "noise". In order to compensate for this unavoidable occurrence, a program was developed to perform polynomial regression to filter out the background "noise" and greatly reduce the number of necessary data points.

The dimensions of each sample varied little from test to test. Therefore the volume of each sample was relatively constant. By knowing significant properties of the sand being tested as well as the volume, a weight of sand could then be determined.

Obviously, there were two separate weights used to get the different desired relative densities. A program named VOID.EXE was helpful in performing the necessary calculations. An input data file was created for each test with all the pertinent data including measured specimen dimensions, weight of sand used, and specific material properties such as the void ratios. From this data file, the program could perform the necessary calculations and give the particular sample's relative density. When first determining the weight of soil to use, a trial and error approach was required. Typical sample dimensions were entered in the program along with a trial weight. This trial weight was varied until the relative density matched the required one.

To analyze the raw data from testing, a program was created to first filter out any unwanted noise and then compress the information into a standard form. This program, FILTER.EXE, used polynomial regression to accurately model the acquired data. From these trend lines, forty points were chosen which effectively compressed the information into the standard format. This served two useful purposes. First, it cut down on the size of the acquired data file and, second, it standardized the information into a form where it could be easily analyzed.

The program, DATCNV3.EXE, was used to take the filtered data file and summarize the information. Settings in the program enabled the output to contain data in both English and SI units. This program also modified the data into the standard format used by the Case Western Reserve University data base. This allowed for easy additions to the data base. Each test was processed by the above programs to completely record the testing results. Figures 2.4 and 2.5 show typical outputs from these programs.

****

This program determines:
1) the expected void ratio and the needed weight of sand,
   after giving the volume of the mold, minimum and maximum
   void ratio, expected relative density and specific gravity;
2) the actual void ratio and relative density obtained,
   after measuring the actual volume of sample.

****************** Liqun Liang (03/21/96) ******************

The thickness of inner membrane	=	0.0121 (in)
The thickness of outer membrane	=	0.0119 (in)
The relative density	=	50.0082 (percentage)
The minimum void ratio	=	0.4900
The maximum void ratio	=	0.7600
The specific gravity	=	2.6400
The volume between two molds	=	12.2000 (in^3)
The volume between two molds	=	12.2519 (in^3)
The weight (g)	=	324.8000 (g)
The weight (lb)	=	0.7161 (lb)
The expected void ratio	=	0.6250
The inner diameter with membrane	=	1.9525 (in)
The outer diameter with membrane	=	2.6370 (in)
The height measured /w caps	=	8.4575 (in)
The inner diameter of specimen	=	1.9768 (in)
The outer diameter of specimen	=	2.6133 (in)
The height of specimen	=	5.0475 (in)
The height of middle specimen	=	4.1000 (in)
The volume of specimen	=	12.2036 (in^3)
The volume of middle specimen	=	9.4077 (in^3)
The actual Gamma_d	=	1.6250 (g/cm^3)
The actual void ratio	=	0.6255
The actual relative density	=	49.8290 (percentage)

Figure 2.4 Typical Output From VOID.EXE Program
(Test #77)

```
---- Test ID ----
Test #77; Torsion-Compression; Drained w/ Vol. Measured
Test Date                 = 03/18/97
Consolidation             = Normal
Back pressure (psi)       = 10.000
Eff. Con. Press (psi)     = 50.000
Add. Axial Stress (psi)   = 0.000
Loading design            = Static
Loading control           = Rotation
Loading rate              = Motor 1/50
Height control            = Free

---- Material ID ----
Name                      = LOIRE
Type                      = Sand
Group symbol              = SP
Specific gravity          = 2.640
Relative density          = 0.670
Minimum void ratio        = 0.4900
Maximum void ratio        = 0.7600

---- Record Information ----
Ch 0 Torque (in)          ( 50.00 inlb/V)
Ch 1 Axial Force (in)     (100.00 lb/V  )
Ch 2 RVDT                 ( 10.00 °/V   )
Ch 3 LVDT (IN)            ( 0.05 in/V   )
Ch 4 LVDT (Out)           ( 0.10 in/V   )
Ch 5 Cell Pressure        ( 20.00 psi/V )
Ch 6 Volume Change        ( 2.50 ml/V   )
Total record point number = 41
Scan rate (number/sec)    = 1.0
Scan duration (sec)       = 3407.0
Elapsed time (sec)        = 3407.7

---- Specimen Dimension ----
Height  (in)              = 4.100
Height change (in)        = 0.005
Inner diameter (in)       = 1.950
Outer diameter (in)       = 2.577
Initial volume (in^3)     = 9.408
Volume change (in^3)      = 0.269

---- Others ----
Beta (deg.)               = 30.18
b_value                   = 0.25
Angle of Friction (deg.)  = 51.17
```

Figure 2.5 Example of Print Out From DATCNV3.EXE (Test #77)

Chapter Three

Digital Image Process and Measurements

3.1 Introduction

To assist in the accuracy of analysis, a new digital imaging process was developed. This procedure involves capturing pictures of the specimen during testing with the use of digital cameras. The images obtained from this process were then, with the aid of a mathematical computer program, analyzed to determine the angle of shear banding. By using this new procedure, a great deal of information was obtained.

3.2 Image Acquisition and Camera Setup

Each hollow cylinder specimen had two grids stamped on the surface. Those two grids covered nearly the entire surface area of the sample. To ensure completeness, four separate cameras were used to view the two grids; two per side. The four cameras were mounted on brackets which were fixed in place. For this reason, the cameras did not move during the test despite the fact that the sample was subjected to rotational displacements. This did not impose a problem, however, since the top of the specimen was fixed as well and therefore a constant reference was maintained.

Figure 3.1 schematically represents the image acquisition system. Here, the dashed lines represent the pathways along which images were transferred and the solid lines show the path that data and feedback control follow. Before the images were received by the first computer (PC2), a switch box was used. This device was needed to take the four separate images and send them along a common circuit. Only one image

**Figure 3.1 Schematic of Testing Setup
(Saada et. al., 1998)**
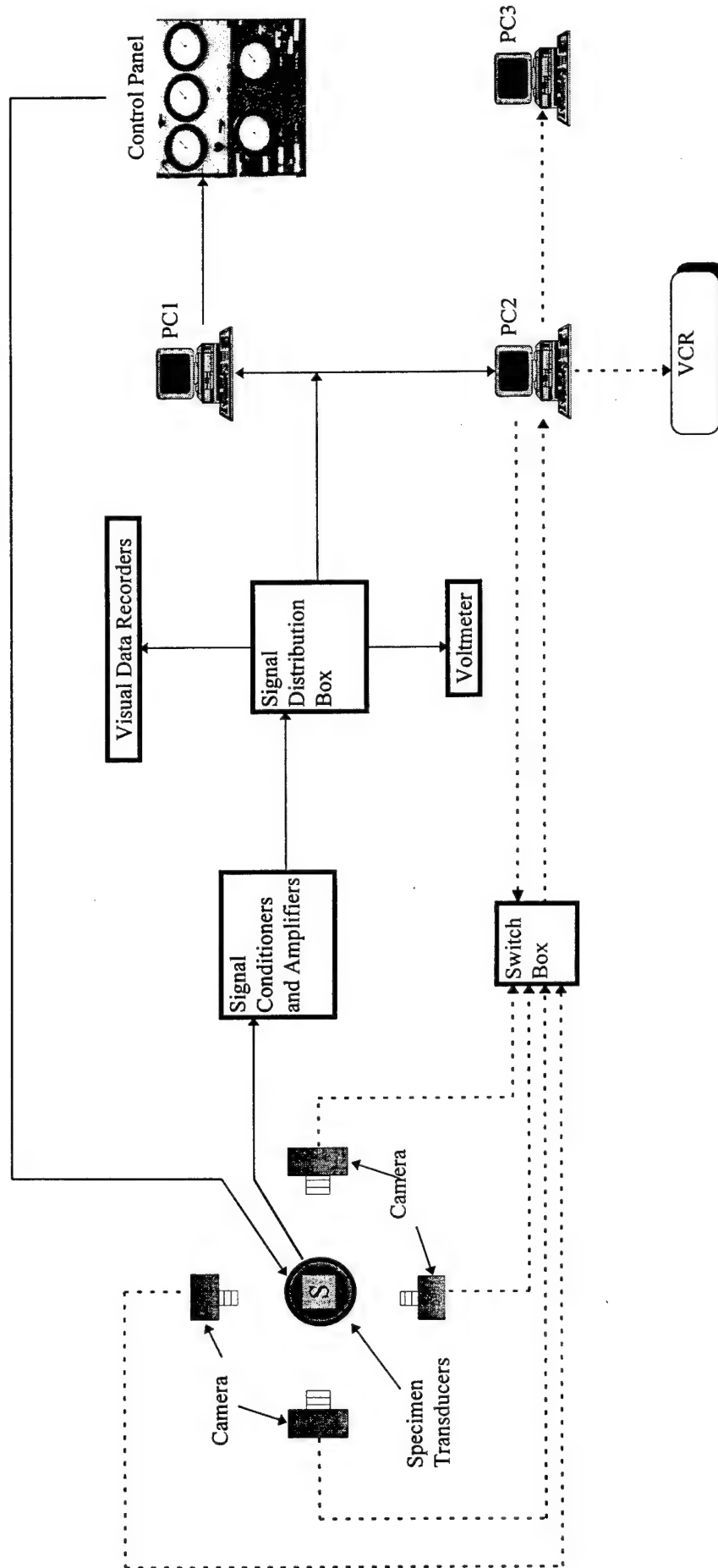
- Solid lines show the path of data acquisition and test control; Dashed lines show the path of image recording.
- PC1 records signals from transducers through a A/D board as voltages, calculates and sends out voltages to control panel through a D/A board.
- Control panel changes the voltages from PC1 to air pressure and supplies air pressure to increase/decrease axial forces and cell pressures.
- PC2 merges the voltage reading and the image, then sends the results to a VCR and PC3.
- Images are continuously recorded by a VCR and selectively by PC3.

could be transferred at a time. For this reason, the acquisition program from PC2 had a

timer programmed in to toggle the image's order. This allowed a complete set of images

to be sent every 20 to 40 seconds depending on the delay between successive images.

Once the pictures were received by PC2, they were assimilated with a template. This

effectively combined the image with information pertinent to the test in process such as

test number, date, time elapsed... etc. Figure 3.2 demonstrates a typical image collected

during a test.
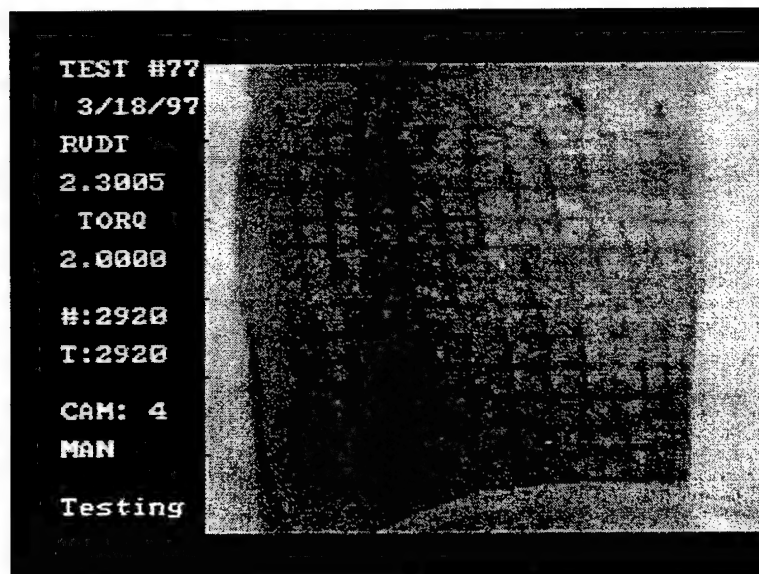
Figure 3.2 Digital Image Combined With Test Information

The images, after being merged with the template at PC2, were then sent to two

separate locations where they were recorded. First, the images were transferred to a video

cassette recorder where they were collected throughout the testing process. Typically, the

images would change every five seconds. Second, the pictures were transferred to PC3

where they were stored as "snapshots". It was these images that were later digitized. For a normal test, "snapshots" were taken at seven pre-selected times. Therefore, a total of 28 images were collected, seven images for each of the four cameras. As a precautionary measure, a standard photographic camera was also used to collect images at the same seven times. This was used only as a back-up in the event of a computer failure.

3.3 Transferal of Grid on Specimen to Digital Coordinates

3.3.1 Initial Tracing

Dr. Liqun Liang created a series of programs using the MATLAB™ software package. This process was discussed in greater detail in the paper "The Use of Digital Image Processing in Monitoring Shear Band Development" (Liang, 1996). Essentially, the digitization procedure involves bringing up the digital snapshot of the sample on a computer and tracing the grid as it appeared on the specimen. In this manner, the deformation of the sample was followed and since each grid point then had a known coordinate, the strains could then be calculated. By using a high resolution monitor, the tracing operation was done with moderate accuracy. However, when the digitized grids were checked with a 600 dots per inch (dpi) printer, the accuracy became significantly greater. In addition to this visual cross checking, a sub-program was developed with MATLAB™ to aid in the fine tuning adjustments. The digitization process is currently very time consuming since the majority of the work still needs to be done manually.

The digital cameras used for capturing images in these experiments covered an area of 3.37 inches (8.56 cm) in the horizontal direction and 3.0 inches (7.62 cm) in the vertical direction. Each camera had a resolution of 512 pixels horizontally and 492 pixels

vertically. This yielded a resultant of 154 pixels per inch (60 pixels/cm) in the horizontal direction and 164 pixels per inch (64 pixels/cm) in the vertical direction. Once an image was captured on the computer, the resolution of the image was changed to 640 pixels (H) by 480 pixels (V). This modification reduced the size of the file and saved time when recording the image. To get an idea of the accuracy of this process, one pixel is equal to roughly 0.008 inches (0.23 mm) and the average grain size of Loire sand (see table 2.1) is 0.023 inches (0.60 mm). Therefore, there are approximately 3 pixels for every grain of Loire sand giving remarkable precision.

3.3.2 Inclusion of Shear Bands in Digitized Images

The digitizing process was performed by manually tracing the intersection points of the grid stamped on the sample. This procedure worked well for initial images and images that did not have a shear band, but a problem arose when trying to digitize pictures that contained a shear band. The issue was that a shear band produces high strains along the slip plane. Bends or kinks in the otherwise smooth grid lines appeared. Those bends occurred at places other than at grid intersections. For this reason, an extra step was included for images that contained a shear band. Those images were digitized like any other image where the grid intersection points were traced, but then another separate digitizing process was performed. The shear band was traced separately
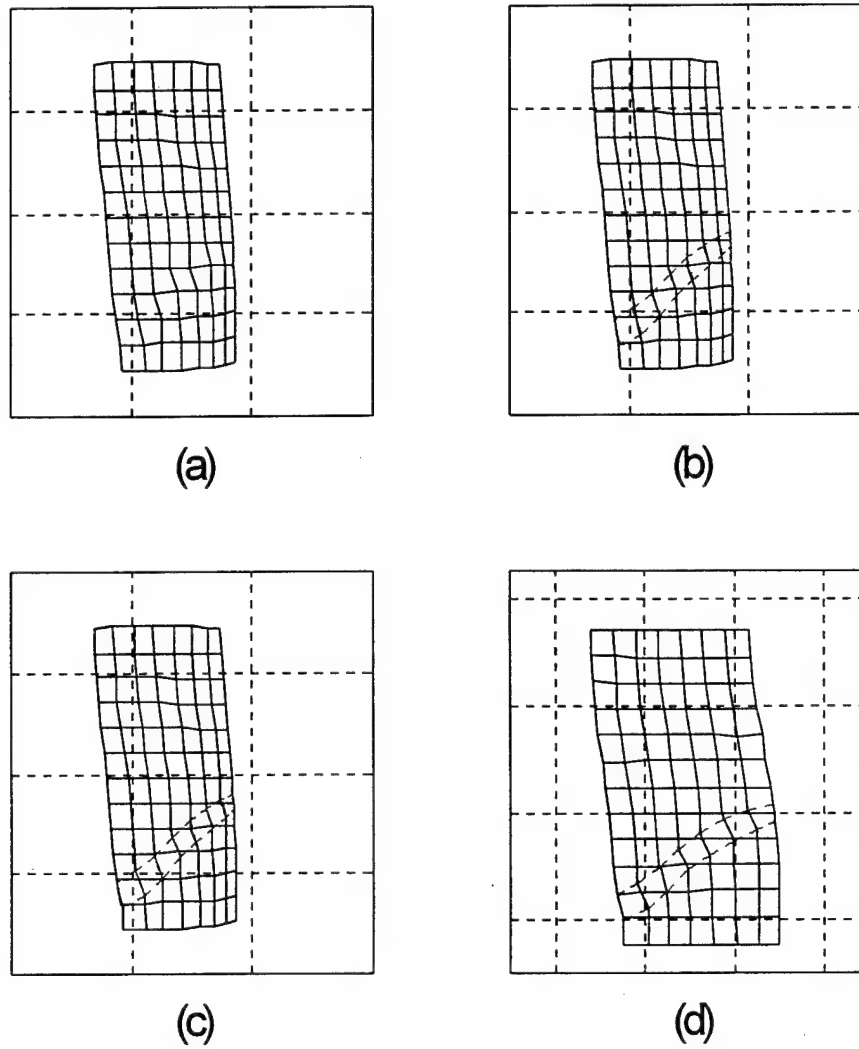
Figure 3.3   a) Initial Digitization of Grid (t=2500 sec)
              b) Shear Band Overlaid on Initial Grid
              c) Shear Band Interlaced with Deformed Grid
              d) Combined Image After Corrections

from the overall image. The bends along the vertical lines were traced. Once the two steps were completed and modified to the desired accuracy, the two images were superimposed to give a complete representation of the shear band. Figure 3.3 shows this process. Figure 3.3a is the image with only the grid intersection points, Figure 3.3b is the images where only the shear band is digitized and, finally, Figure 3.3c is the final digitized image including both necessary parts. The fourth image, Figure 3.3d, is the same as Figure 3.3c except the modifications correcting for surface curvature and refraction are implemented. These corrections are discussed in the next two sections.

3.3.3 Horizontal Corrections for Surface Curvature

Since a two dimensional picture represents a three dimensional object, a correction needed to be incorporated in the calculations for the surface curvature. Each camera recorded approximately one quarter of the samples surface. However, since the sample was cylindrical in shape, the vertical lines appeared to converge together the further they were from the center. Theoretically, the correction could be determined mathematically. This relationship was resolved by consulting Figure 3.4. and is seen below (Equation 3.1):

$$S = R \sin^{-1} \frac{L}{R} \qquad\qquad (3.1)$$

R = outer radius of the specimen

L = horizontal length from centerline of the image

S = corrected horizontal length
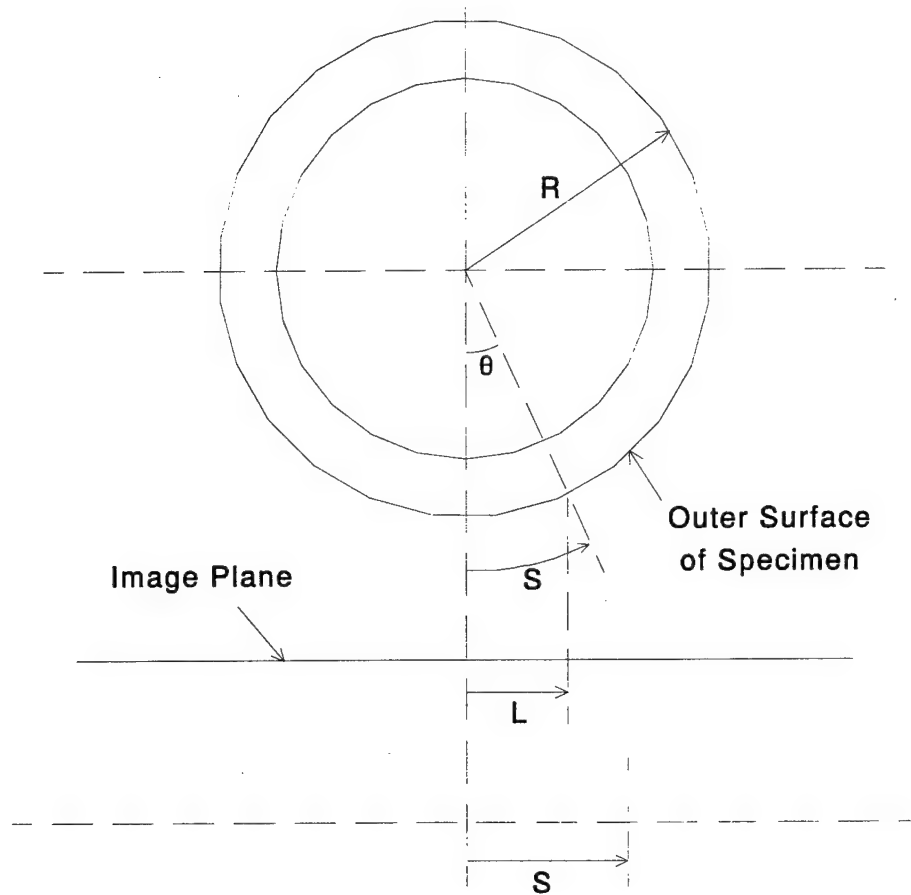
**Figure 3.4 Correlation Between Perceived Length on Image and Actual Length
on Surface of Specimen**

Equation 3.1 would be the correction factor used to find the true length between

vertical lines if the curvature of the sample was the only parameter that needed to be

considered. This, however, was not the case. One more variable needed to be examined.

The phenomenon of refraction was also considered. As Snell's Law (equation 3.2) points

out, the angle at which the image is being viewed from and the coefficients of refraction

of both the oil and the air needed to be considered.
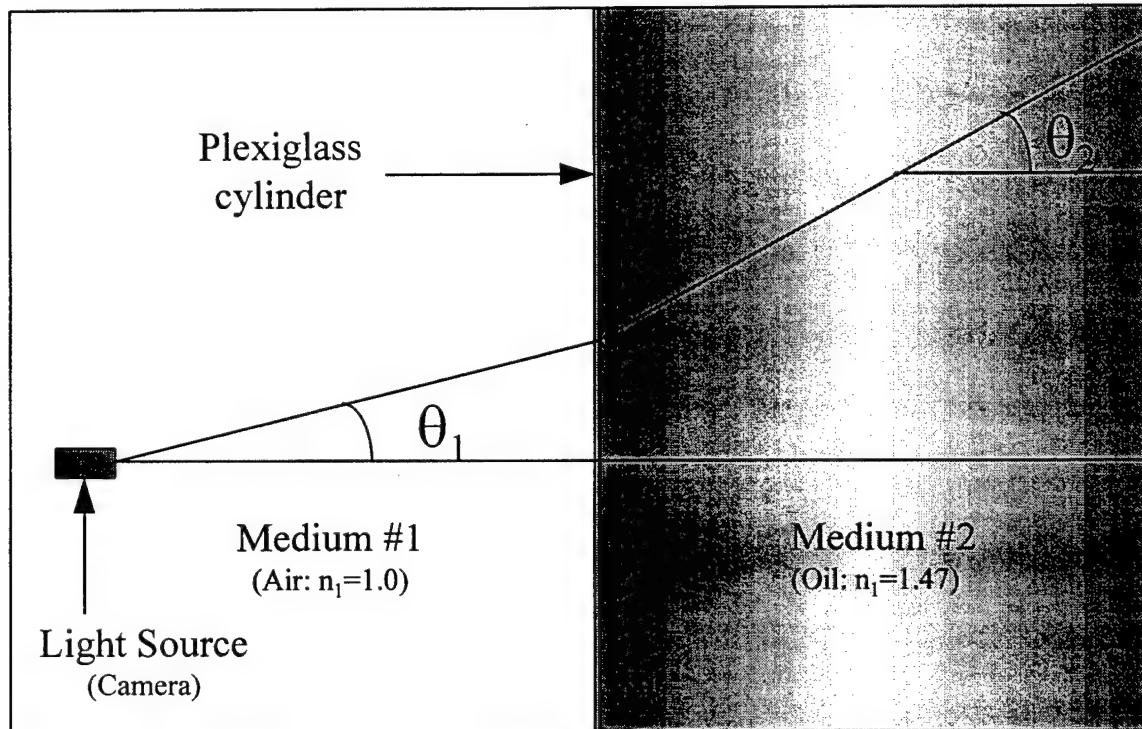
Figure 3.5 Snell's Law

$$n_1 * \sin(\theta_1) = n_2 * \sin(\theta_2) \tag{3.2}$$

n_1 = Index of Refraction of First Medium (Air)

θ_1 = Angle of Site Upon Object

n_1 = Index of Refraction of Second Medium (Oil)

θ_2 = Angle of Refraction

Obviously, when the camera was aimed directly at the sample (i.e. when $\theta_1 = 0$), there was no refraction. However, once a deviation from the center line was made, the problem of refraction needed to be considered. In addition to the oil, the plexiglass cylinder and the membrane should be considered as having contributions to the overall refraction results. A correction formula was therefore devised by using the fact that the initial grid had known horizontal dimensions. Specifically, the difference between each vertical line was 0.25 inches (0.64 cm). This gave a correlation between L (perceived length) and S (actual length) based upon the distance from the center of the specimen. To determine the center line, a curve plotting the average horizontal coordinates of each vertical line on the x-axis and the difference between the highest and lowest point of each vertical line on the y-axis was created. By finding the peak of this curve, the center line was established. The reasoning behind this was that the farther from the center a vertical line is the closer the upper and lower most points appeared. Figure 3.6 shows an example of how the center of a given image was found. With the center determined, the correction equation was found. This correction was automatically found by the MATLAB™ software for each initial image based upon the principal that each vertical line should be the same distance apart. Figure 3.7 graphically depicts the theoretical correction with the one found using the known grid spacing. The subsequent images from each camera were subjected to this same correction as the initial image from the same camera. The assumption was that the center of the image remained at the same place. This was true since every test was a combination of torsional and axial loading but never translational

Test #77; 3/18/97; Torsion-compression; ECP=50 psi; Loire; Video #3; t=0000 sec.
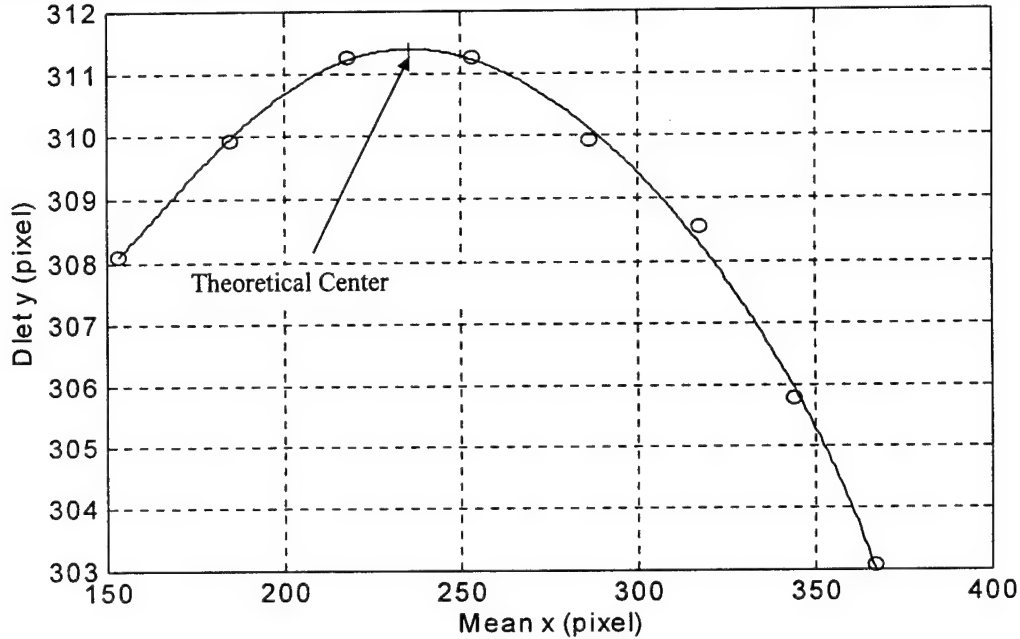
Figure 3.6 Plot Used to Determine Center of Image

movement, guaranteeing a constant center. For example, the center of the initial image

from camera #1 was found and a correction curve was found for this camera. Each image

digitized from camera #1 thereafter was subjected to this same correction. This

correction gave the most accurate information after considering the effects of refraction

and surface curvature. Figure 3.8 shows Figure 3.3d without the horizontal line

correction. In this image, the difference between vertical lines appears to be relatively

constant unlike an image without this correction (Figure 3.3c).

Test #77; 3/18/97; Torsion-compression; ECP=50 psi; Loire; Video #3; t=0000 sec.
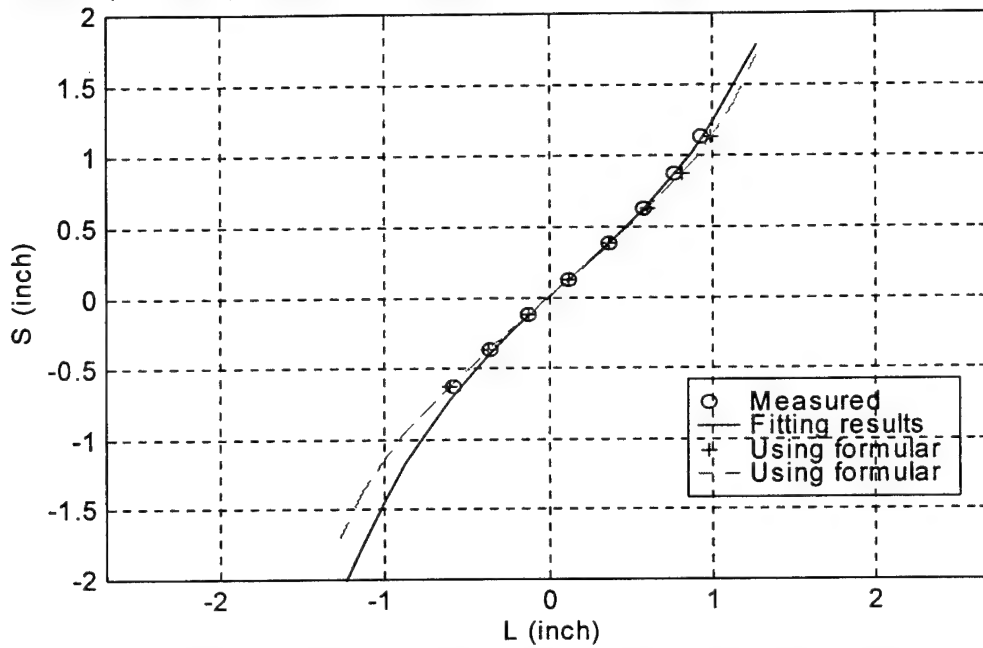
Figure 3.7 Theoretical and Regression Correction Curves

Test #77; 3/18/97; Torsion-compression; ECP=50 psi; Loire; Video #1; t=2500 sec.
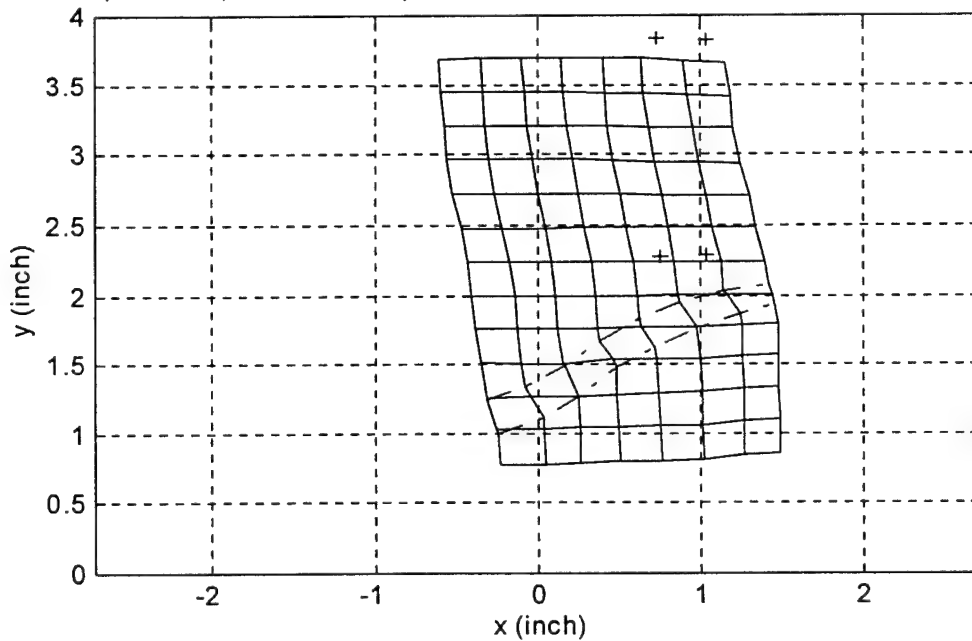
Figure 3.8 Digitized Grid Corrected In Horizontal Direction

3.3.4 Vertical Corrections for Surface Curvature

The need to correct the vertical lines to obtain their true position was a consideration as well. The horizontal lines appear to curve slightly on the digitized images. Part of this was due to the refraction of the light as it passed through the different media and another part was due to camera orientation. The upper lines appeared to curve downward while the lower lines curved upward. Since the actual grid was initially comprised of only straight lines with known spacing differentials, a correction was developed to account for this problem.

Each grid had thirteen horizontal lines. The seventh, or middle, line appeared to remain a straight line. On the other hand, the top and bottom lines seem to be curved the most. The correction used to account for this phenomenon was implemented at the last stage of the digitizing process just prior to calculating an output. At that stage, the center of the image was already determined using the method mentioned in the previous section. With the center established, the coordinates of the uppermost and lowermost horizontal lines were changed. Since the grid was known to be 3.0 inches (7.62 cm) tall, and the middle horizontal line was equidistant from the top and bottom lines, the vertical line nearest the calculated center was assigned coordinates corresponding to this information. Next, the top and bottom lines were given the same y-coordinates as this center line. The intermediate lines were then proportionally stretched to make them truly horizontal according to their relative distance from the center line. Figure 3.9 demonstrates the need for the horizontal line correction and how the upper and lower lines were modified.
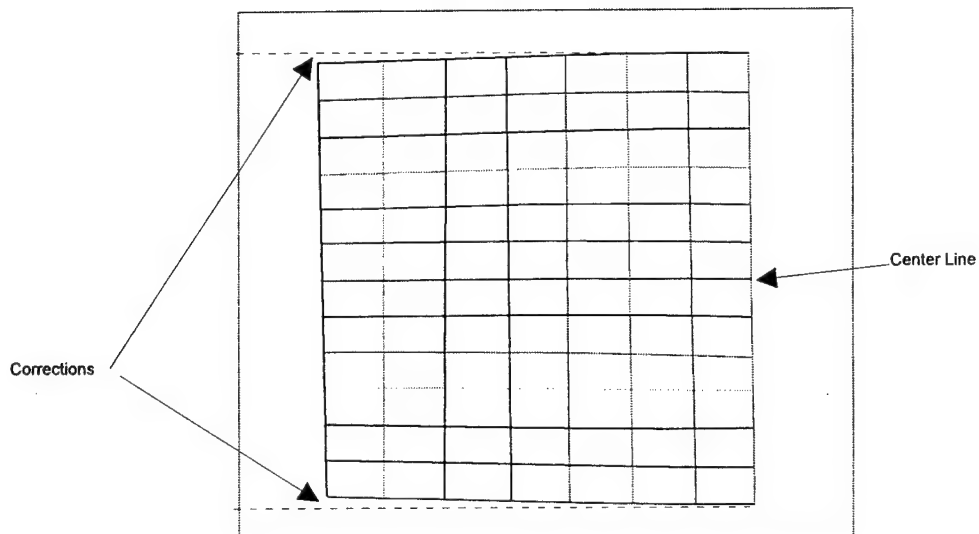
Figure 3.9 Horizontal Line Correction

3.4 Analysis of Shear Bands

To determine the angle of the shear band, each image first needed to be digitized and corrected for curvature. The displacements, strains, and many other components were then determined by a direct comparison to their respective initial images. Figure 3.10 shows an initial image overlaid upon a later image with a shear band. The MATLAB™ software package then performed the necessary calculations to find the inclination of the shear band, the thickness of the shear band, and the strains in and around the shear band. The appendix of this thesis contains many printouts and charts to expand upon the digitizing process.

Test #77; 3/18/97; Torsion-compression; ECP=50 psi; Loire; Video #1; t=3200 sec.
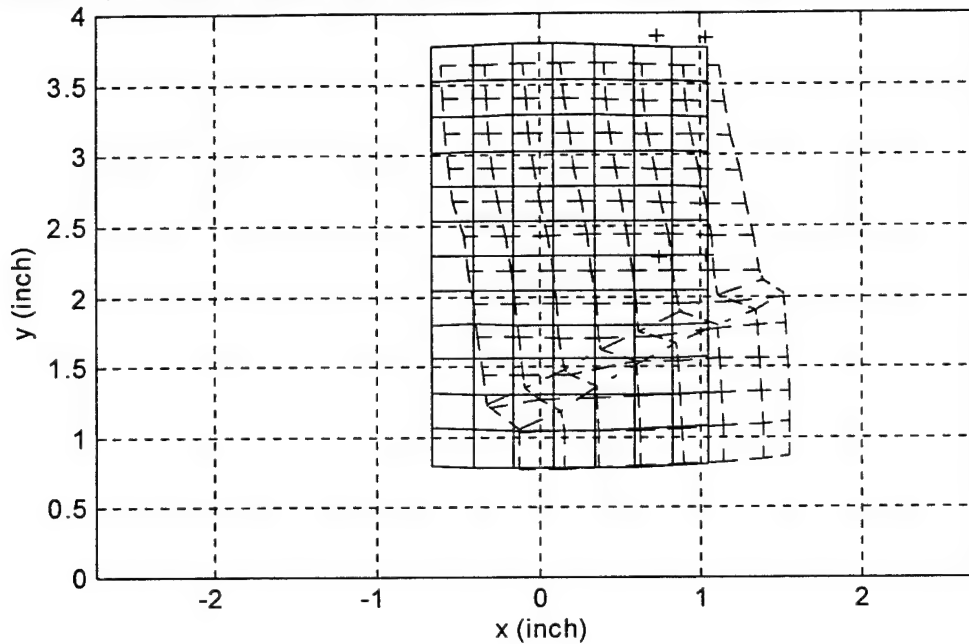
Figure 3.10 Initial Grid and Deformed Grid After Horizontal Correction

Typically, of the seven times in which images were taken, only four were necessary to accurately determine the data pertinent to the onset and inclination of the shear band. These images were usually the first, third, fifth and last ones taken. Since there were four cameras, a total of sixteen images were digitized per test. To determine the inclination of the shear band, a combined average angle of all four images was used. Figure 3.11 shows the appearance of these images when combined together. Due to time constraints of this lengthy process, only three tests were digitized. These tests were #77, #78a and #79. All other shear band inclinations were determined by careful observation and are summarized in Chapter Five.

Test #78a; 8/14/97; Pure Torsion; ECP=50 psi; Loire
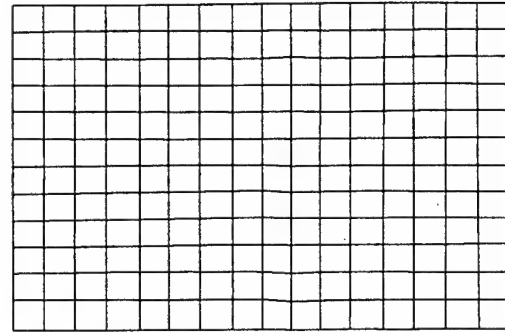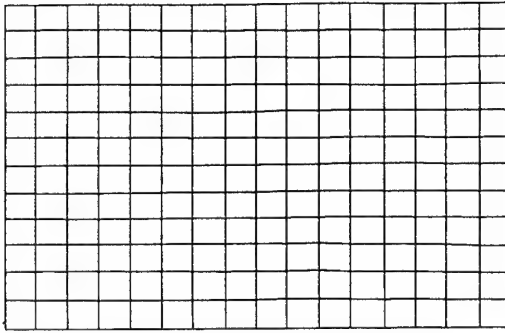
(1) t=0000 sec.
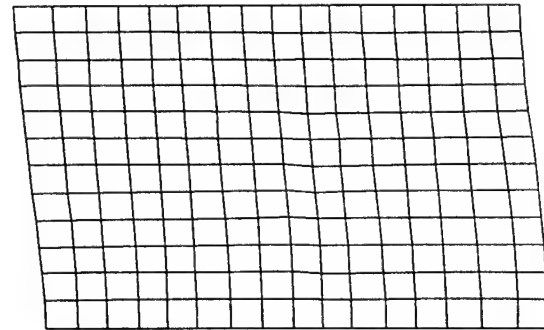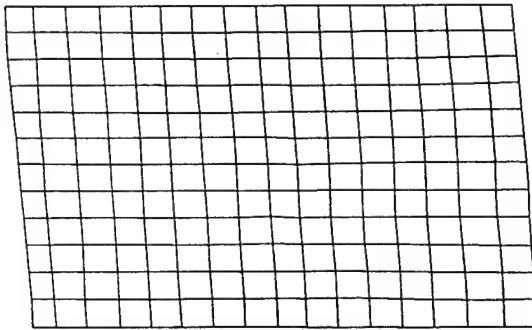
(2) t=1500 sec.
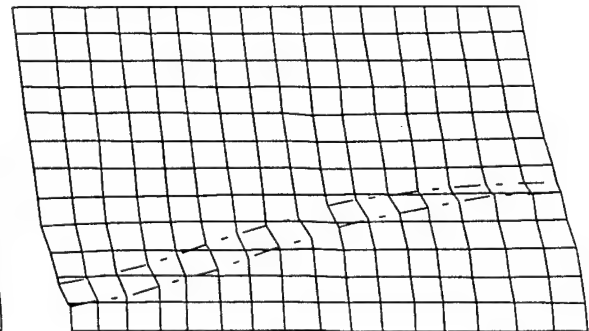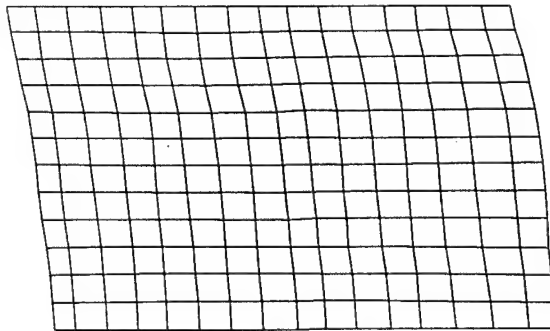
(3) t=2500 sec.
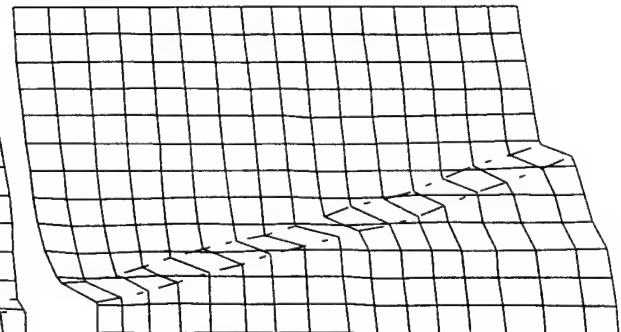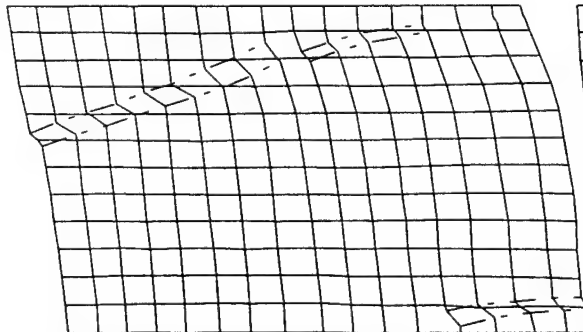
(4) t=3400 sec.

Figure 3.11 Digitized Images at Various Time Intervals After Corrections

3.5 Accuracy of Digitization Method

The digitization process generates a great deal of information about shear bands. This data can give a new insight in the shear banding phenomenon. In order to fully understand the quality of this new process, the accuracy must be evaluated. This was accomplished by comparing the results produced from digitization to the data collected from the various testing gauges. It was found that these two methods resulted in information which was in excellent agreement with each other prior to the formation of the dominant shear band (Saada, 1998).

The issue of how accurately a grid could be digitally reproduced was also a concern. Each grid line was approximately 0.04 inches (0.10 cm) or 3 to 4 pixels wide. It was noticed that these ink lines were darker in the middle and lighter near the edges. When these lines were digitized, either the second or third pixel was chosen. This leads to a possible error of 4 percent. By incorporating the use of a polynomial fitting curve, this error was reduced to 2 percent which was considered more than adequate for this study (Saada, 1998). Figure 3.12 demonstrates the above.
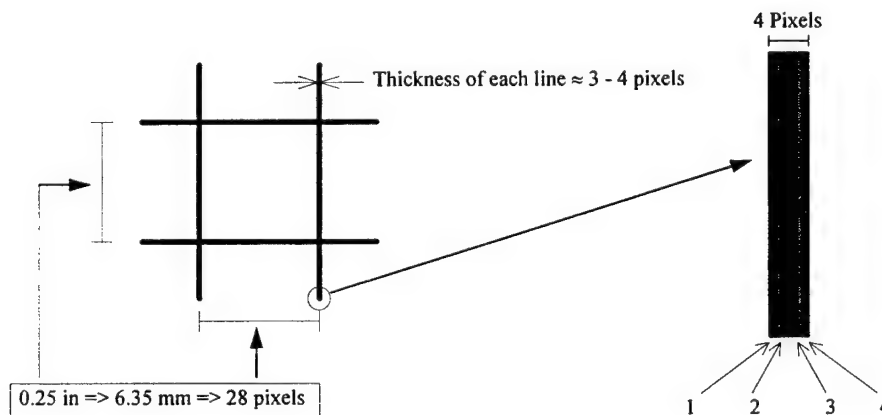
Figure 3.12 Estimation of the Error Associated with the Digitization Process (Saada, 1998)

Chapter Four

Results

4.1 Introduction

The majority of the data used in this experiment was taken from the data acquisition program. However, in order to use this information in full confidence, there must be no doubt of the accuracy of this data. To guarantee this, the information was checked against manually collected results and expected behavior. For this section, three specific tests are examined in great detail to ascertain their precision and validity. This investigation will also give a better understanding of the behavior of the sand used and of non-cohesive, granular materials in general. A tabulation of the results along with the parameters used in the several theories is presented in this section.

4.2 Evaluation of Acquired Data

4.2.1 Explanation of Tests Evaluated

With the experiments performed on the Loire sand being the last portion of the overall research, the expected behavior was relatively predictable. This made the evaluation of the results much easier and poor experiments could be spotted and repeated. Three tests are discussed in depth as a representation of the general research. These tests are: Test #77 (GL22TF), Test #78a (GL24TF), and Test #79 (GL26TF). All of these experiments were conducted at 50 psi (345 kPa) and 50% initial relative density. Each test was also generalized and the specimens had a dogbone shape with complete saturation. The major differences in these tests were the stress paths. The first test (Test #77), was a torsion-compression test ($\beta=30°$), the second (Test #78a), was a pure torsion

test ($\beta=45°$), and the last (Test #79), was a torsion-extension test ($\beta=60°$). The last two tests in this series (Tests #76a and #80) were pure compression and pure extension tests respectively. However, these types of tests do not always develop clear shear bands and, therefore, will not be discussed.

4.2.2 Description of Plotted Data

Five types of plots are presented in this section. As previously mentioned, there is a separate plot for each of the three tests being analyzed. Figures 4.1 a,b,c plot the changes in torque, cell pressure and axial force versus the change in the angle of rotation. These figures show that these tests were indeed generalized since the cell pressure increased for a decrease in axial load. An important note to make is that the axial force has units of Newton's (force) while cell pressure has units of kilopascals (pressure). Therefore, in order to complete the comparison, the cross sectional area of the sample needed to be introduced. However, the feedback program automatically accounted for this and the mean stress remained the same.

Figures 4.2 a,b,c compare the axial force to the axial displacement up to and even beyond the failure. Note that for all tests, at the maximum or minimum axial force (depending on the type of test), the axial displacement underwent a change of inflection. This was usually indicative of the formation of the shear band. In Figure 4.2 b, the axial force and displacements were almost nonexistent since this test was a pure torsion test.

Figures 4.3 a,b,c further illustrate the concept of generalized tests. These plots show the three principal stresses and how they changed. The stresses shown were all effective stresses due to the constant 10 psi (69 kPa) back pressure. They are similar to

figures 4.1 a,b,c but they have converted the axial force to a stress. Also, the mean of all three stresses is plotted. This effective mean stress remained constant throughout the duration of the test at a value of approximately 50 psi (345 kPa). This number was the initial confining pressure minus the back pressure of all three tests.

Figures 4.4 a,b,c plot the volume changes of each test versus the angle of rotation. As is typical of loose samples (50% initial relative density), an initial decrease in volume happened due to the motion of the particles. After this decrease, the volume tended to increase for the remainder of the test up to failure. Once a shear band was fully formed, the volume remained constant. This occurrence was often used as an indication of the tests completion.

Figures 4.5 a,b,c show how the principal strains change. This was necessary to obtain the maximum rate of change of $((\varepsilon_1 / \varepsilon_3)_{max})$ for calculating the angle of dilation (ψ) for plain strain.
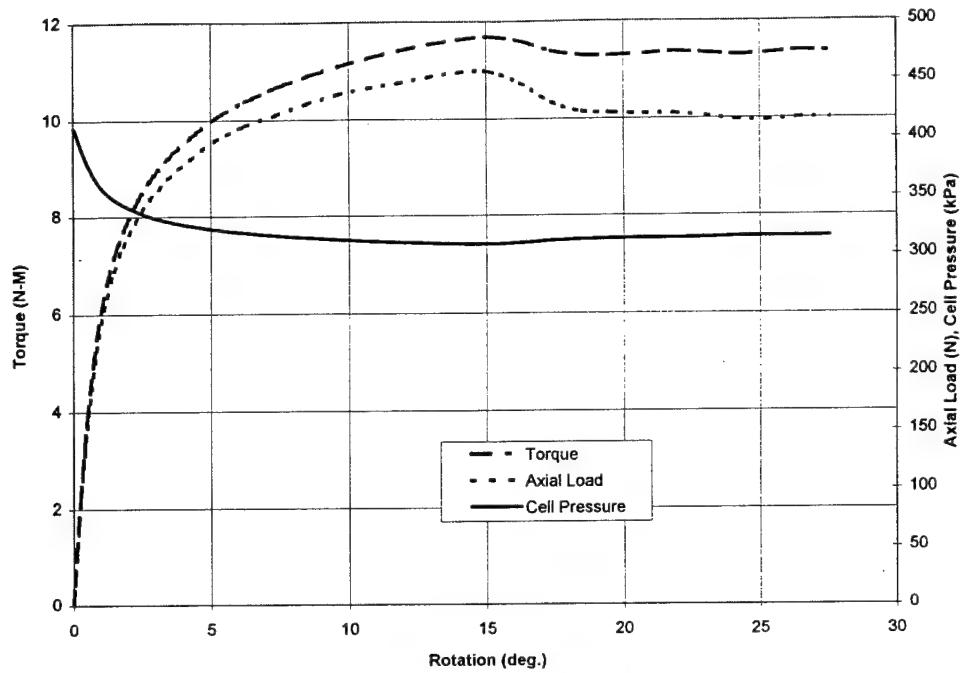
Figure 4.1a Torque, Axial Load and Cell Pressure
GL22TF, Test #77 (Torsion-Compression)
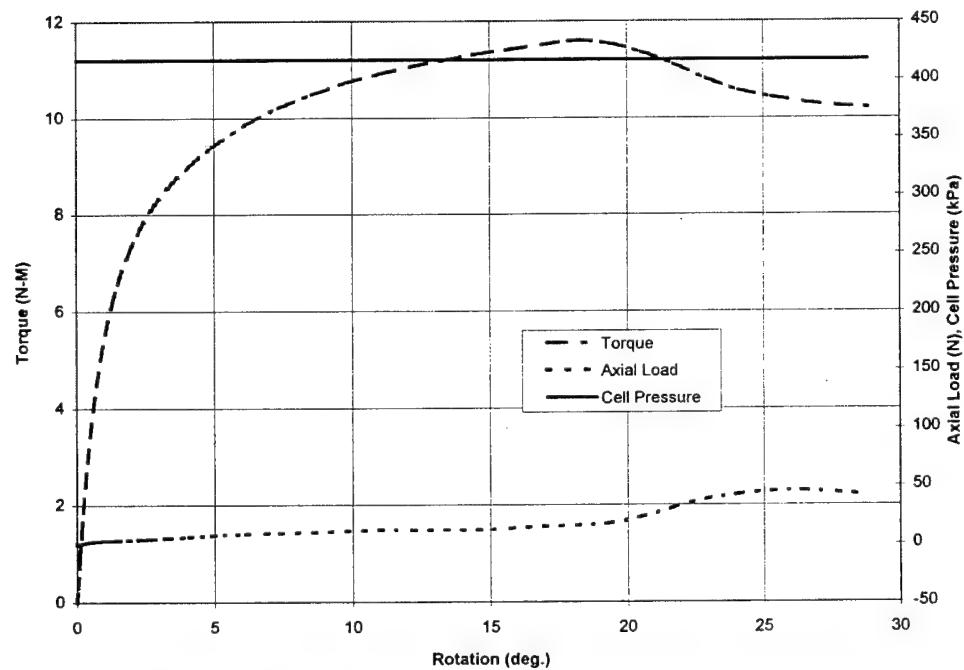
Figure 4.1a Torque, Axial Load and Cell Pressure
GL22TF, Test #78a (Pure-Torsion)
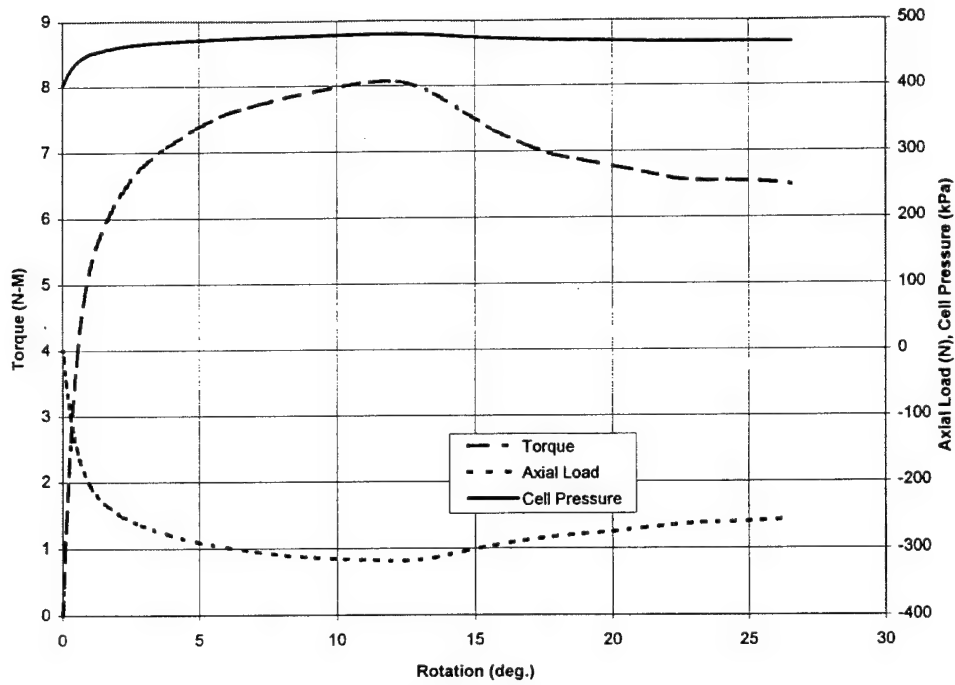
Figure 4.1a Torque, Axial Load and Cell Pressure
GL22TF, Test #78a (Pure-Torsion)
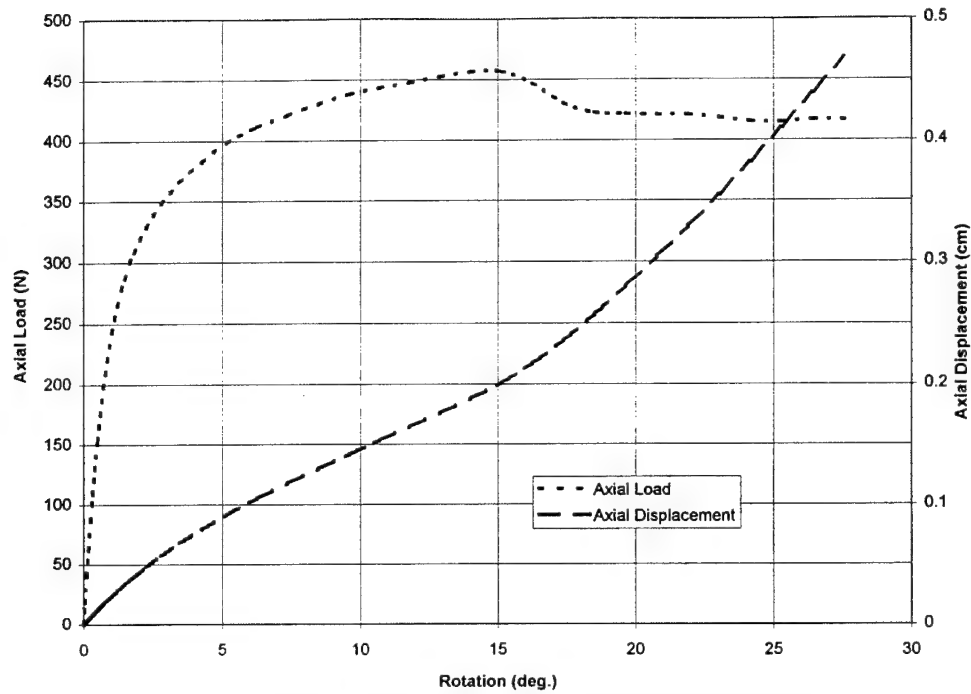
Figure 4.2a Axial Load and Displacement
GL22TF, Test #77 (Torsion-Compression)
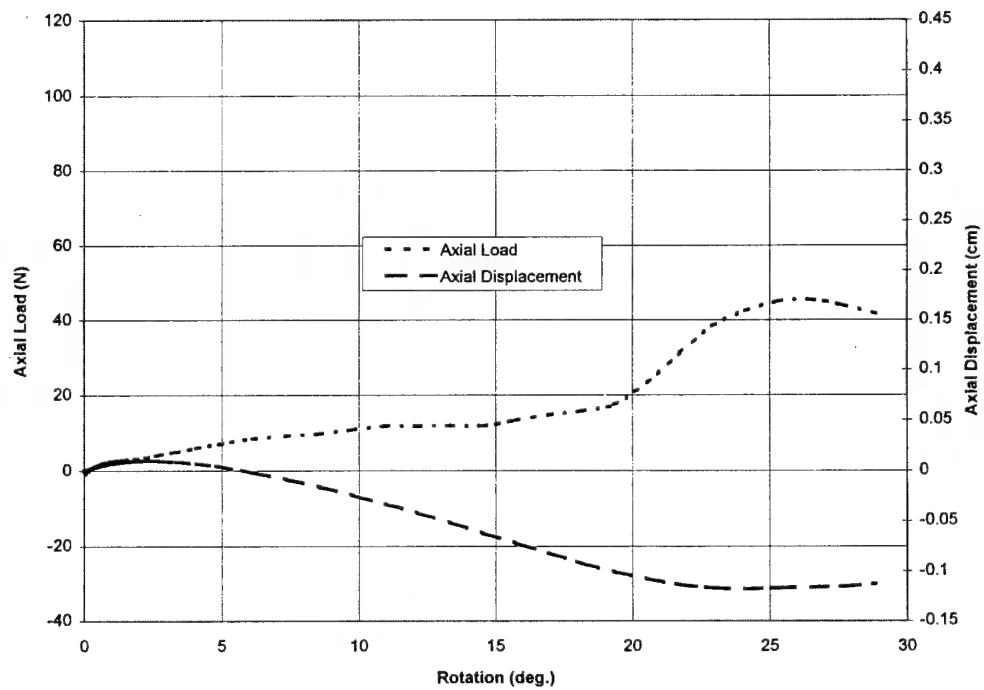
Figure 4.2b Axial Load and Displacement
GL24TF, Test #78a (Pure-Torsion)
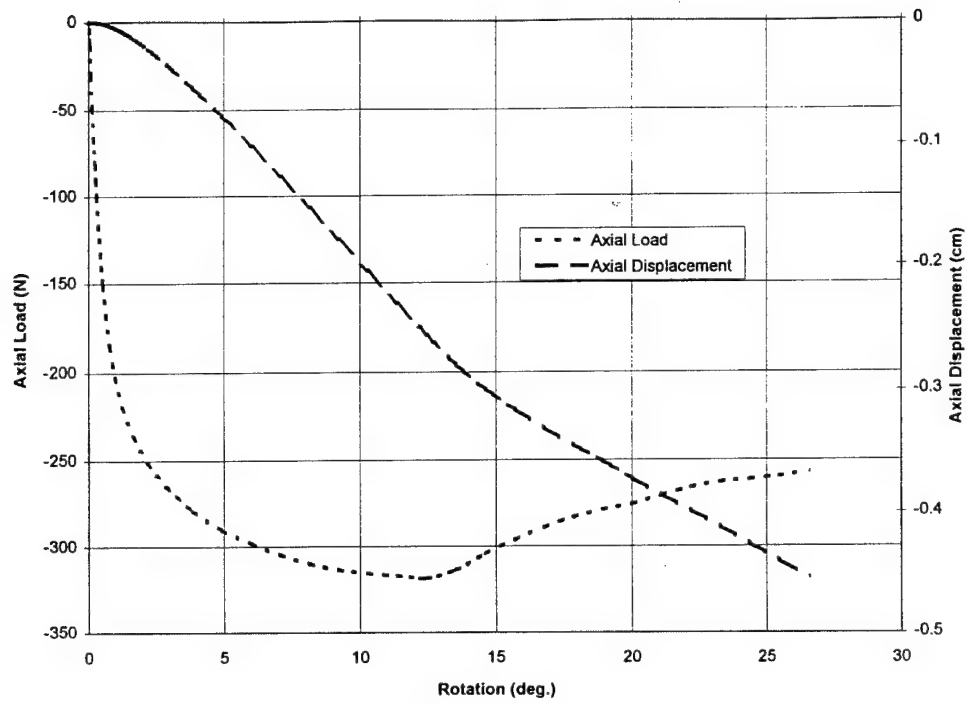
Figure 4.2c Axial Load and Displacement
GL26TF, Test #79 (Torsion-Extension)
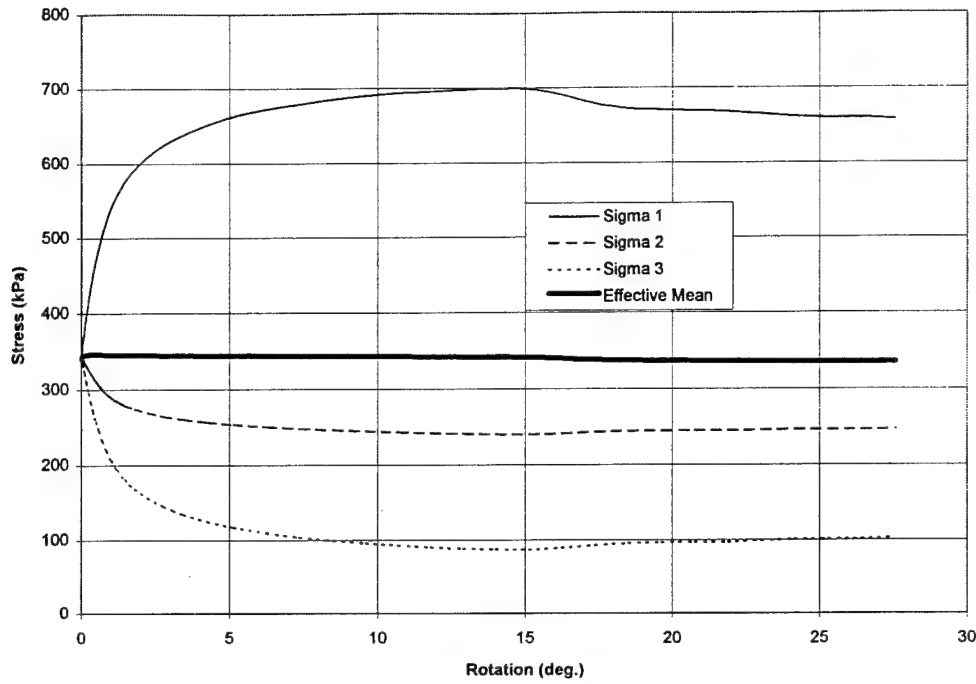
Figure 4.3a Effective Principal Stresses
GL22TF, Test #77 (Torsion-Compression)
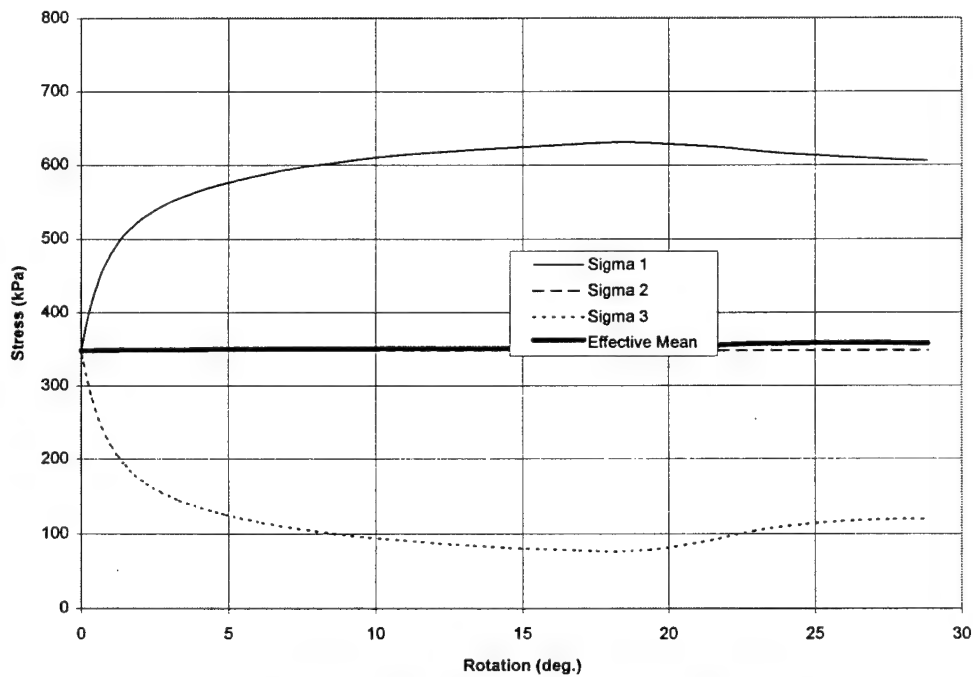
Figure 4.3b Effective Principal Stresses
GL24TF, Test #78a (Pure-Torsion)
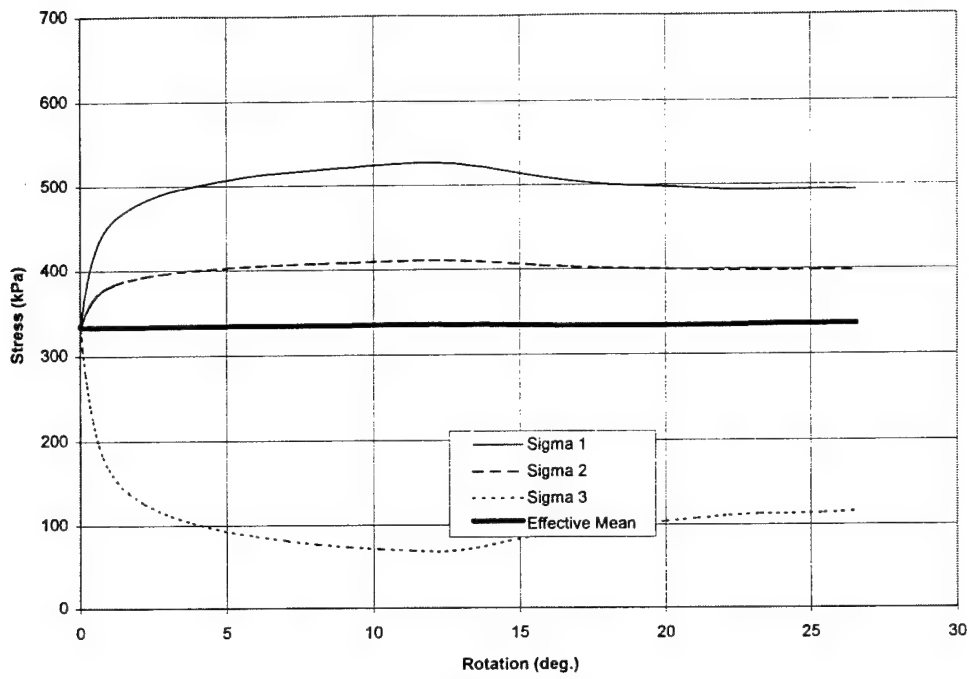
Figure 4.3c Effective Principal Stresses
GL26TF, Test #79 (Torsion-Extension)
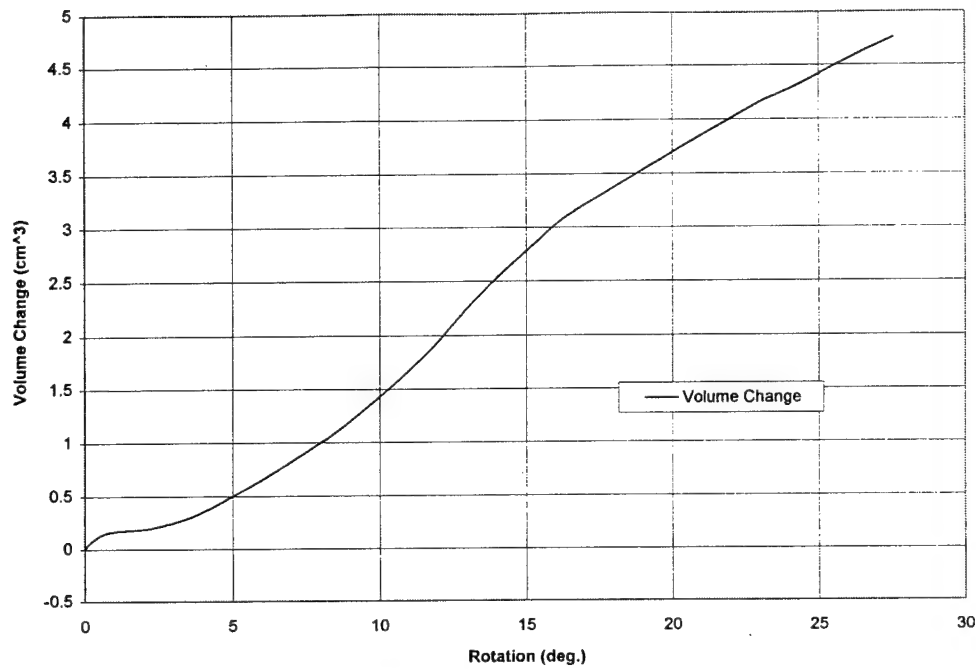
Figure 4.4a Volume of Specimen
GL22TF, Test #77 (Torsion-Compression)
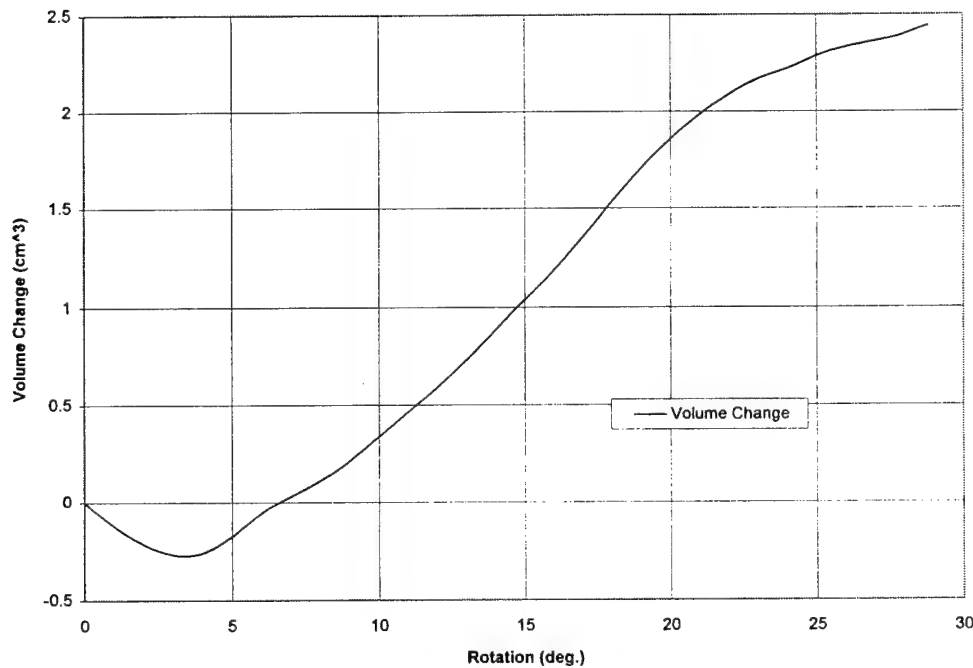
Figure 4.4b Volume of Specimen
GL24TF, Test #78a (Pure-Torsion)
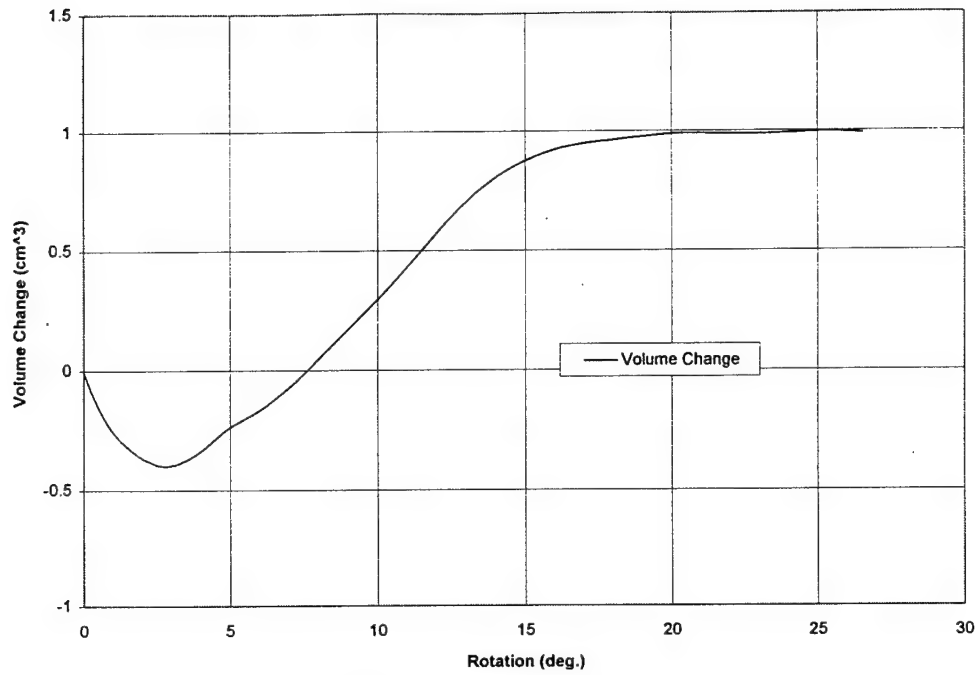
Figure 4.4c Volume of Specimen
GL26TF, Test #79 (Torsion-Extension)
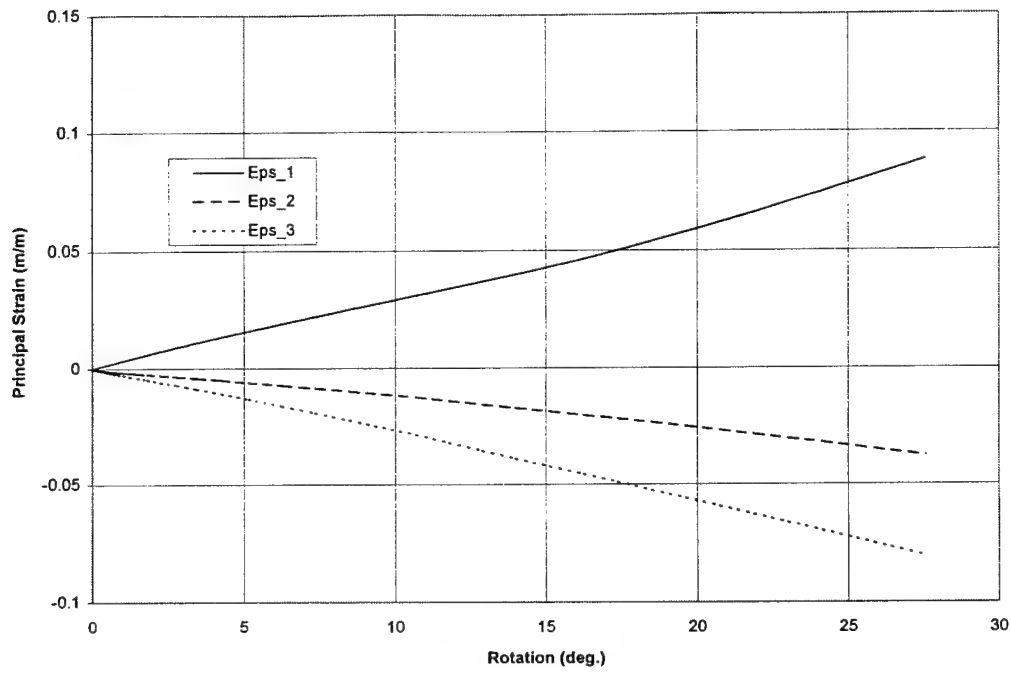
Figure 4.5a Displacement Principal Strain
GL22TF, Test #77 (Torsion-Compression)
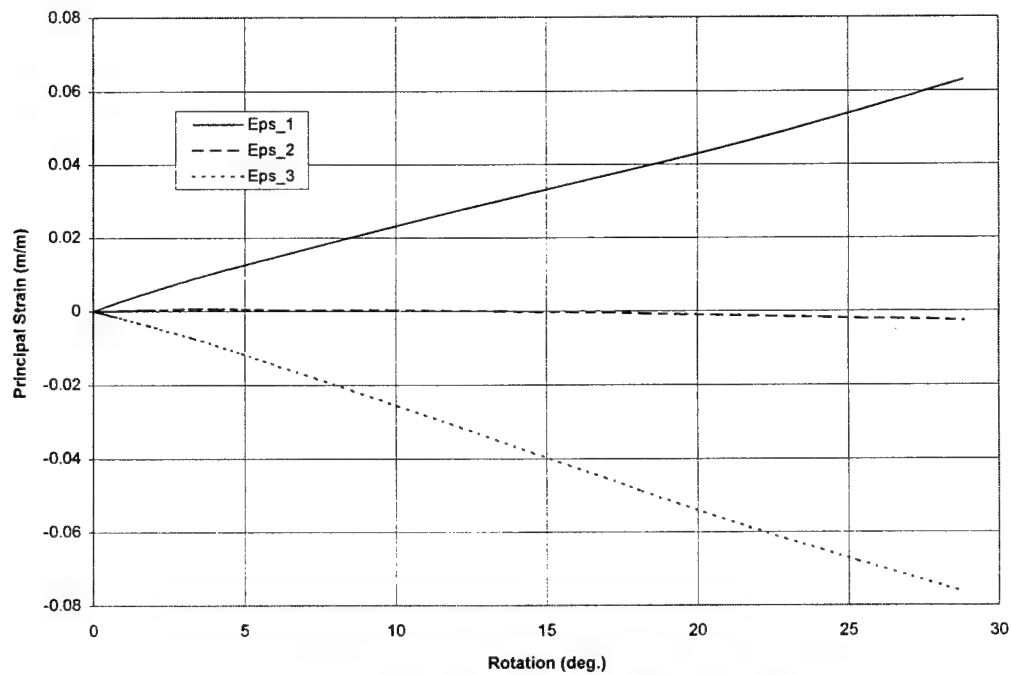
Figure 4.5b Displacement Principal Strain
GL24TF, Test #78a (Pure-Torsion)
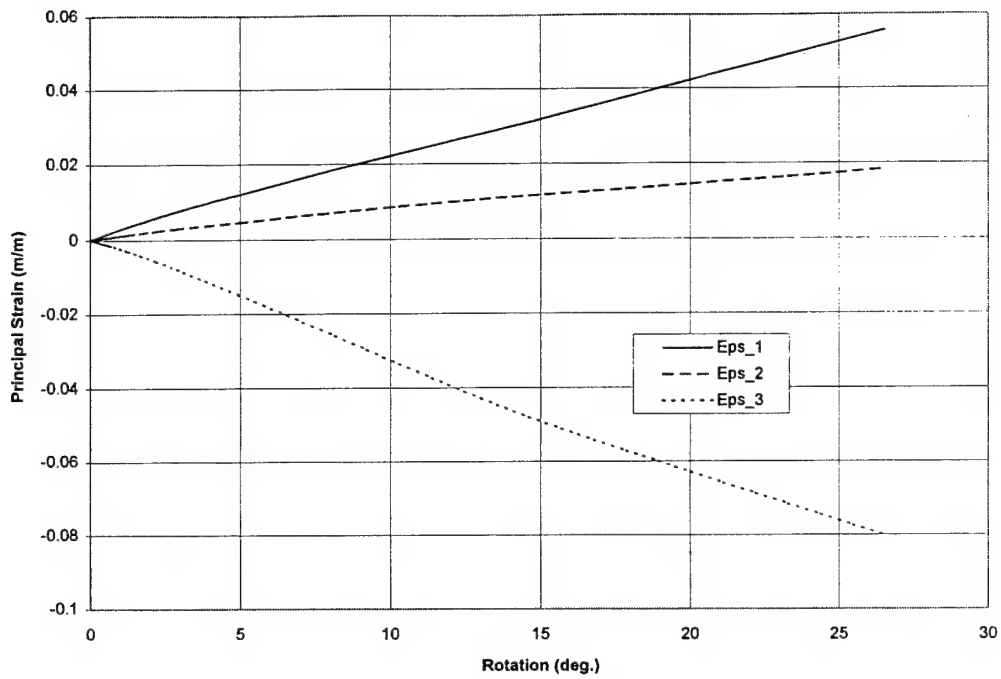
Figure 4.5c Displacement Principal Strain
GL26TF, Test #79 (Torsion-Extension)

4.3 Calculation of the Effective Angle of Friction (ϕ')

The effective angle of friction was determined using the standard Mohr's circle approach. For this method, a tangent line was drawn from the origin to the Mohr's circle, which was found by using the effective major and minor principle stresses throughout the duration of the test. Figure 4.6a illustrates the described method.
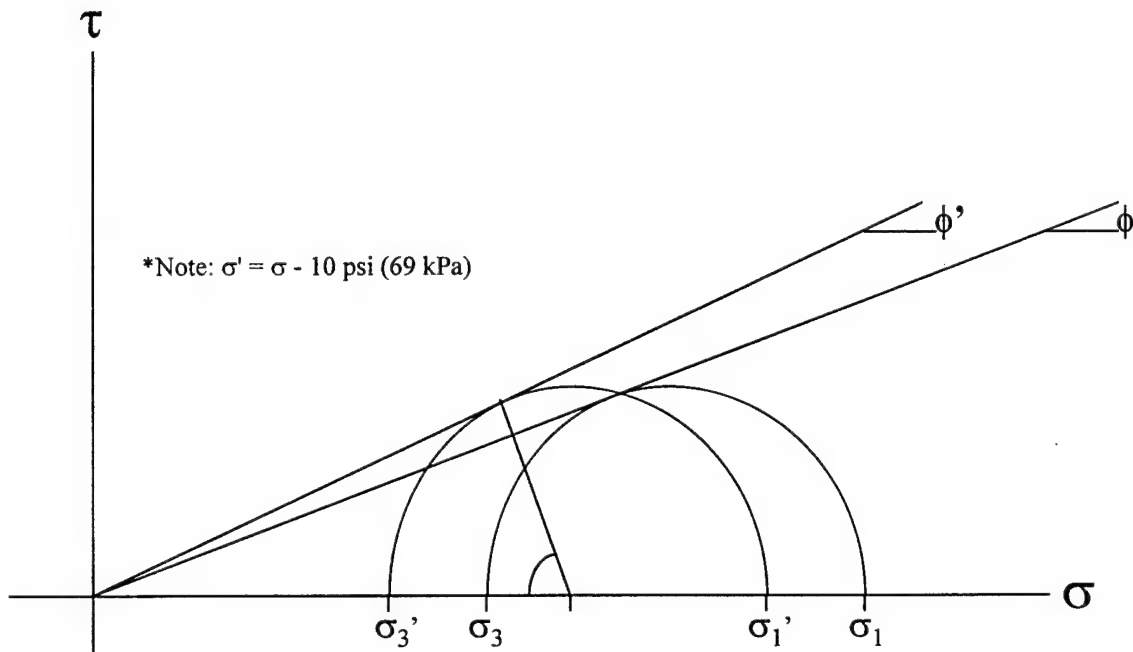
Figure 4.6a
Use of Mohr's Circle to Determine ϕ'

The angle formed by the intersection of this line and the horizontal axis gives the angle of obliquity. The maximum angle of obliquity is better known as the effective friction angle. This parameter can be found mathematically using equation 4.1, assuming the soil is non-cohesive.

$$\sin \phi'_{max} = \left[\frac{(\sigma 1'/\sigma 3')\, max - 1}{(\sigma 1'/\sigma 3')\, max + 1} \right] \qquad (4.1)$$
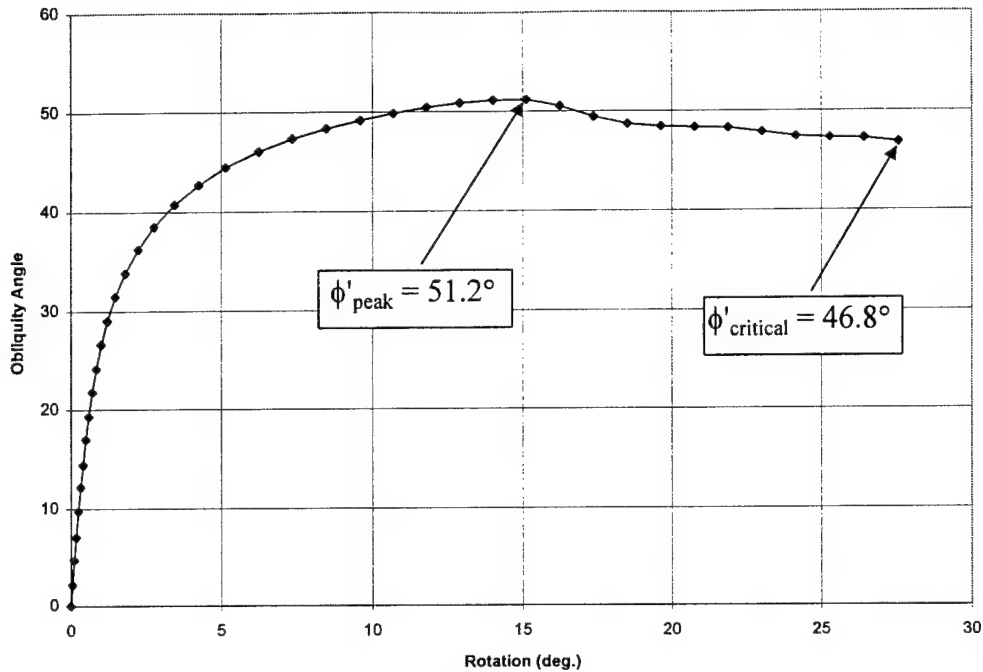
Figure 4.6b Change in Obliquity Angle
GL22TF, Test #77 (Torsion-Compression)

Figure 4.6b demonstrates the determination of this key parameter for Test #77. For this particular test, the peak friction angle was 51.2°, and the ultimate friction angle, close to the critical state, was 46.8°.

Pure compression tests were also used to determine the critical friction angle for each set (Saada et. al., 1994). Table 4.1, found later in this chapter, summarizes the peak and critical friction angles as found for each test.

4.4 Determination of the Angle of Dilation (ψ)

As described in chapter 1.3, there were several methods for finding the angle of dilation. Bolton's (1986) method (see equation 1.1c) used the term $(d\varepsilon_1/d\varepsilon_3)_{max}$ which was easily found from a plot of the rate of dilation versus rotation. Figures 4.7 a,b,c demonstrate how this quantity was found for Tests #77, #78a, and #79 respectively. In

addition to the maximum rate of dilation, these figures also plot shear stress (τ_{oct}) versus

rotation to demonstrate where the maximum value of dilation rate occurred in reference to

maximum value of shear stress. Notice that the two peak values occurred at

approximately the same rotation. Bolton's theory exploited the concept of plane strain

which the hollow cylinder tests closely resembled in pure torsion. This was especially

true once the dominant shear band fully formed (from discussion with University of

Grenoble).
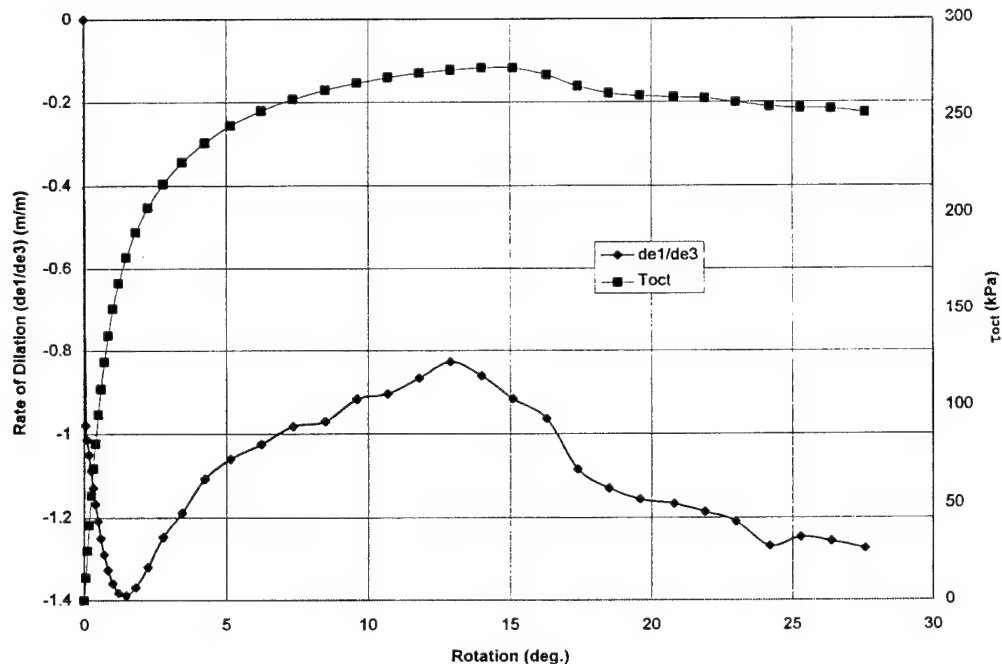
Figure 4.7a Maximum Rate of Dilation
GL22TF, Test #77 (Torsion-Compression)
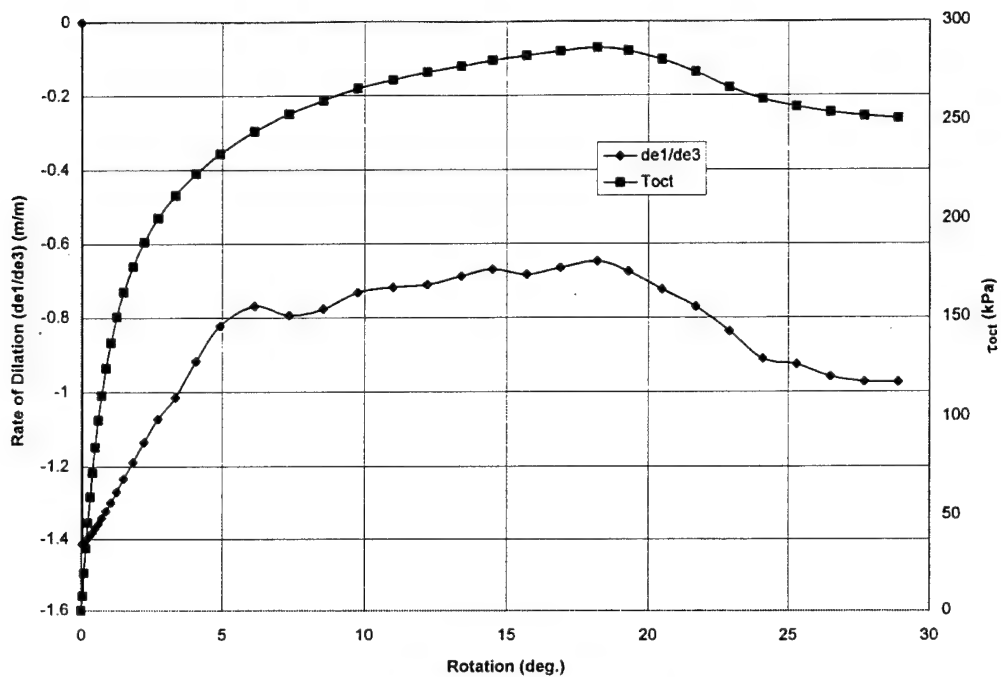
Figure 4.7b Maximum Rate of Dilation
GL24TF, Test #78a (Pure-Torsion)
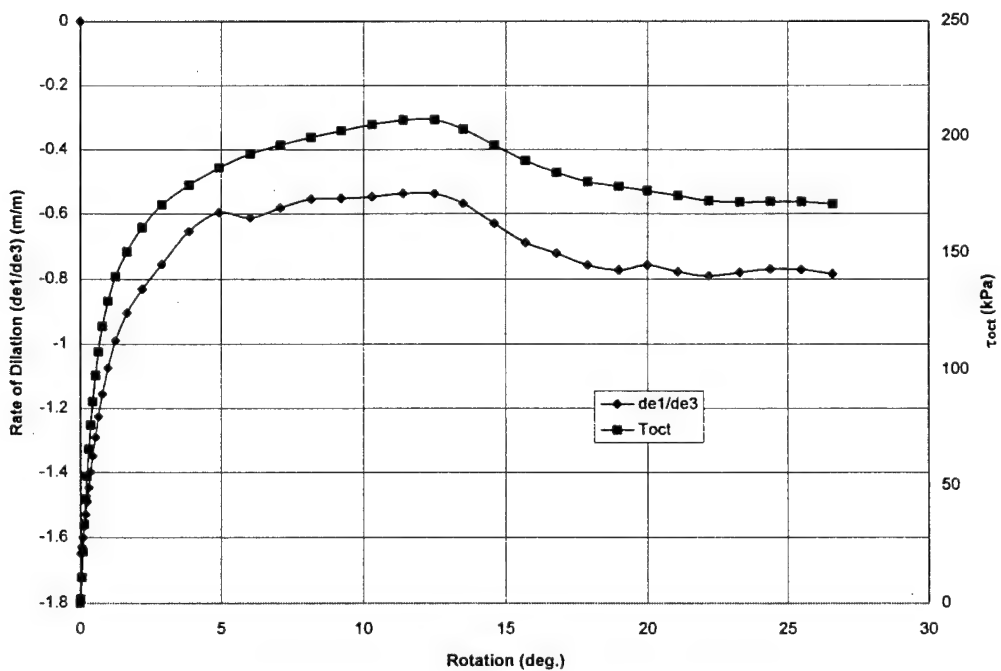
Figure 4.7c Maximum Rate of Dilation
GL26TF, Test #79 (Torsion-Extension)

The second method for finding ψ, as suggested by Zitouni (see equation 1.3),

incorporated the angle θ. Figures 4.8 a,b,c show this method for Test #77, #78a, and #79,

as well as plot the shear stress (τ_{oct}) versus strain (ε_1) for ease of comparison. The line

from which θ was found is tangent to the ε_3 versus ε_1 curve. Also, notice that this

tangency stops at around the maximum shear stress. Both methods used for calculating ψ

should give approximately the same value.
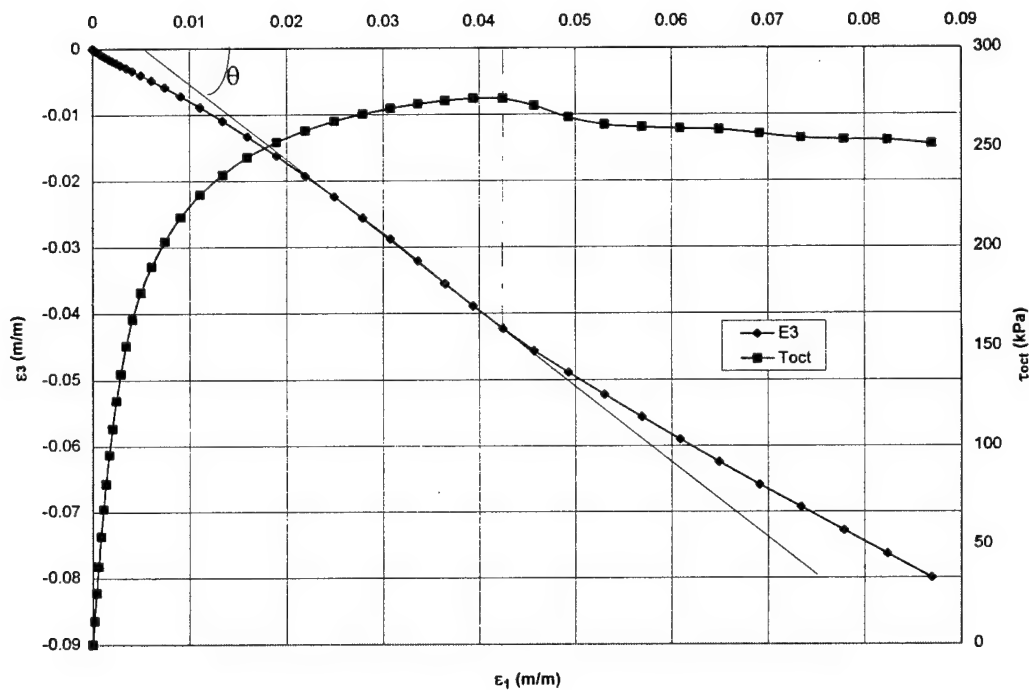
Figure 4.8a Zitouni's Method for Determining Ψ
GL22TF, Test #77 (Torsion-Compression)
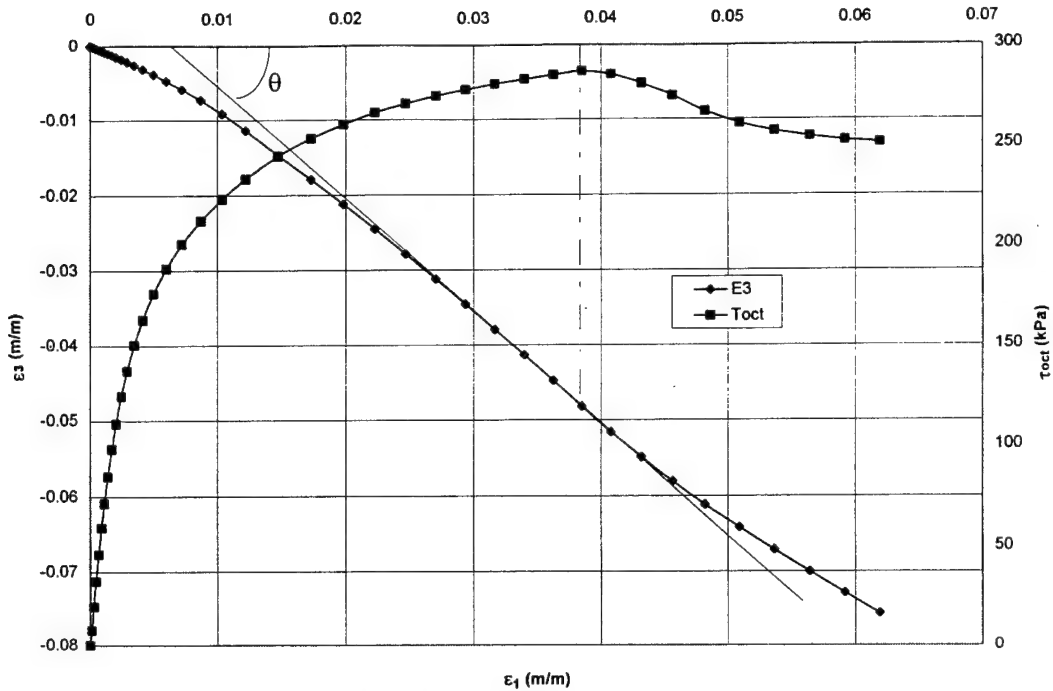
Figure 4.8b Zitouni's Method for Determining Ψ
GL24TF, Test #78a (Pure Torsion)
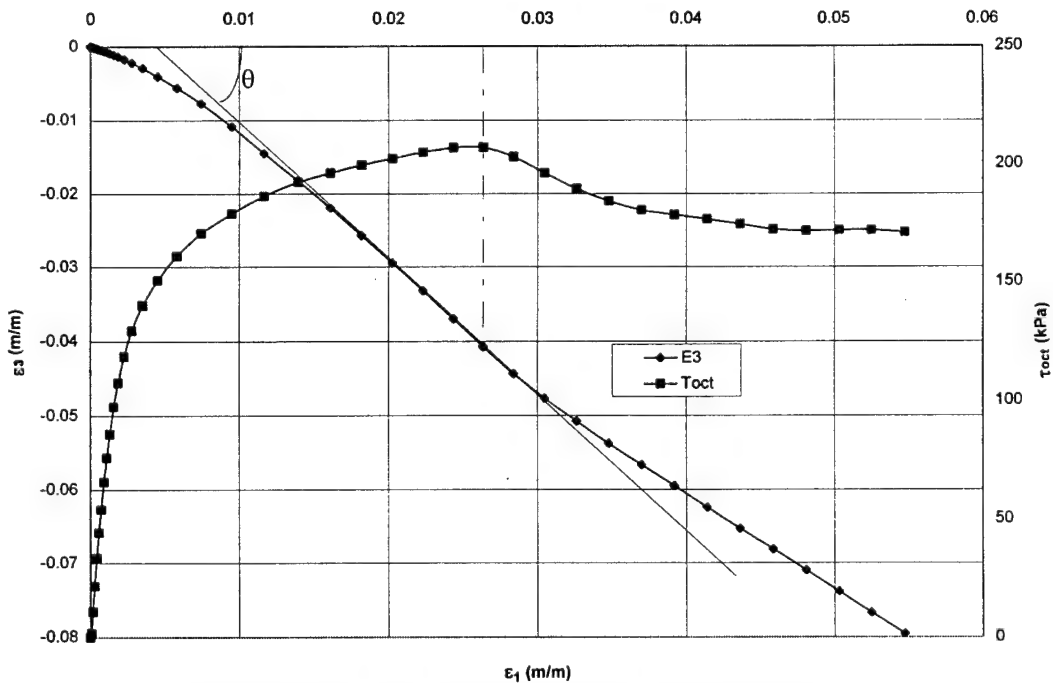
Figure 4.8c Zitouni's Method for Determining Ψ
GL26TF, Test #79 (Torsion-Extension)

Table 4.1 summarizes the resultant friction and dilation angles as found for each test. Both computed values of Ψ are listed here. Notice that these two dilation angles are very close to one another.

Table 4.1 Summary of the Angles of Friction and Dilation

Confining Pressure	Initial Relative Density	Test Number	β	φ′ (Peak)	φ′ (Critical)	ψ (Zitouni)	ψ (Plane Strain)
30 psi	50%	71	0	42.8	31.6	---	---
30 psi	50%	72	30	54.1	50.3	6.0	6.9
30 psi	50%	73	45	53.0	46.4	14.4	16.5
30 psi	50%	74b	60	55.6	45.9	19.8	21.3
30 psi	50%	75	90	41.2	26.4	---	---
50 psi	50%	76a	0	39.9	32.1	---	---
50 psi	50%	77	30	51.2	46.8	2.9	5.4
50 psi	50%	78a	45	51.6	42.0	11.0	12.4
50 psi	50%	79	60	50.5	38.4	16.3	17.5
50 psi	50%	80	90	41.9	20.0	---	---
70 psi	50%	81b	0	41.9	36.2	---	---
70 psi	50%	82	30	51.8	46.2	2.2	3.7
70 psi	50%	83a	45	49.1	40.0	10.2	9.1
70 psi	50%	84a	60	48.1	35.0	15.3	17.1
70 psi	50%	85	90	39.8	15.7	---	---
30 psi	80%	86a	0	43.3	37.1	---	---
30 psi	80%	87a	30	54.1	50.3	5.8	6.1
30 psi	80%	88	45	53.0	46.4	14.5	15.3
30 psi	80%	89	60	66.0	47.8	25.7	27.6
30 psi	80%	90	90	48.3	26.4	---	---
50 psi	80%	91a	0	44.3	37.5	---	---
50 psi	80%	92	30	55.4	50.5	4.2	5.7
50 psi	80%	93a	45	63.1	46.8	16.5	18.4
50 psi	80%	94d	60	48.4	34.0	19.5	20.7
50 psi	80%	95	90	33.3	10.4	---	---

70 psi	80%	96a	0	43.2	34.0	---	---
70 psi	80%	97a	30	53.6	46.5	5.5	14.2
70 psi	80%	98	45	59.5	46.6	5.9	14.2
70 psi	80%	99c	60	44.2	32.1	22.8	26.1
70 psi	80%	100a	90	48.5	20.0	---	---

4.5 Summary and Conclusions

The results of the testing schedule can be seen by analyzing figures 4.1 a,b,c through figures 4.5 a,b,c. Tests #77, #78a, and #79 demonstrated typical behavior of torsion-compression, pure torsion, and torsion-extension tests. Chapter Five will give further detail on the effect of the different parameters studied. However, several conclusions can be drawn from how the different parameters effect the angles of friction and dilation. Based on the results listed in table 4.1, the following observations were made.

- The angle of friction did appear to be slightly affected by confining pressure and relative density. However, these differences were slight and no trends could be established. It was noticed that the inclination of the major principal stress (β) did affect the friction angle. Pure compression and extension tests yielded lower angles of friction.

- The angle of dilation was not considerably affected by either confining pressure or relative density. The stress path, on the other hand, had a noticeable impact on the angle Ψ. As was expected, the greater the angle β, the higher the resultant angle of dilation turned out to be.

Chapter Five

Analysis

5.1 Introduction

For this chapter, the results of the various tests will be analyzed. The two key topics discussed will be the validity of the equations predicting the angle of shear banding (as presented in Chapter One) and the effect of the different testing conditions. Also, a comparison will be made to analyze the similarities and differences between the Loire sand and the LSI-30 sand. Specifically, the effect of grain size will be discussed to investigate the validity of theory presented by Koender et al. (1990).

5.2 Analysis of Shear Band Equations

The three theories investigated in this chapter are as follows:

- Coulomb's Theory $\Rightarrow (45 - \phi'/2)$

- Roscoe's Theory $\Rightarrow (45 - \psi/2)$

- Arthur-Vardoulakis's Theory $\Rightarrow (45 - (\psi + \phi')/4)$

These theories predict the angle of the shear band with respect to the major principal axis. However, there were several different methods to determine the angles of friction (ϕ') and dilation (ψ) as presented in Chapter Four. For this study, there were three methods used to find the angle of friction and two formulas were used to obtain

the angle of dilation. The three values of ϕ' used were: the angle of friction measured at the peak for a pure compression test, the angle of friction measured at the peak for the particular test being investigated, and the angle of friction measured at the critical state for the particular test being investigated. The two values of Ψ used were: the angle of dilation as calculated from a plain strain formula, and the angle of dilation as calculated by Zitouni's formula. This gave many different predictions using the above formulas. Figures 5.1 a,b to 5.6 a,b graphically compare the precision of those theories to the observed angle of shear banding. The plots were set up to show the accuracy of Coulomb's and Roscoe's theories on the first chart and Arthur-Vardoulakis' theory below on the second chart. In each of those plots, the angles were corrected to account for the different beta angles for ease of comparison. Essentially, the shear band angle with respect to the horizontal is added to the angle beta. Notice that the charts presenting the Arthur-Vardoulakis theories have a total of seven predicted lines. Six of these are the different combinations of ϕ' and ψ, while the one, entitled Art-Vard (best), was the most accurate theory discovered by Saada et al. in the paper "Bifurcation and Shear Band Propagation in Sands" (1997). This particular theory suggested the use of the angle of friction obtained at the peak value for pure torsion in combination with the angle of dilation found from the equation 1.1c for plane strain. This variation of the Arthur-Vardoulakis theory still appears to give accurate results, however, it does not appear to outweigh the others in precision for the Loire sand.

Figures 5.1 a,b to 5.6 a,b plot the actual shear band inclination along with the several inclinations predicted by the various theories. Inspection of these figures reveals that the Arthur-Vardoulakis theory is much more accurate then either Coulomb's or Roscoe's. In general, Coulomb's theory tended to overestimate the angle of shear banding while, in contrast, Roscoe's theory underestimated the angle. since the Arthur-Vardoulakis theory is a direct average of those two predictions, this theory gives more accurate results.
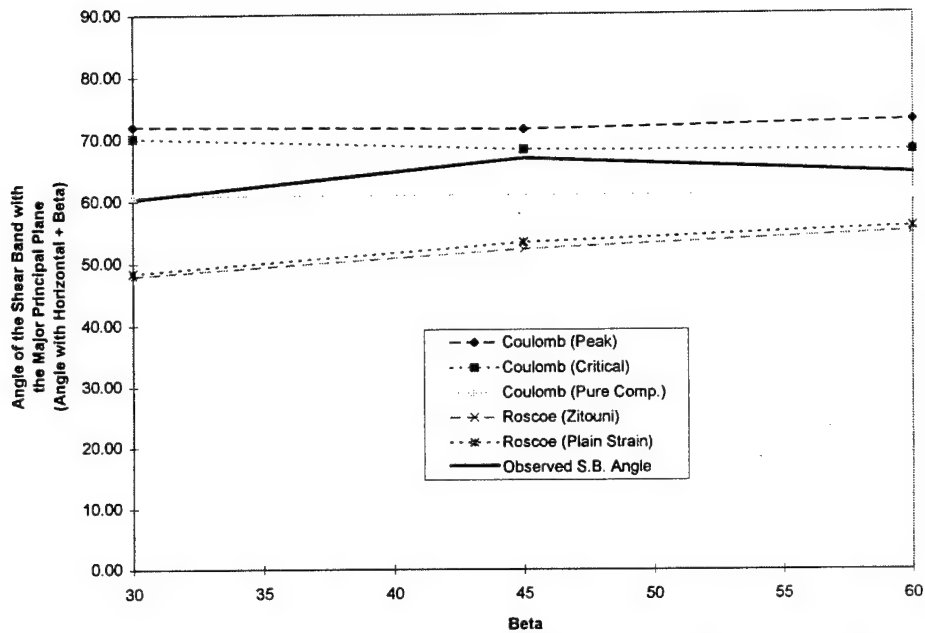
Figure 5.1a Predicted Inclinations with Respect to the Major Principal Plane (Coulomb & Roscoe)
Tests #72, #73 & #74a
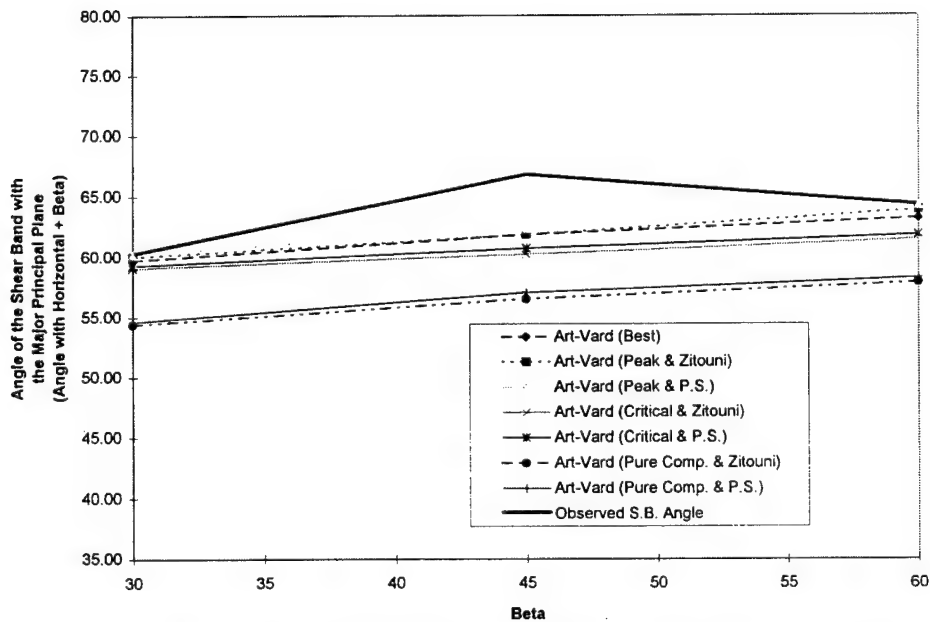
Figure 5.1b Predicted Inclinations with Respect to the Major Principal Plane (Arthur-Vardoulakis)
Tests #72, #73 & #74a

A closer inspection might indicate that the relative density had a minor effect on the shear band inclination. Figure 5.9b averaged the angles found for each density. In other words, the shear band angles observed from the three generalized tests at 50% initial density were averaged and compared to the corresponding average angles at 80%. By visual inspection of this graph, there is a small variation indicating that the angles of the dense sample are slightly greater then the loose samples. Notice that there are counteracting effects that tend to act in favor of the Arthur-Vardoulakis equation; some factors that lead to an increase in ϕ' might lead to a decrease in ψ.
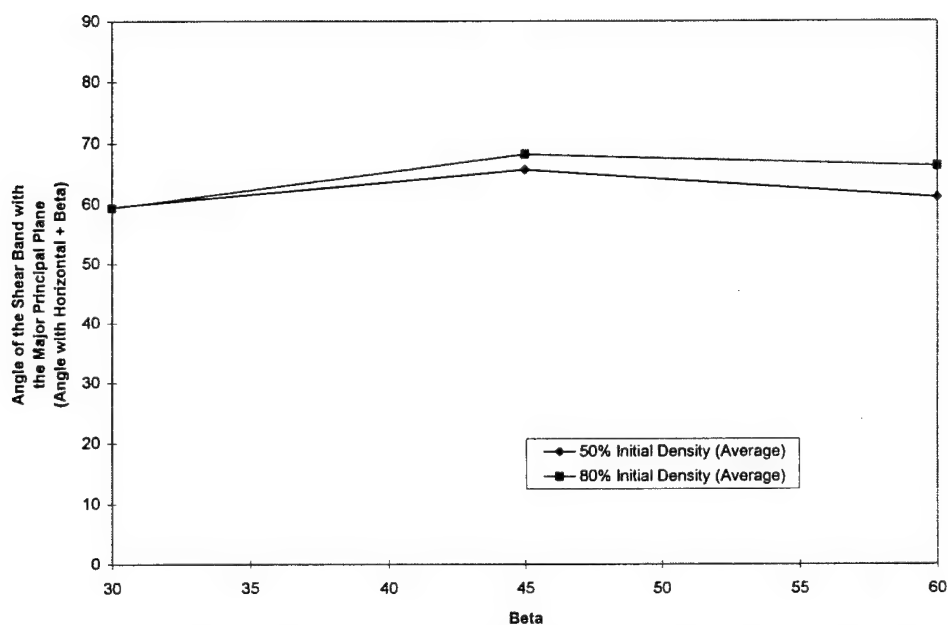
Figure 5.9b Effect of Relative Density on Shear Band Inclination
Averaged Values

5.5 Comparison Between LSI-30 and Loire Sand

5.5.1 Overview

Many predictions and generalizations can be developed using the results from the various tests conducted for this research. A potential problem might arise, however, when applying the same conclusions to another sand. For this reason, a systematic comparison between the Loire and LSI-30 sand was needed. To make this analysis, a summary of the LSI-30 information was required. The thesis by C. Tucker Cope (1997) contained this information which is presented in this section for comparison. The physical properties of the two sands (the resultant friction and dilation angles) and the prediction theories for each sand are compared.

5.5.2 Physical Properties

Some of the differences between the two studied sands were discussed earlier in Chapter Two. The general finding was that the Loire sand closely imitated the LSI-30 sand in type and grain size distribution. By consulting figure 2.1, it is clear that each of the grain size distribution curves are essentially parallel to one another. The main difference between these two media was obviously the actual particle sizes. On average, the Loire sand was approximately 50% larger then the LSI-30. Subtle differences between the sands exist in the specific gravity and void ratio characteristics but these were not as important as the average grain size.

5.5.3 Angles of Friction and Dilation Comparison

Chapter Four summarized the various angles of friction and dilation from the various tests. Table 5.2 presents the corresponding table as found by Cope for the LSI-30 sand. Half of the tests run on the finer sand did not measure the volume change so this summary has only four sets of tests. The angles of dilation were measured in two different fashions. The first is the same method as used for the Loire sand, this being the plane strain assumption (equation 1.1c). The second one uses the triaxial formula (equation 1.2). Notice that the angles of friction and dilation for the Loire sand were, on average, about five degrees greater then the LSI-30.

Table 5.2 Summary of the Angles of Friction and Dilation
(LSI-30 sand, generalized tests)
(Cope, 1997)

Confining Pressure	Initial Relative Density	Test Number	β	ϕ' (Peak)	ϕ' (Critical)	ψ (Plane Strain)	ψ (Triaxial)
30 psi	50%	21	0	38.6	24.5	---	---
30 psi	50%	22	30	50.1	49.2	1.12	11.17
30 psi	50%	23	45	47.1	45.1	9.36	11.58
30 psi	50%	24	60	44.6	42.0	14.49	8.84
30 psi	50%	25	90	42.8	25.4	---	---
50 psi	50%	26	0	38.9	24.1	---	---
50 psi	50%	27	30	45.4	43.1	-0.26	8.92
50 psi	50%	28	45	47	43.5	7.92	9.48
50 psi	50%	29a	60	42.9	34.2	17.05	12.42
50 psi	50%	30	90	41.7	19.5	---	---
70 psi	50%	31	0	37.9	21.8	---	---
70 psi	50%	32	30	44.4	40.9	-1.23	7.64
70 psi	50%	33	45	48.9	41.3	7.24	8.53
70 psi	50%	34	60	43	31.3	14.66	8.14
70 psi	50%	35	90	42	20.1	---	---

From this observation, the assumption was made that the actual inclinations of the shear bands for the Loire sand should be approximately two to three degrees greater then the LSI-30. Table 5.3 lists the observed angles of shear banding for the two sands to see if the Loire sand did indeed have the slightly sharper angles.

Table 5.3 Summary of the Actual Shear Band Inclinations
(LSI-30 & Loire sand)

Eff. Con. Pres.	Initial Relative Density	Beta (β)	Test (LSI-30)	Test (Loire)	Actual (LSI-30)	Actual (Loire)
30 psi	50%	30	22	72	26.0	30.3
30 psi	50%	45	23	73	15.8	21.8
30 psi	50%	60	24	74b	0.7	4.3
50 psi	50%	30	27	77	29.6	31.0
50 psi	50%	45	28	78a	15.5	21.8
50 psi	50%	60	29a	79	4.7	-1.7
70 psi	50%	30	32	82	29.4	27.3
70 psi	50%	45	33	83a	15.3	18.4
70 psi	50%	60	34	84a	0.9	0.9
30 psi	80%	30	37	87a	28.1	27.8
30 psi	80%	45	38	88	20.6	26.6
30 psi	80%	45	39	89	1.2	12.3
50 psi	80%	30	42	92	32.0	30.0
50 psi	80%	45	43	93a	19.0	14.0
50 psi	80%	60	44	94d	0.0	4.8
70 psi	80%	30	47	97a	29.5	30.4
70 psi	80%	45	48	98	18.9	29.0
70 psi	80%	60	49	99c	0.0	1.6

In general, it does appear that the Loire sand has the greater shear band angles, but there does not seem to be enough evidence to strongly argue this point. It was the finding of Cope that the Arthur-Vardoulakis theory produced the most accurate angle predictions. Specifically, the peak angle of friction in combination with the angle of dilation found using the plane strain formula (same combination as Table 5.1b, Column 3), and the combination of plane strain dilation angle with the angle of friction from the pure torsion test (same combination as Table 5.1b, Column 1) gave the best results. These conclusions agree with the ones using the Loire sand.

5.6 Summary and Conclusions

The analysis of the three theories predicting the failure angle (Coulomb, Roscoe, and Arthur-Vardoulakis) reinforced the findings of Cope. Coulomb's theory had the tendency to over estimate the actual inclination of the shear band and, in a similar fashion, Roscoe's theory would under estimate the angle. The theory suggested by Arthur and Vardoulakis takes an average of the first two. This gave the best prediction of the shear band inclination. As mentioned previously, specific combinations of each formula might yield slightly more accurate results. The two best predictions were different combinations of the Arthur-Vardoulakis theory. Each of these predictions used the angle of dilation as found by using the plane strain formula. The angle of friction used was either the general peak friction angle or the angle of friction found from a pure torsion test. For the most part, the peak angles of

friction for the torsion related tests (β=30°, 45°, & 60°) gave the same angles of friction. This explains the relative similarity between the two theories.

The findings on the influence of the various parameters investigated in this research also agreed very well with Cope. The confining pressure, generalized versus direct testing, and relative density were all shown to have minimal effects on the inclination of the shear band.

Another important variable that this research studied was the effect of grain size on the failure angle. Koenders et. al. (1990) (Table 1.1) suggested that the average grain size would determine which of the three proposed theories would be the most accurate. The combined research of this project disagrees with that proposal. According to Koenders, Coulomb's theory should give the best predictions for both the LSI-30 and the Loire sands, since the average grain size (D_{50}) of each is smaller then 0.65 mm. In both cases, the Arthur-Vardoulakis theory yielded the most accurate prediction.

Chapter Six

Conclusions

6.1 Summary

The research done for this thesis conducted a total of 35 different tests to study the factors influencing the inclination of shear banding in non-cohesive, coarse-grain sands. The testing was done using a hollow cylinder torsional triaxial device. The capabilities of this set up were such that tests could be conducted while the mean stress remained constant. The majority of the tests were conducted under these conditions. Other parameters that were examined were the relative density, confining pressure and stress path. Samples were tested at two different relative densities, namely 50% and 80%. Three initial effective confining pressures were chosen of 30, 50, and 70 psi (207, 345, and 483 kPa). Finally, the specimens were subjected to five different stress paths. These tests had the principle stress applied at angles of 0, 30, 45, 60, and 90 degrees from the vertical axis. All the tests were drained to measure the volume change in the specimen. The volume change was necessary to calculate the angle of dilation, a crucial variable in several prediction theories. The testing program was modeled after the research done by C. Tucker Cope (1997) to investigate the effect of particle size on shear banding.

6.2 Results and Conclusions

Three theories predicting the angle of failure were studied to determine the most accurate one. This was the primary focus of this thesis. Based on the results, it was clear that the Arthur-Vardoulakis theory gave the best results. However, the quantities needed to calculate the angle could be found using different methods. For this reason, there were

friction (ϕ') obtained from the peak stress and the angle of dilation using the plane strain formula (ψ_{ps}) were used. This combination proved to be the most accurate in nearly half of all the tests conducted where a shear band formed. This finding matched the conclusion as noted by Cope.

The second goal of this research was to determine the effect of various testing variables on the shear band. Of the various parameters studied, only the stress path influenced the angle of shear banding. The angle beta, or the angle of principle stress in relation to the vertical axis, was the only variable that clearly affected the inclination of the shear band. All others parameters were observed to have only minimal effects.

Finally, the last objective was to study the influence of grain size on the shear band angle. The results of the tests on both the LSI-30 and Loire sands led to the same conclusions. Each one indicated that the Arthur-Vardoulakis theory was the most accurate, despite the noticeable difference in the average grain size. This points to the conclusion that, at least within reasonable limits, the grain size will not effect the shear band angle.

6.3 Suggestions for Future Research

While great care was taken to keep strict control over various factors, a program of testing might be recommended to try and reproduce the results as found from the existing data. Sand is anisotropic by nature and by running several tests with the same parameters might help to observe the accuracy of this research. As can be seen by consulting the summary of tests, it was common to rerun a test. This was done to guarantee that no mistakes were made.

Another suggestion to improve on the conclusions might be to test samples under a larger variety of stress paths. For this thesis, only three different useful beta angles (β= 30°, 45° & 60°) were studied. Perhaps a better understanding would arise from testing samples at angles of 15° and 75°. This would give a total of five points from which to draw conclusions from instead of three.

The variation of the medium used might help to broaden the results as found with the LSI-30 and Loire sands. Perhaps an extremely fine sand and a very coarse sand (sands finer then LSI-30 and coarser then Loire) should be studied to analyze if indeed there is a trend that depends on grain size. In general, it would help to draw conclusions with more then just two sets of data.

Finally, the results from the digitization process should be studied in greater detail. Appendix B of this thesis contains the results of the digital imaging procedure for Tests # 77, 78a & 79. This information details the shear band inclinations, the strains in and around the shear band and also the width of the shear band. Eventually a model can be developed from this information to accurately simulate the genesis and propagation of a shear band.

Appendix A

References

Arthur, J.R.F. and Dunstan T. (1982) Rupture Layers in Granular Media. Proc. IUTAM *Conference Deformation and Failure of Granular Materials*, Delft, 453-459.

Arthur, J.R.F., Dunstan T., Al-Ani Q.A.J.L. & Assadi A. (1977) "Plastic Deformation and Failure in Granular Media," *Geotechnique,* 27, No.1, 53-74.

Balasubramaniam, A.S. (1976) "Local Strains and Displacement Patterns in Triaxial Specimens of Saturated Clay," *Soil Foundations,* 16, No. 1, 101-114.

Bolton, M. D. (1986) "The Strength and Dilatancy of Sands," *Geotechnique,* 36, No.1, 65-78.

Cope, C. Tucker (1997) *Shear Banding In Sand Under Combined Stress Paths,* Masters Thesis, Department of Civil Engineering, Case Western Reserve University, Cleveland, Ohio.

Houlsby, G.T. and Wroth, C.P. (1980) "Strain and Displacement Discontinuities in Soils," *Journal of Engineering Mechanics Division of American Society of Civil Engineers,* 117, EMA, Aug., 753-772.

Koenders, M.A., Arthur, J.R.F., and Dunstan, T. (1990) "The Behaviour of Granular Materials at Peak Stress," *Yielding, Damage, and Failure of Anisotropic Solids,* J.P. Boehler, Ed., London, Mechanical Engineering Publications. pg. 805-818.

Lade, P.V., Yamamuro, J.A., and Skyers, B.D., "*Effects of Shear Band Formation in Triaxial Extension Tests,*" Geotechnical Testing Journal, GTJODJ, Vol. 19, No.4, December 1996, 398-410.

Liang, L. (1995) *Development of an Energy Method for Evaluating the Liquefaction Potential of a Soil Deposit,* Ph.D. Thesis, Department of Civil Engineering, Case Western Reserve University, Cleveland, Ohio.

Liang, L., Saada, A.S., Figueroa, J.L., Cope, C.T. (1996) *The Use of Digital Image Processing in Monitoring Shear Band Development,* Department of Civil Engineering, Case Western Reserve University, Cleveland, Ohio.

Schantz, T. and Vermeer, P.A. (1996) "Angles of Friction and Dilatancy of Sand," *Geotechnique,* Vol. 46, No.1, 145-151.

Vardoulakis, I. (1980) "Shear Band Inclination and Shear Modulus of Sand in Biaxial Tests," *International Journal of Numerical and Analytical Methods in Geomechanics*, Vol. 4, 103-119.

Veemer, P.A. (1990) "The Orientation of Shear Bands in Biaxial Tests," *Geotechnique,* Vol. 40, No. , 223-236.

Yoshida, T., Tatsuoka, F., Siddiquee, M.S.A., Kamegai, Y. & Park C.S. (1994) "Shear Banding in Sands Observed in Plane Strain Compression," *Localization and Bifurcation Theory for Soils and Rocks,* Chambon, Desrues, Vardoulakis, 165-178.

Appendix B

Digitization Results

B.1 Explanation of Appendix Graphs

Upon completion of the digitization process, several graphs were created. These plots summarize the various strains found using this new procedure. Three tests were completely digitized and the graphs from digitization are included in this appendix. The three test were Test #77 (Torsion-Compression), Test #78a (Pure Torsion) and Test #79 (Torsion-Extension). Each of these tests were conducted at 50 psi (345 kPa) initial effective confining pressure and 50% initial relative density. For each of the three tests, four images were digitized per camera. By analyzing this digitized data, the MATLAB™ software was able to create seven plots for each camera. A total of 28 plots for each test were generated, because four cameras were needed to completely capture the entire surface of the specimen.

The digitization process assigns coordinates to each grid intersection point. By knowing the coordinates at the initial and subsequent times, the strains of a rectangle composed of four of these points could be found. Figure A demonstrates this method.
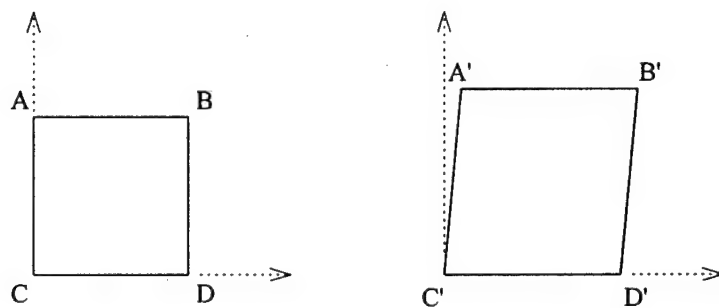
Figure A

The rectangle on the left (which initially begins as a square) is created when connecting lines between points A through D. At some subsequent time, the rectangle on the right can be created by connecting lines between points A' through D'. The actual coordinates are not as important as the length of the line segments connecting two points, since the strain is computed by dividing the change in length over the original length. Each of the seven plots are explained in greater detail below.

Figure 1: This figure contains four separate graphs.

- **Top left plot (τ_{oct} vs. time)**: Shows the shear stress (Tau Octahedral) verses time along with the four times images were taken and digitized. Typically, the first two times were taken before failure (peak of the t_{oct} vs. time) and the last two were taken after failure.

- **Top right plot (γ vs. time)**: Shows the average shear strains of elements in various locations. These locations are at the top of the grid, at the bottom and the average of these two. Referring to Figure A, the shear strain is found by determining the angle between the vertical axis and line A'C' or B'D'. These two angles are averaged for each element and then averaged over the number of elements used. Typically, this is done for two or three rows of elements to obtain a more accurate measurement. In addition, a global shear strain curve is included to show the strain found using the rotation of sample as measured with the RVDT. This line is included for the sake of comparison. In the case where a shear band is at the top or bottom of a grid the results may appear to be inaccurate. This is due

to the fact that in areas near the shear band, larger deformations have occurred. When a shear band is at the upper or lower limits of the grid, only one row of elements is available to use for an average. This line indicating the strains at the top or bottom of the grid are typically inaccurate under these conditions.

- **Bottom left plot ($\varepsilon_{vert.}$ vs. time)**: This plot demonstrates the vertical strains of elements in several locations (same as previous graph). To calculate the vertical strain, the height change of the element is divided by the original height; where the height change is taken as the average height change between the two horizontal lines (segments A'B' and C'D' in Figure A). The global vertical strain is also included.

- **Bottom right plot ($\varepsilon_{horiz.}$ vs. time)**: This graph is very similar to the vertical strain plot. In this plot however, the horizontal strains are shown. They are determined by finding the average horizontal change between two vertical lines (A'C' and B'D' in Figure A) and dividing this quantity by the original width of the element. As with the previous two graphs, a global strain is also shown.

Figure 2: This figure contains four separate graphs. These four plots are identical to the ones seen in Figure 1. However, in addition to the four curves for the strain plots, a fifth line is also plotted. This line is the average strains (shear, vertical, and horizontal) of just those elements within the shear band. These strains are typically much larger than those calculated outside the shear band and therefore the scale is adjusted accordingly.

Figure 3: This figure contains four separate graphs. These plots present data similar to Figure 2 except a rotation of axis is incorporated. The axis were rotated to be along and normal to the shear band. This figure is useful when making comparisons.

Figure 4: This figure shows three separate plots. These three graphs show the various strains (shear, vertical, and horizontal) as calculated for each row of elements. In other words, the strains are shown along the height of the specimen. Each plot has three curves which represent the strains as calculated at the second, third, and fourth times. For this figure, the strains are calculated at the nodes.

Figure 5: This figure shows three separate plots. For this figure, the same information from Figure 4 is calculated except for this plot the strains are calculated at the center of each element.

Figure 6: This figure shows three separate plots. The various curves from Figures 4 and 5 are superimposed here. The lines are from Figure 4 while the points are from Figure 5.

Figure 7: This figure shows three separate plots. This figure joins the various points from Figure 6 and creates a combination of the two curves.

B.2 Test #77

- **Torsion-Compression ($\beta = 30°$)**
- **Effective Confining Pressure = 50 psi (345 kPa)**
- **50% Initial Relative Density**
- **Generalized Test**
- **Digitized Times Intervals: 0000, 1600, 2500 & 3200 sec.**

Test #77; 3/18/97; Torsion-compression; ECP=50 psi; Loire, Video a
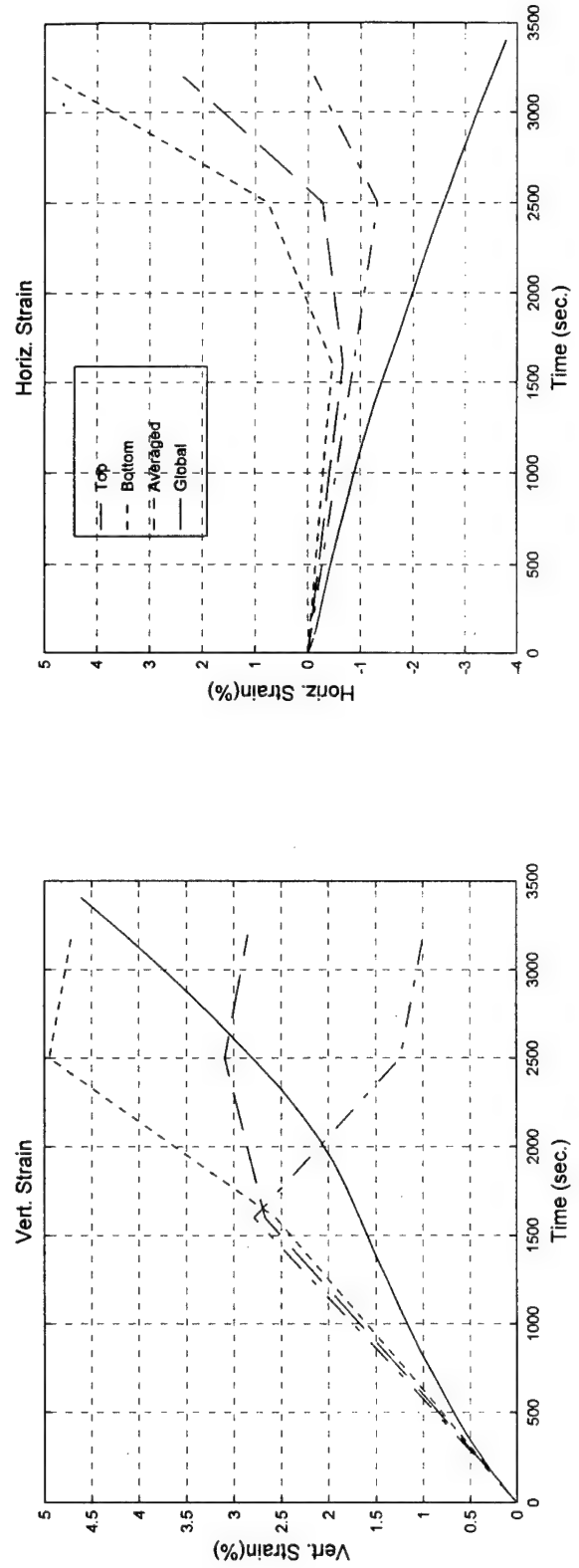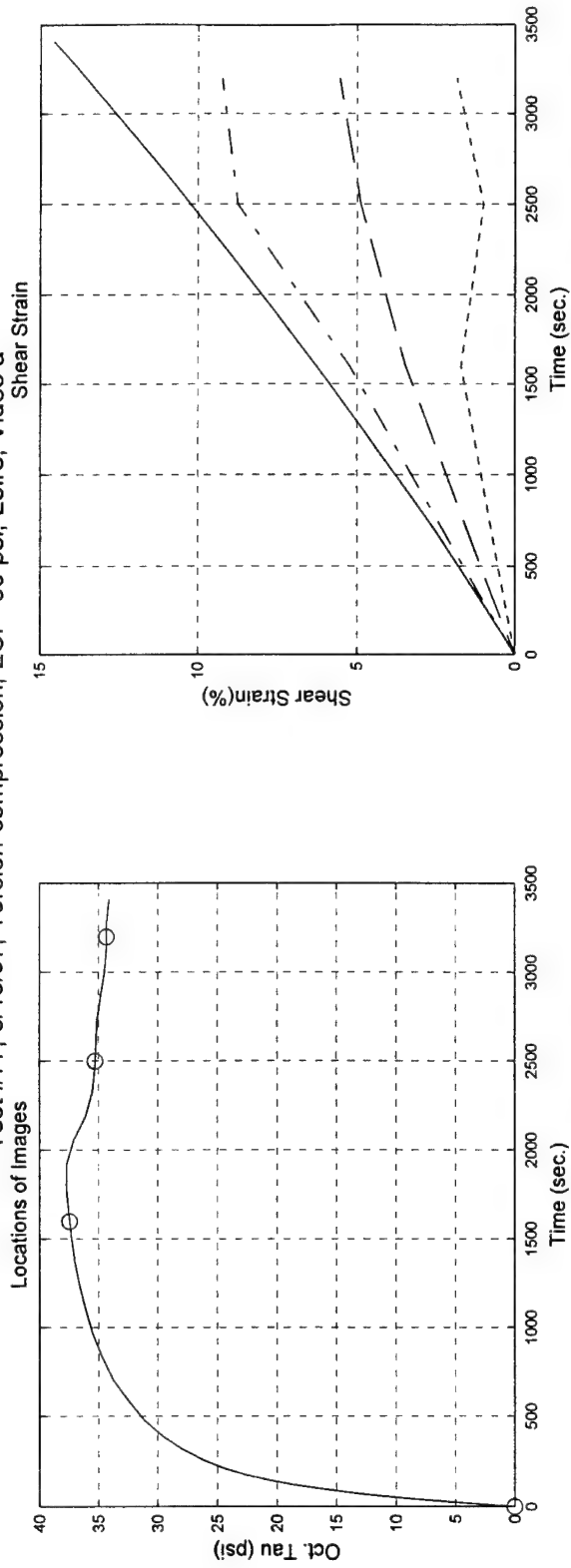
Test #77, Camera #A, Figure 1
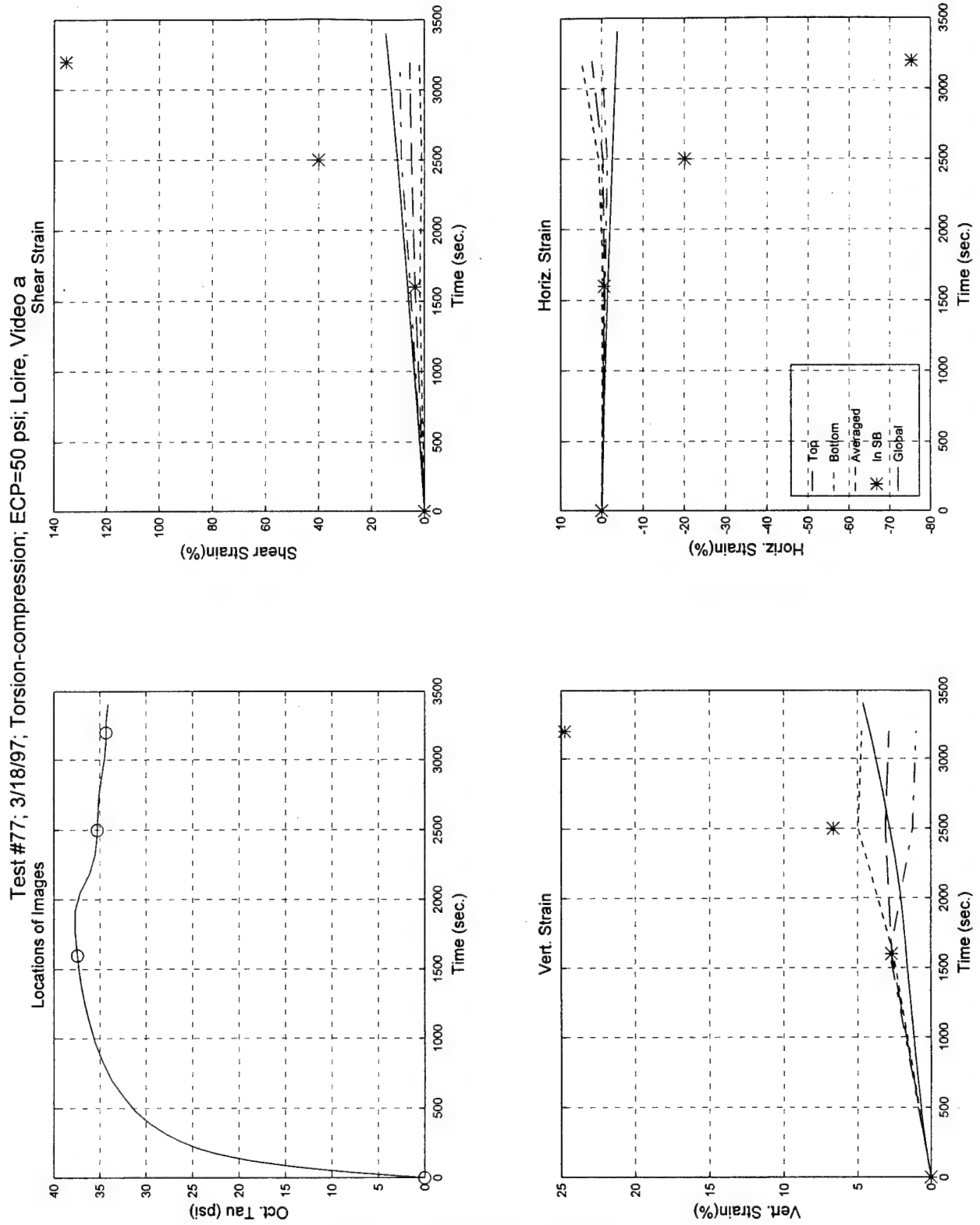
Test #77, Camera #A, Figure 2

108
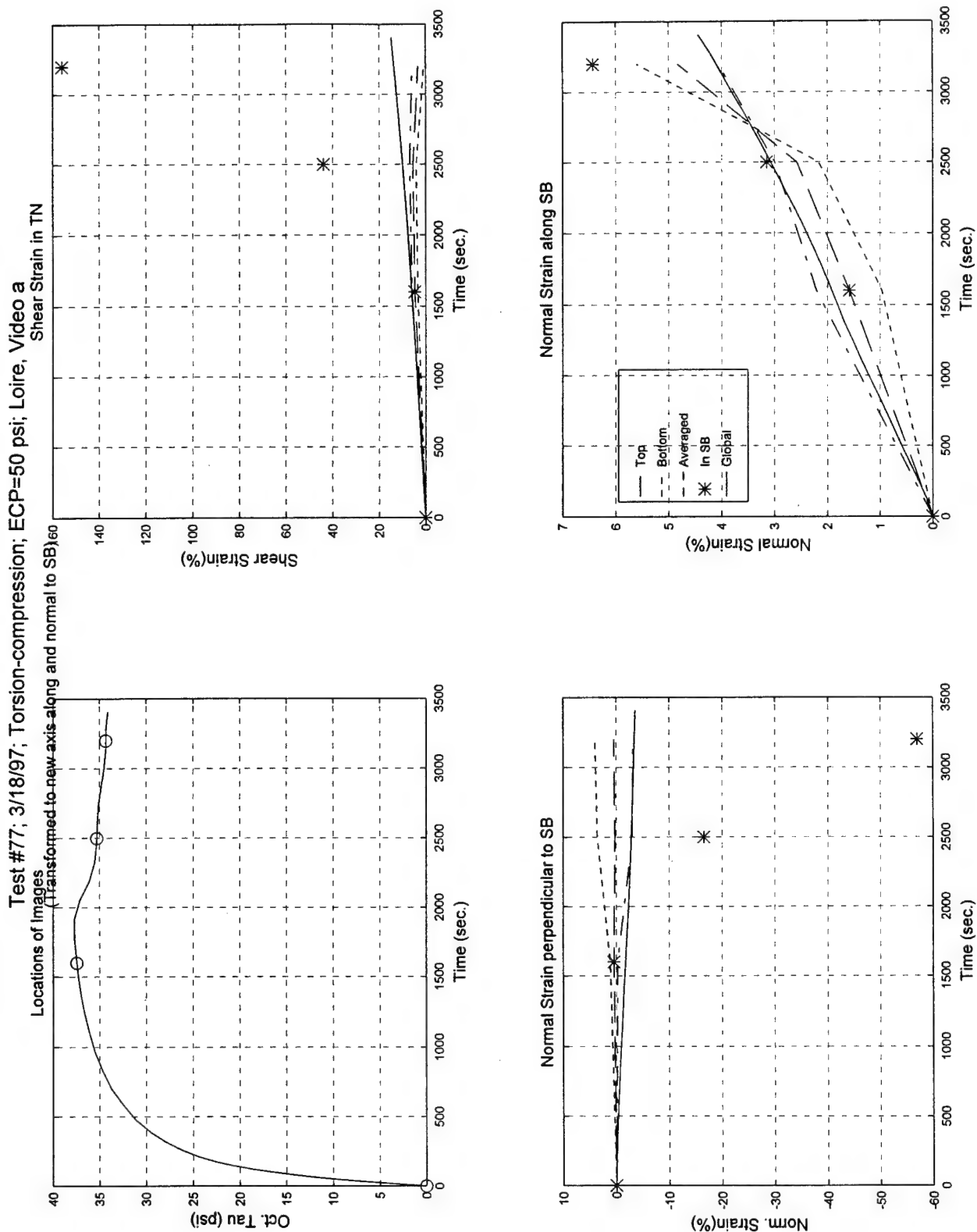
Test #77, Camera #A, Figure 3

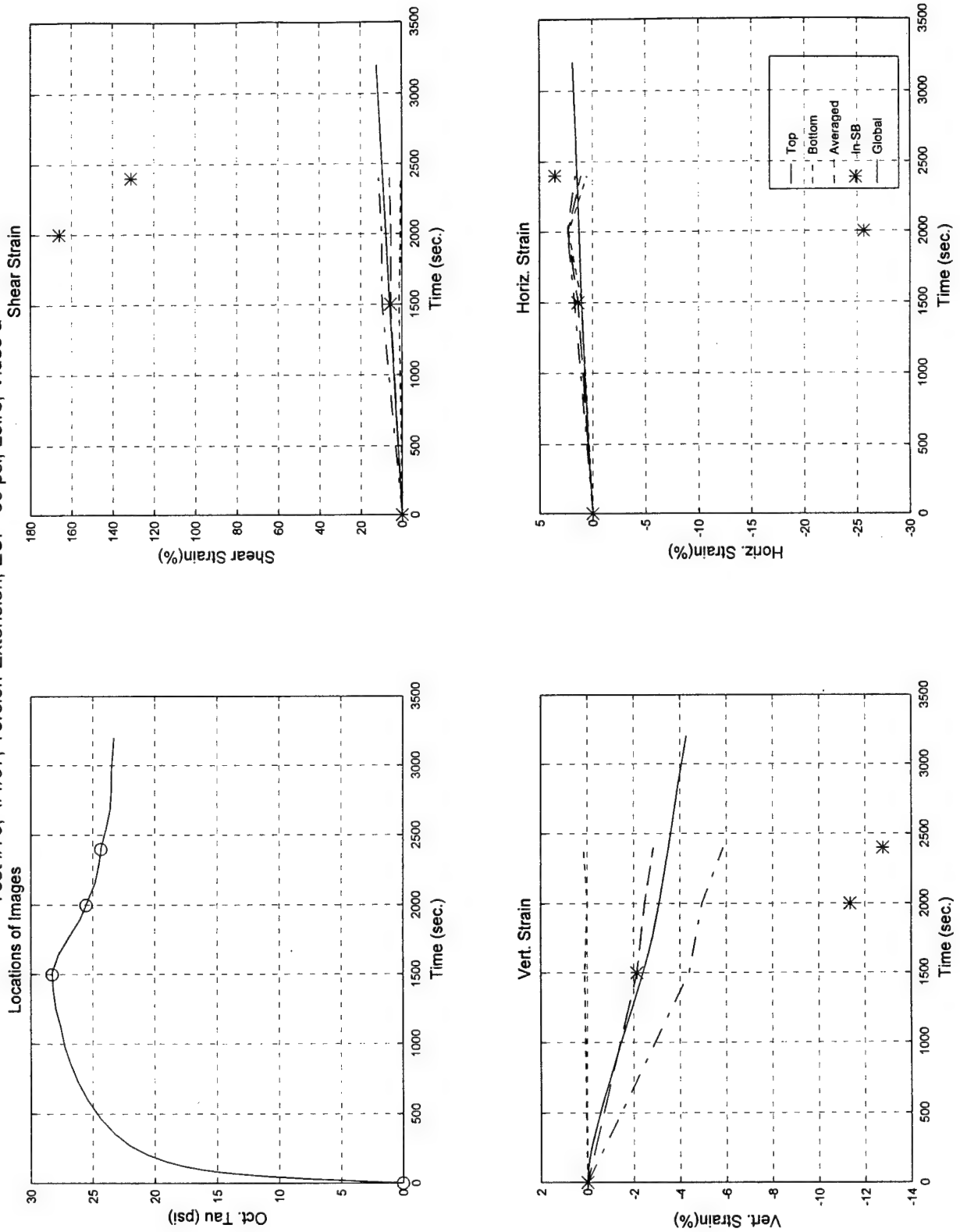Test #77; 3/18/97; Torsion-compression; ECP=50 psi; Loire, Video a

Vert. Strain

Horiz. Strain

Shear Strain
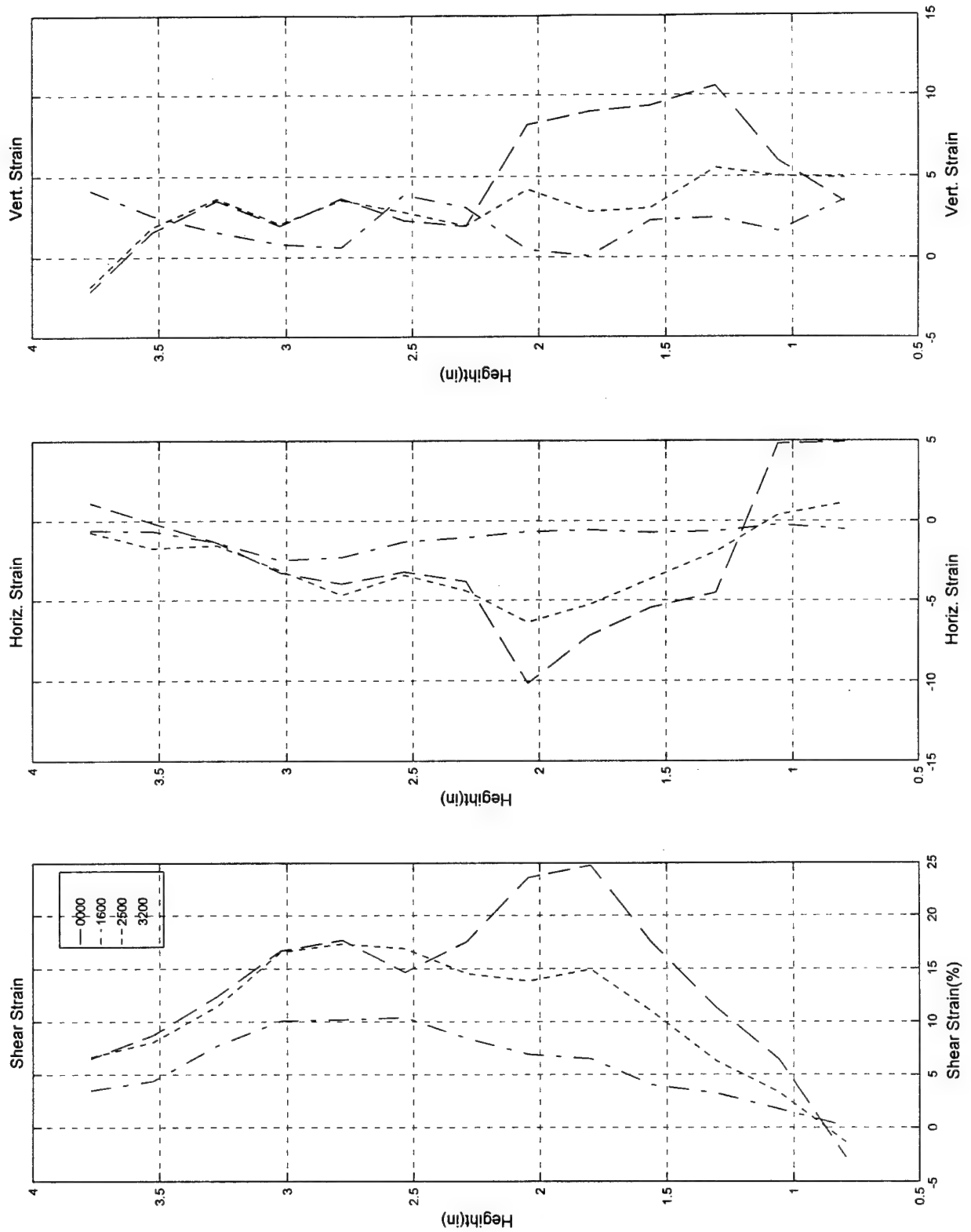
Test #77, Camera #A, Figure 4

Test #77; 3/18/97; Torsion-compression; ECP=50 psi; Loire, Video a
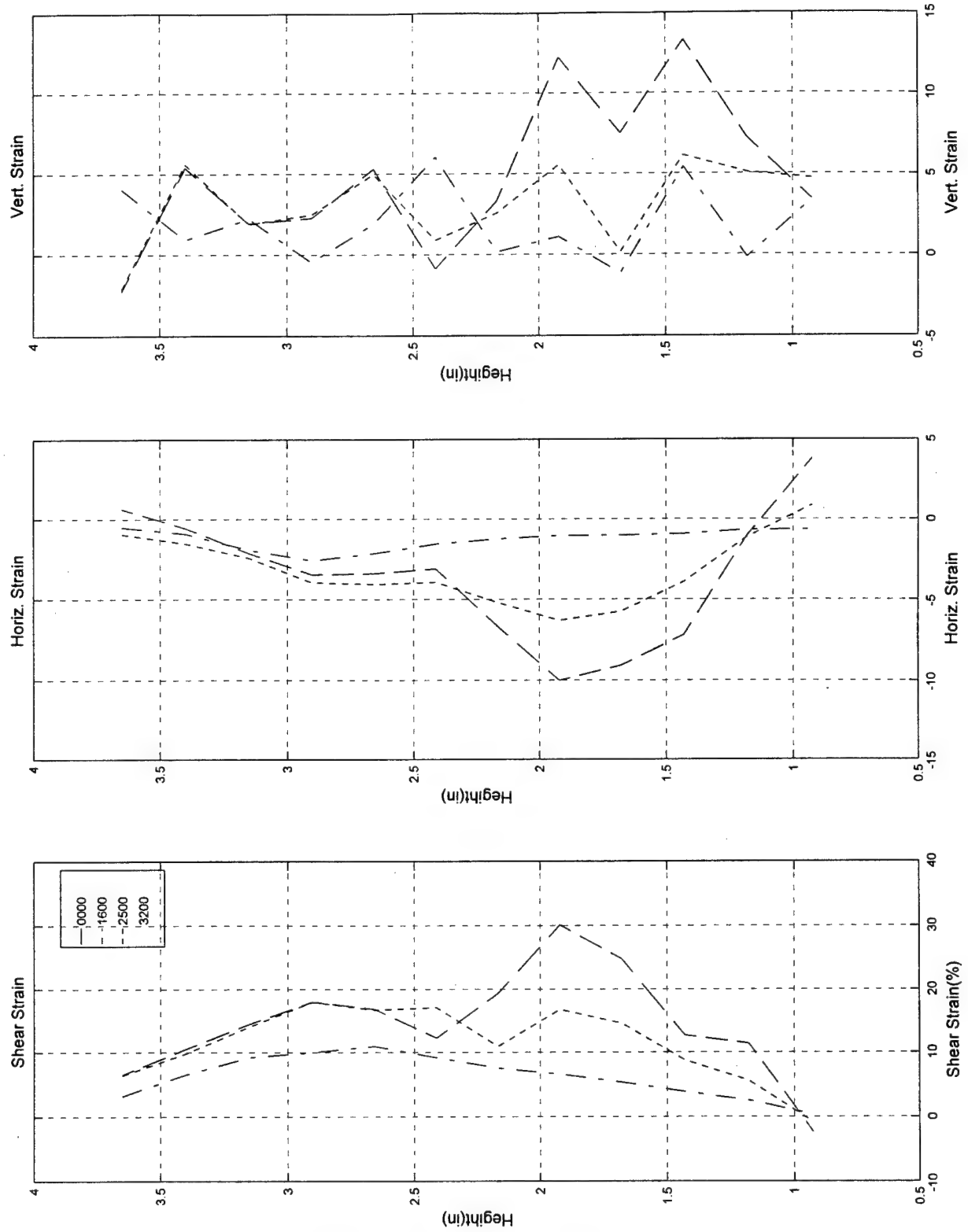
Test #77, Camera #A, Figure 5

Test #77; 3/18/97; Torsion-compression; ECP=50 psi; Loire, Video a
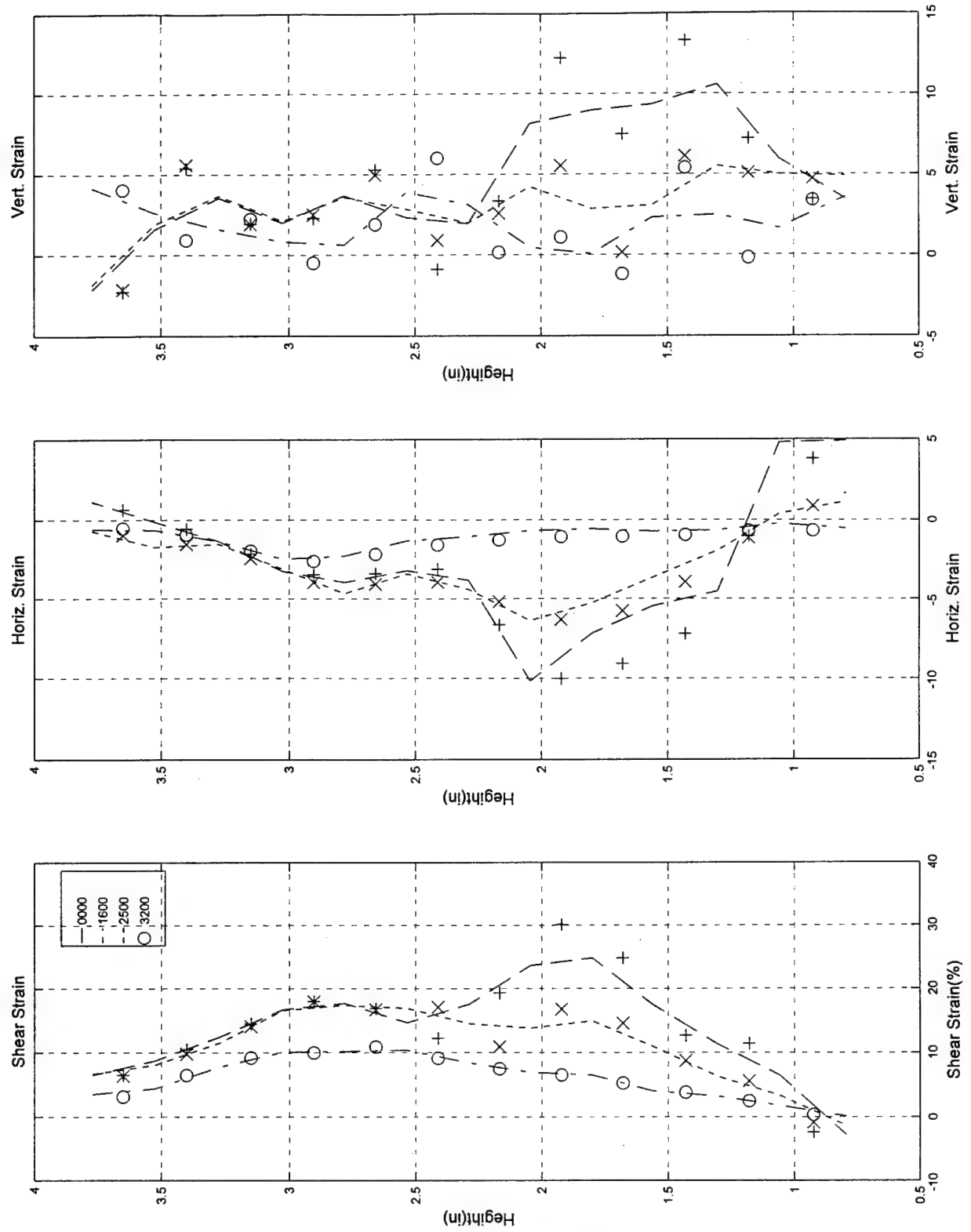
Test #77, Camera #A, Figure 6

Test #77, Camera #A, Figure 7
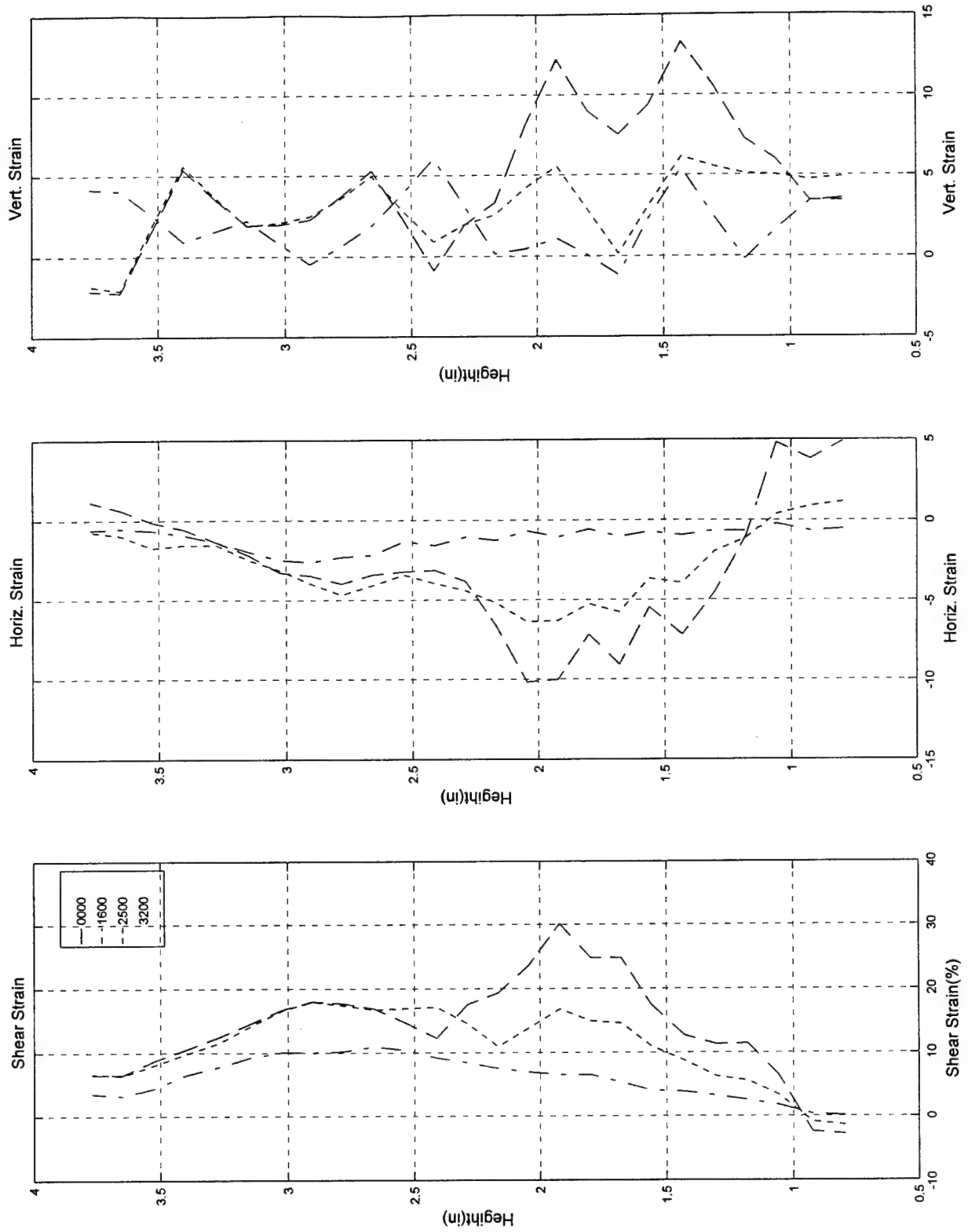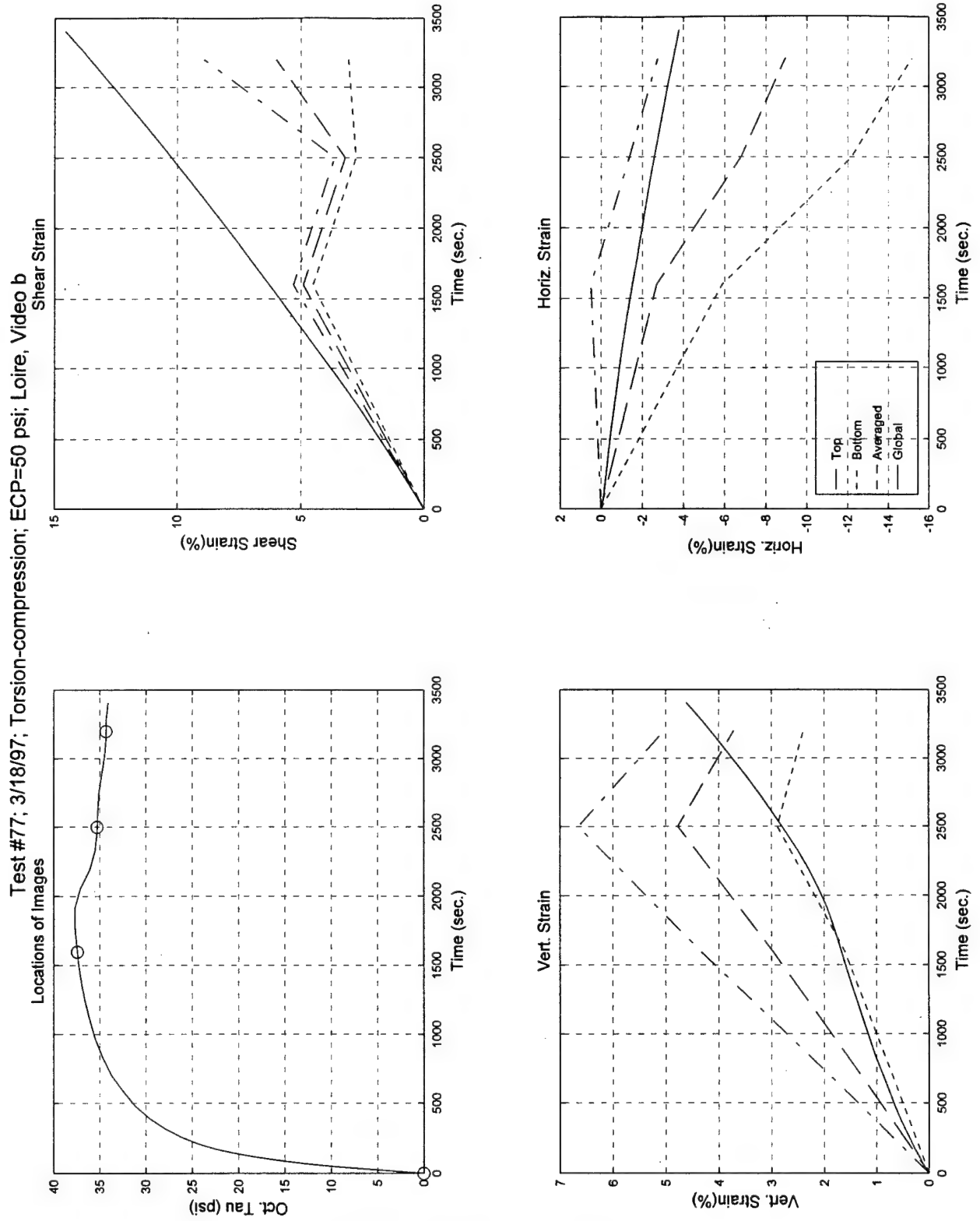
Test #77; 3/18/97; Torsion-compression; ECP=50 psi; Loire, Video b

Test #77, Camera #B, Figure 1

Test #77, Camera #B, Figure 2
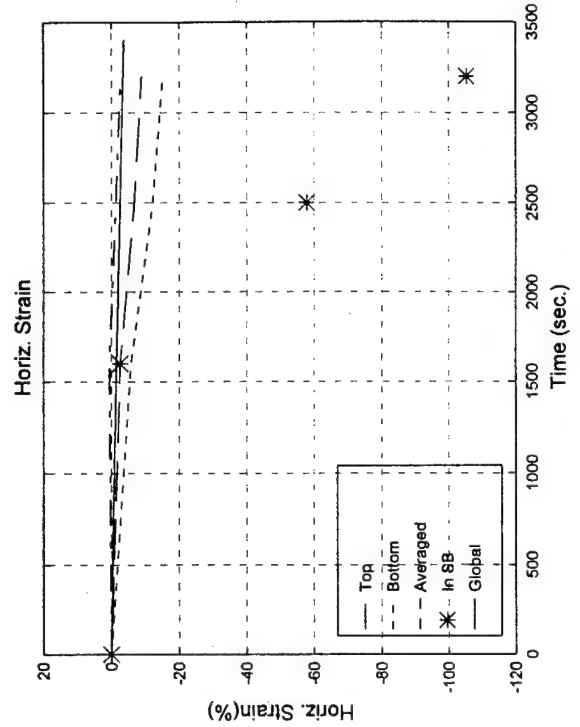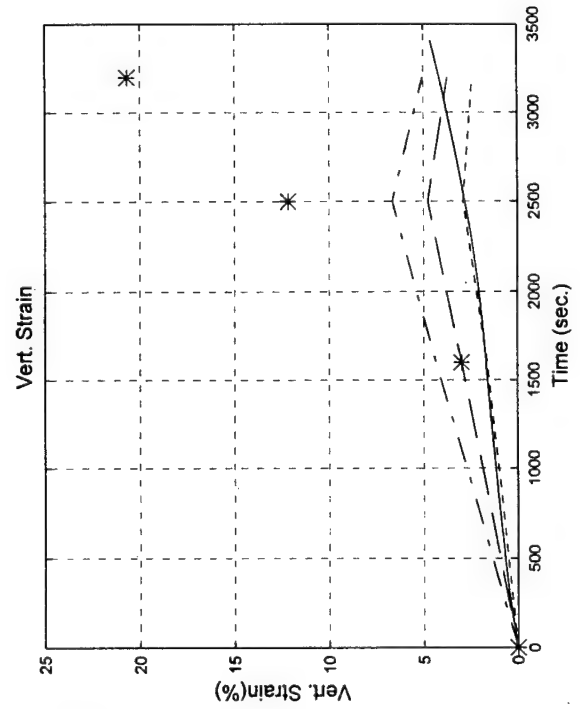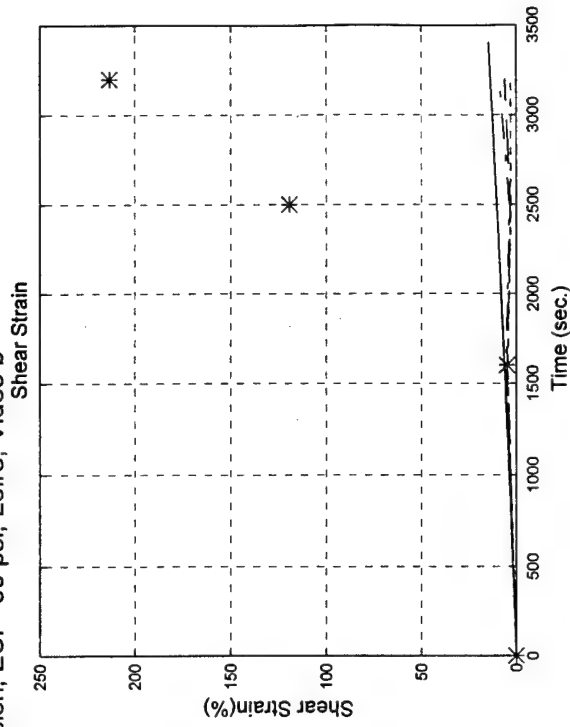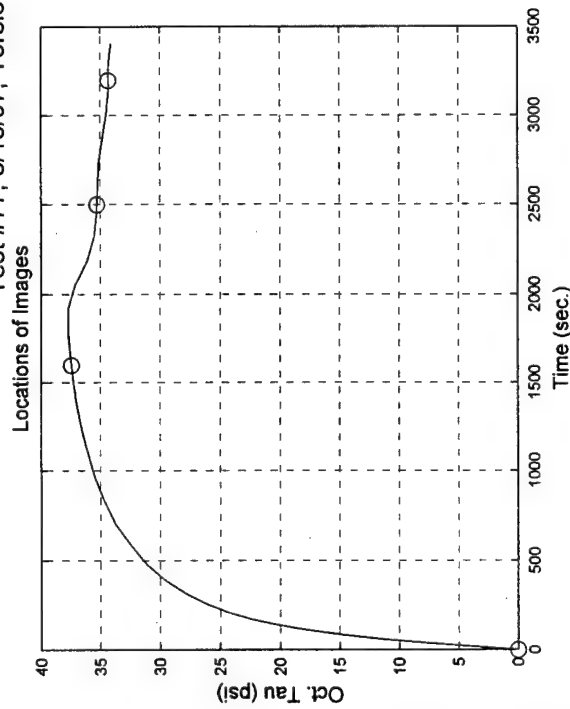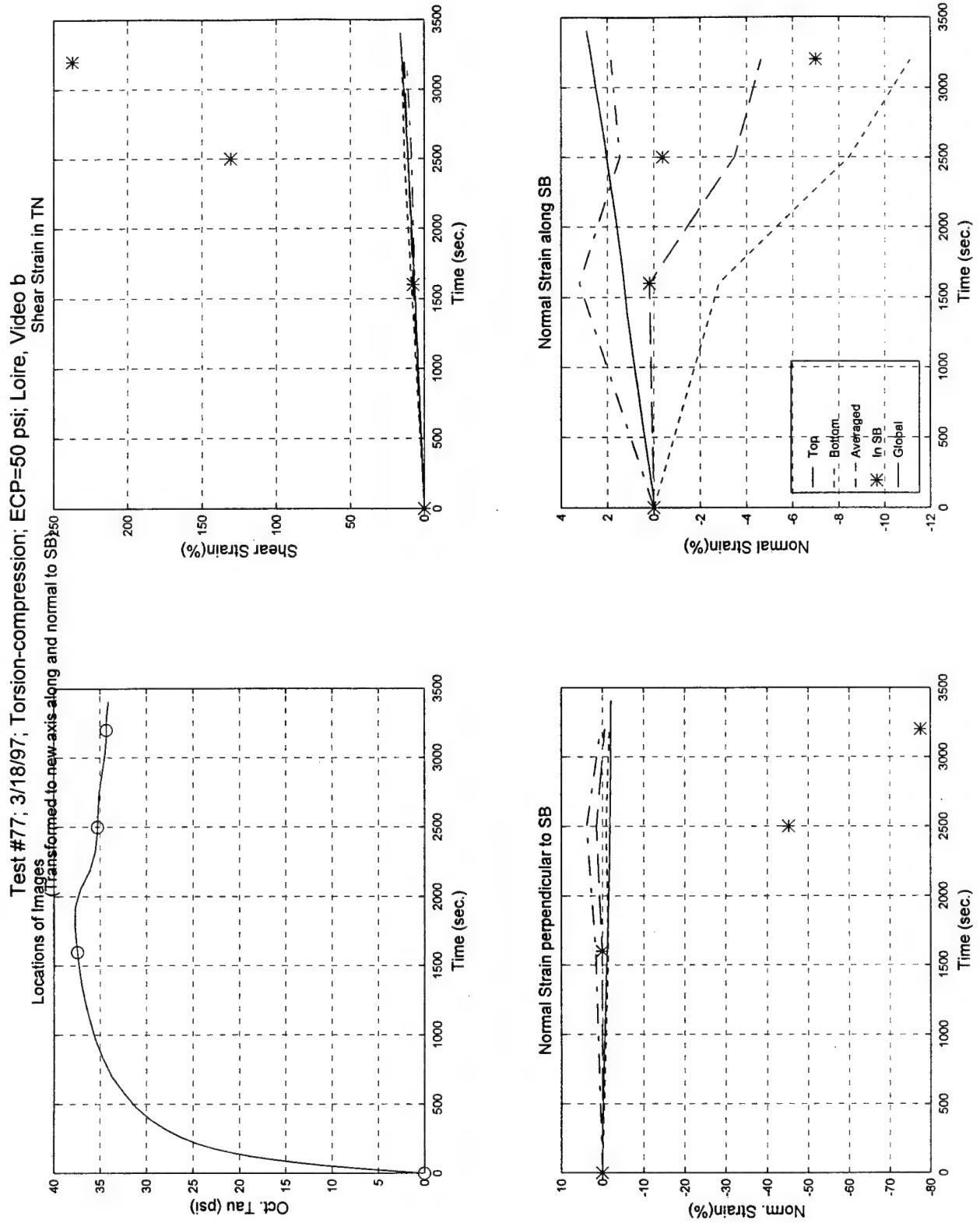
115

Test #77; 3/18/97; Torsion-compression; ECP=50 psi; Loire, Video b

Locations of Images
(Transformed to new axis along and normal to SB)

Shear Strain in TN

Normal Strain along SB

Normal Strain perpendicular to SB

Test #77, Camera #B, Figure 3
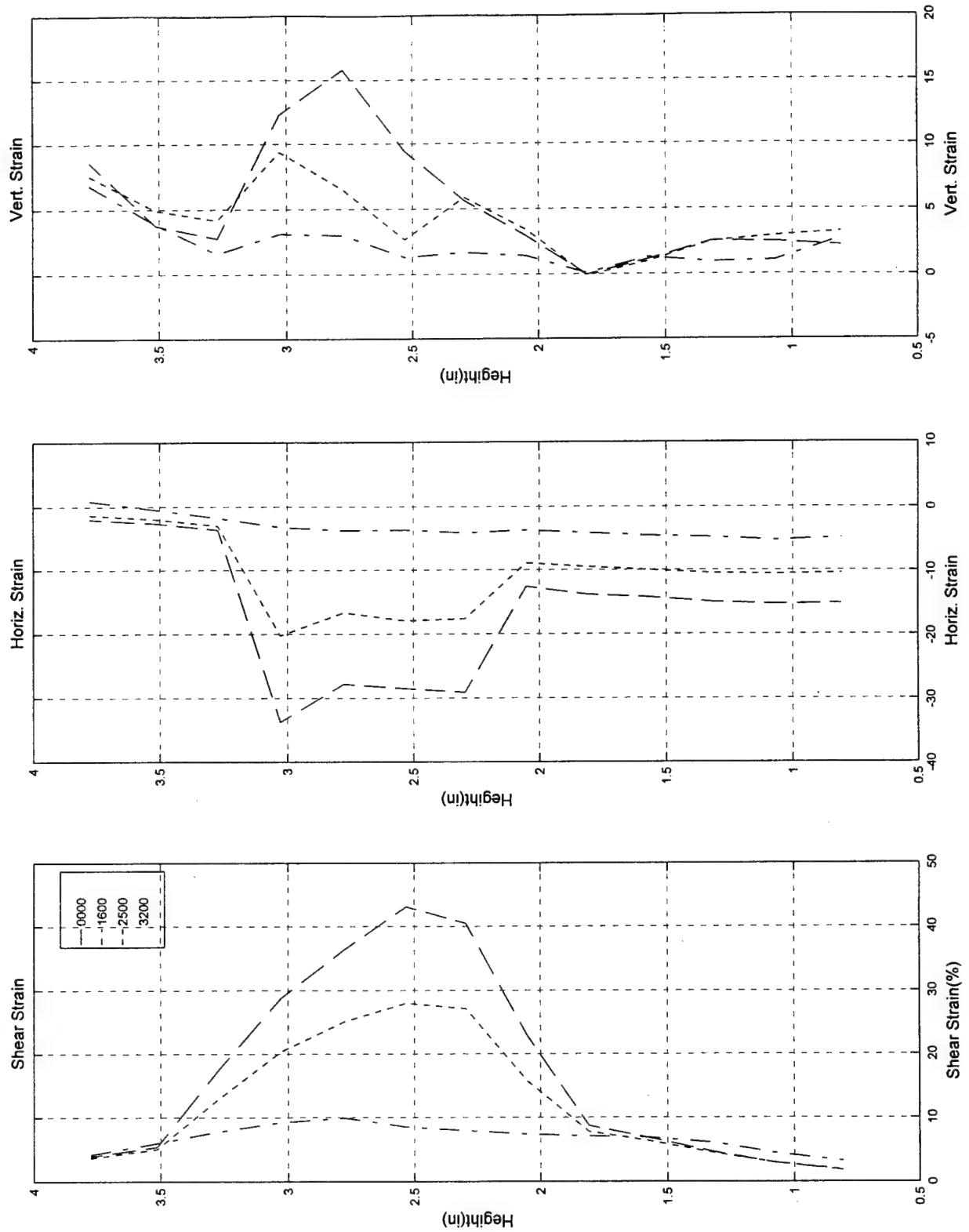
Test #77, Camera #B, Figure 4
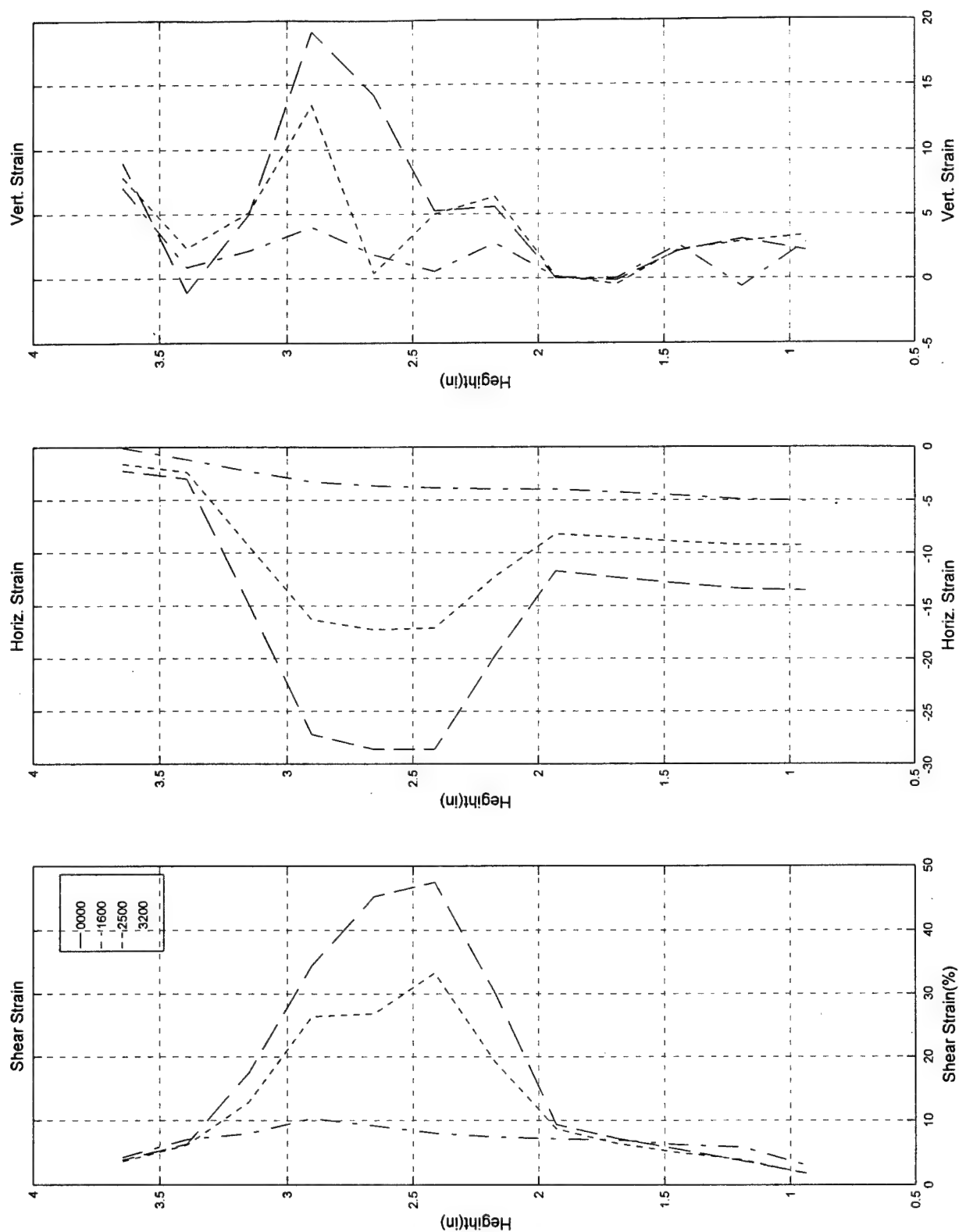
Test #77, Camera #B, Figure 5

Test #77; 3/18/97; Torsion-compression; ECP=50 psi; Loire, Video b
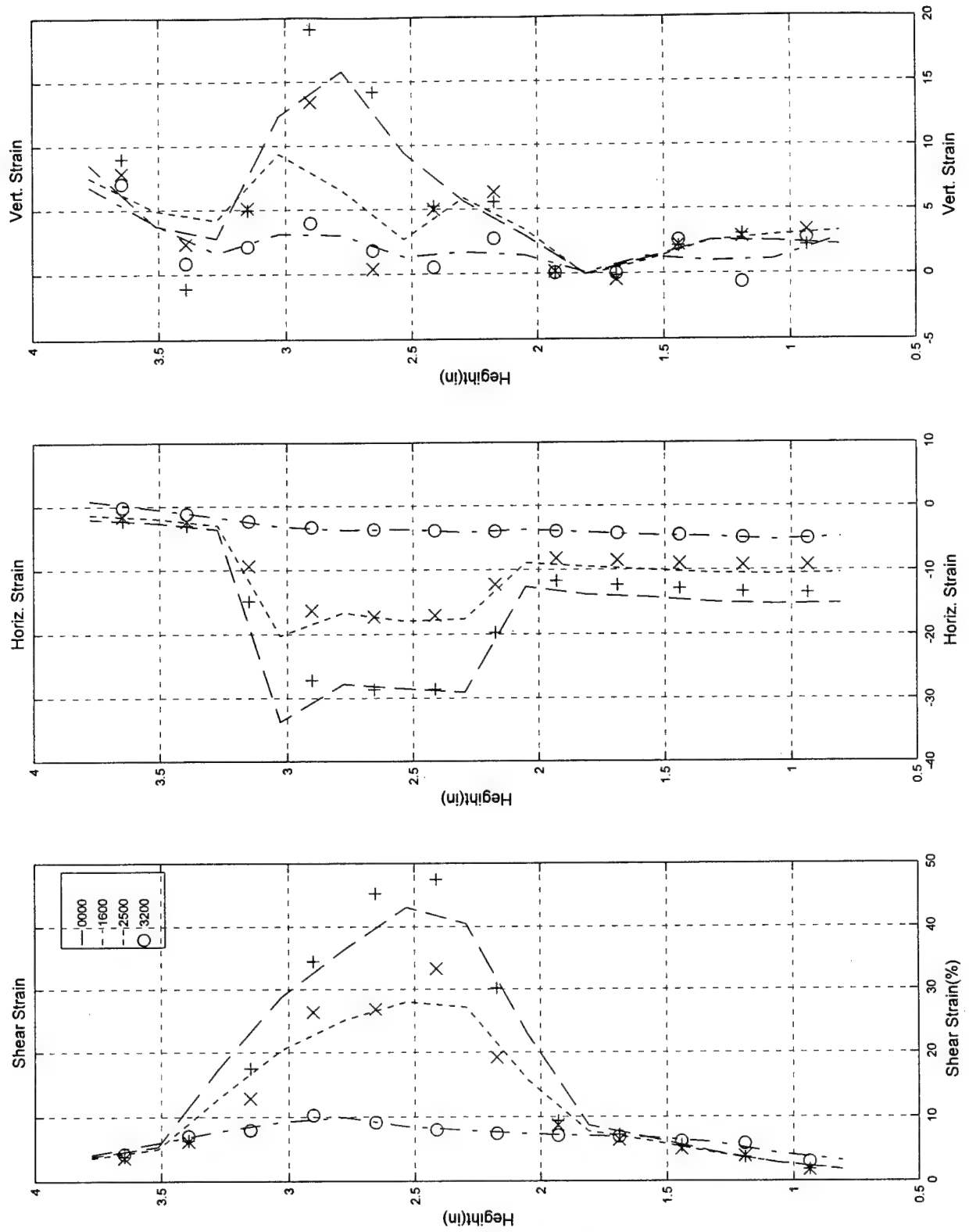
Test #77, Camera #B, Figure 6
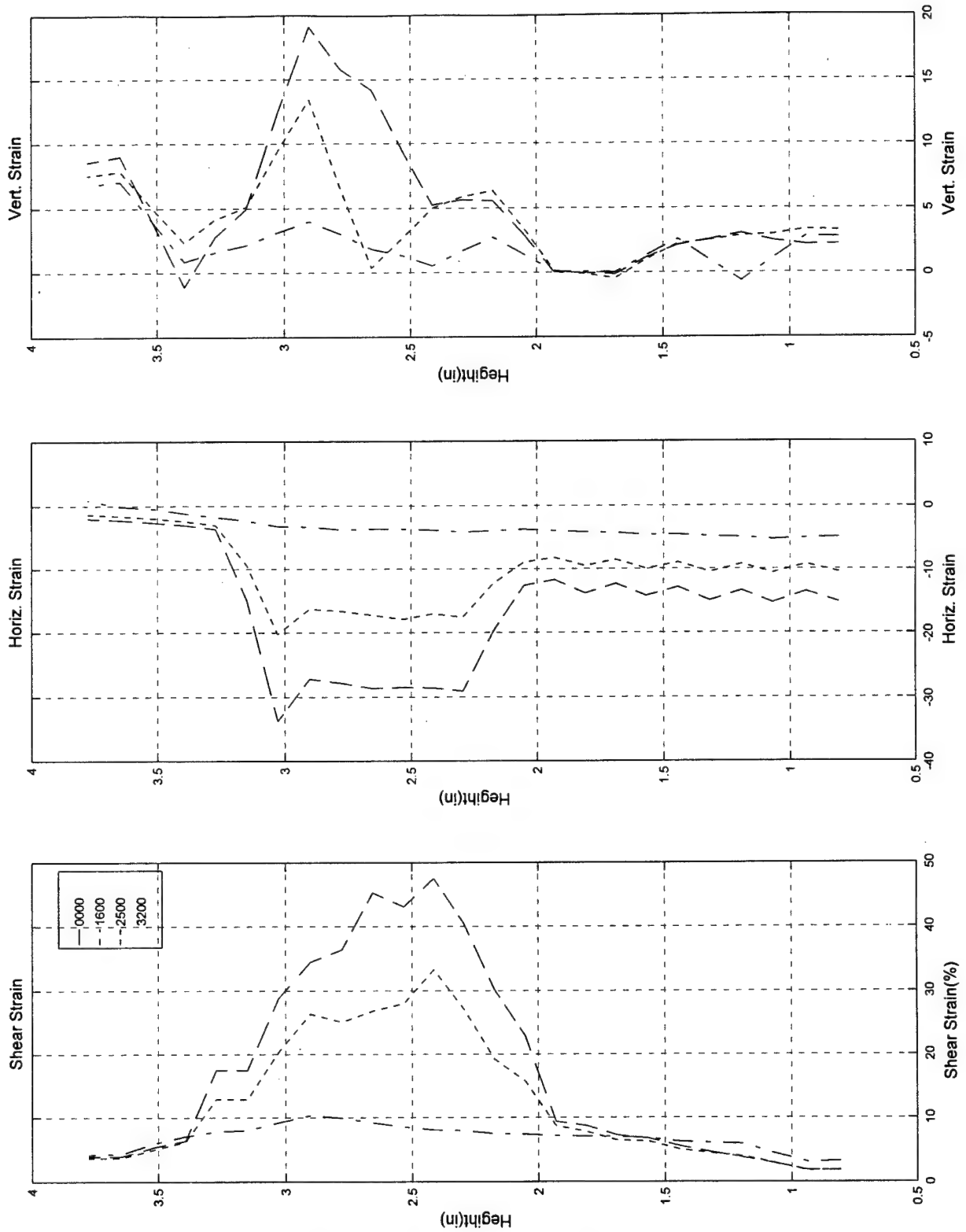
Test #77, Camera #B, Figure 7

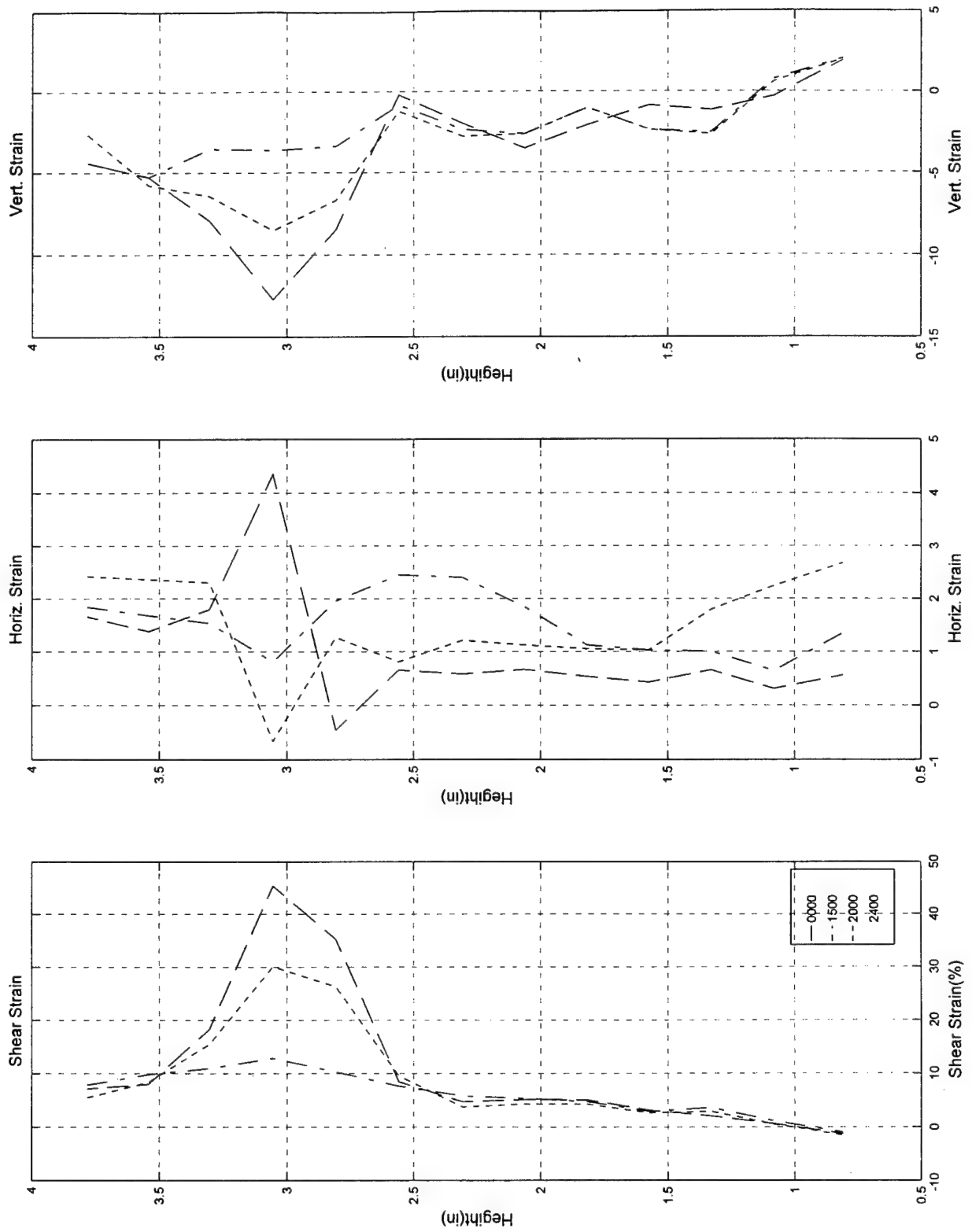Test #77; 3/18/97; Torsion-compression; ECP=50 psi; Loire, Video c

Test #77, Camera #C, Figure 1

121

Test #77; 3/18/97; Torsion-compression; ECP=50 psi; Loire, Video c
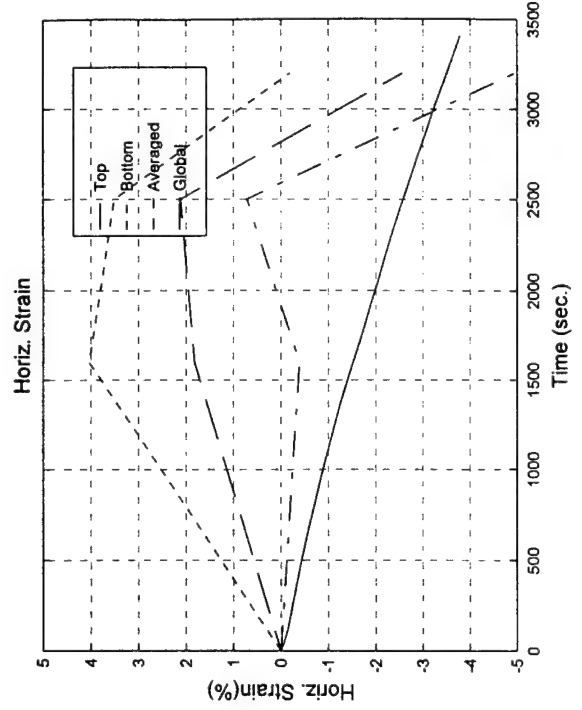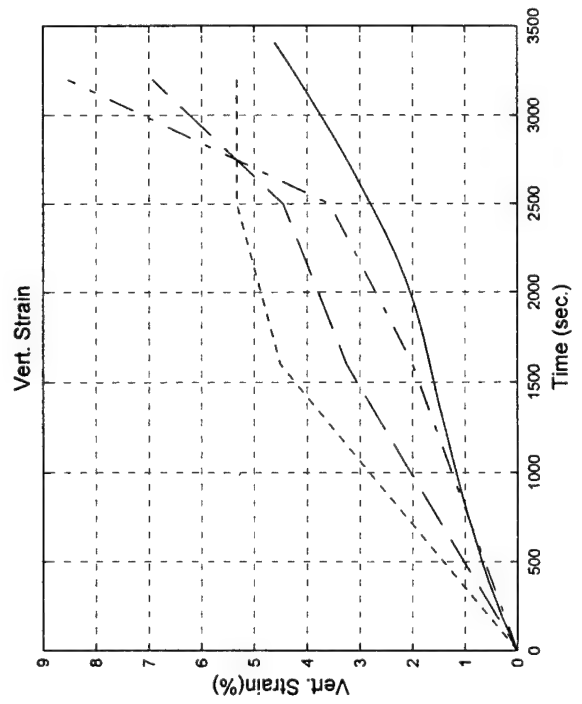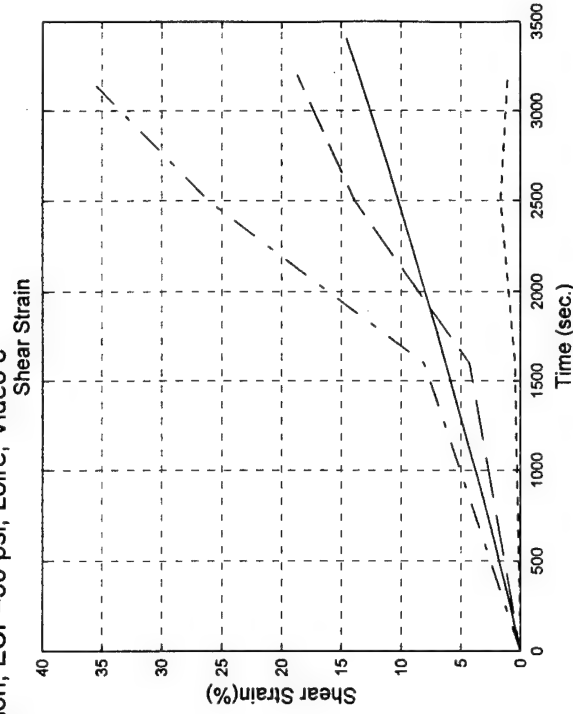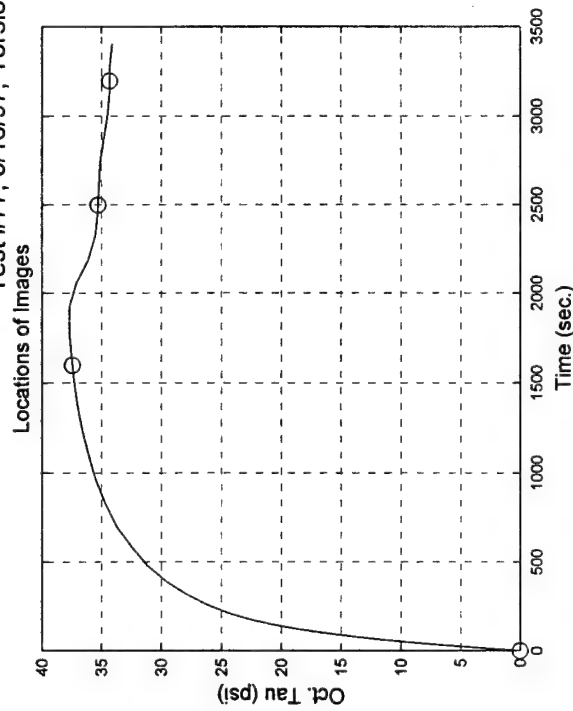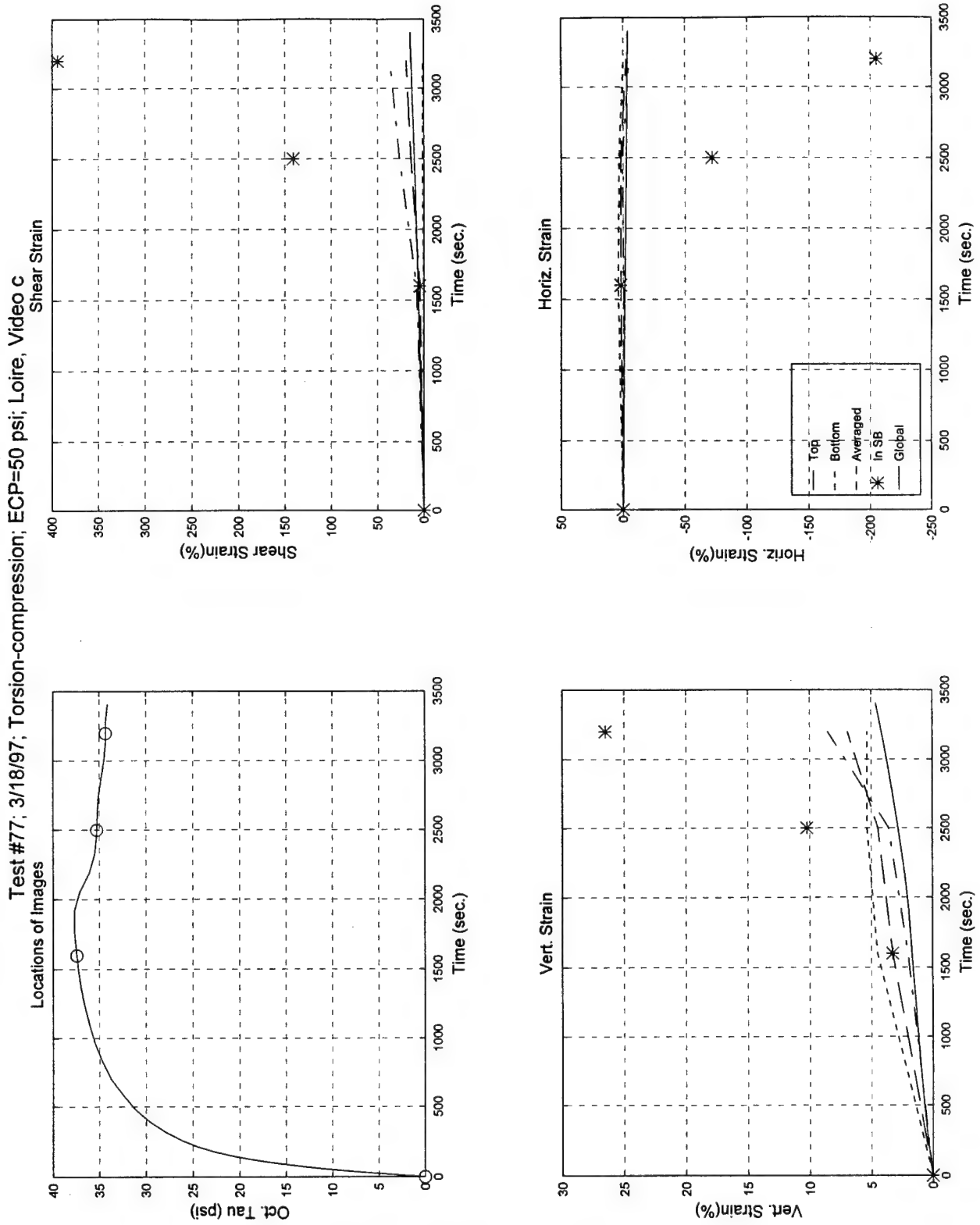
Test #77, Camera #C, Figure 2

Test #77; 3/18/97; Torsion-compression; ECP=50 psi; Loire, Video c
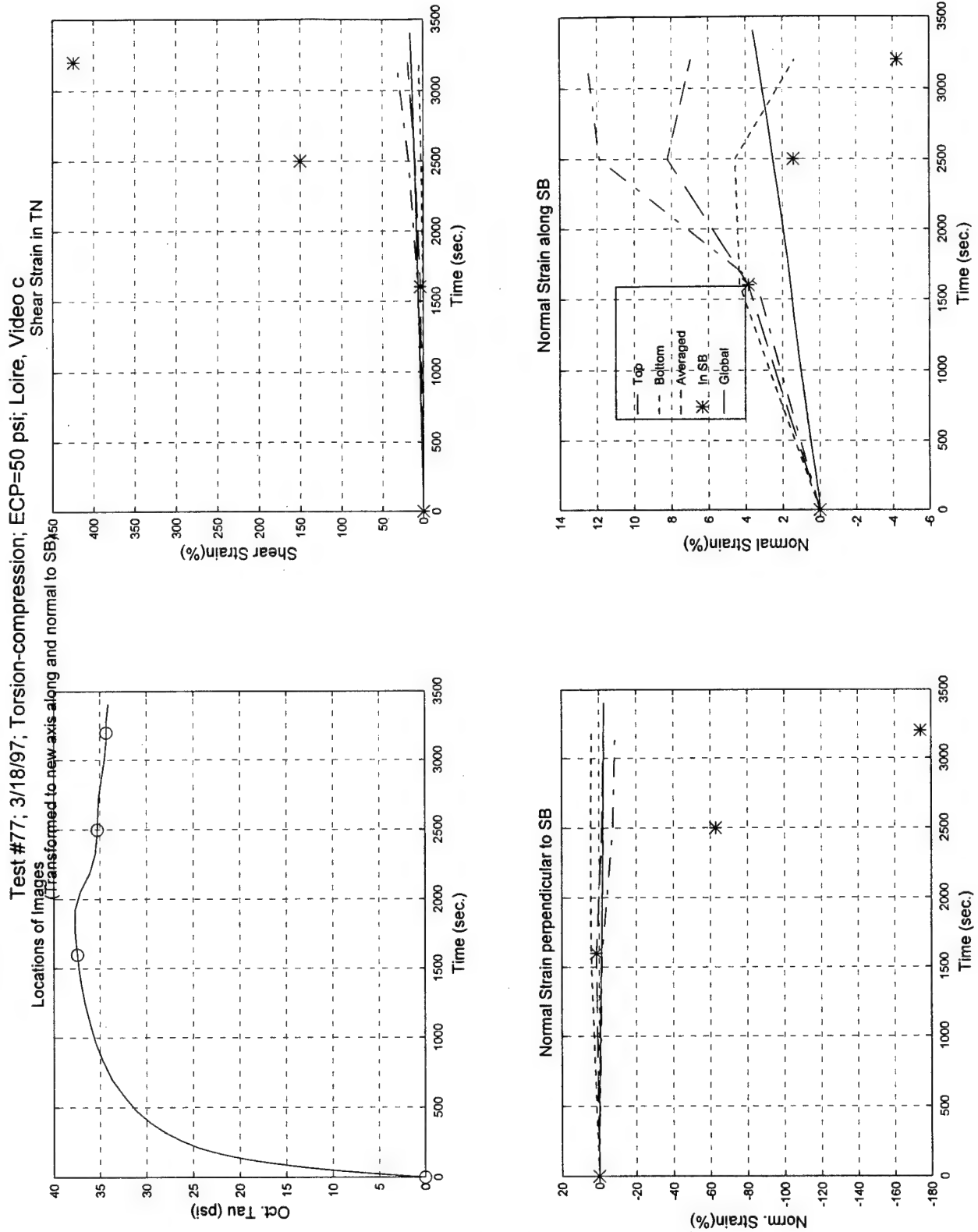
Test #77, Camera #C, Figure 3

Test #77; 3/18/97; Torsion-compression; ECP=50 psi; Loire, Video c
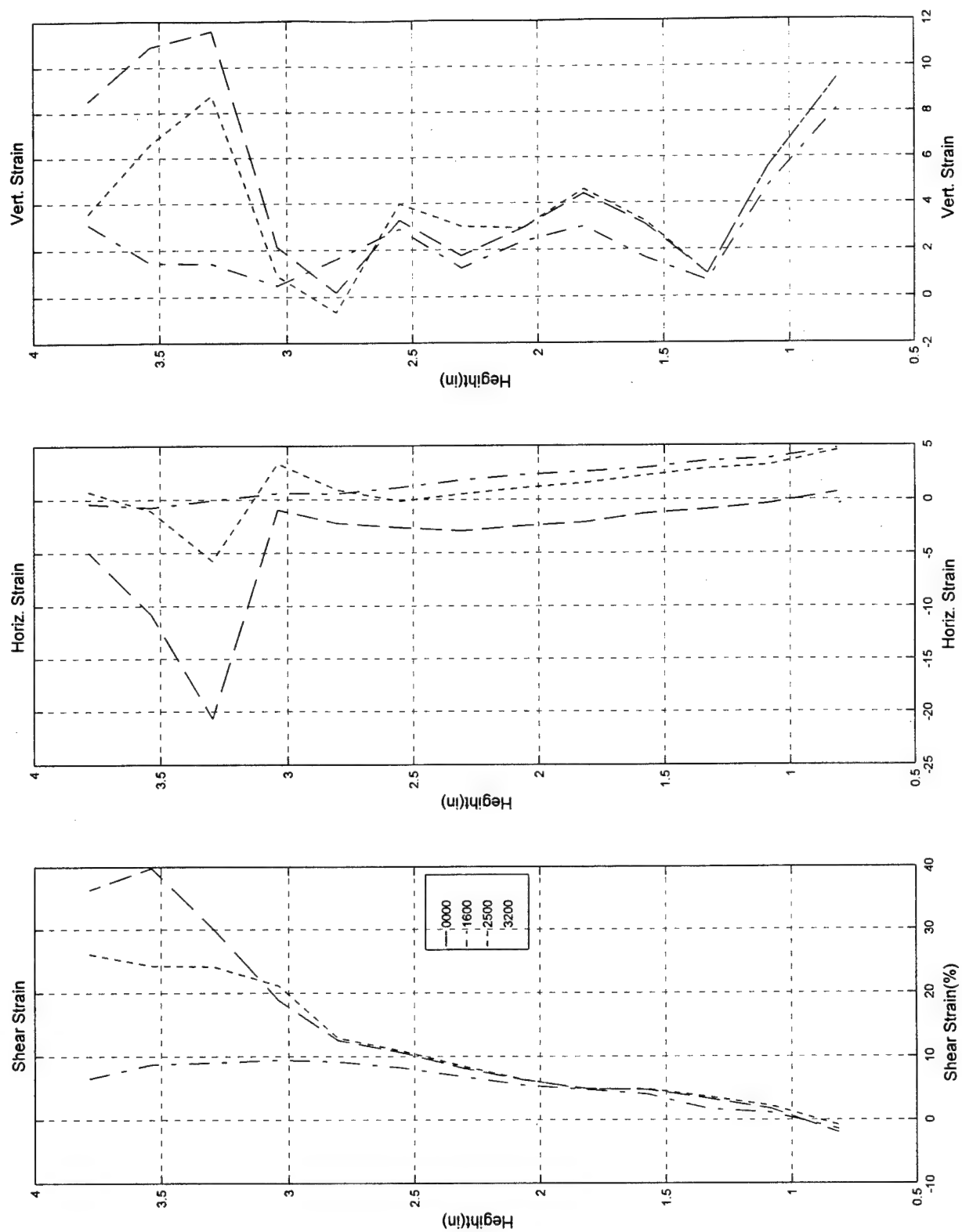
Test #77, Camera #C, Figure 4

Test #77, 3/18/97; Torsion-compression; ECP=50 psi; Loire, Video c
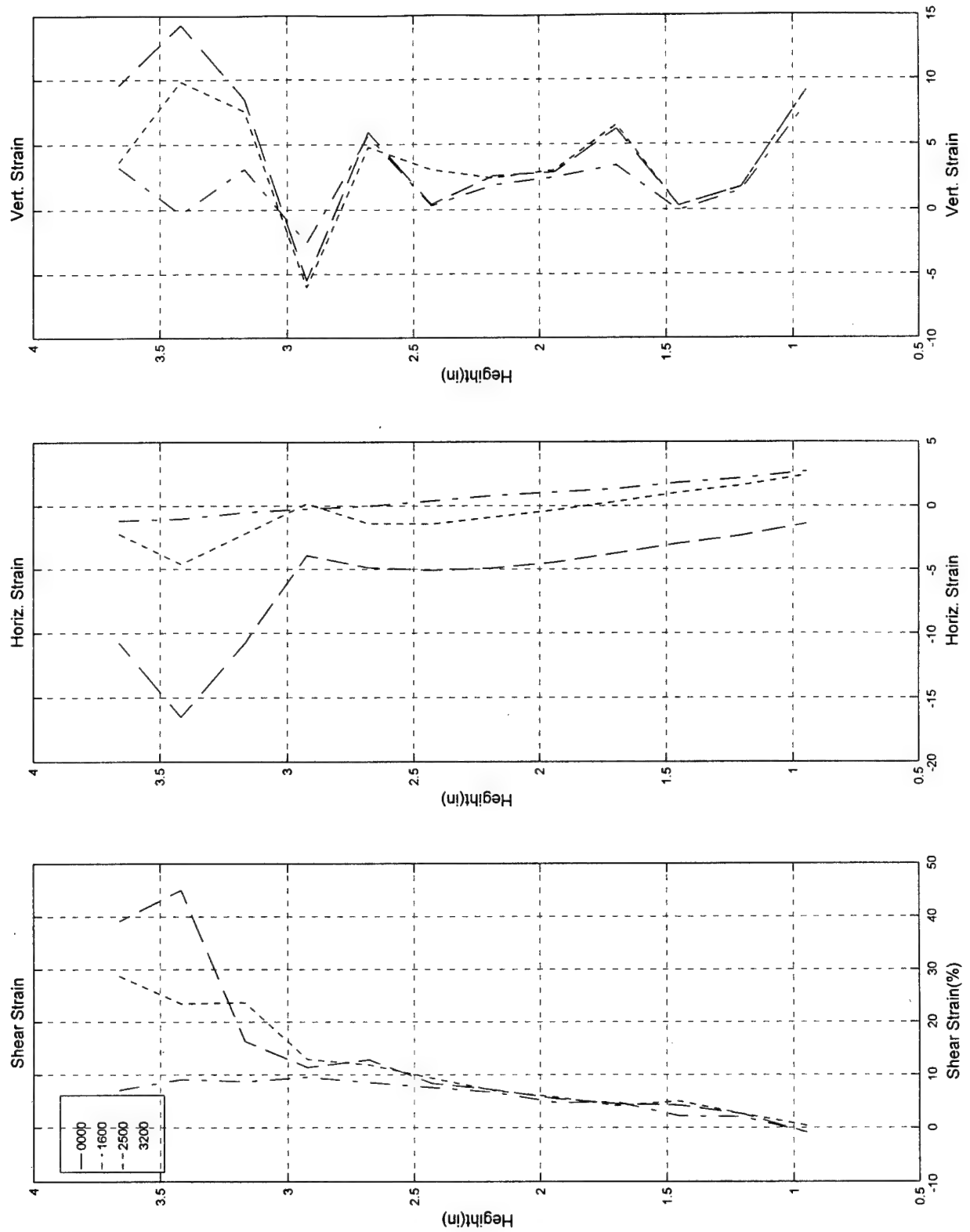
Test #77, Camera #C, Figure 5
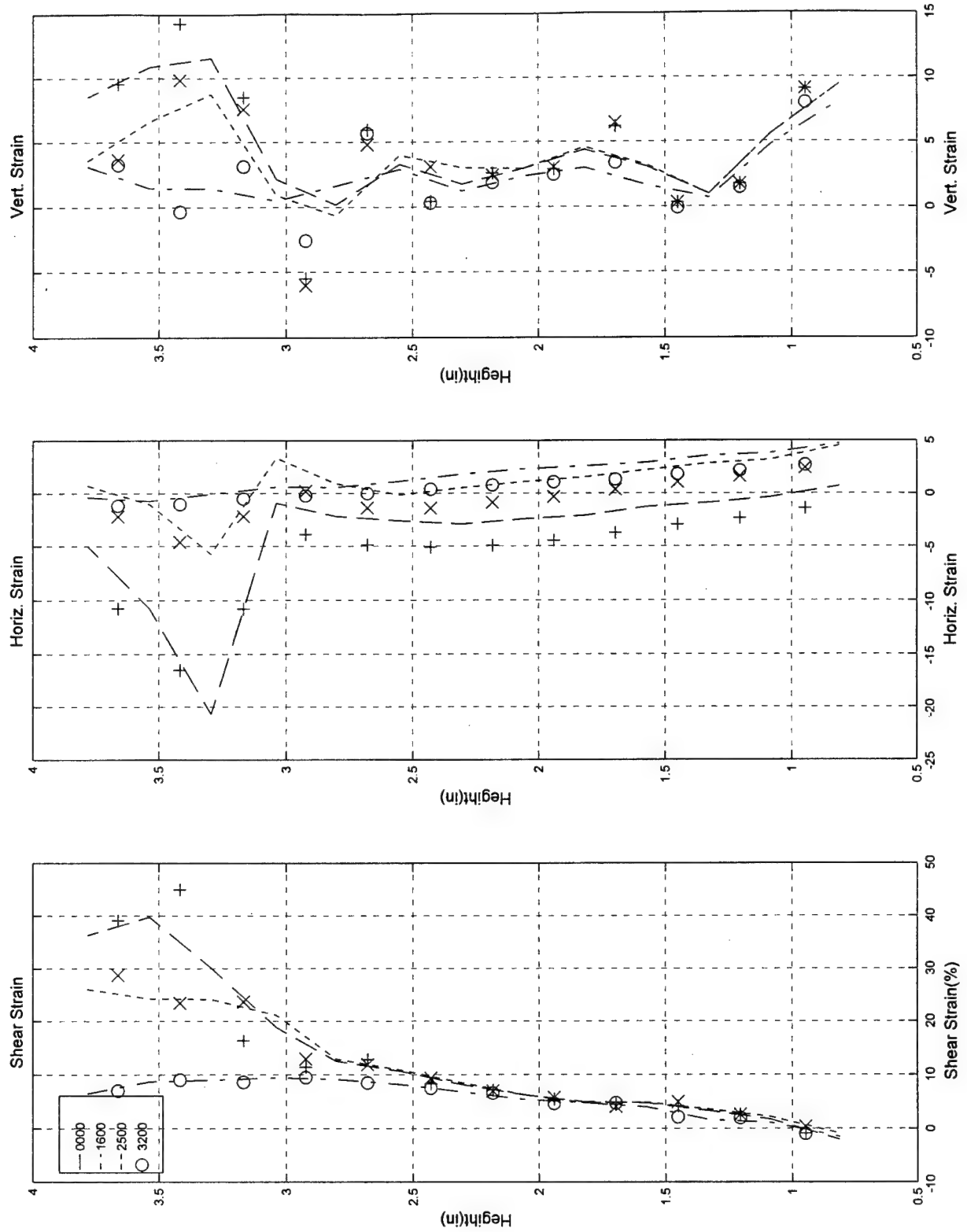
Test #77, Camera #C, Figure 6

Test #77; 3/18/97; Torsion-compression; ECP=50 psi; Loire, Video c
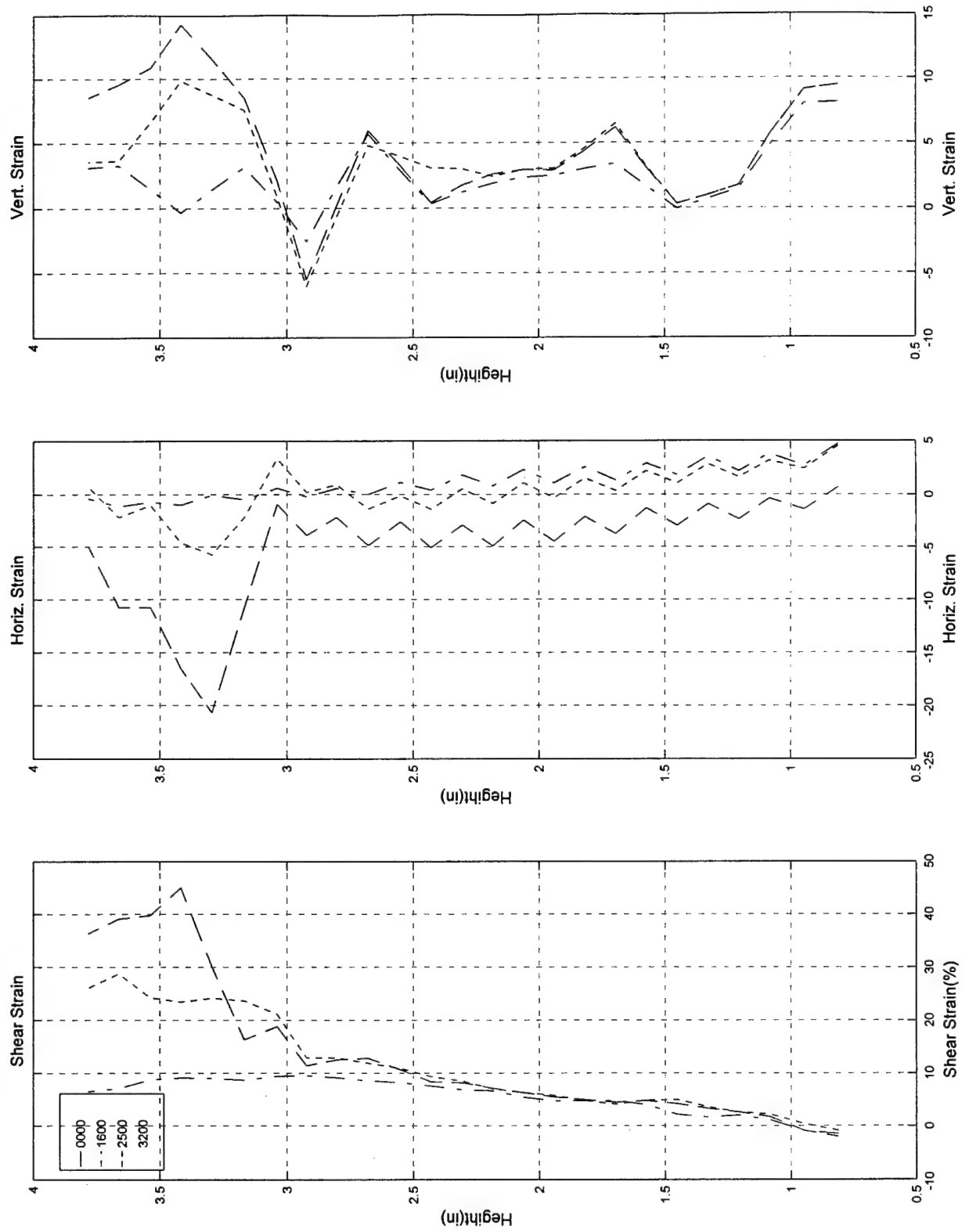
Test #77, Camera #C, Figure 7

Test #77, Camera #D, Figure 1

128

Test #77, Camera #D, Figure 2
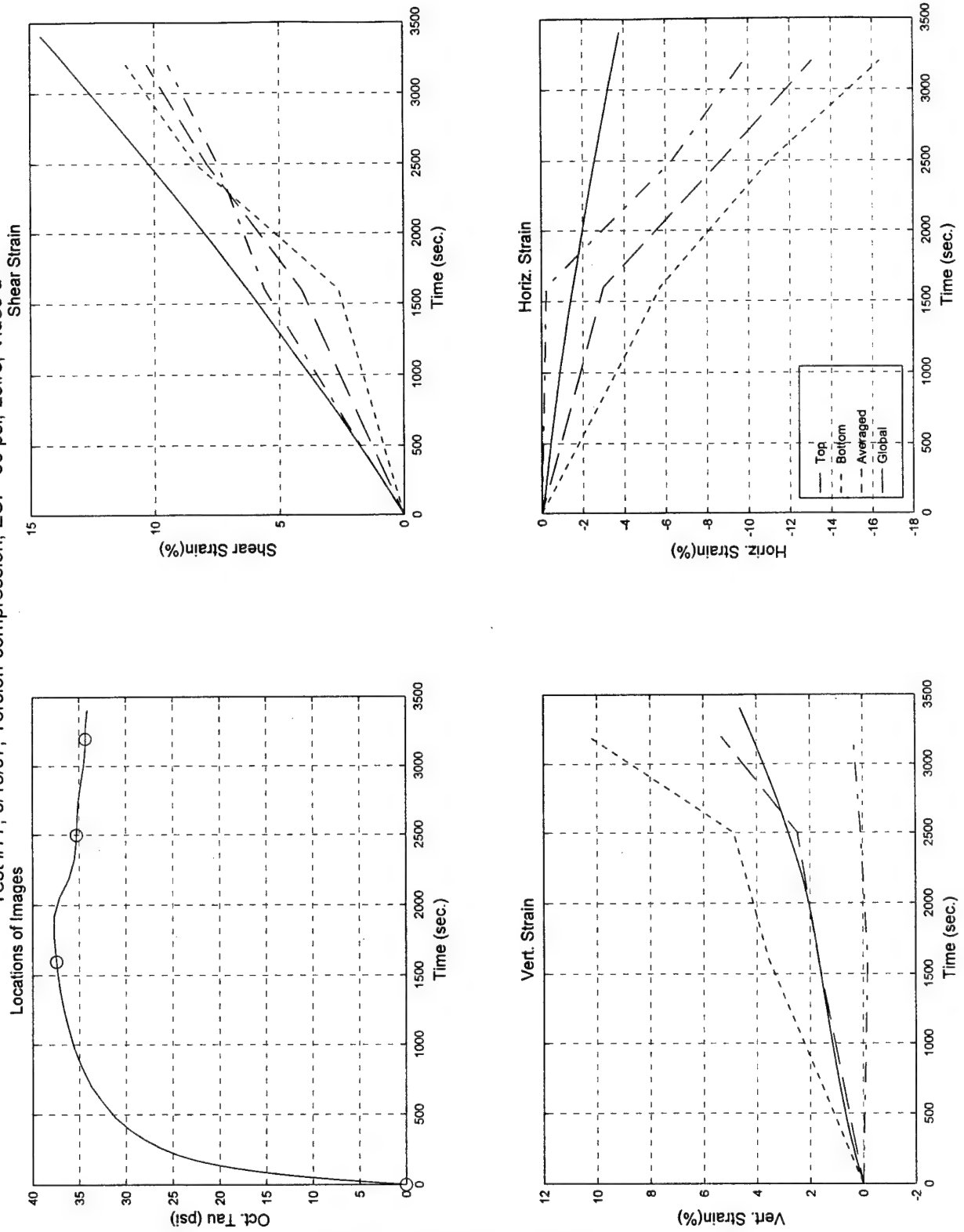
Test #77; 3/18/97; Torsion-compression; ECP=50 psi; Loire, Video d
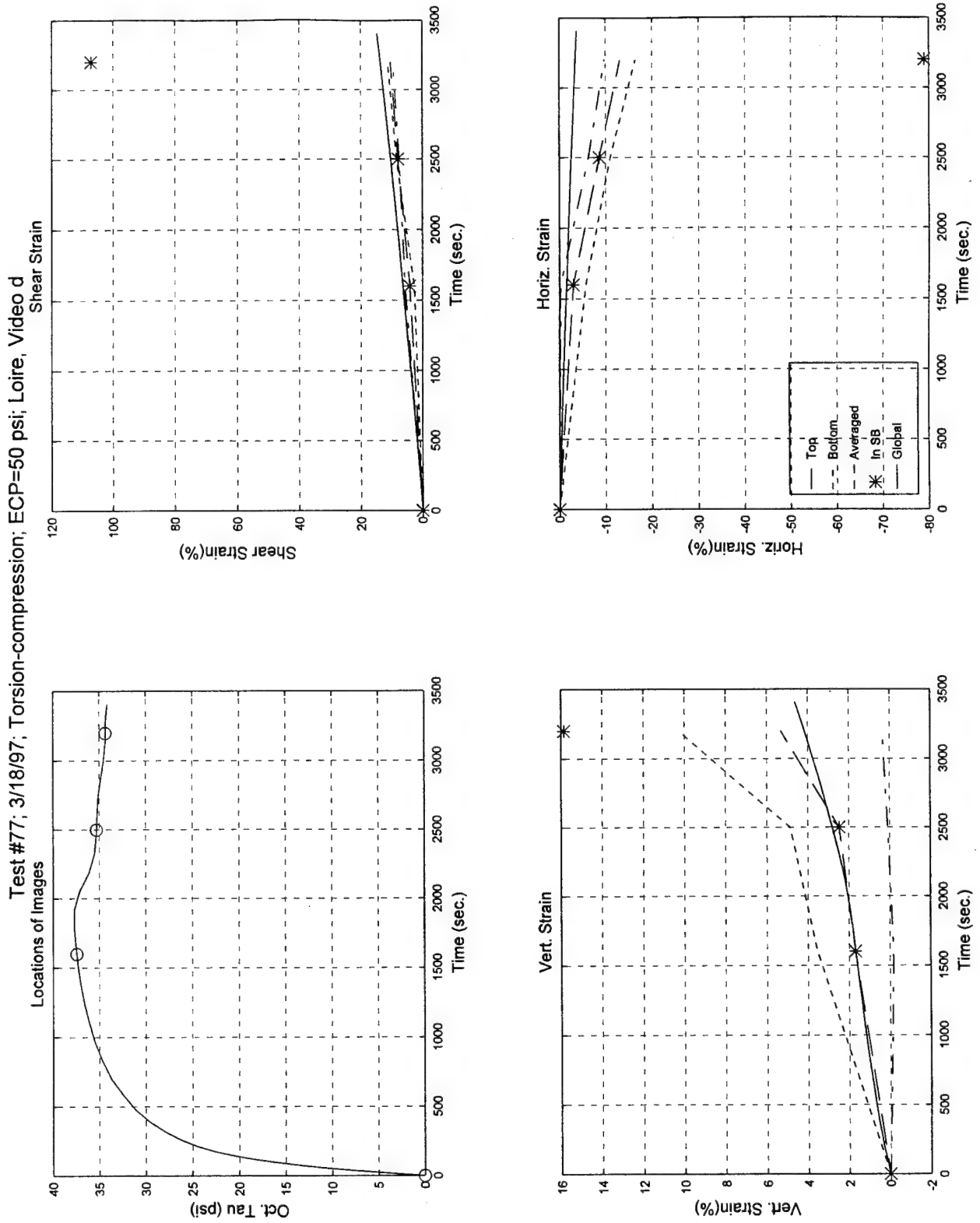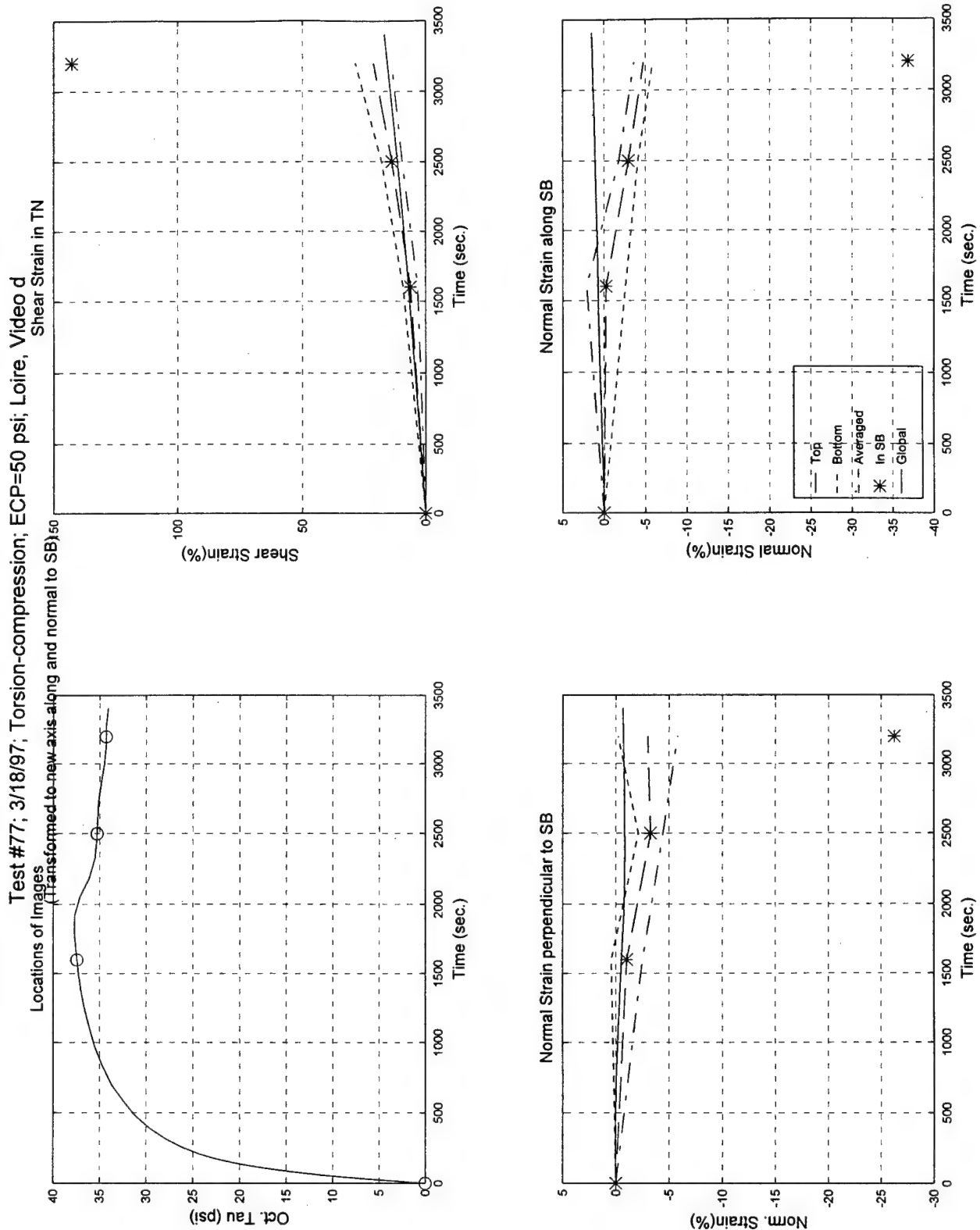
Test #77, Camera #D, Figure 3

Test #77; 3/18/97; Torsion-compression; ECP=50 psi; Loire, Video d
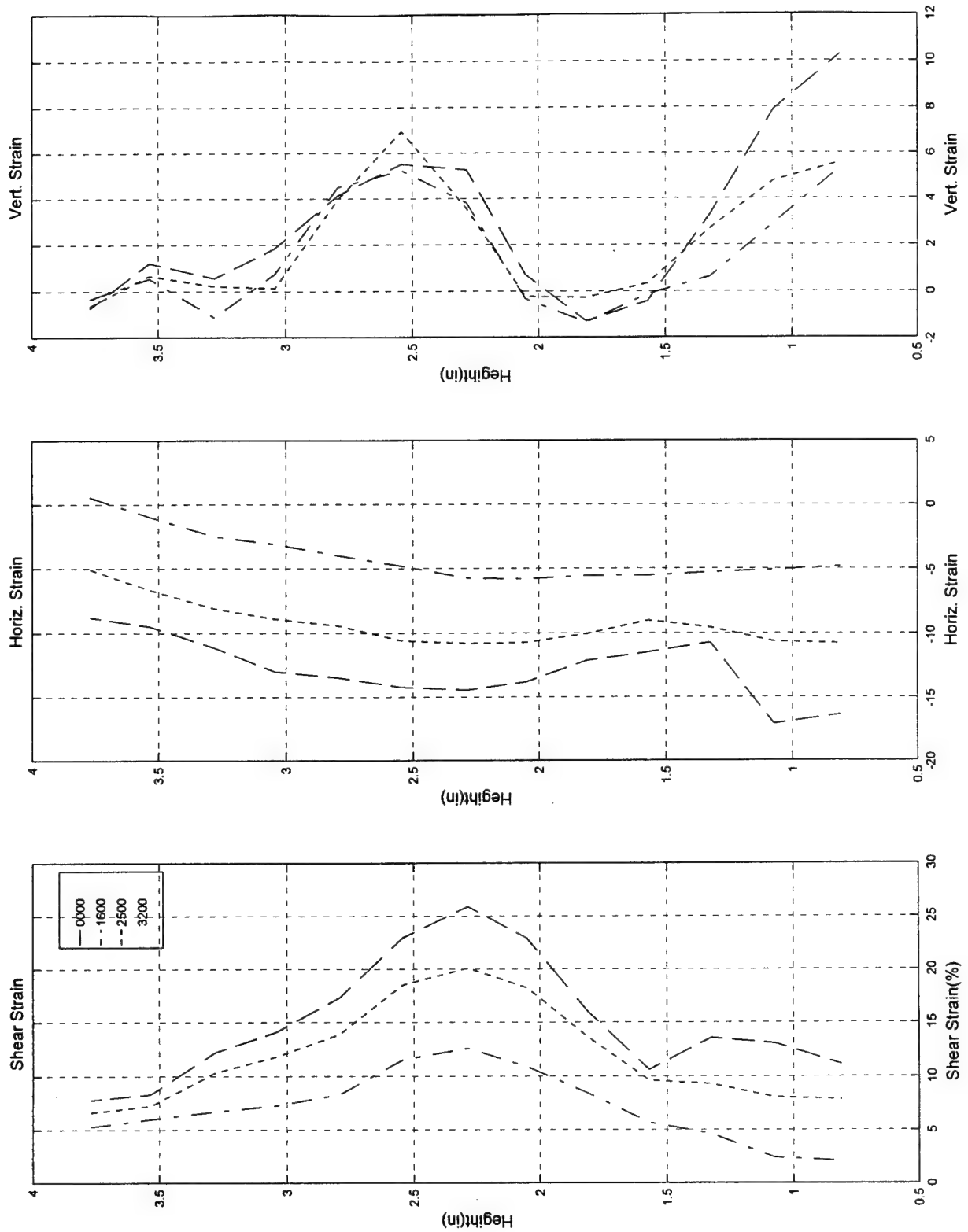
Test #77, Camera #D, Figure 4

Test #77; 3/18/97; Torsion-compression; ECP=50 psi; Loire, Video d
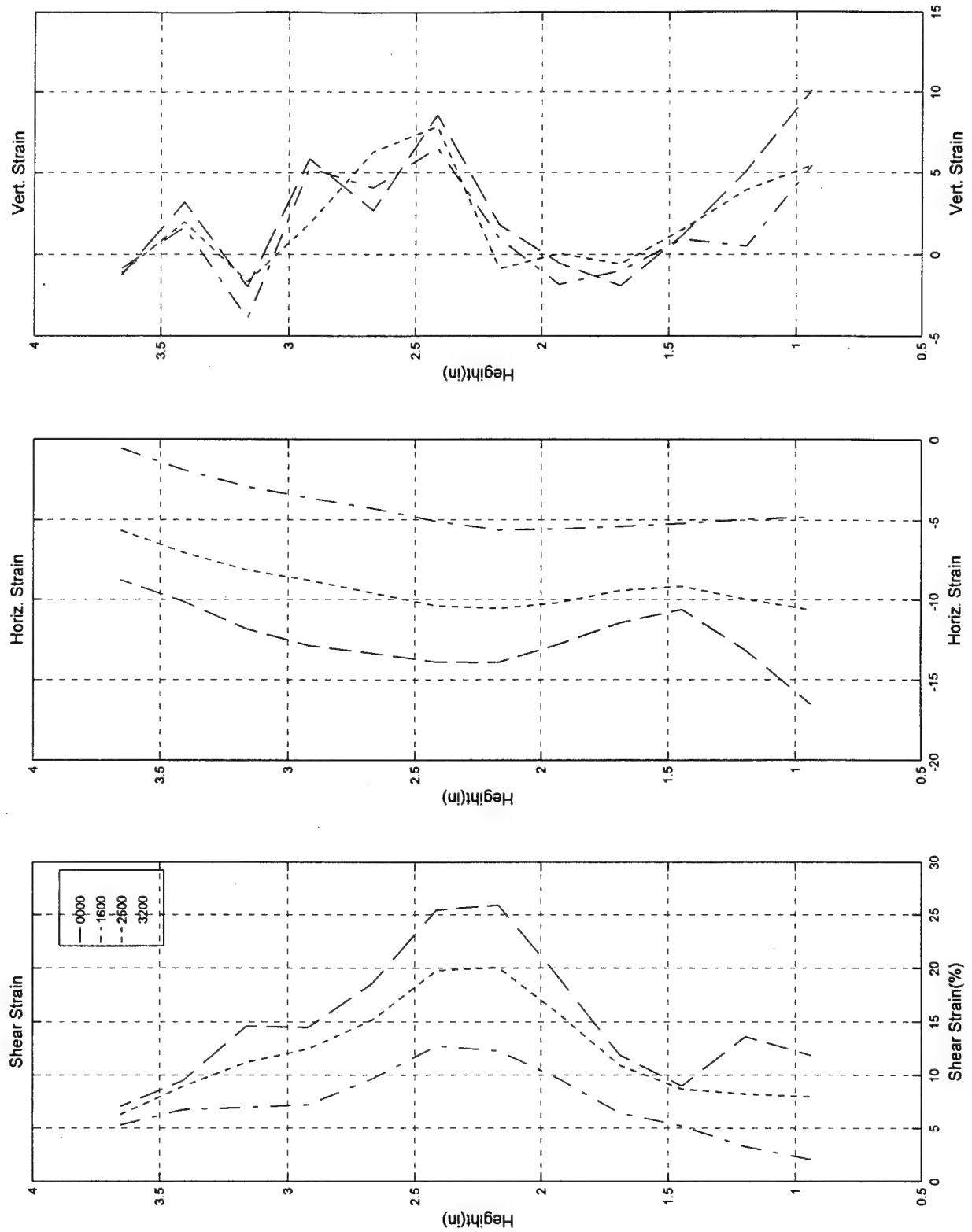
Test #77, Camera #D, Figure 5

Test #77; 3/18/97; Torsion-compression; ECP=50 psi; Loire, Video d
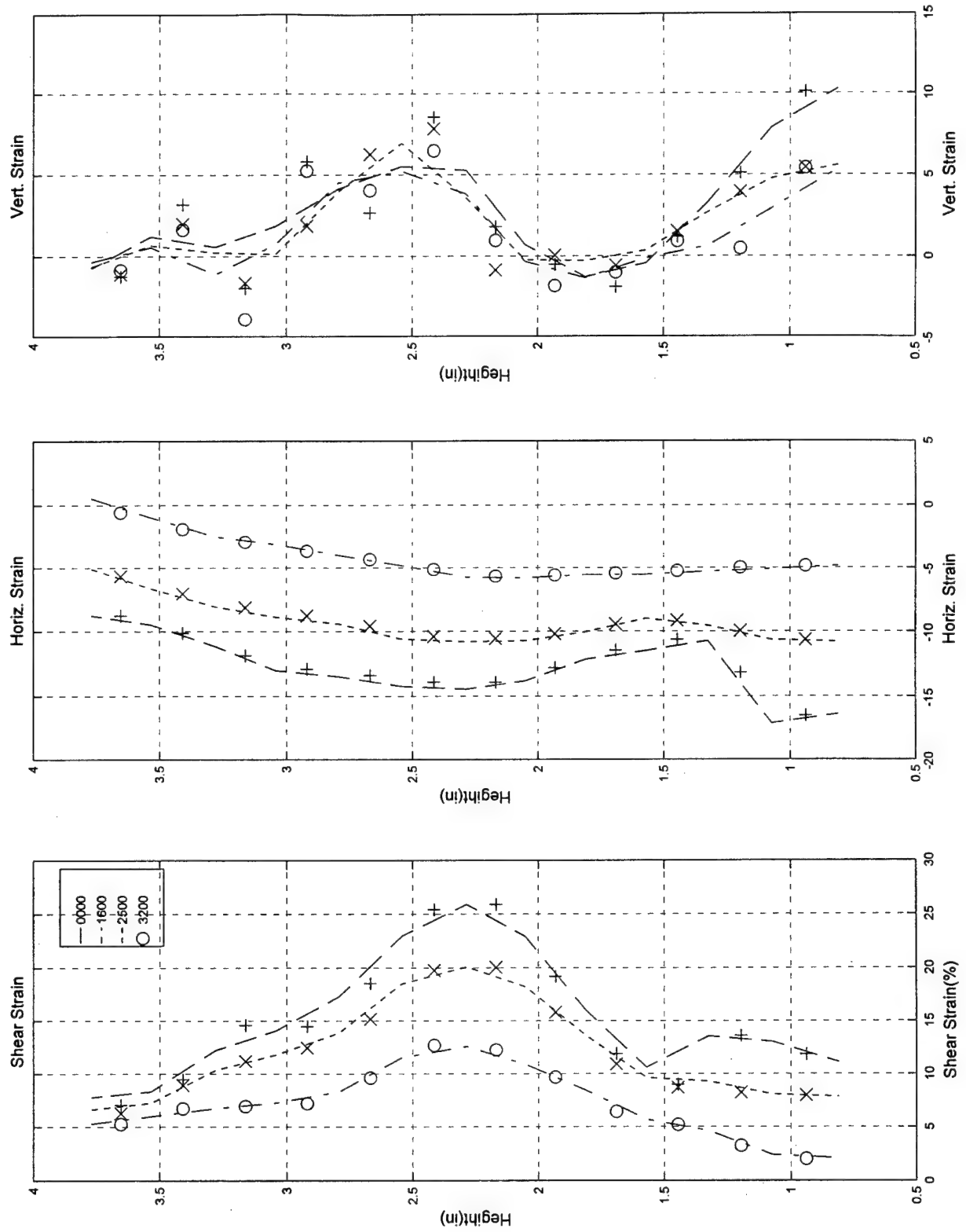
Test #77, Camera #D, Figure 6

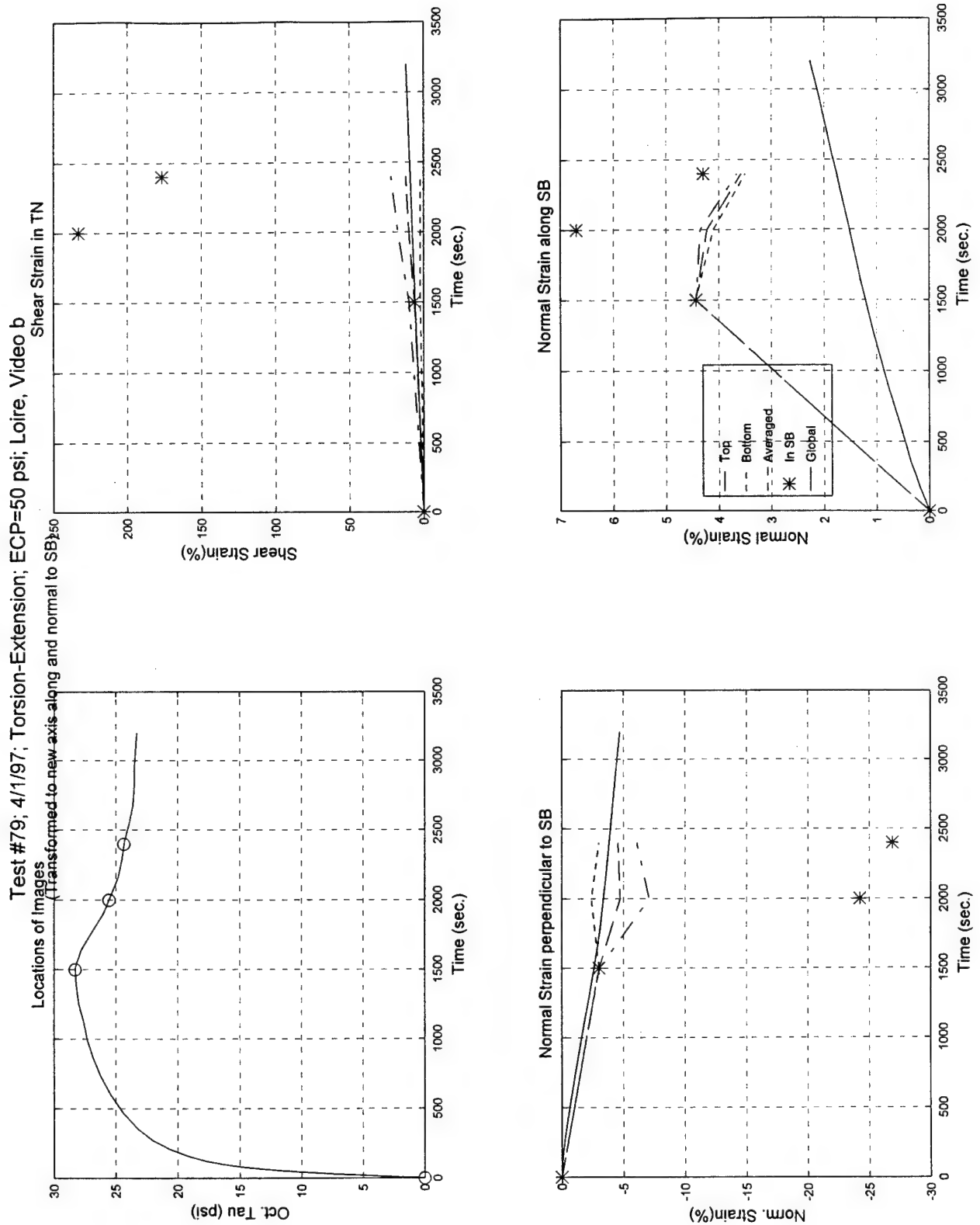Test #77; 3/18/97; Torsion-compression; ECP=50 psi; Loire, Video d
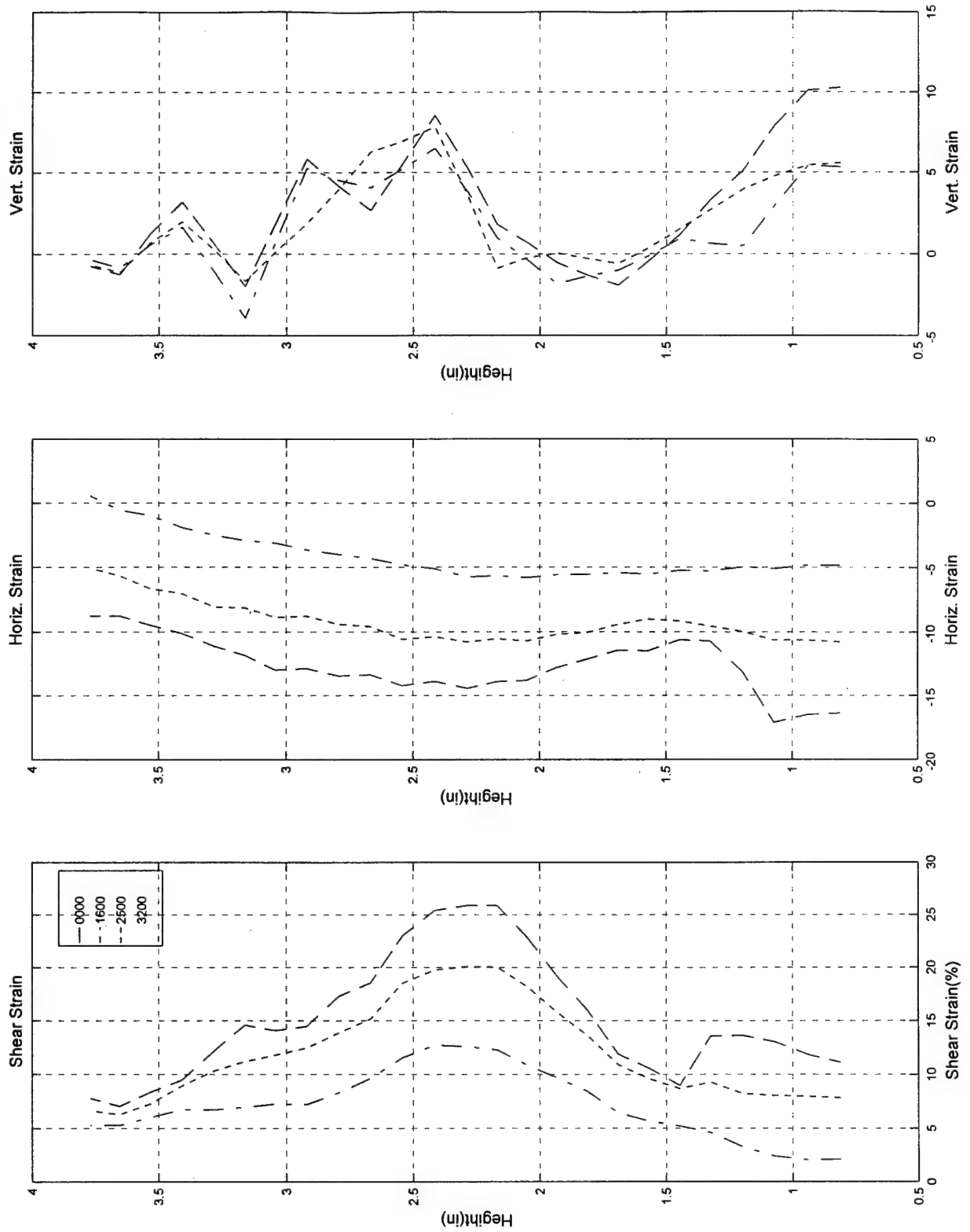
Test #77, Camera #D, Figure 7

B.3 Test #78a

- **Pure Torsion ($\beta = 45\,°$)**
- **Effective Confining Pressure = 50 psi (345 kPa)**
- **50% Initial Relative Density**
- **Generalized Test**
- **Digitized Times Intervals: 0000, 1500, 2500 & 3400 sec.**

Test #78a, Camera #A, Figure 1
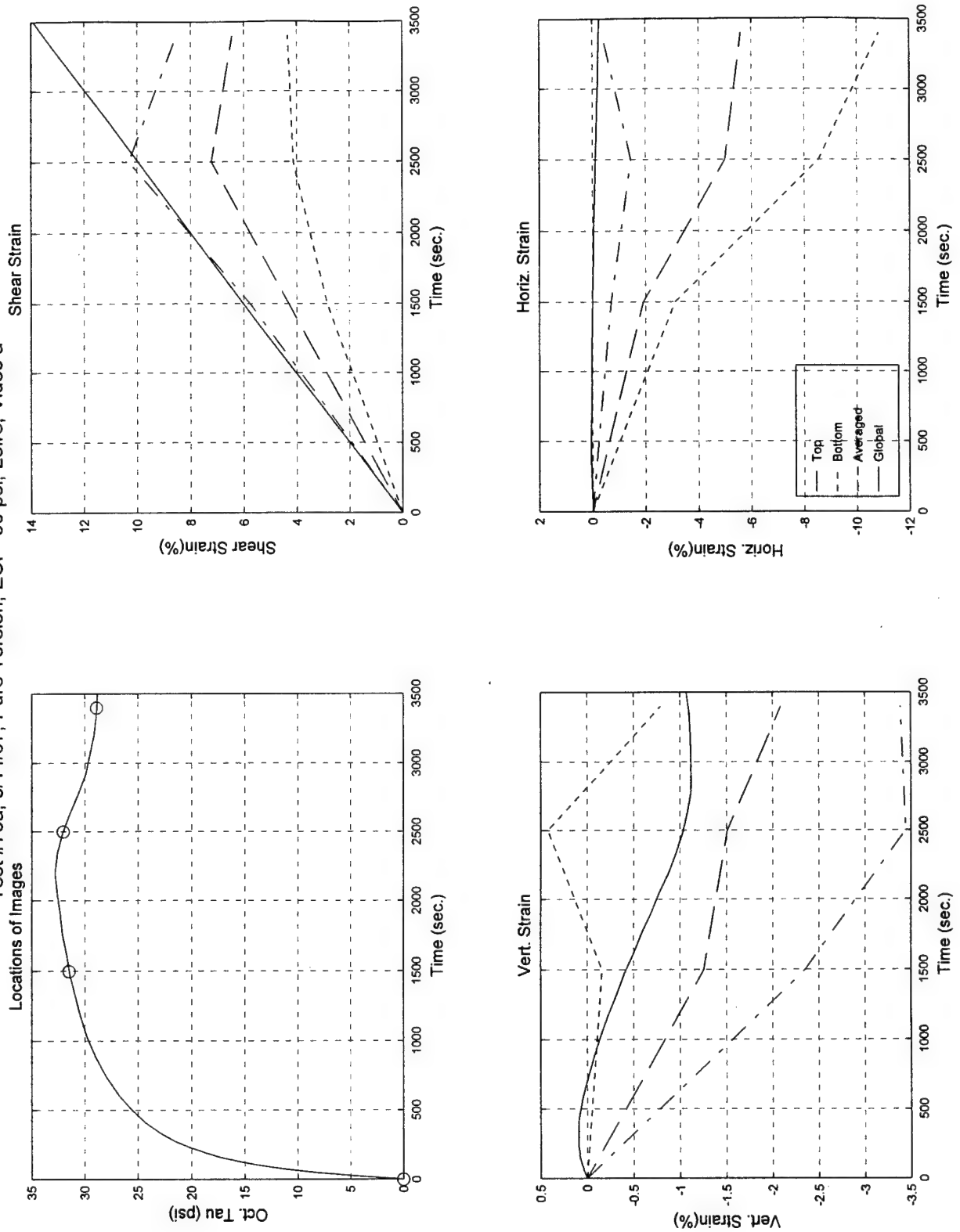
136
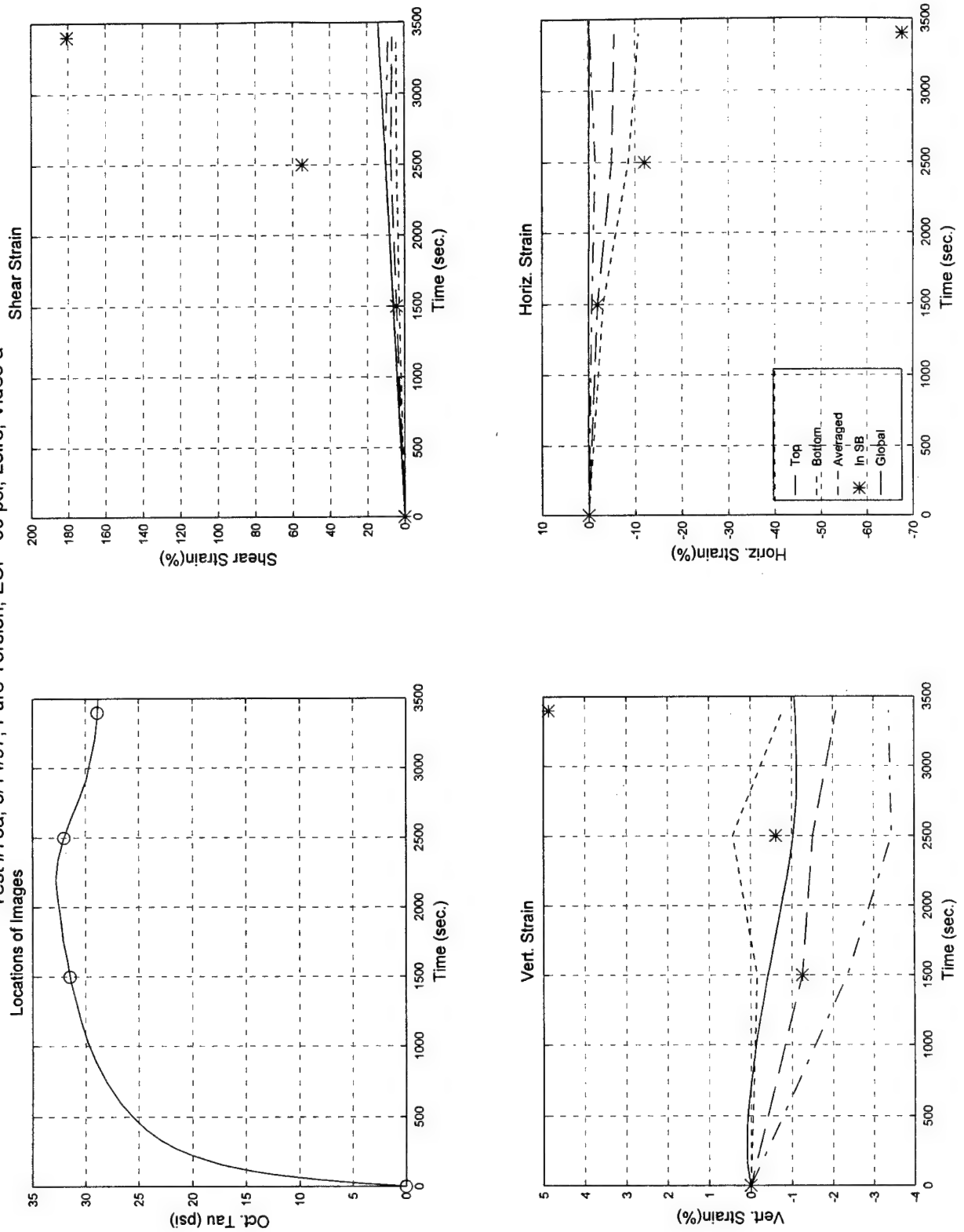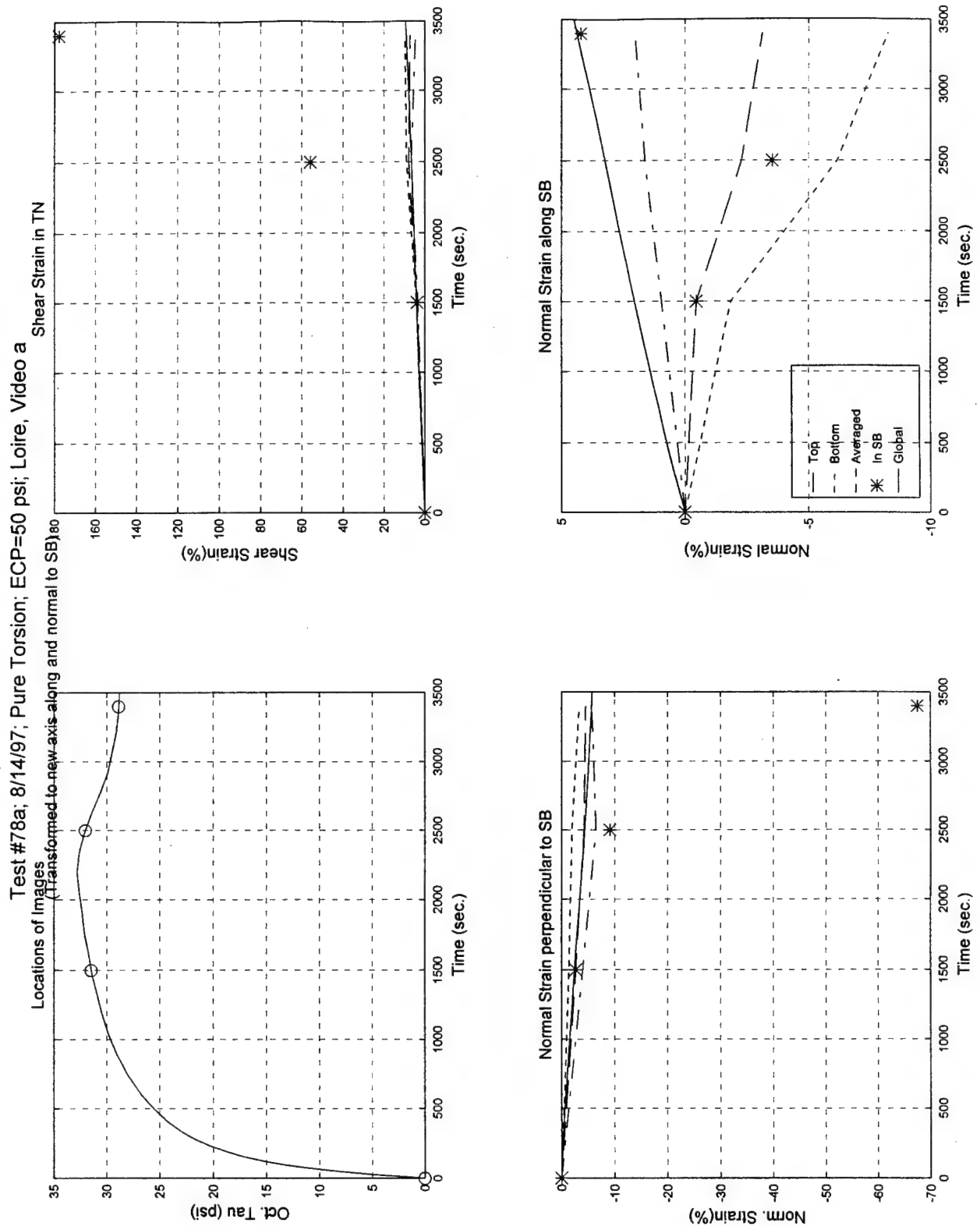
Test #78a, Camera #A, Figure 2

Test #78a, Camera #A, Figure 3

Test #78a, Camera #A, Figure 4
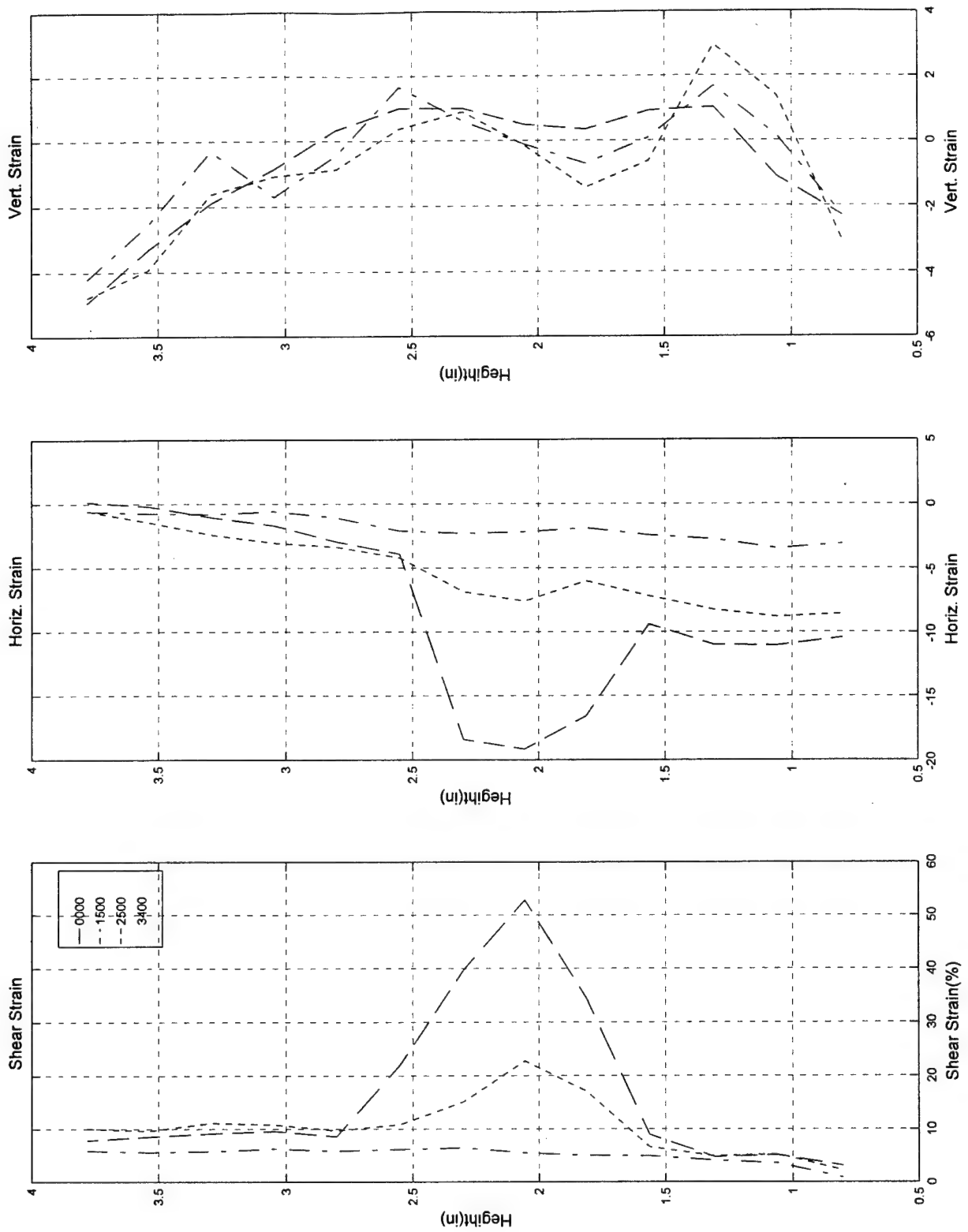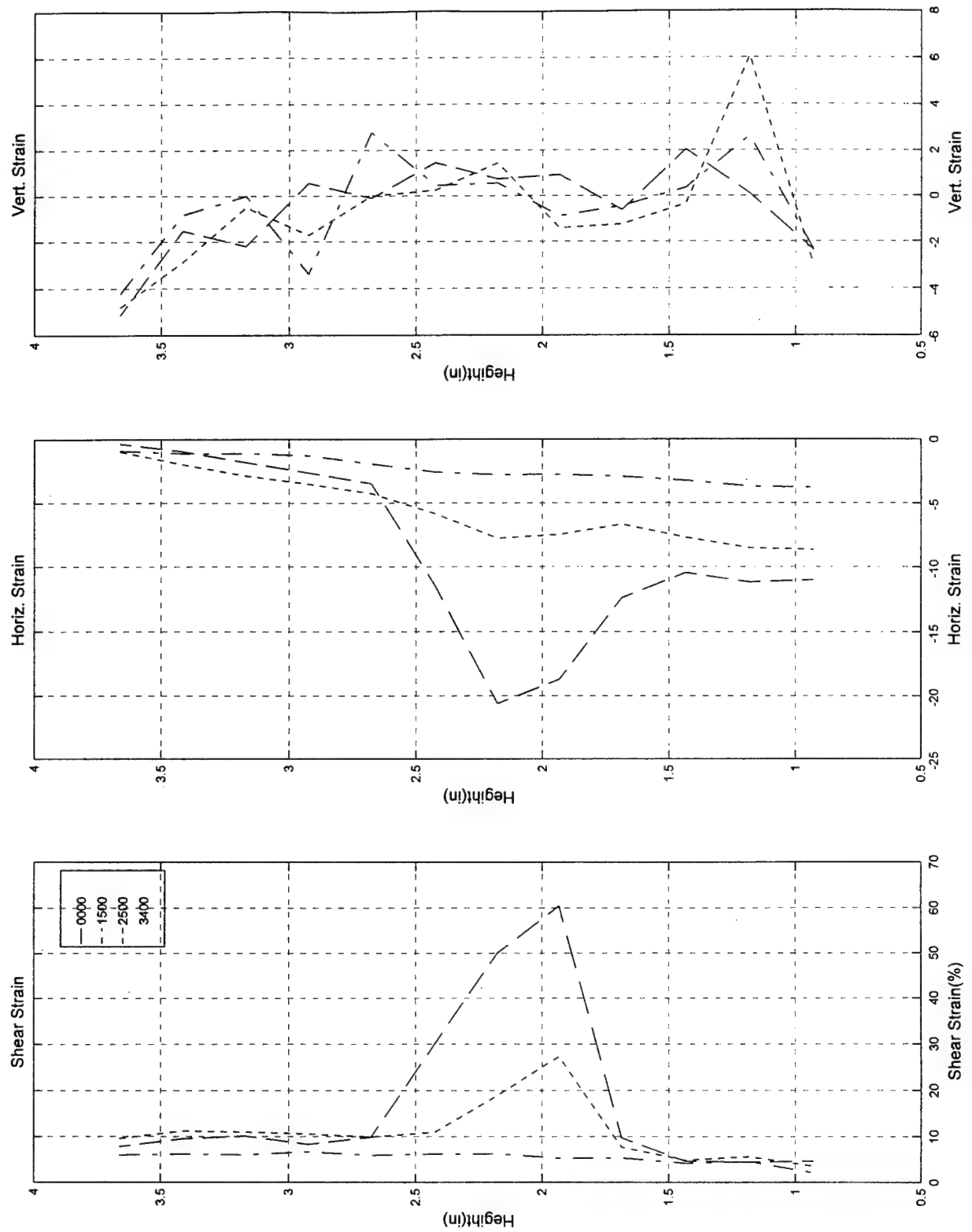
Test #78a, Camera #A, Figure 5

Test #78a; 8/14/97; Pure Torsion; ECP=50 psi; Loire, Video a
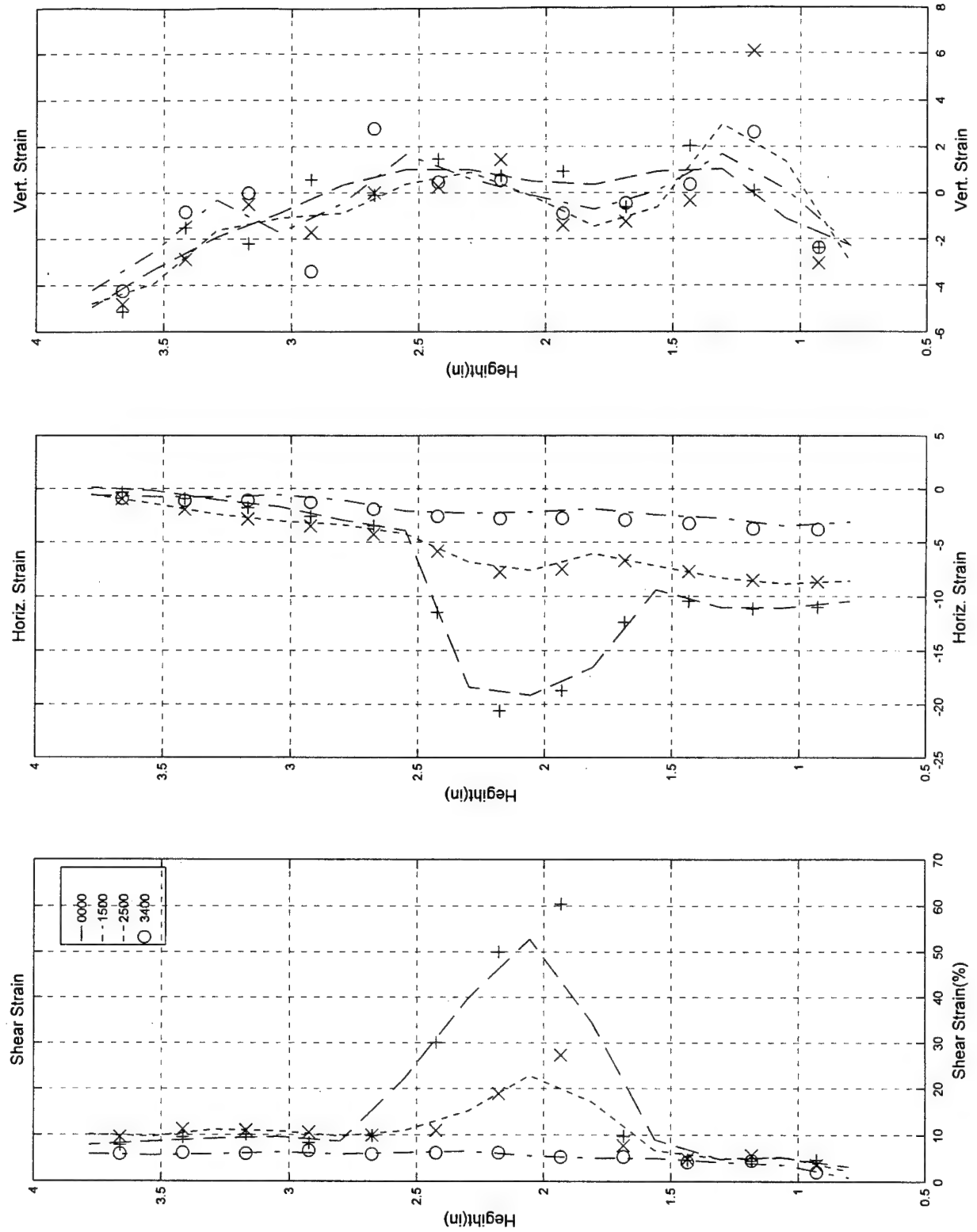
Test #78a, Camera #A, Figure 6

Test #78a; 8/14/97; Pure Torsion; ECP=50 psi; Loire, Video a
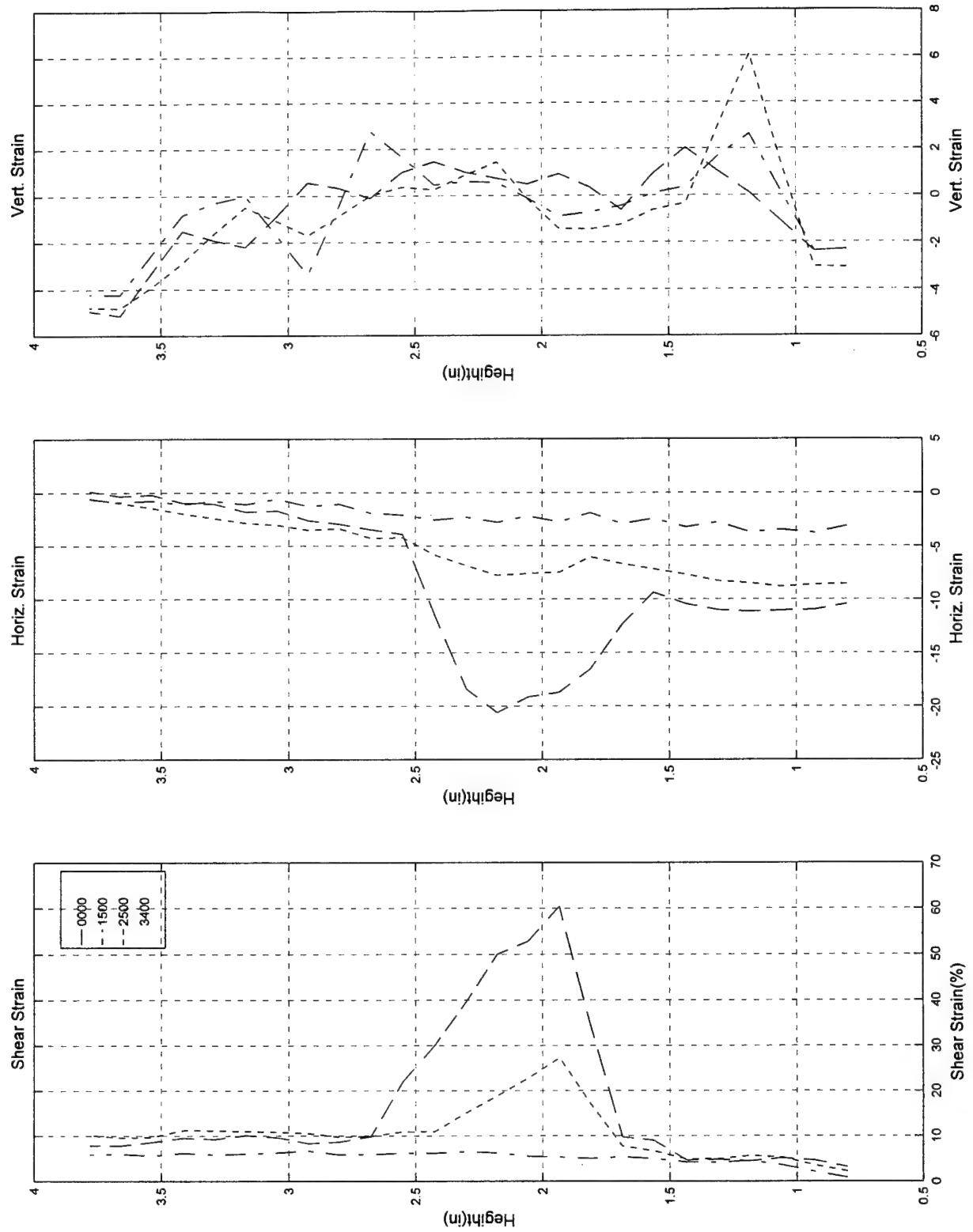
Test #78a, Camera #A, Figure 7

142

Test #78a; 8/14/97; Pure Torsion; ECP=50 psi; Loire, Video b

Test #78a, Camera #B, Figure 1

Test #78a; 8/14/97; Pure Torsion; ECP=50 psi; Loire, Video b
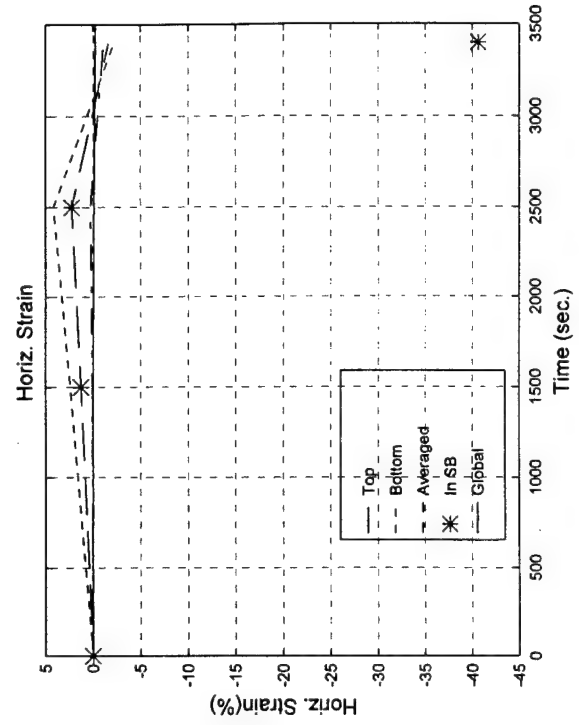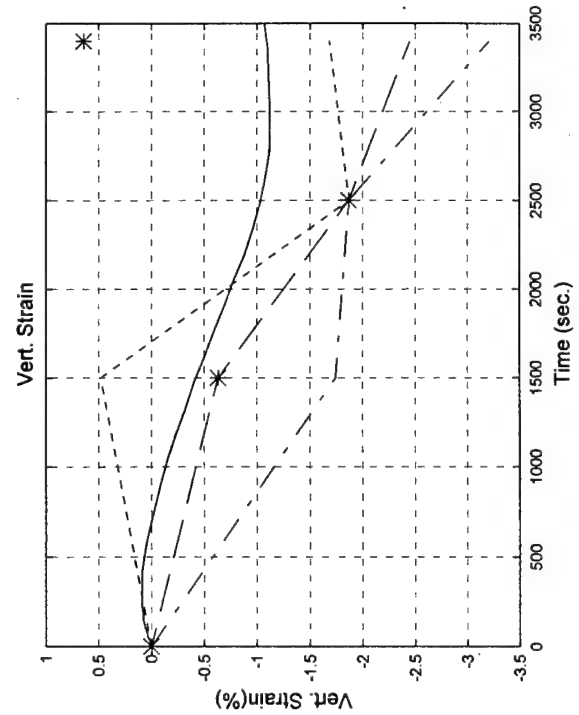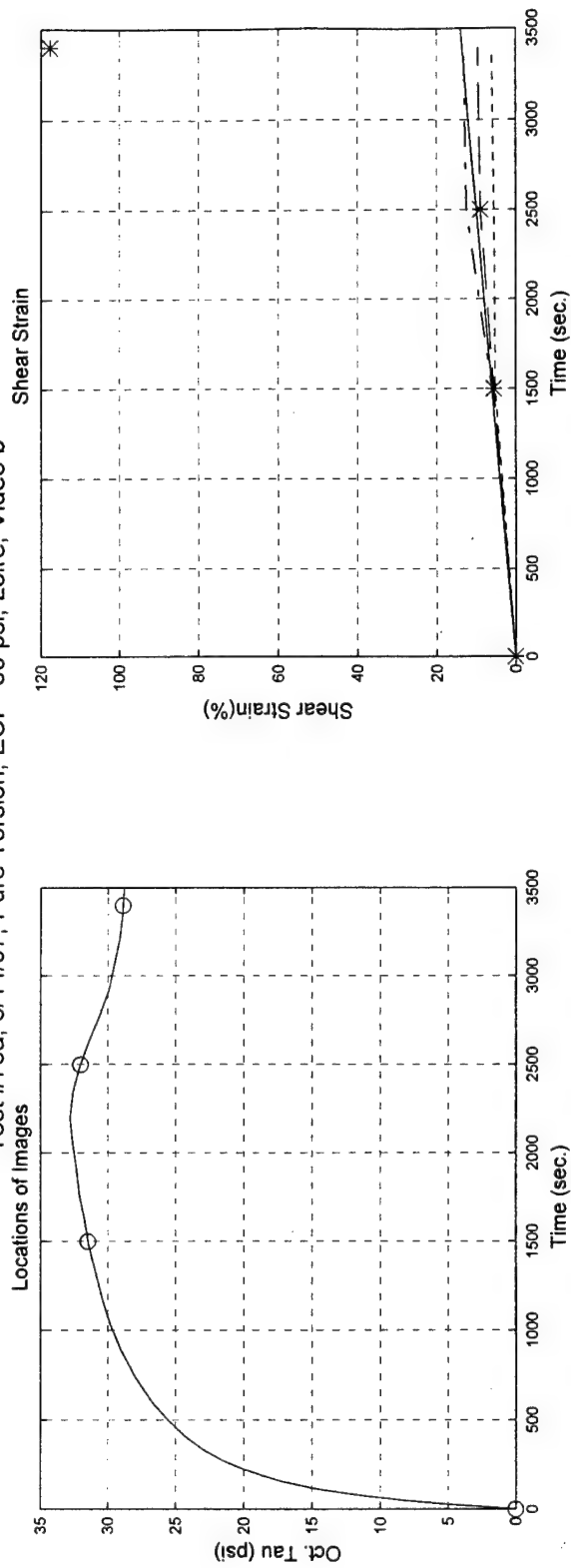
Test #78a, Camera #B, Figure 2

144
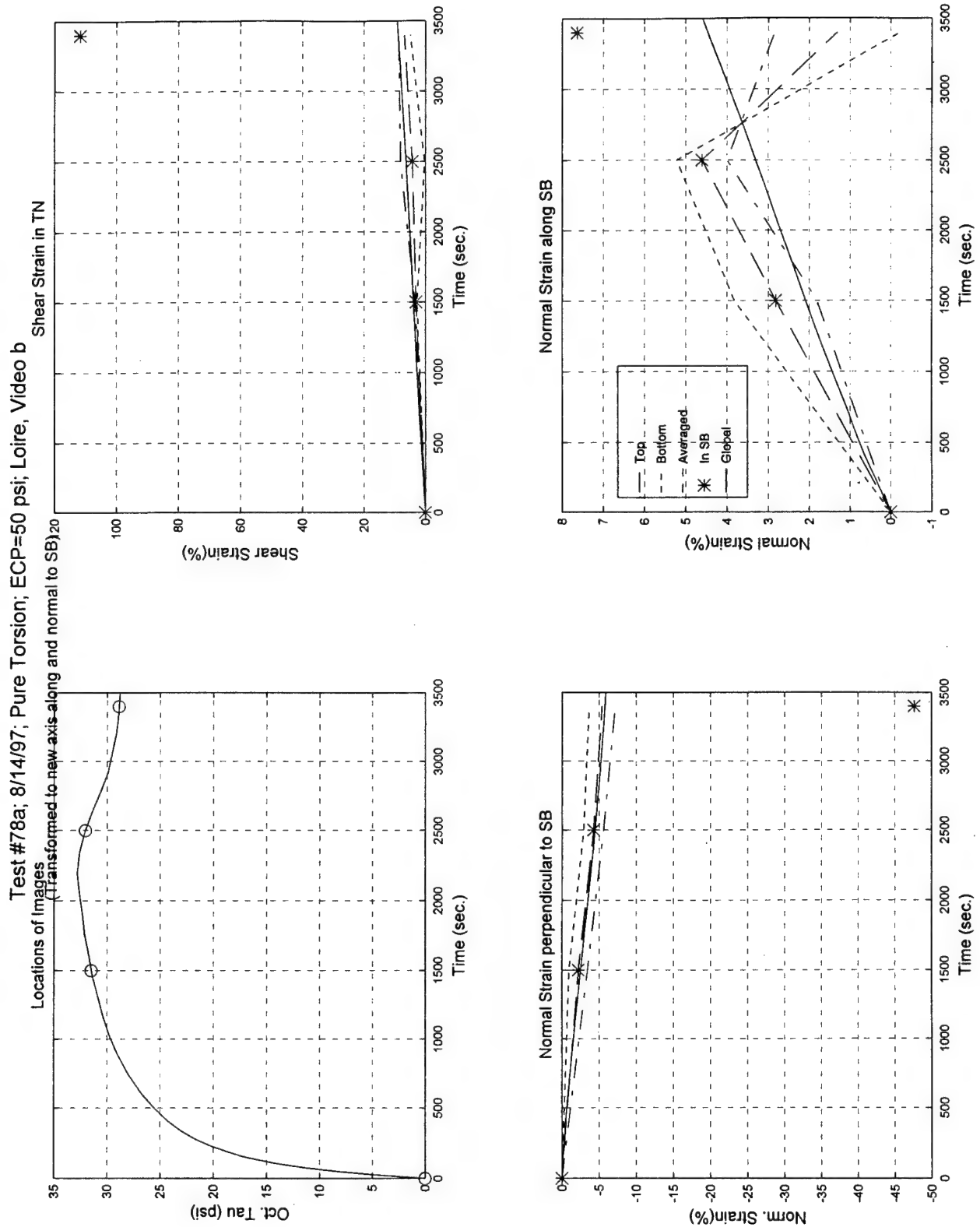
Test #78a, Camera #B, Figure 3

Test #78a; 8/14/97; Pure Torsion; ECP=50 psi; Loire, Video b
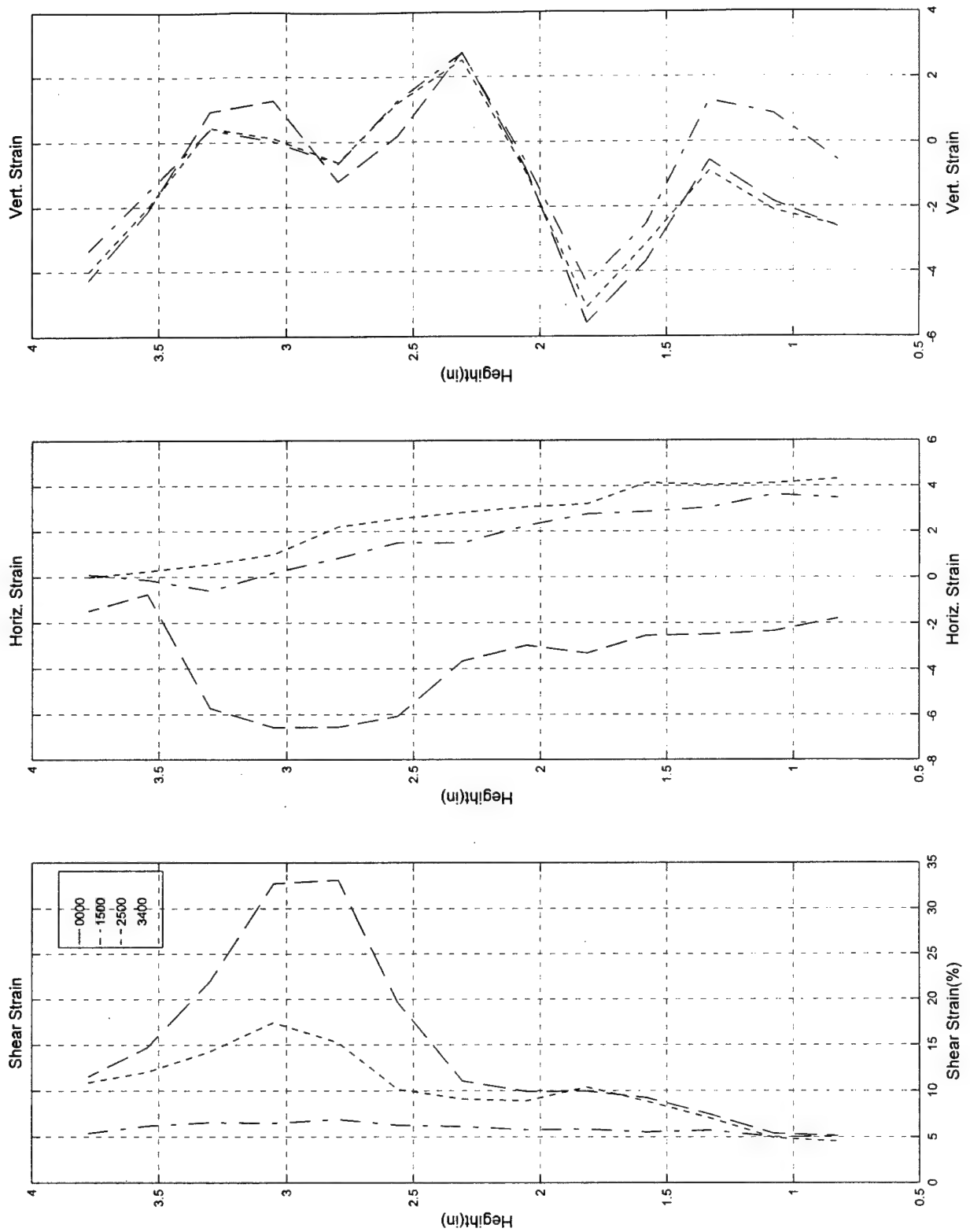
Test #78a, Camera #B, Figure 4

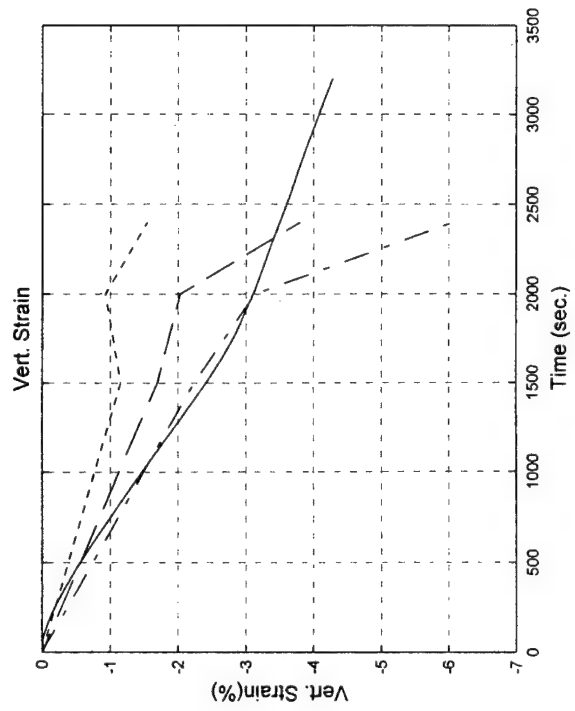Test #78a; 8/14/97; Pure Torsion; ECP=50 psi; Loire, Video b
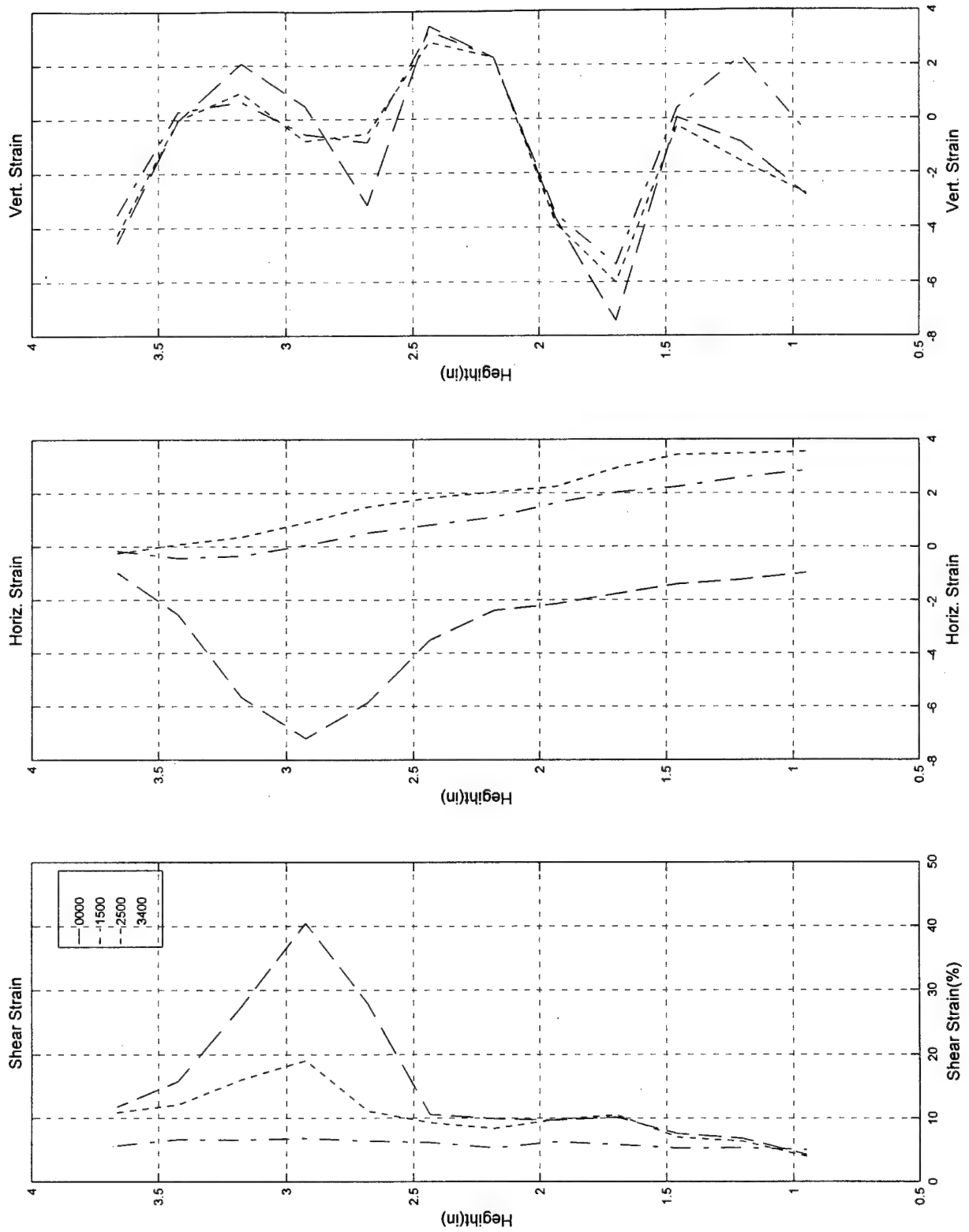
Test #78a, Camera #B, Figure 5
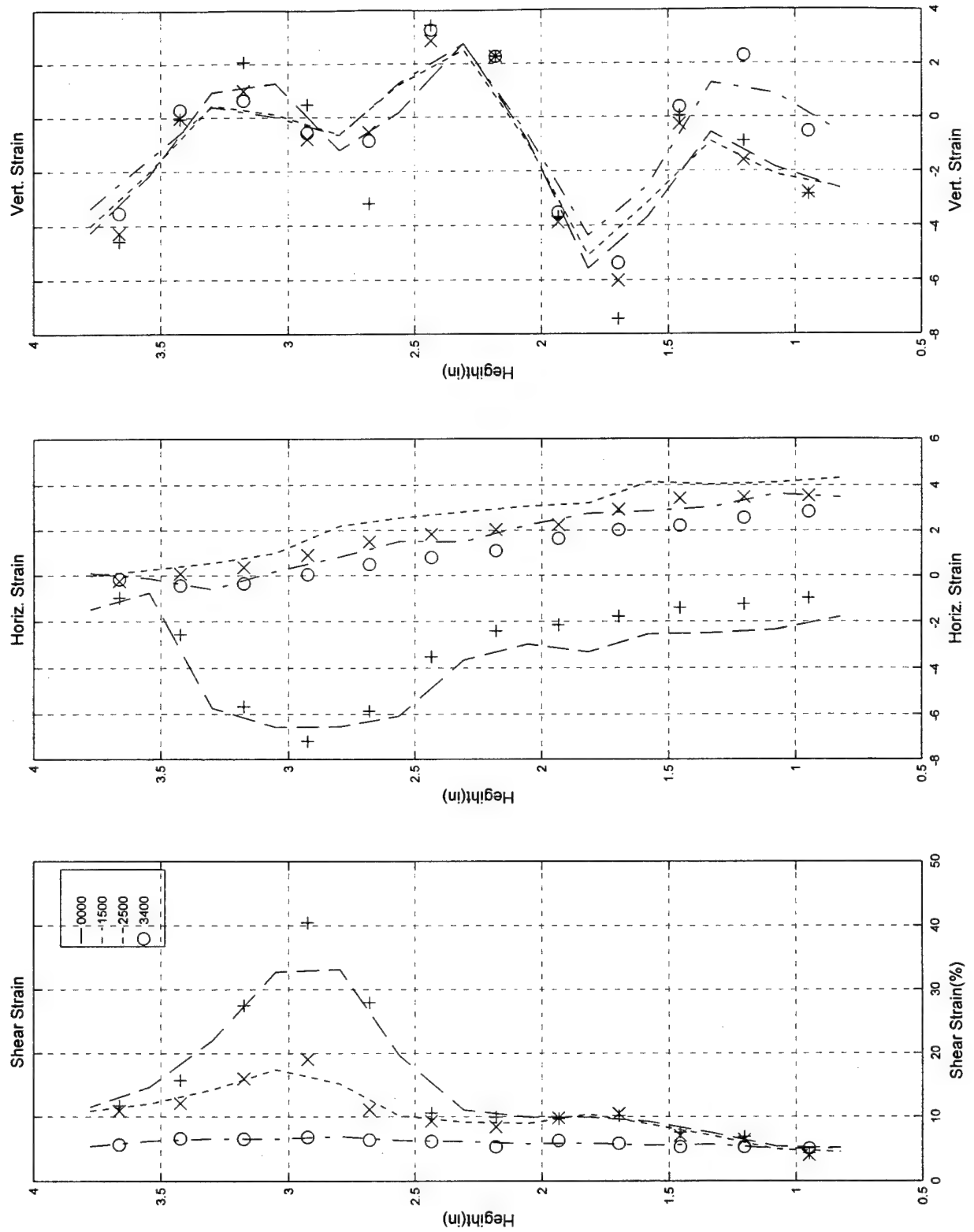
Test #78a, Camera #B, Figure 6

Test #78a; 8/14/97; Pure Torsion; ECP=50 psi; Loire, Video b
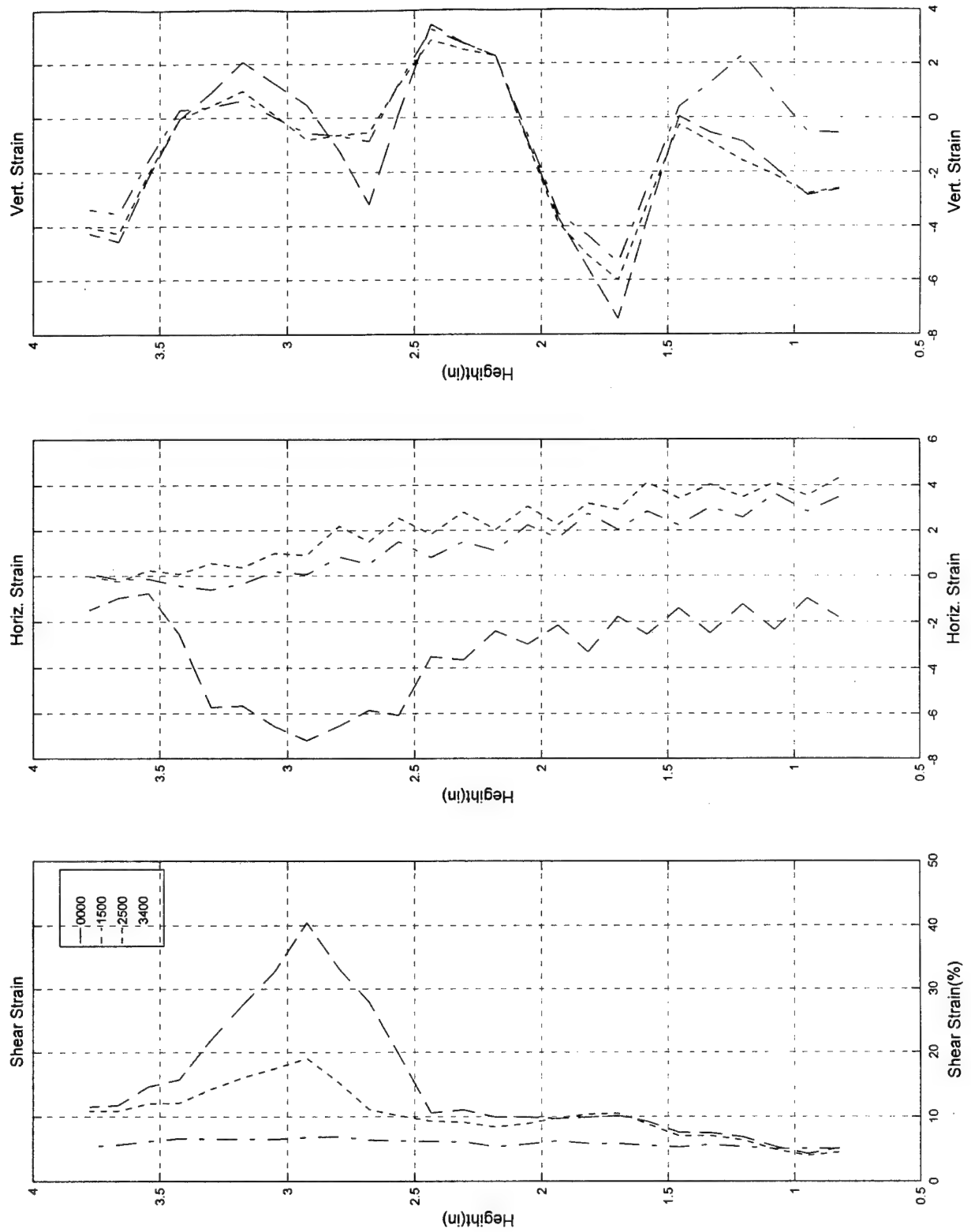
Test #78a, Camera #B, Figure 7

Test #78a; 8/14/97; Pure Torsion; ECP=50 psi; Loire, Video c
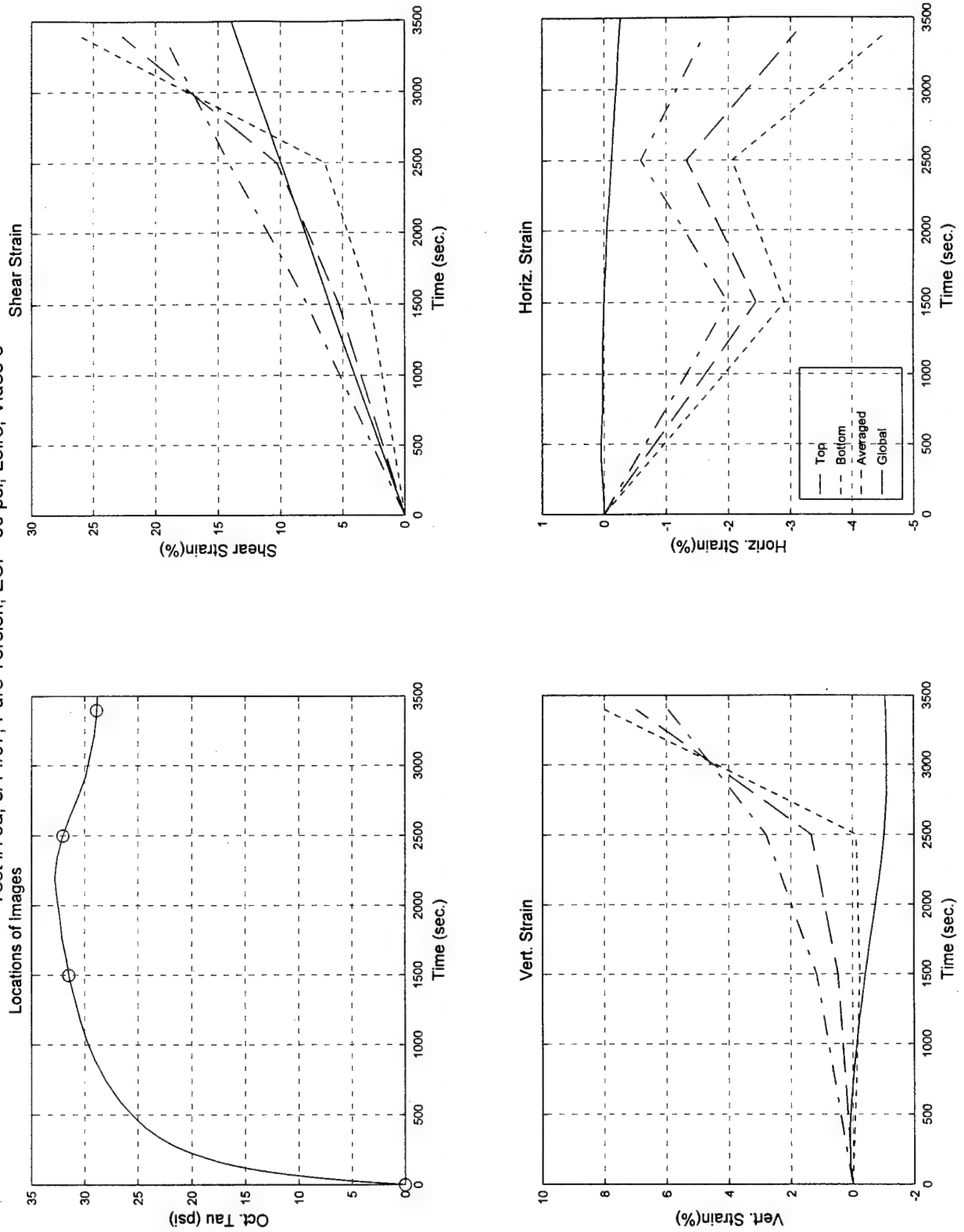
Test #78a, Camera #C, Figure 1

Test #78a; 8/14/97; Pure Torsion; ECP=50 psi; Loire, Video c
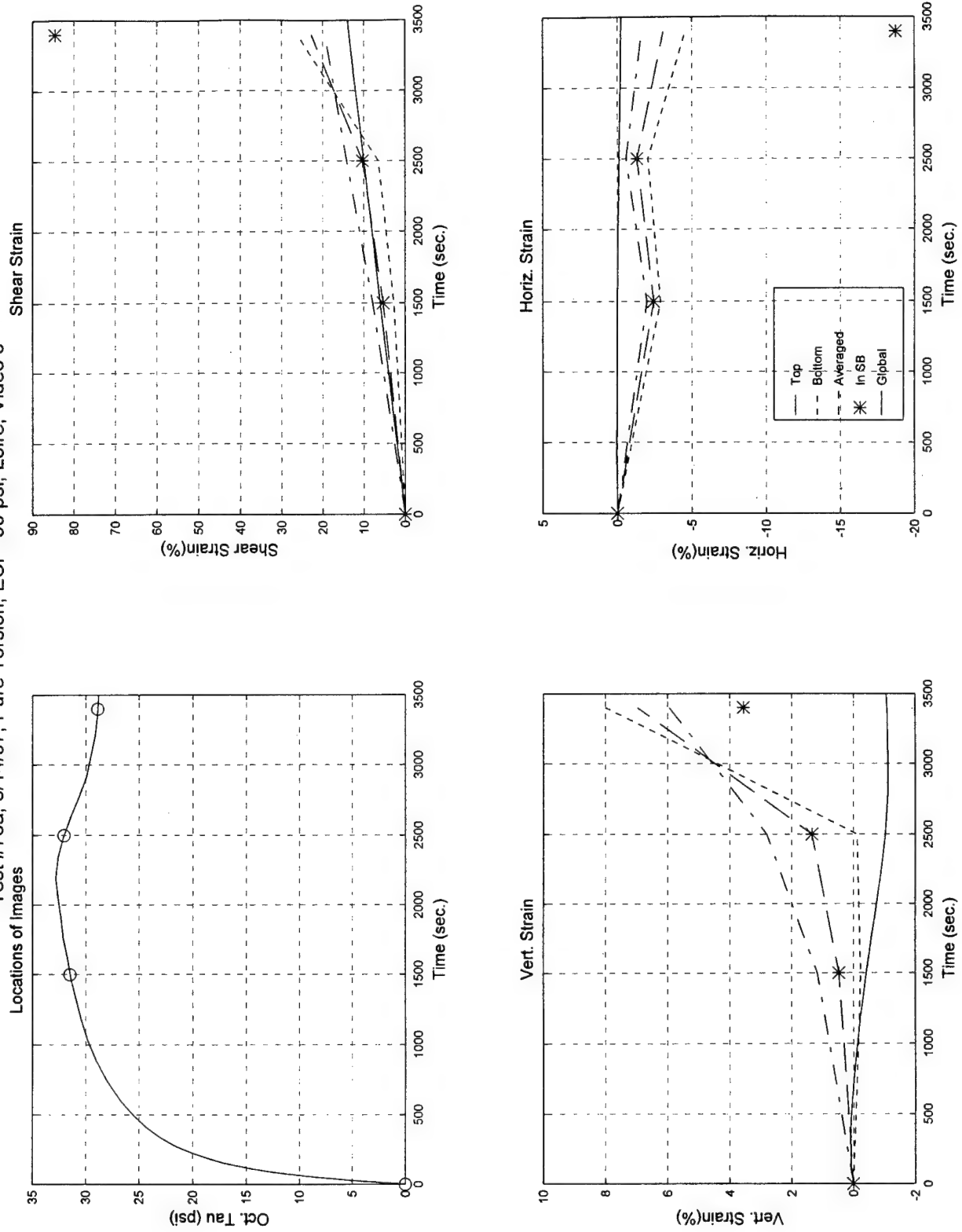
Test #78a, Camera #C, Figure 2

151
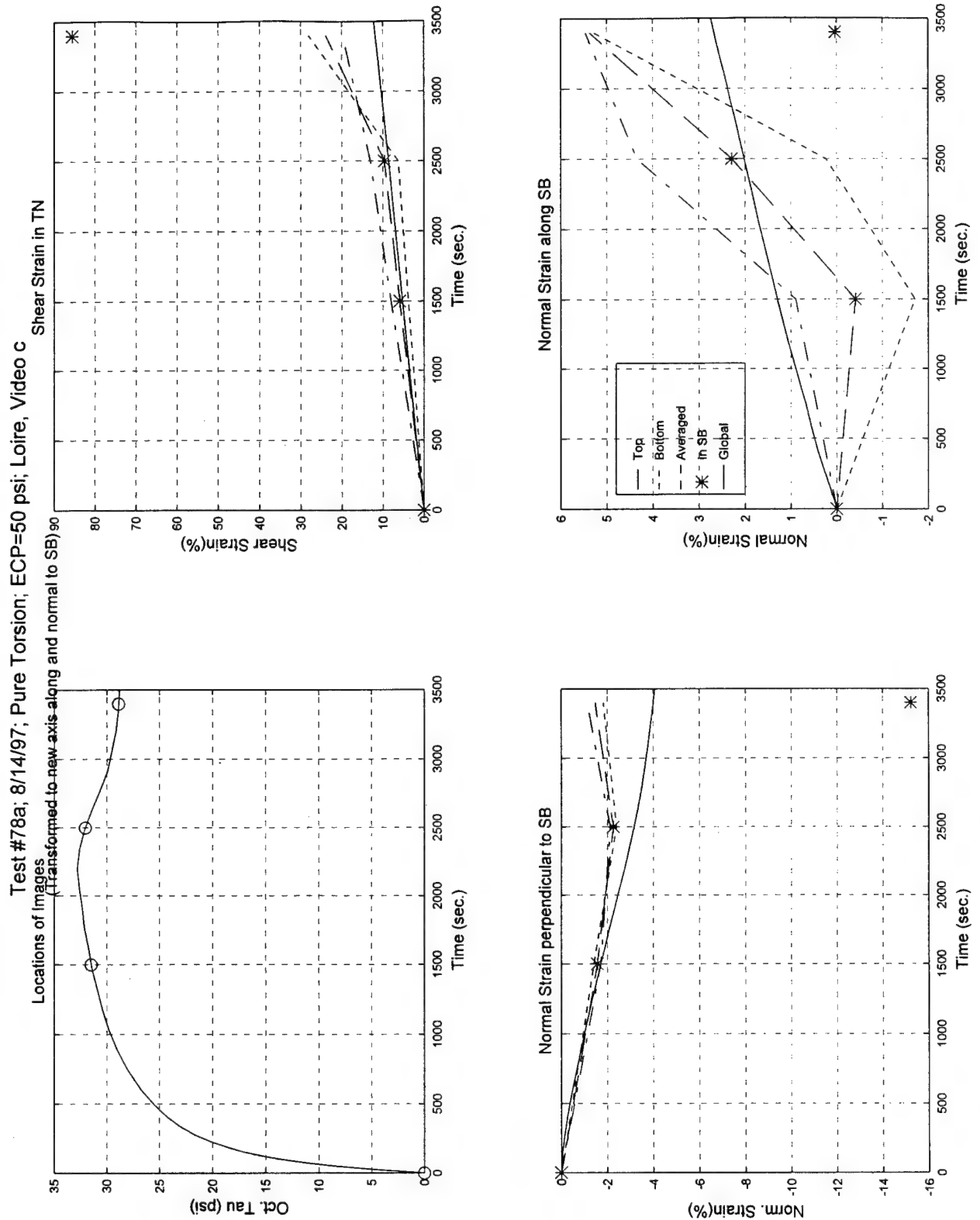
Test #78a, Camera #C, Figure 3

Test #78a; 8/14/97; Pure Torsion; ECP=50 psi; Loire, Video c
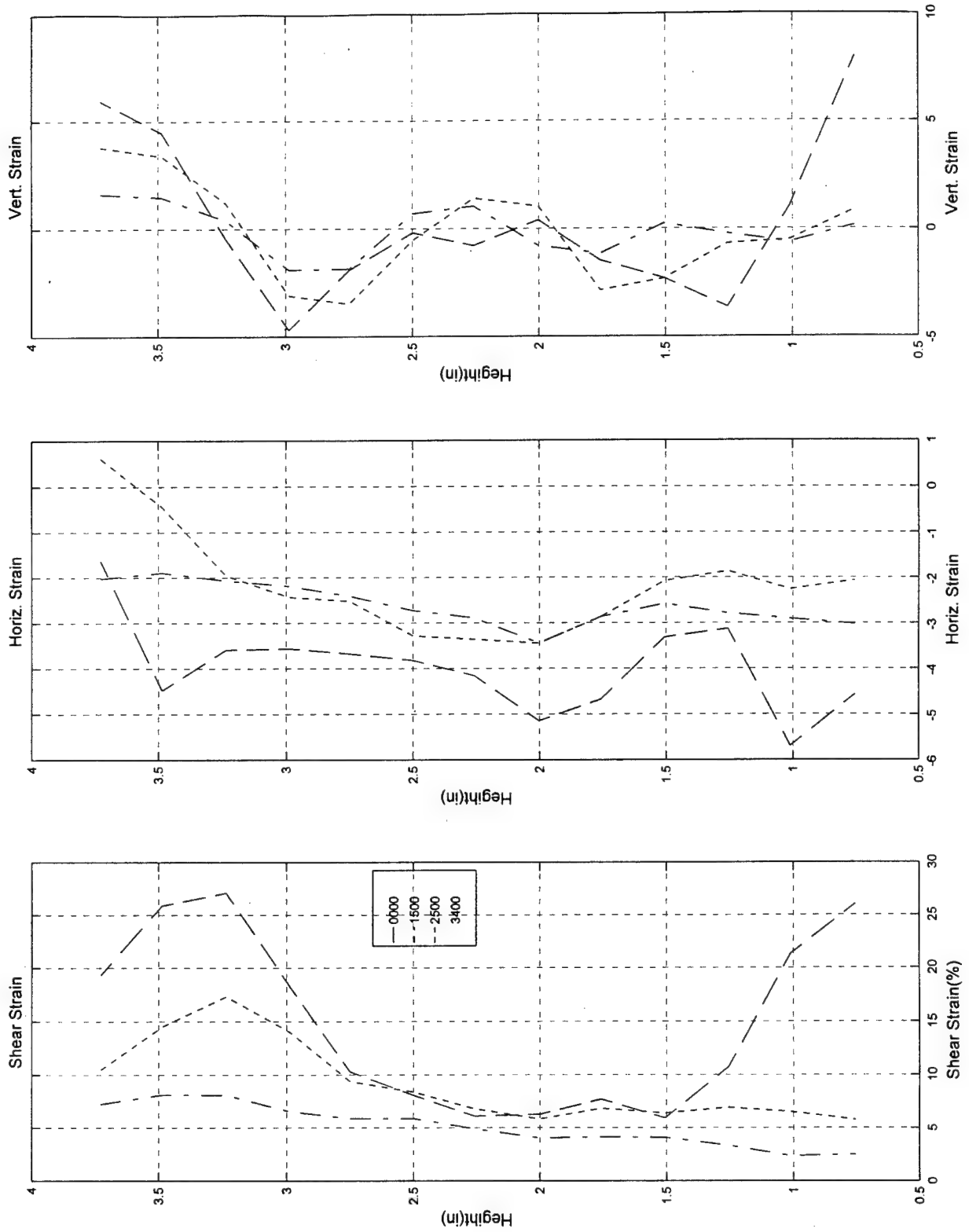
Test #78a, Camera #C, Figure 4

Test #78a; 8/14/97; Pure Torsion; ECP=50 psi; Loire, Video c
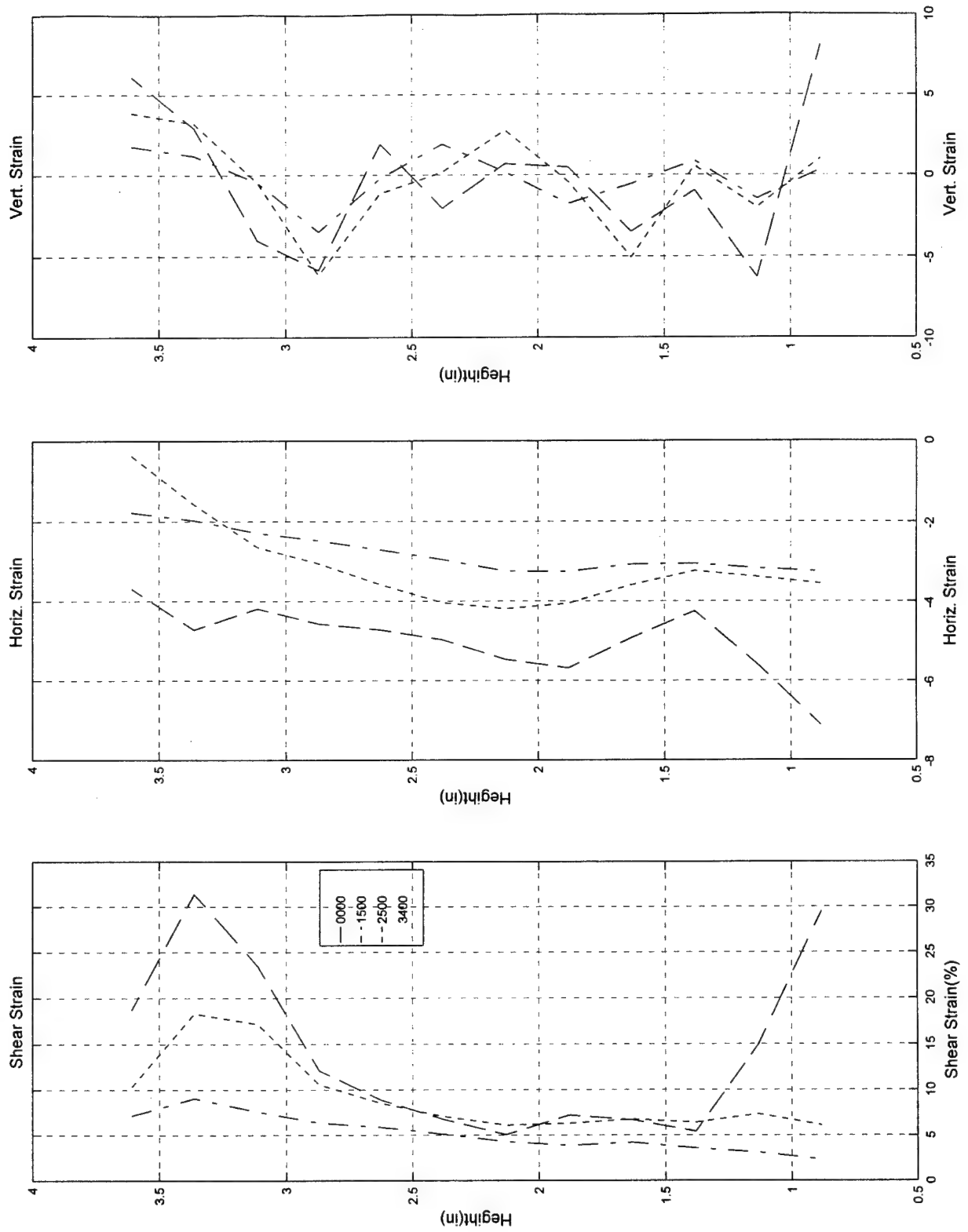
Test #78a, Camera #C, Figure 5

154

Test #78a; 8/14/97; Pure Torsion; ECP=50 psi; Loire, Video c
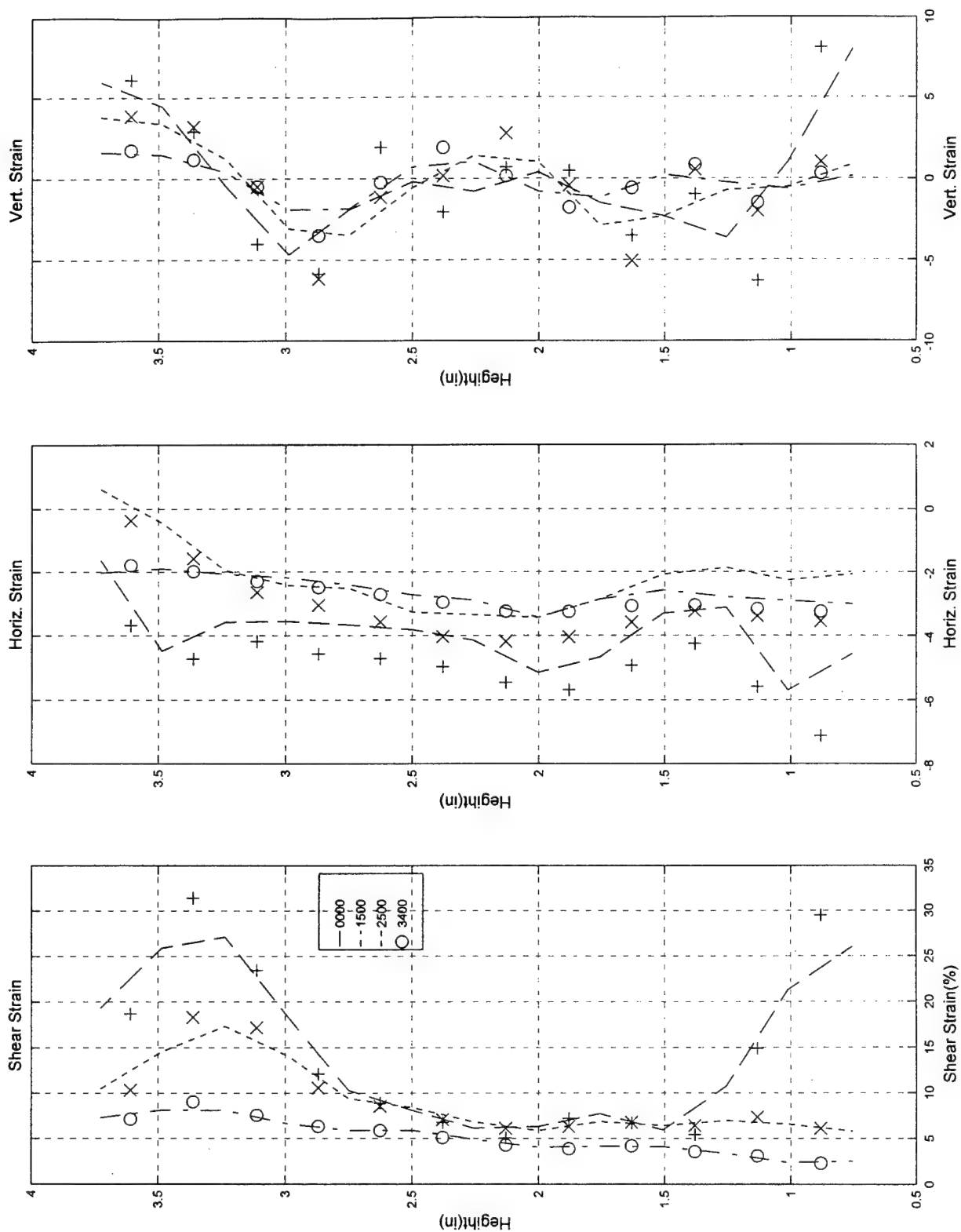
Test #78a, Camera #C, Figure 6

Test #78a; 8/14/97; Pure Torsion; ECP=50 psi; Loire, Video c

Test #78a, Camera #C, Figure 7

156

Test #78a, Camera #D, Figure 1

Test #78a; 8/14/97; Pure Torsion; ECP=50 psi; Loire, Video d
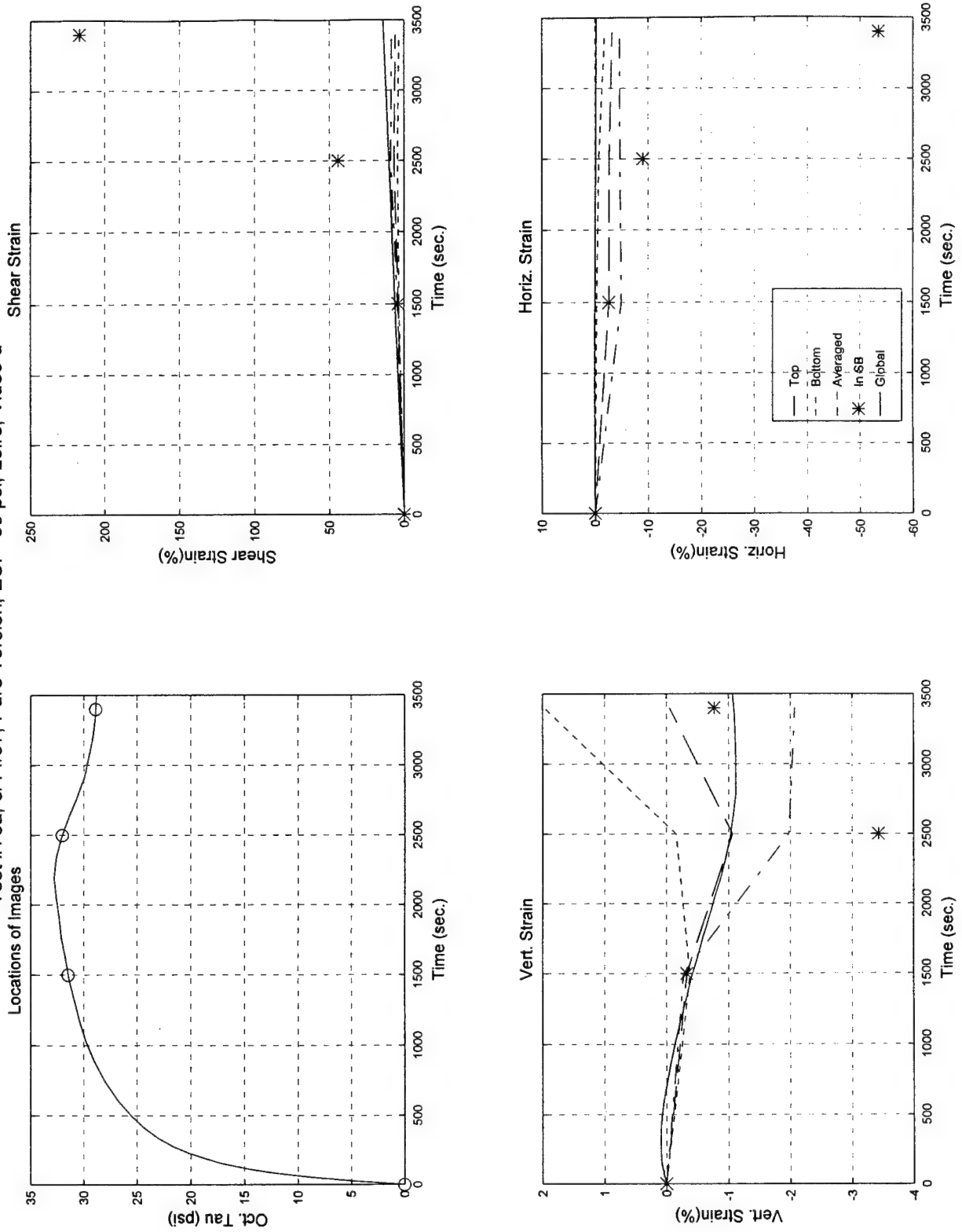
Test #78a, Camera #D, Figure 2
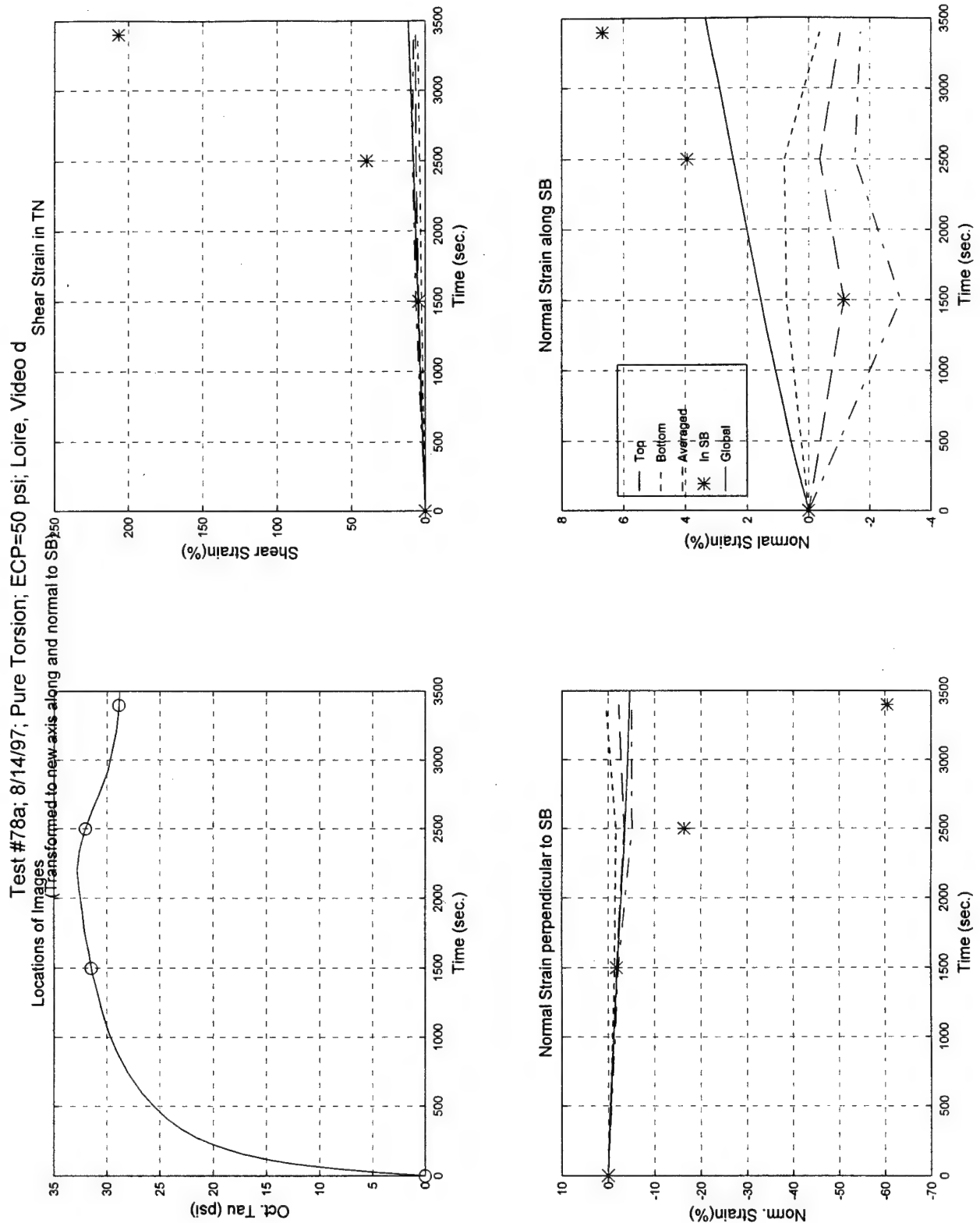
Test #78a; 8/14/97; Pure Torsion; ECP=50 psi; Loire, Video d

Test #78a, Camera #D, Figure 3
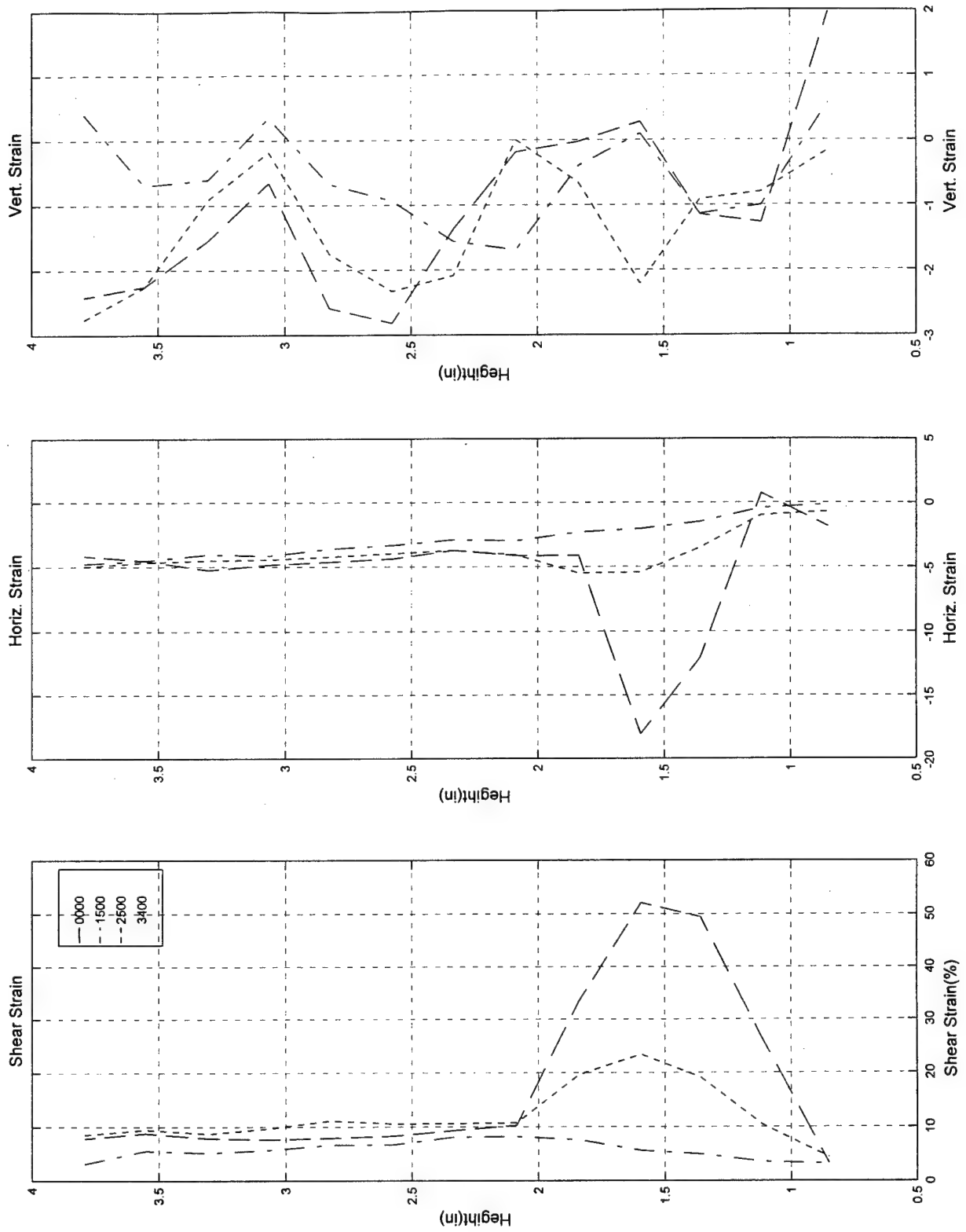
Test #78a, Camera #D, Figure 4

Test #78a; 8/14/97; Pure Torsion; ECP=50 psi; Loire, Video d
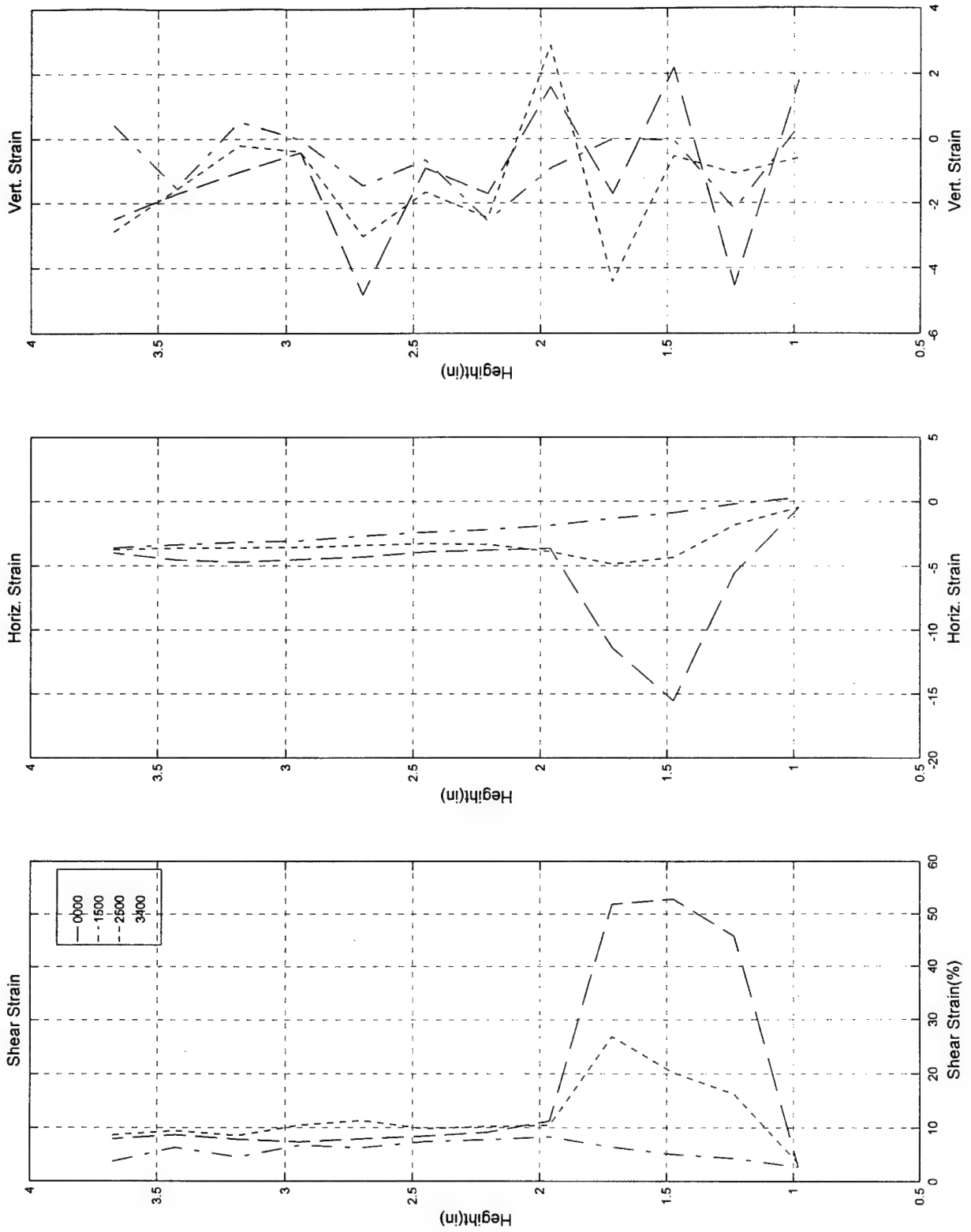
Test #78a, Camera #D, Figure 5

Test #78a; 8/14/97; Pure Torsion; ECP=50 psi; Loire, Video d
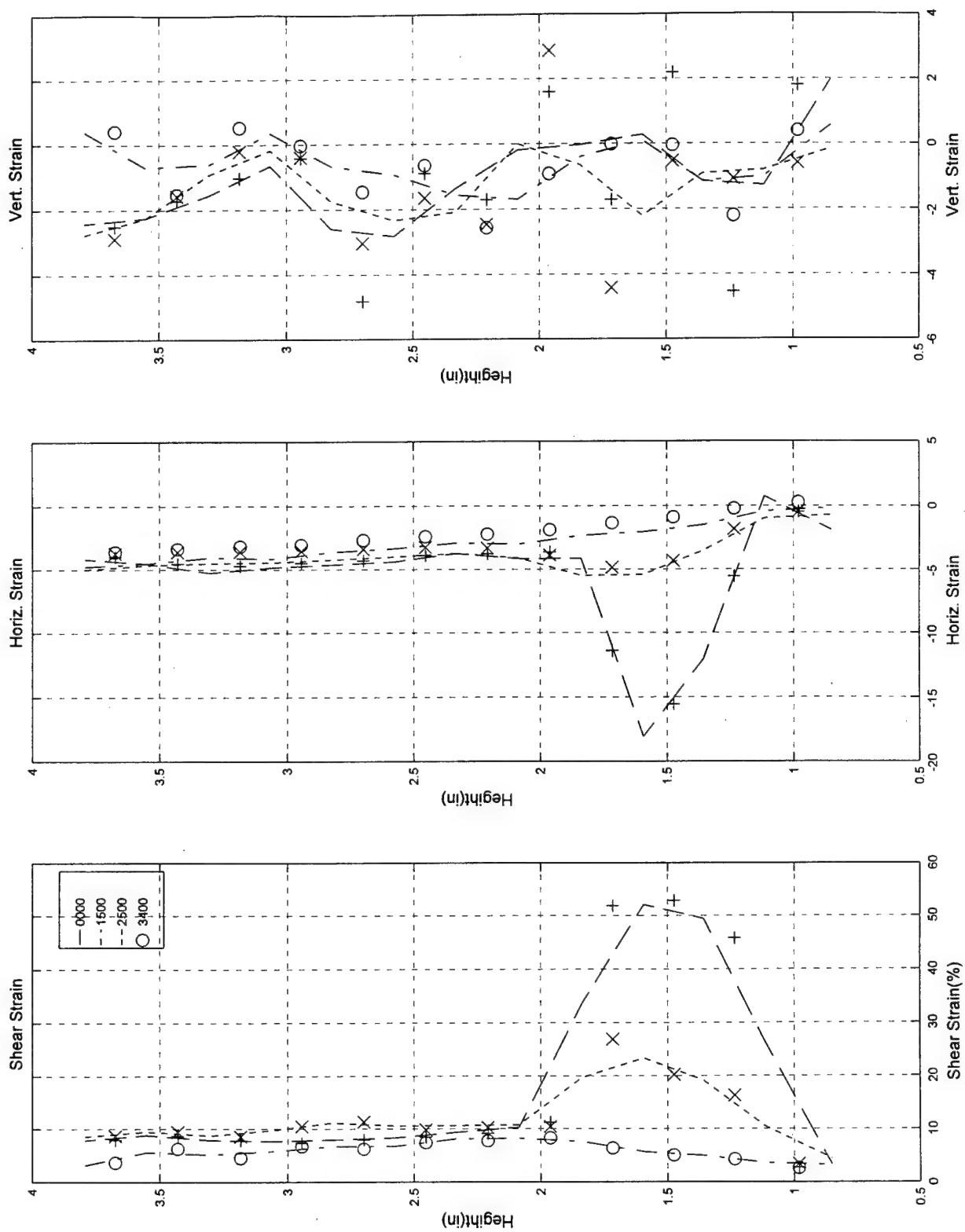
Test #78a, Camera #D, Figure 6
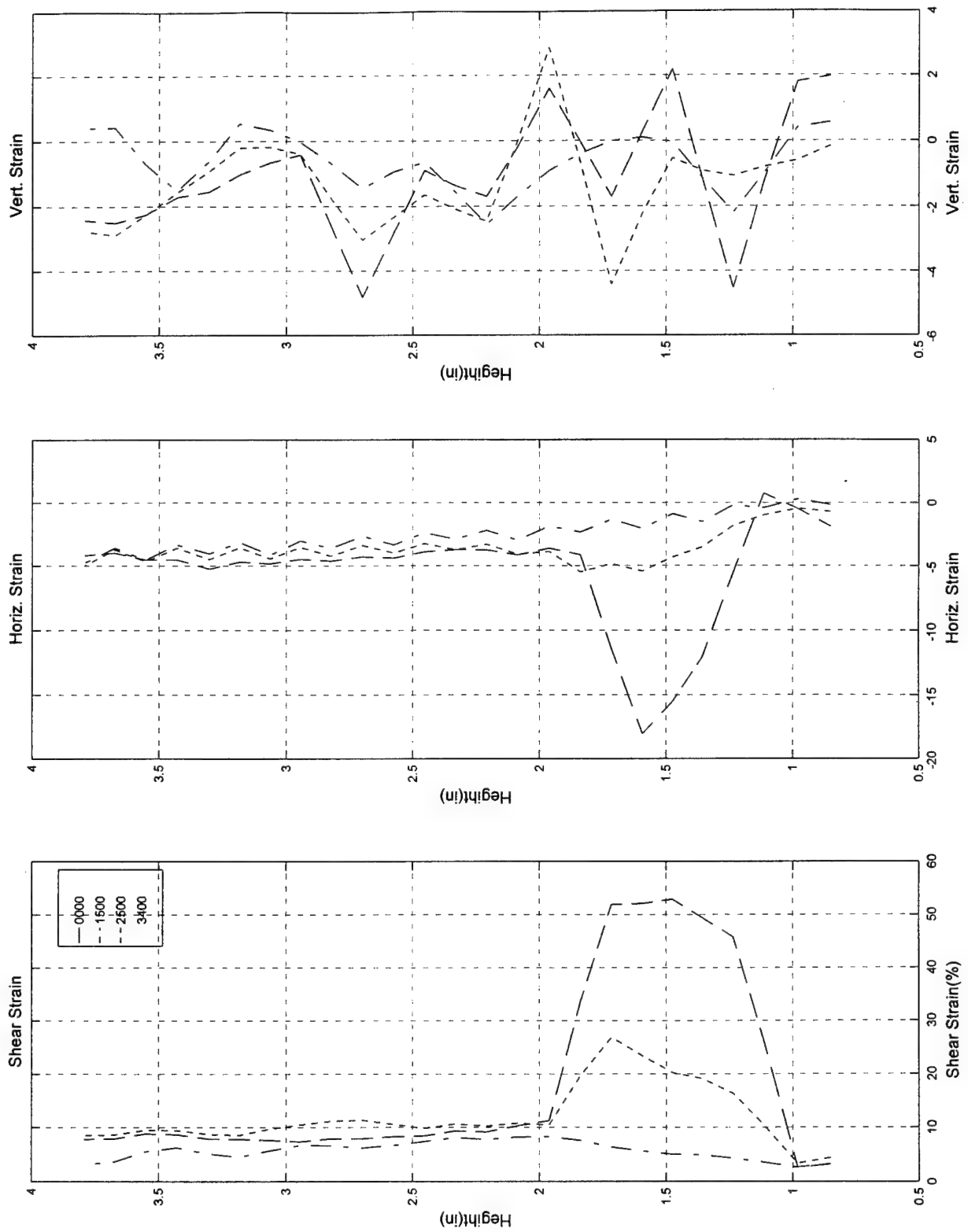
Test #78a, Camera #D, Figure 7

B.4 Test #79

- **Torsion-Extension ($\beta = 60$ °)**
- **Effective Confining Pressure = 50 psi (345 kPa)**
- **50% Initial Relative Density**
- **Generalized Test**
- **Digitized Times Intervals: 0000, 1500, 2000 & 2400 sec.**

Test #79, Camera #A, Figure 1
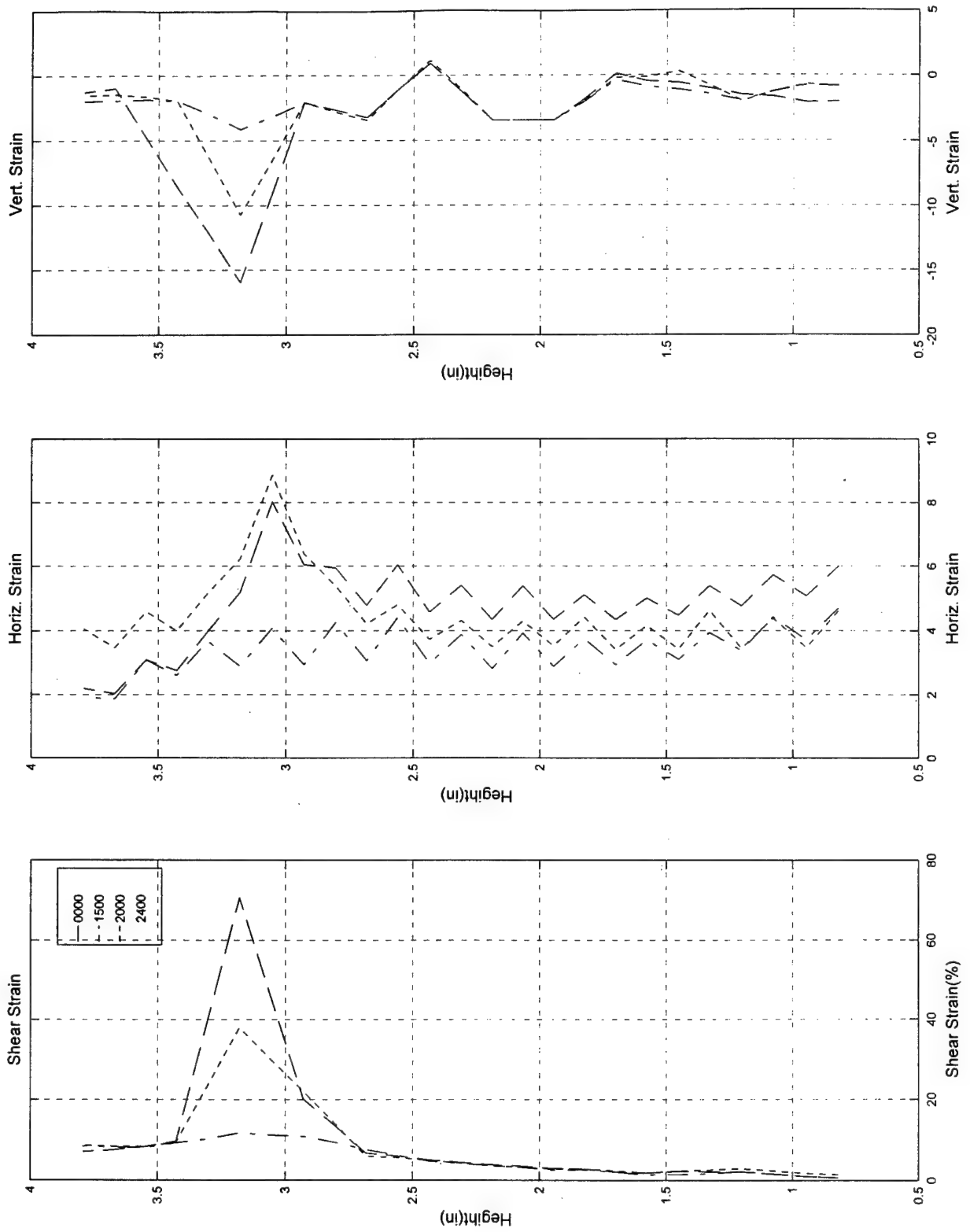
Test #79, Camera #A, Figure 2

166

Test #79, Camera #A, Figure 3

Test #79; 4/1/97; Torsion-Extension; ECP=50 psi; Loire, Video a

Test #79, Camera #A, Figure 4

168

Test #79: 4/1/97; Torsion-Extension; ECP=50 psi; Loire, Video a
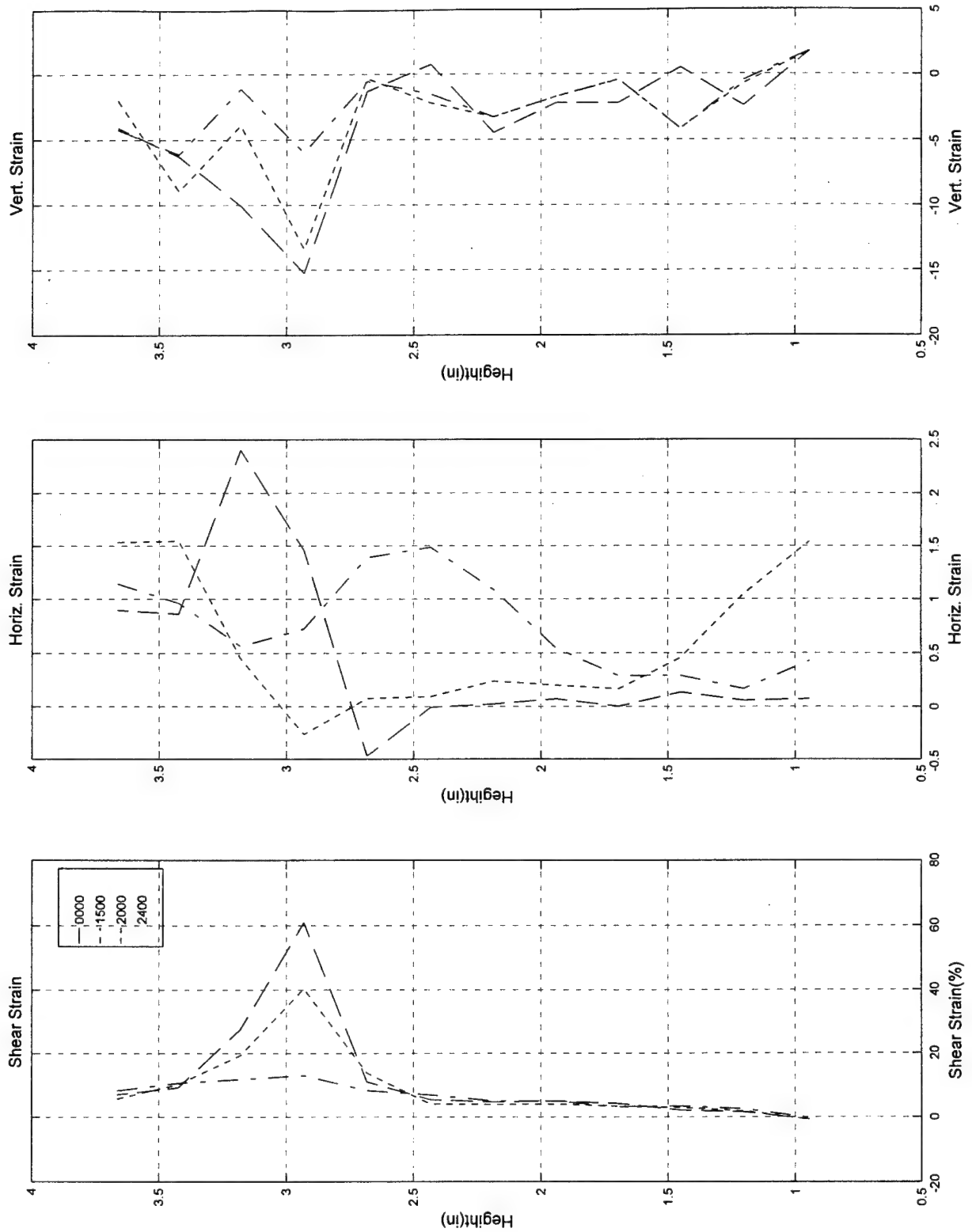
Test #79, Camera #A, Figure 5

Test #79; 4/1/97; Torsion-Extension; ECP=50 psi; Loire, Video a
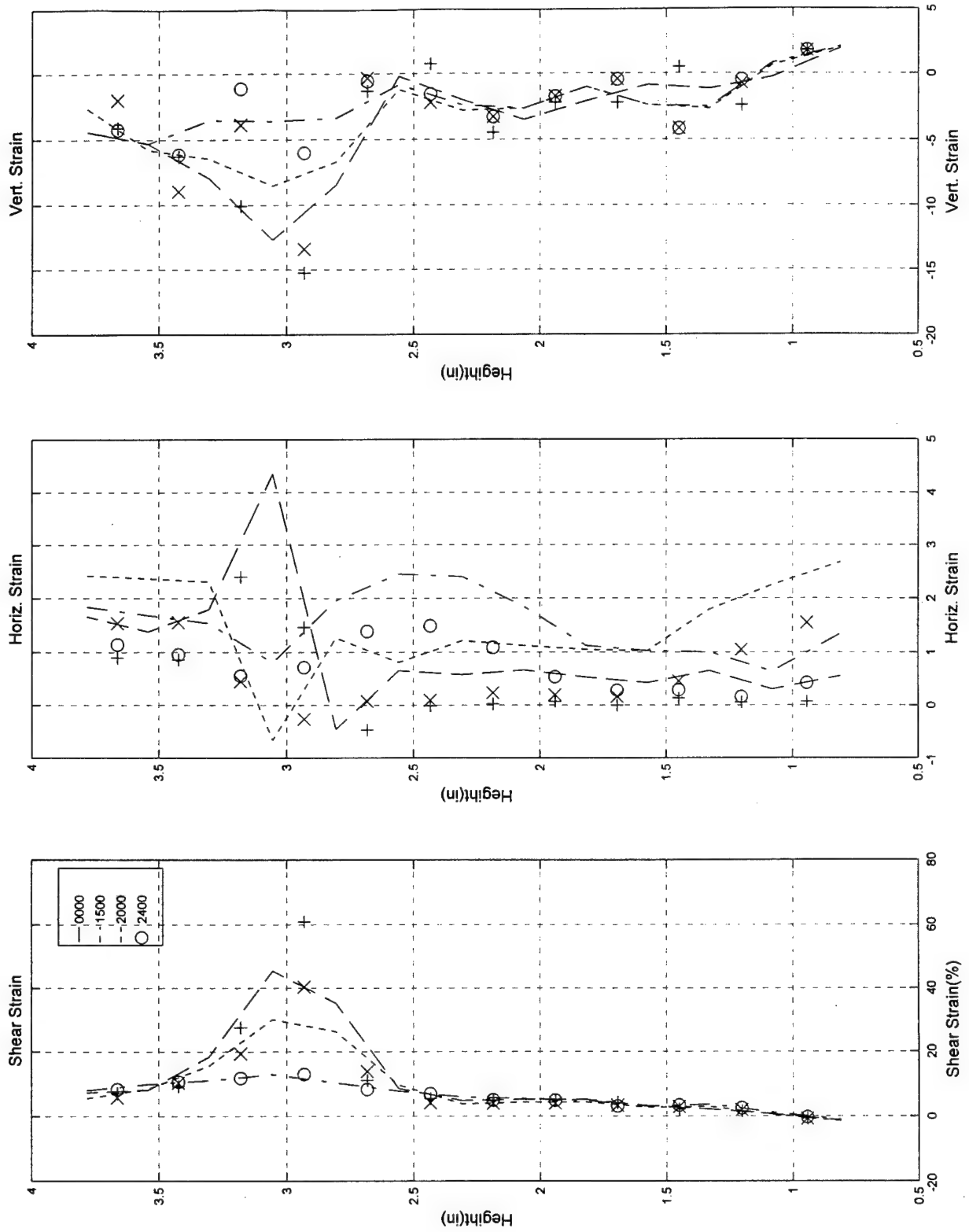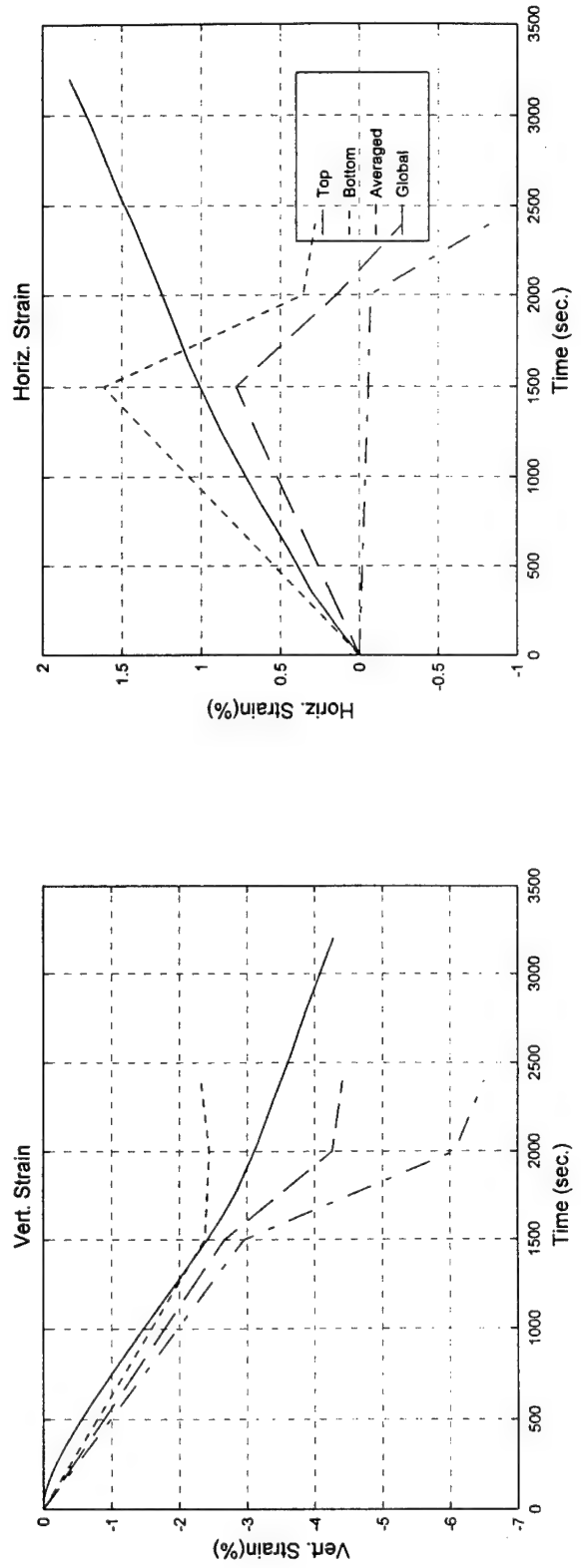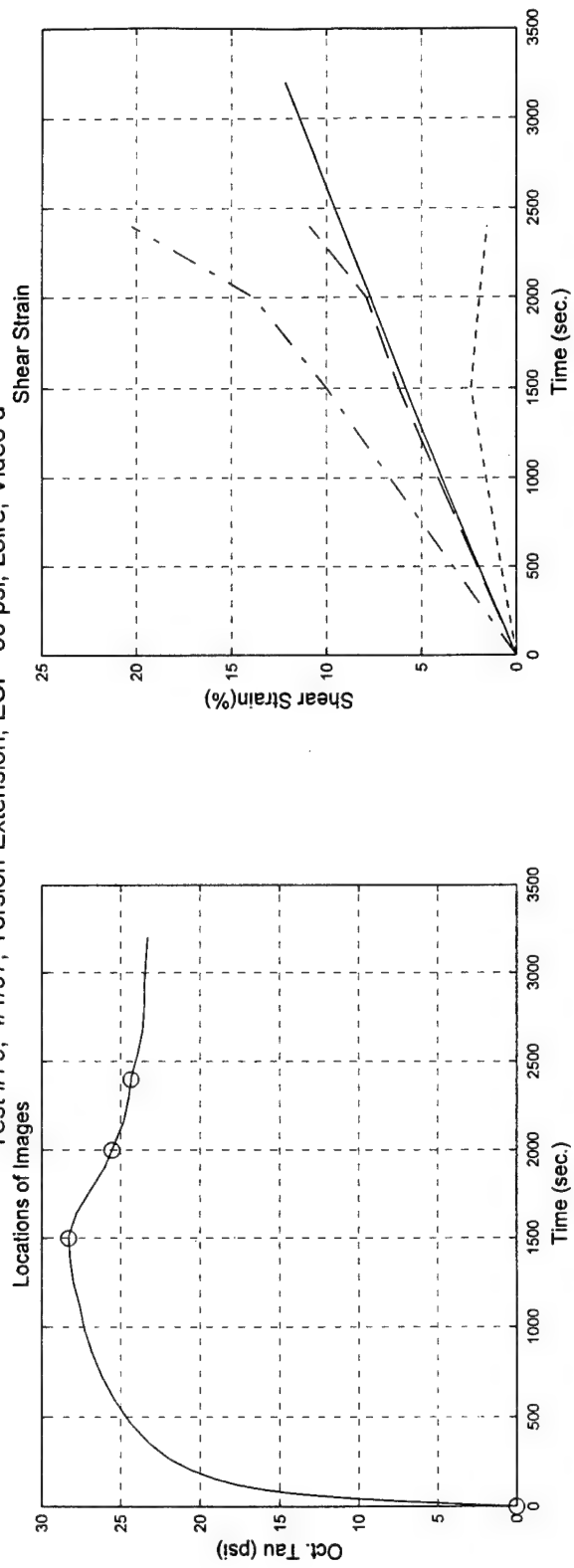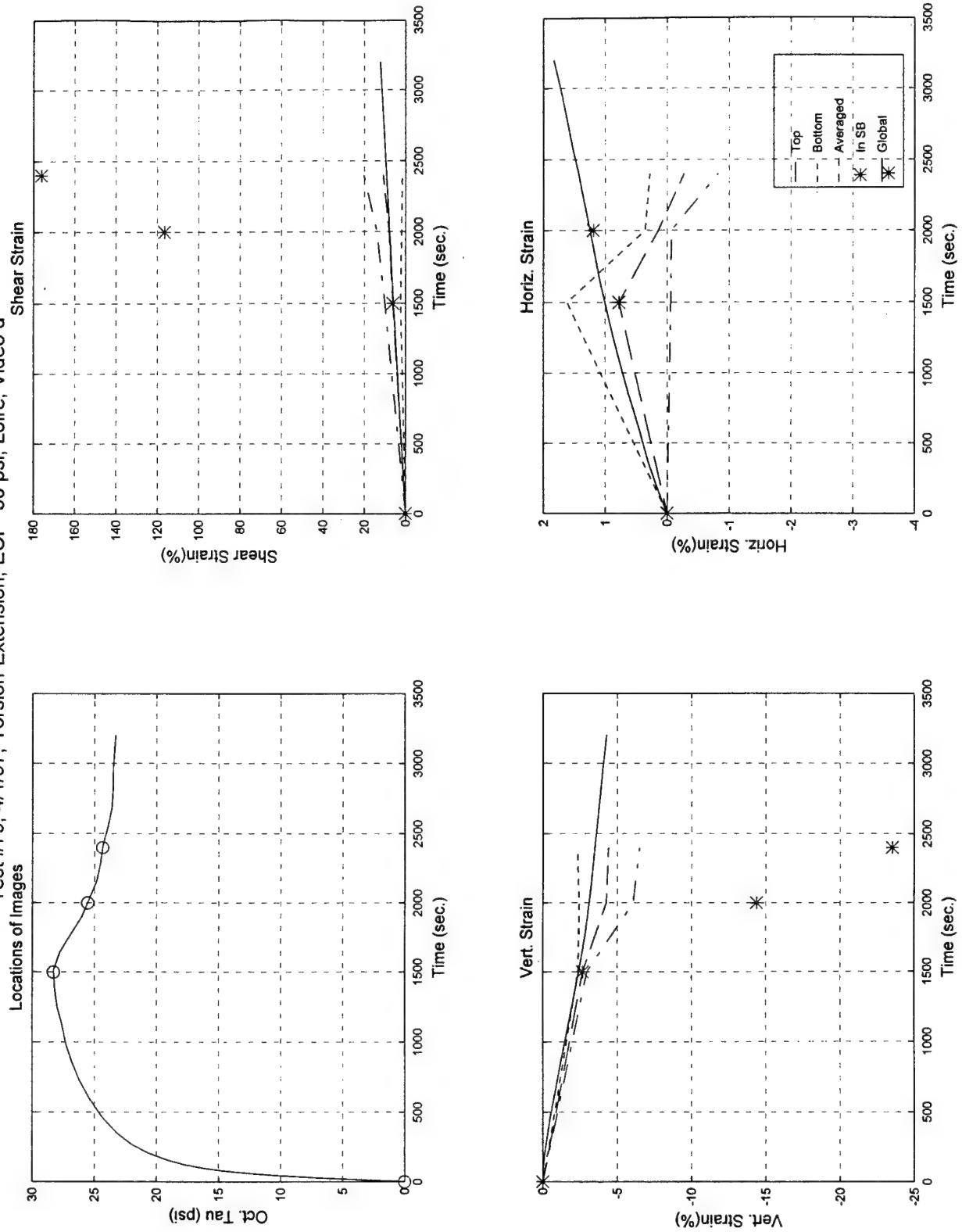

Test #79, Camera #A, Figure 6

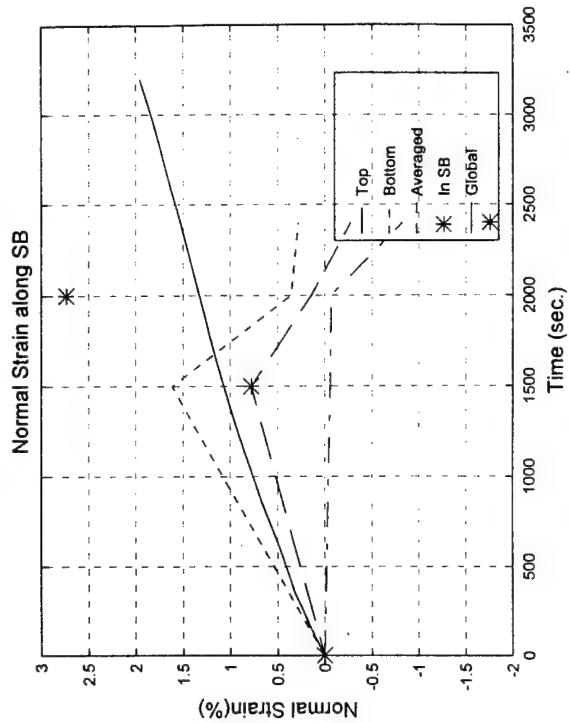Test #79; 4/1/97; Torsion-Extension; ECP=50 psi; Loire, Video a
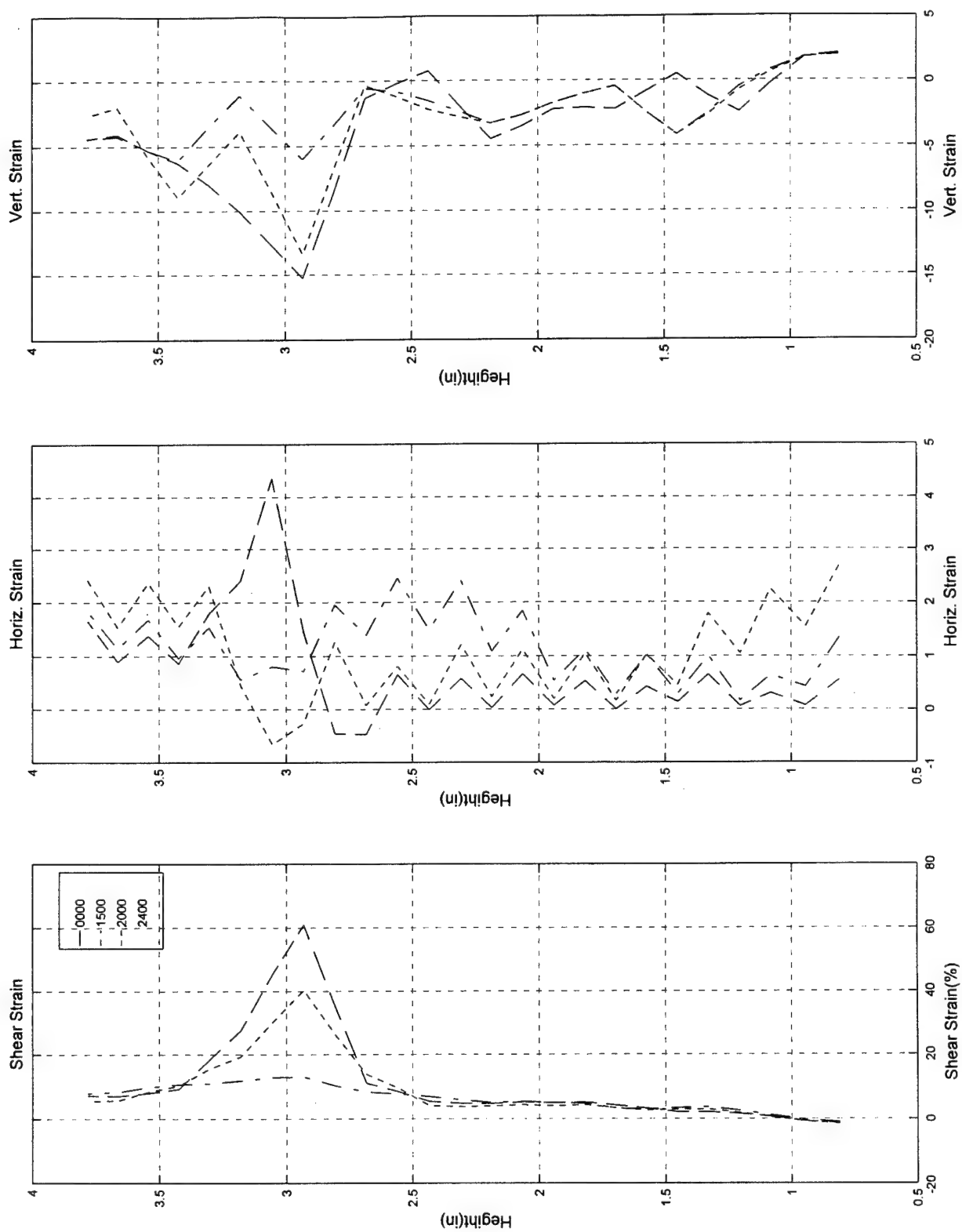
Test #79, Camera #A, Figure 7

Test #79; 4/1/97; Torsion-Extension; ECP=50 psi; Loire, Video b
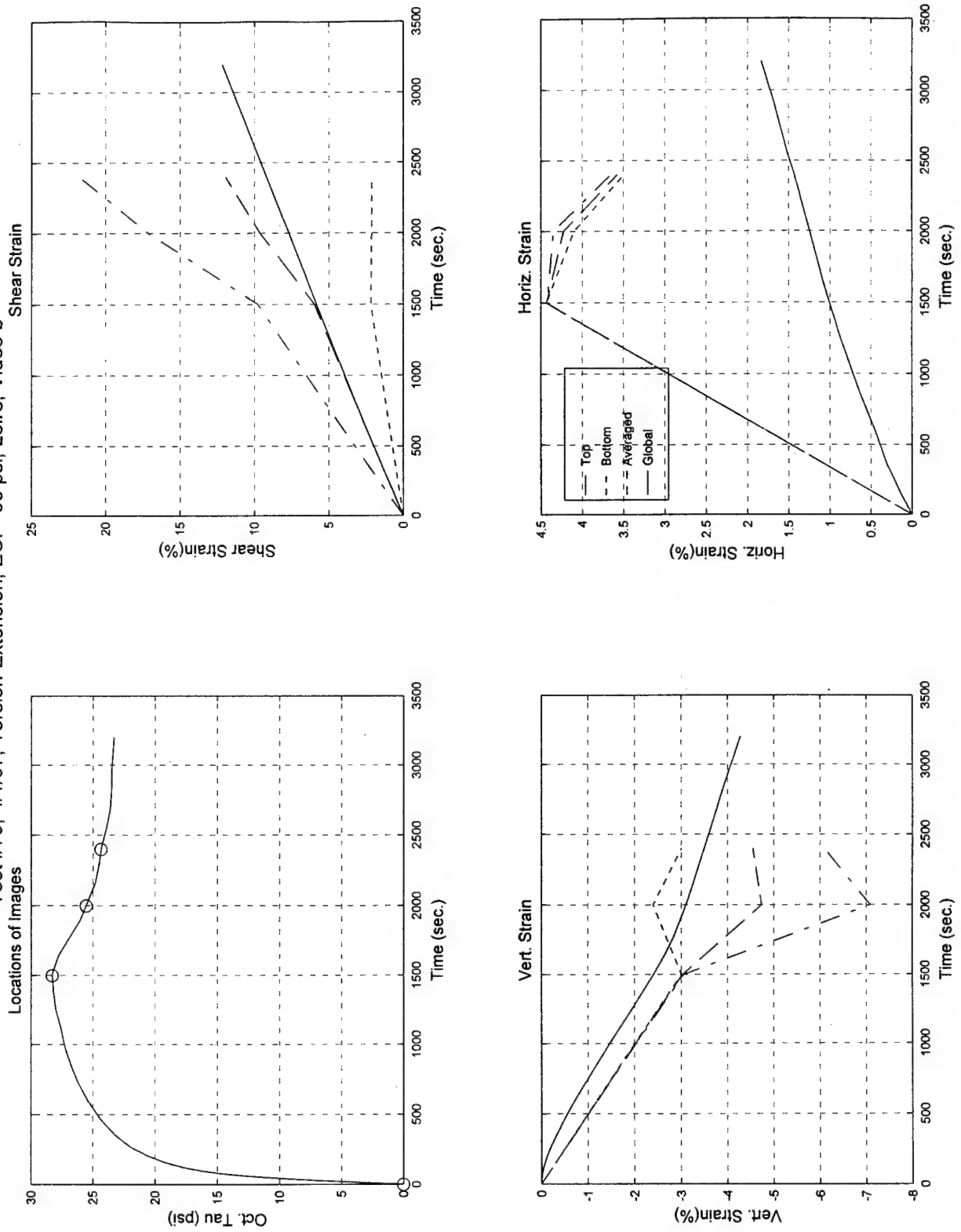
Test #79, Camera #B, Figure 1

172

Test #79, Camera #B, Figure 2

Test #79; 4/1/97; Torsion-Extension; ECP=50 psi; Loire, Video b

Test #79, Camera #B, Figure 3

Test #79; 4/1/97; Torsion-Extension; ECP=50 psi; Loire, Video b
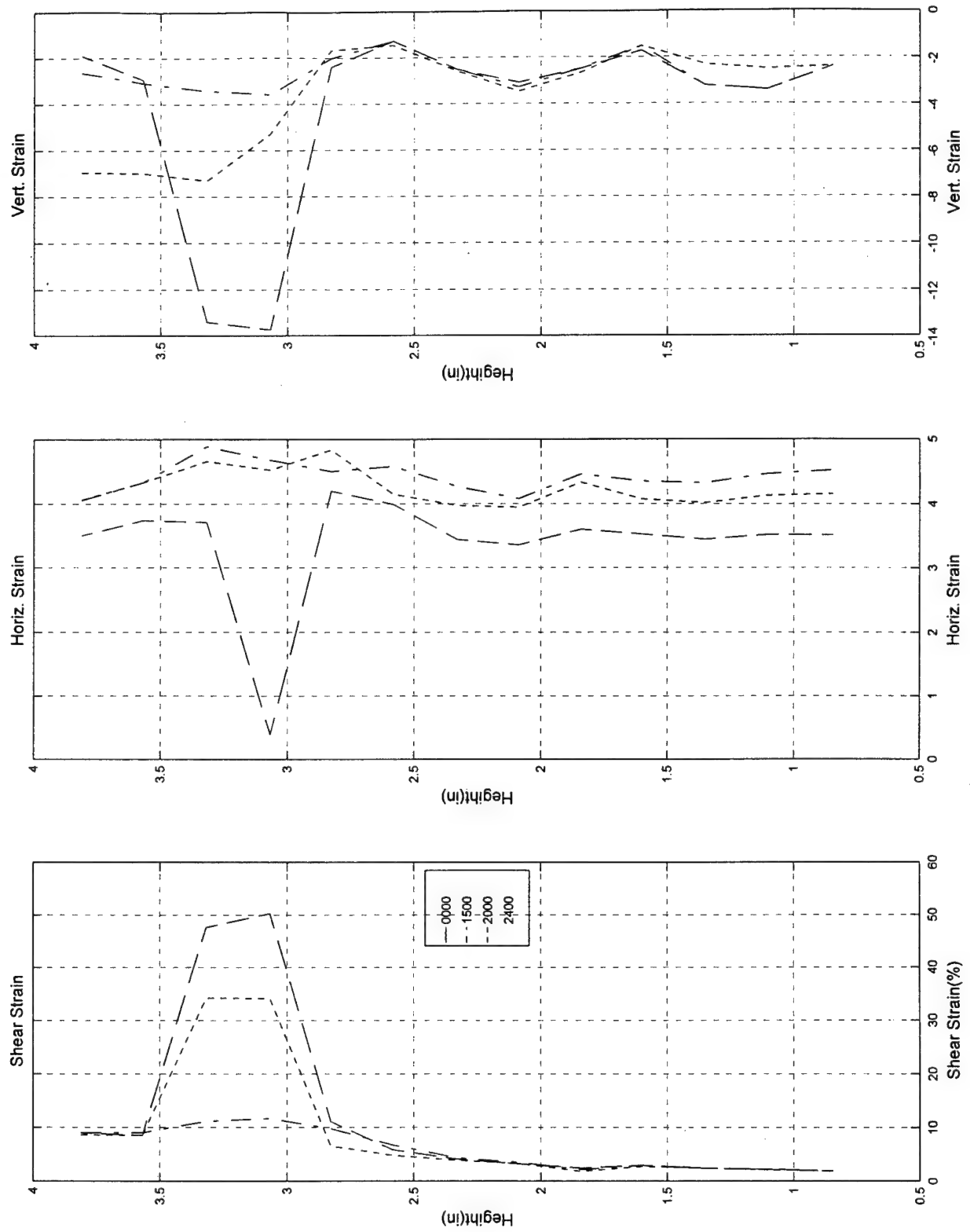
Test #79, Camera #B, Figure 4

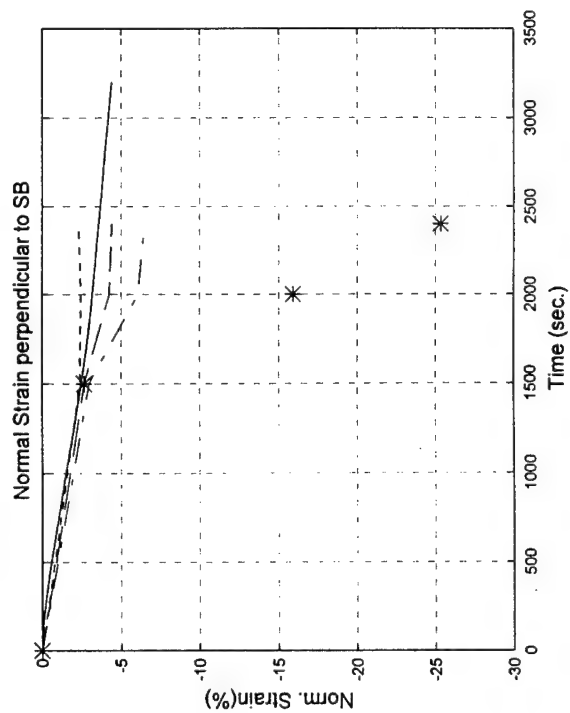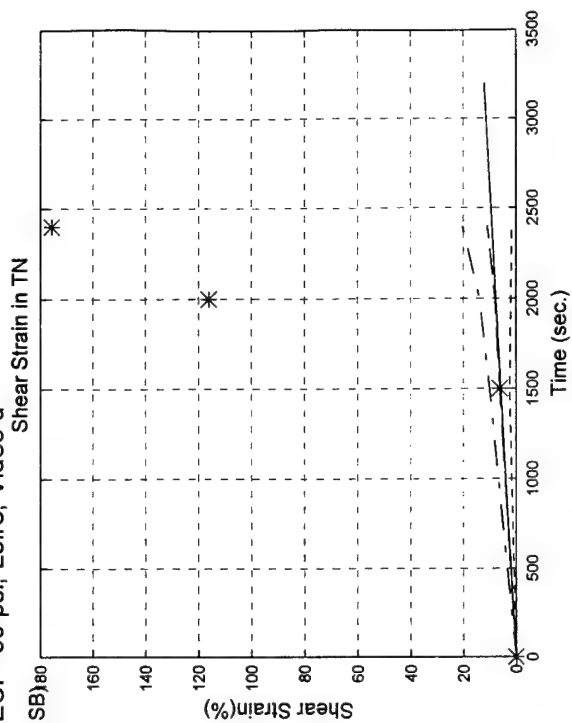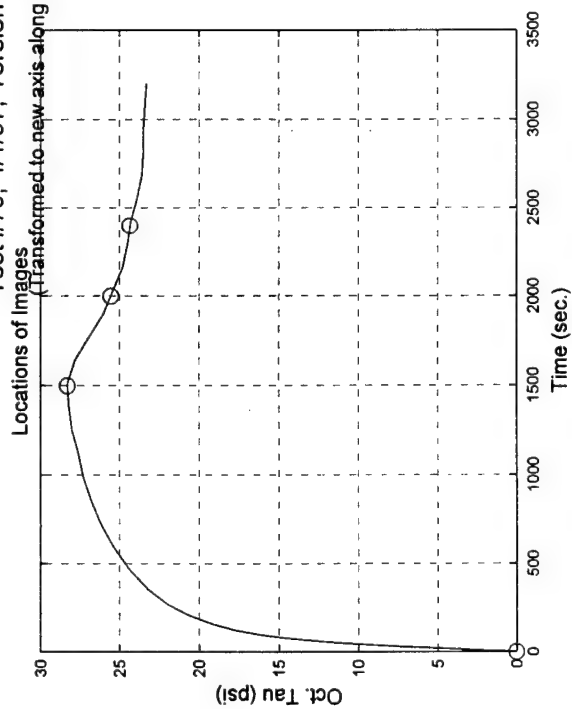Test #79; 4/1/97; Torsion-Extension; ECP=50 psi; Loire, Video b
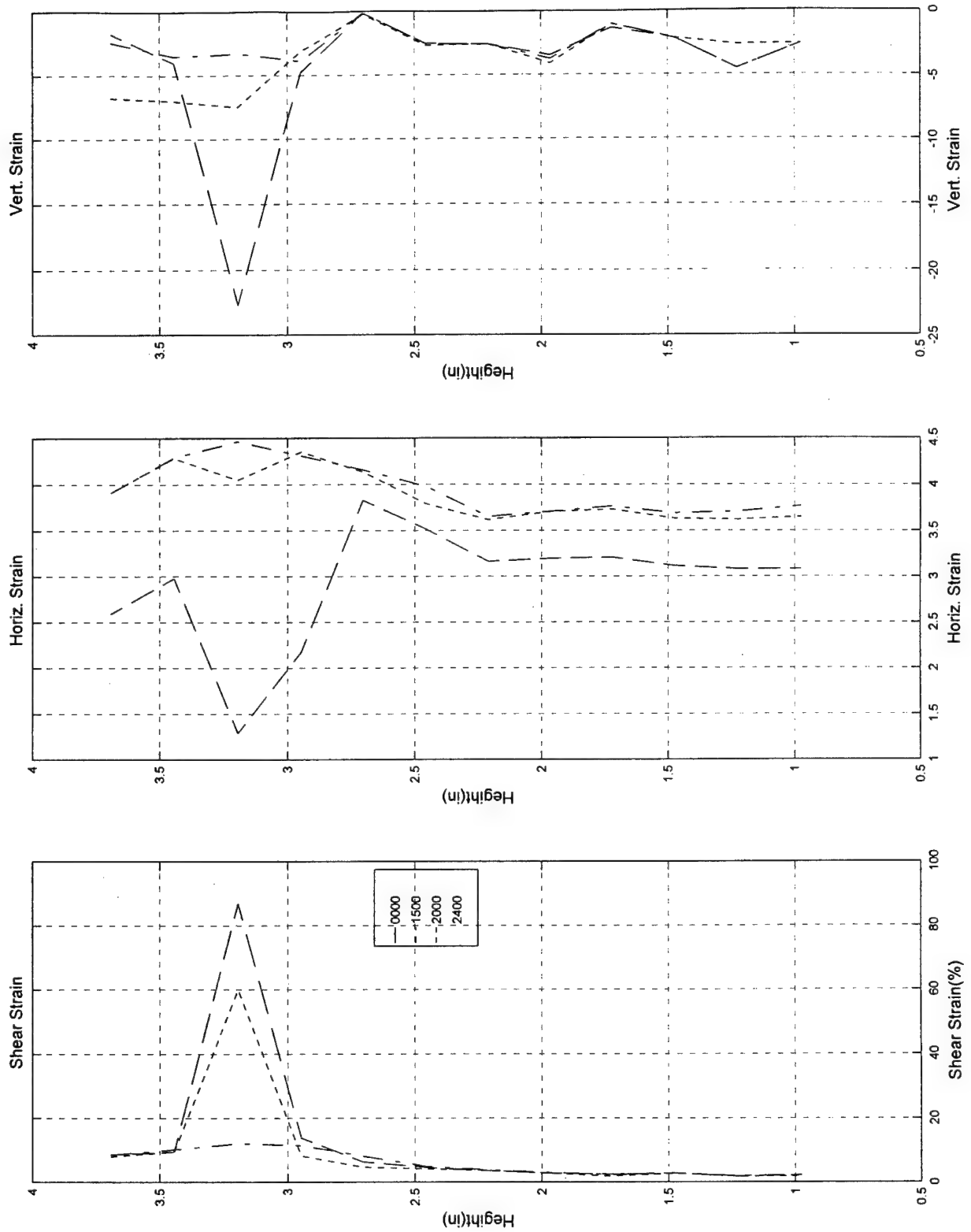
Test #79, Camera #B, Figure 5
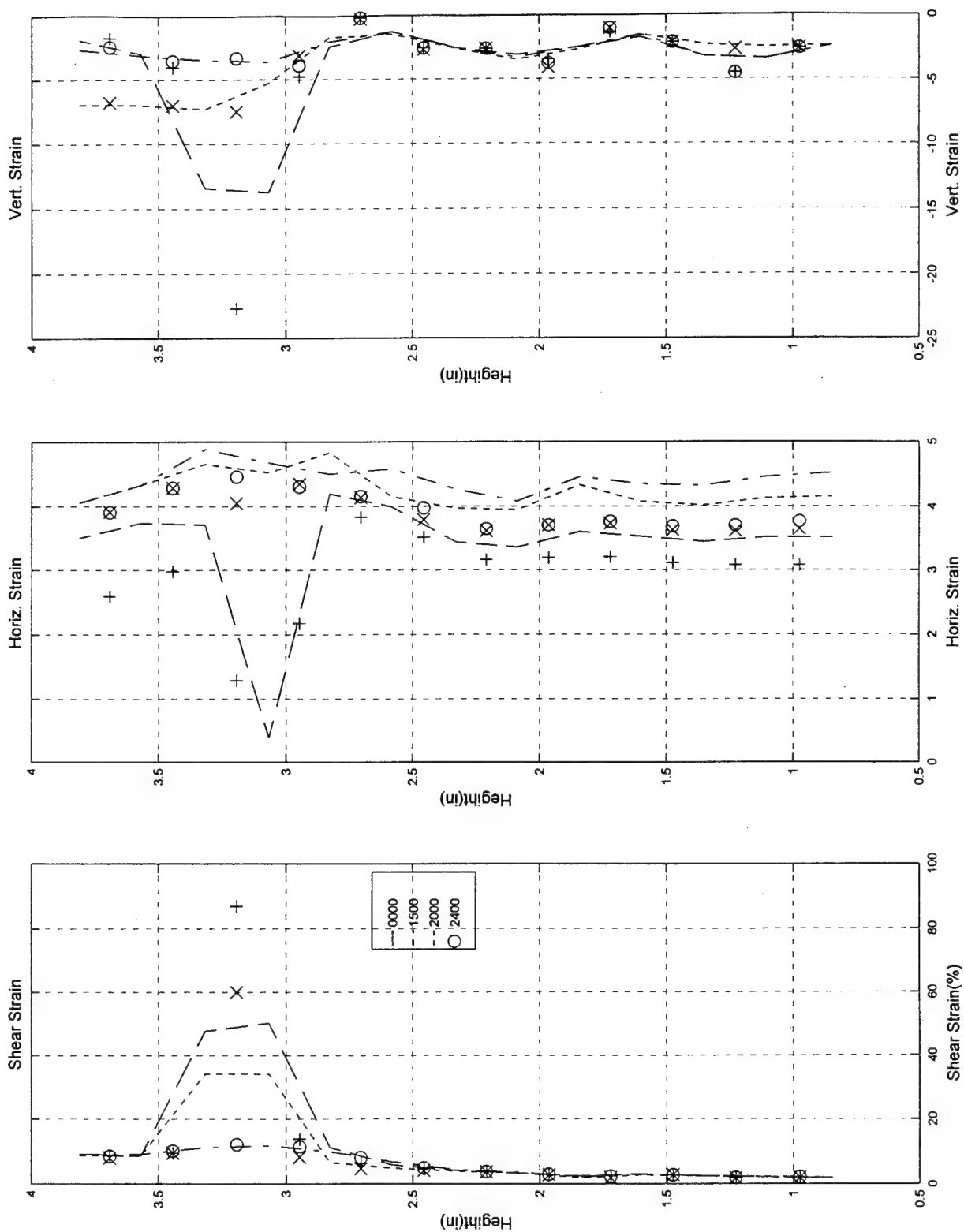
Test #79, Camera #B, Figure 6

Test #79; 4/1/97; Torsion-Extension; ECP=50 psi; Loire, Video b

Test #79, Camera #B, Figure 7
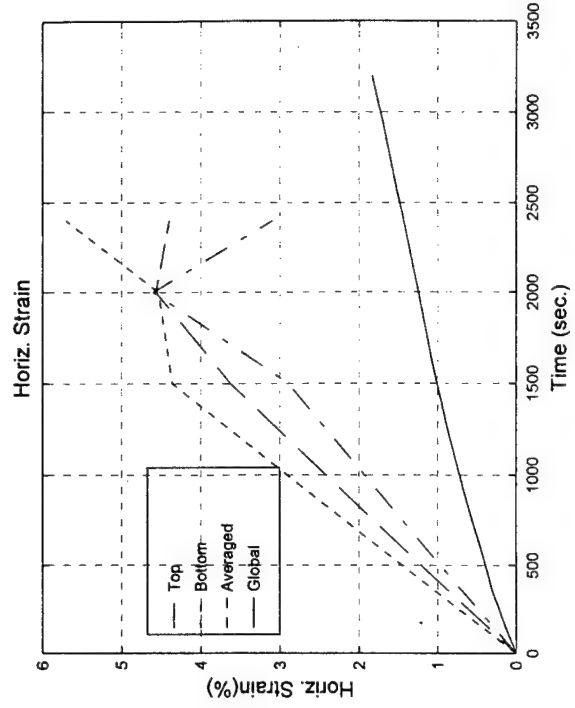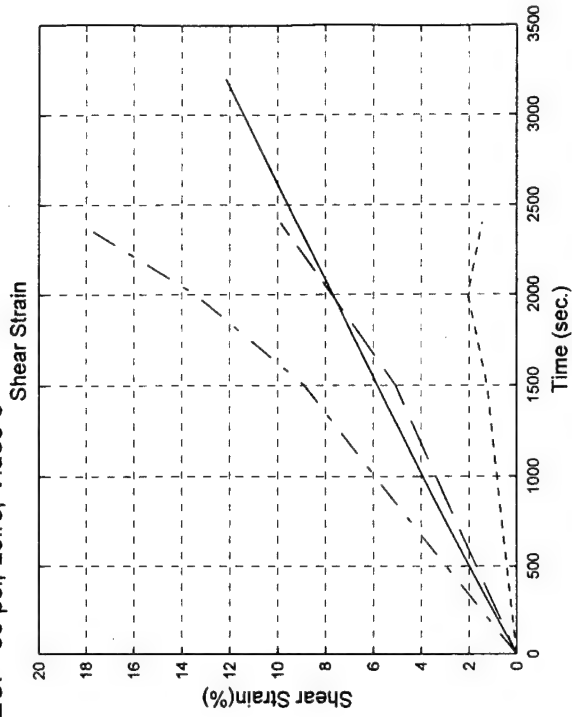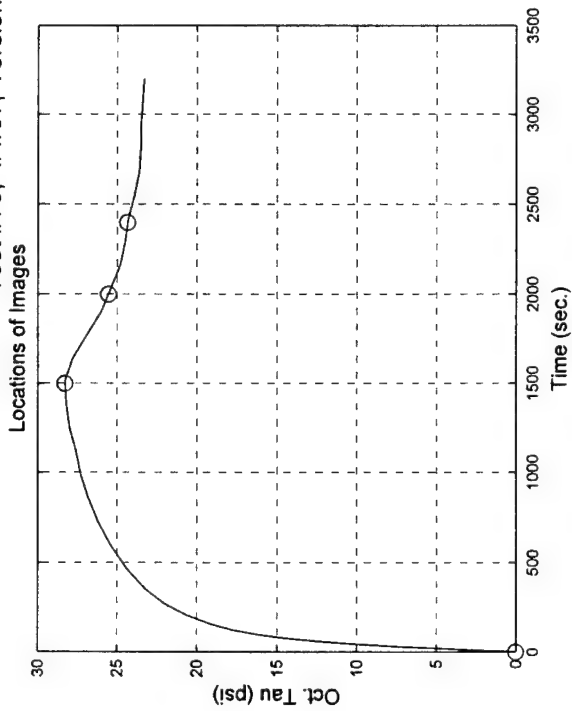
Test #79, Camera #C, Figure 1

Test #79; 4/1/97; Torsion-Extension; ECP=50 psi; Loire, Video c

Test #79, Camera #C, Figure 2
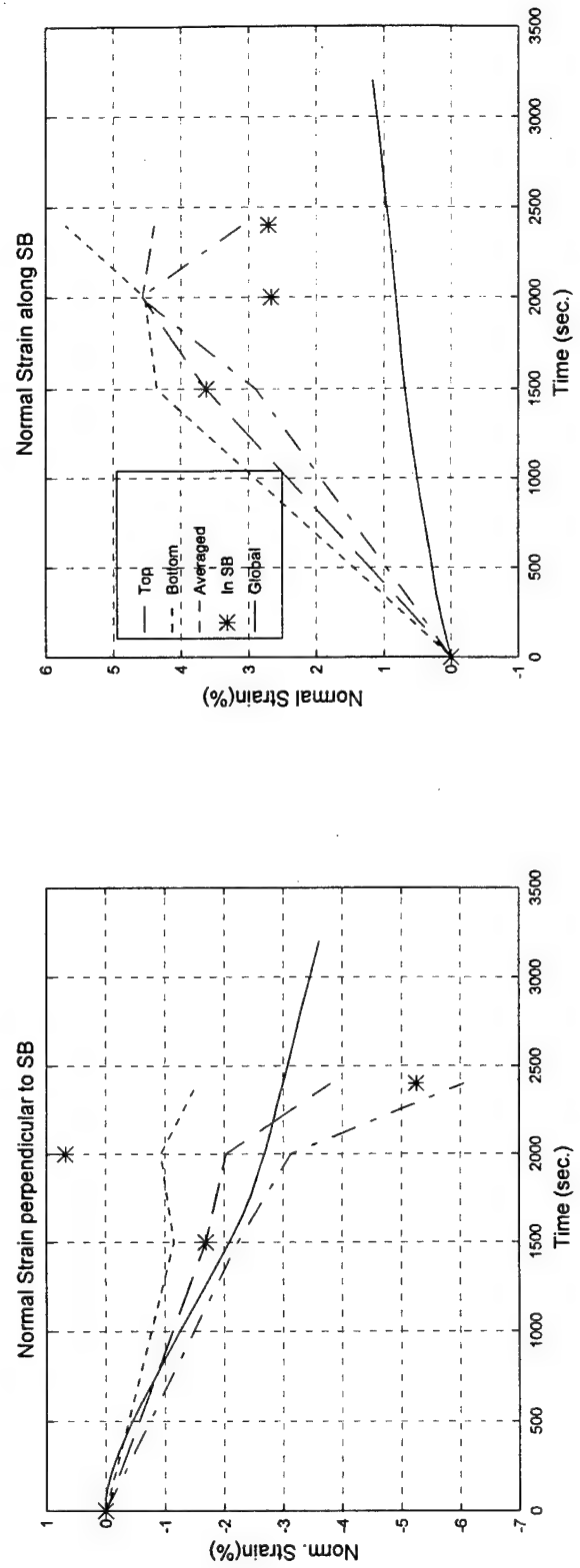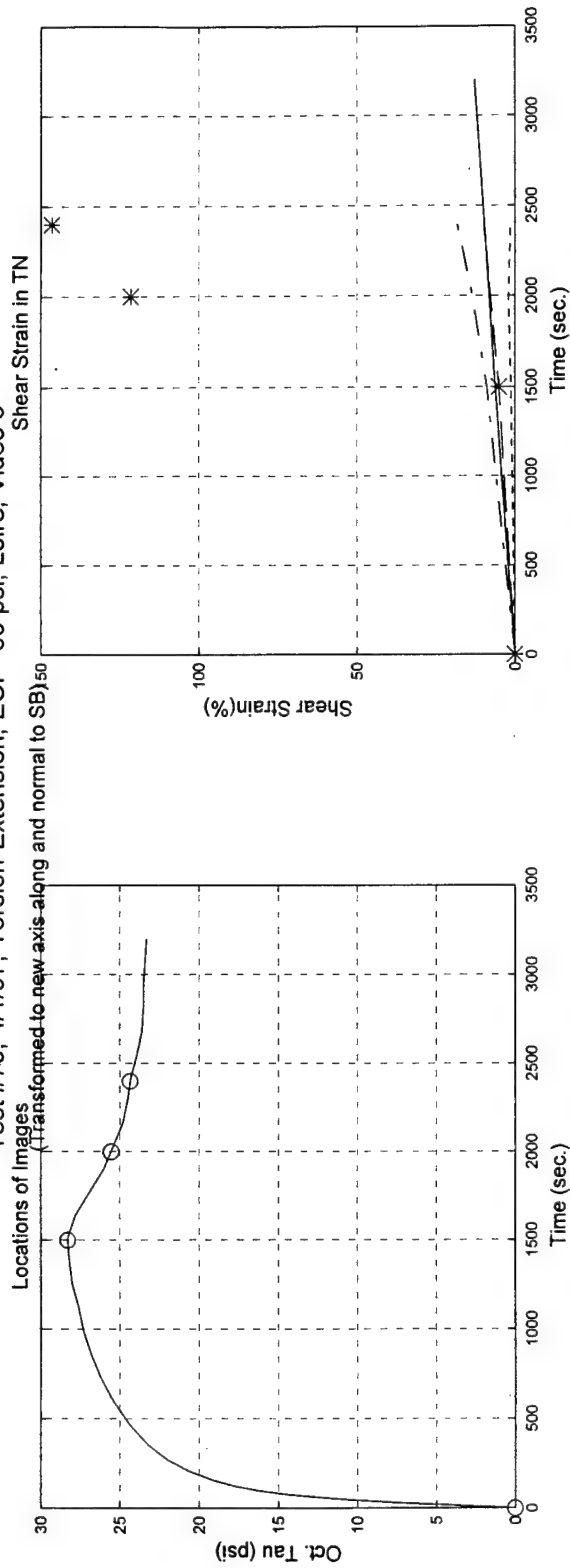
Test #79, Camera #C, Figure 3

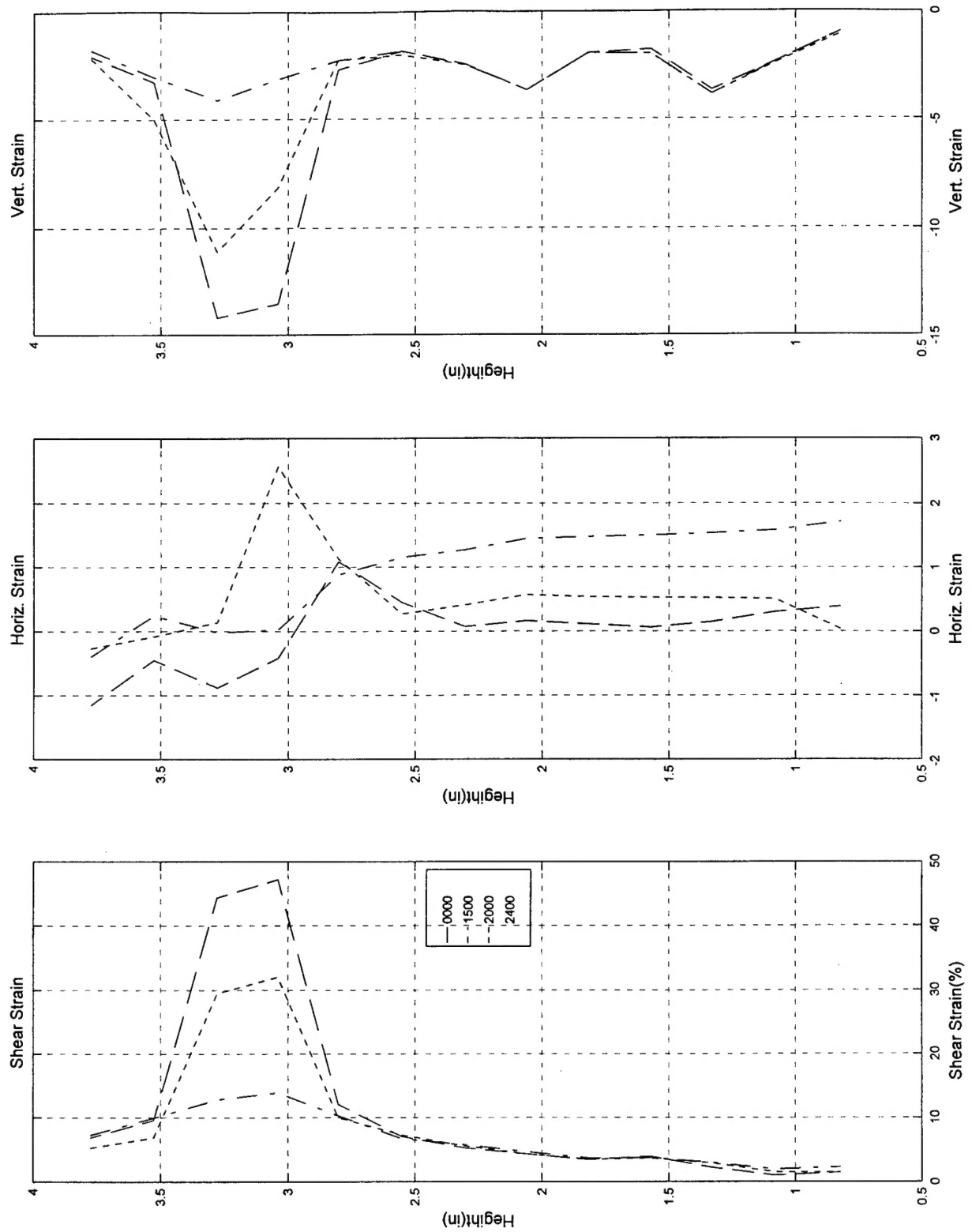Test #79; 4/1/97; Torsion-Extension; ECP=50 psi; Loire, Video c

Test #79, Camera #C, Figure 4

Test #79, Camera #C, Figure 5

Test #79, Camera #C, Figure 6

Test #79; 4/1/97; Torsion-Extension; ECP=50 psi; Loire, Video c

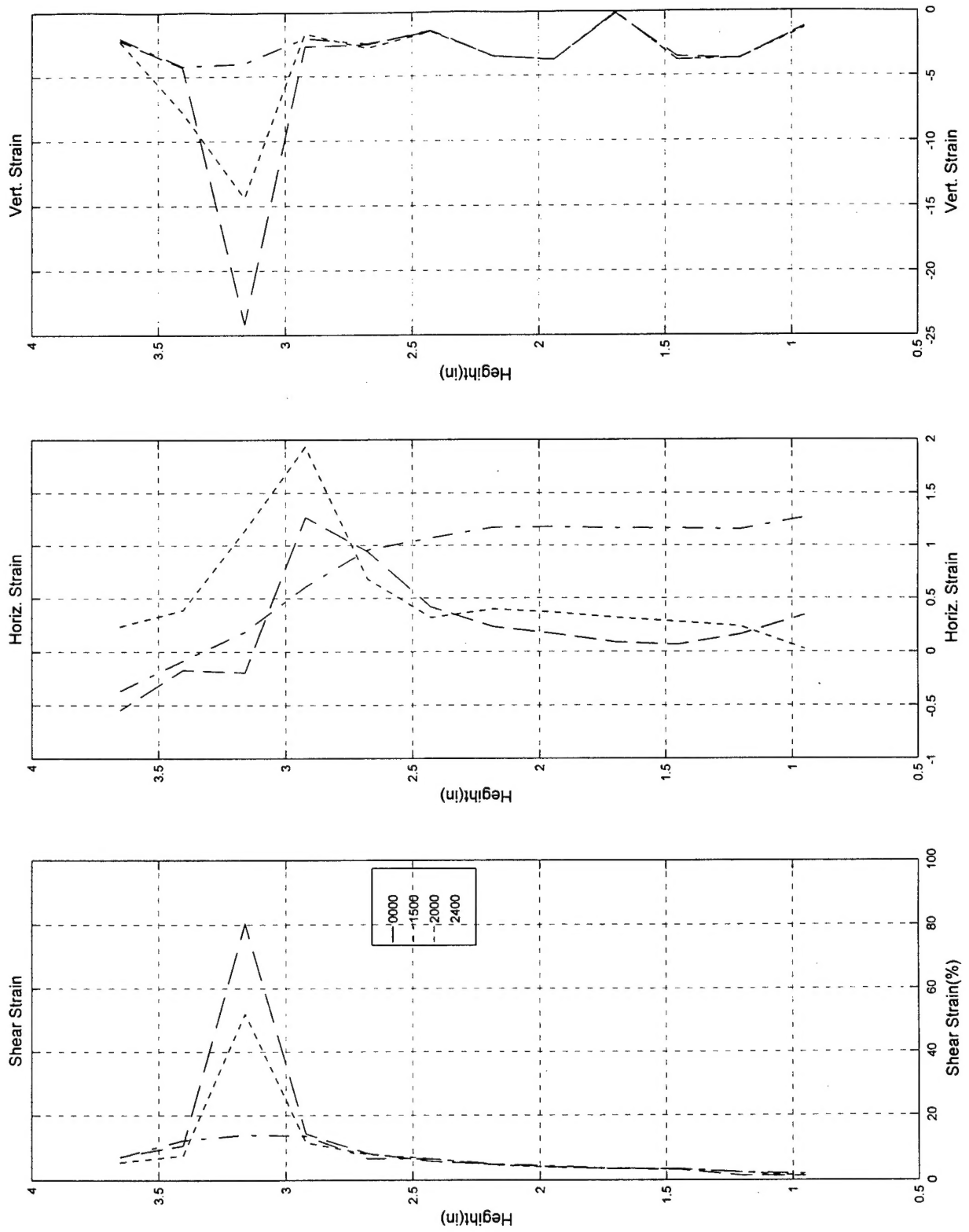**Test #79, Camera #C, Figure 7**

Test #79, Camera #D, Figure 1

Test #79, Camera #D, Figure 2

187

Test #79; 4/1/97; Torsion-Extension; ECP=50 psi; Loire, Video d

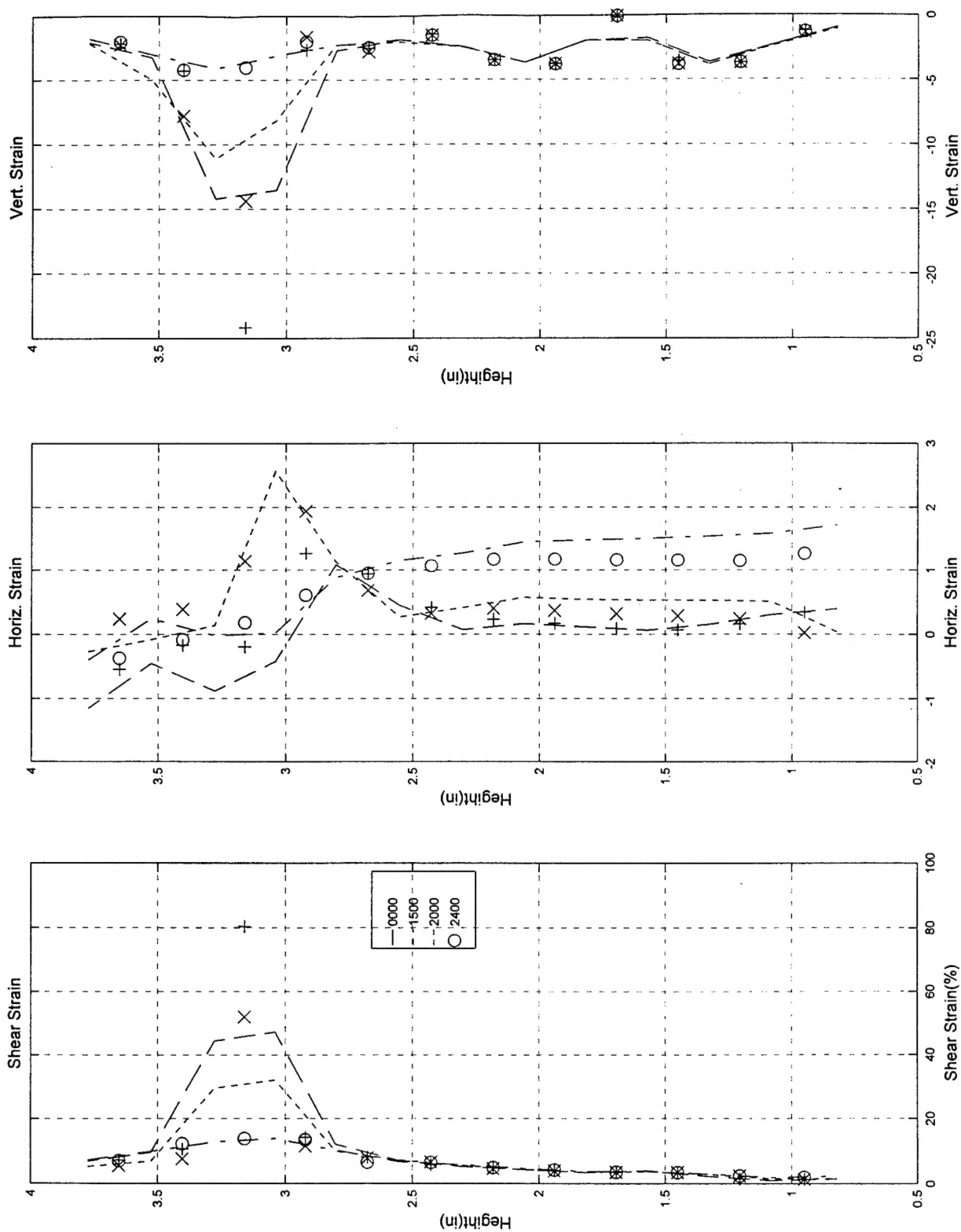Test #79, Camera #D, Figure 3

Test #79, Camera #D, Figure 4

Test #79; 4/1/97; Torsion-Extension; ECP=50 psi; Loire, Video d

Test #77, Camera #D, Figure 5

Test #79; 4/1/97; Torsion-Extension; ECP=50 psi; Loire, Video d

Test #79, Camera #D, Figure 6

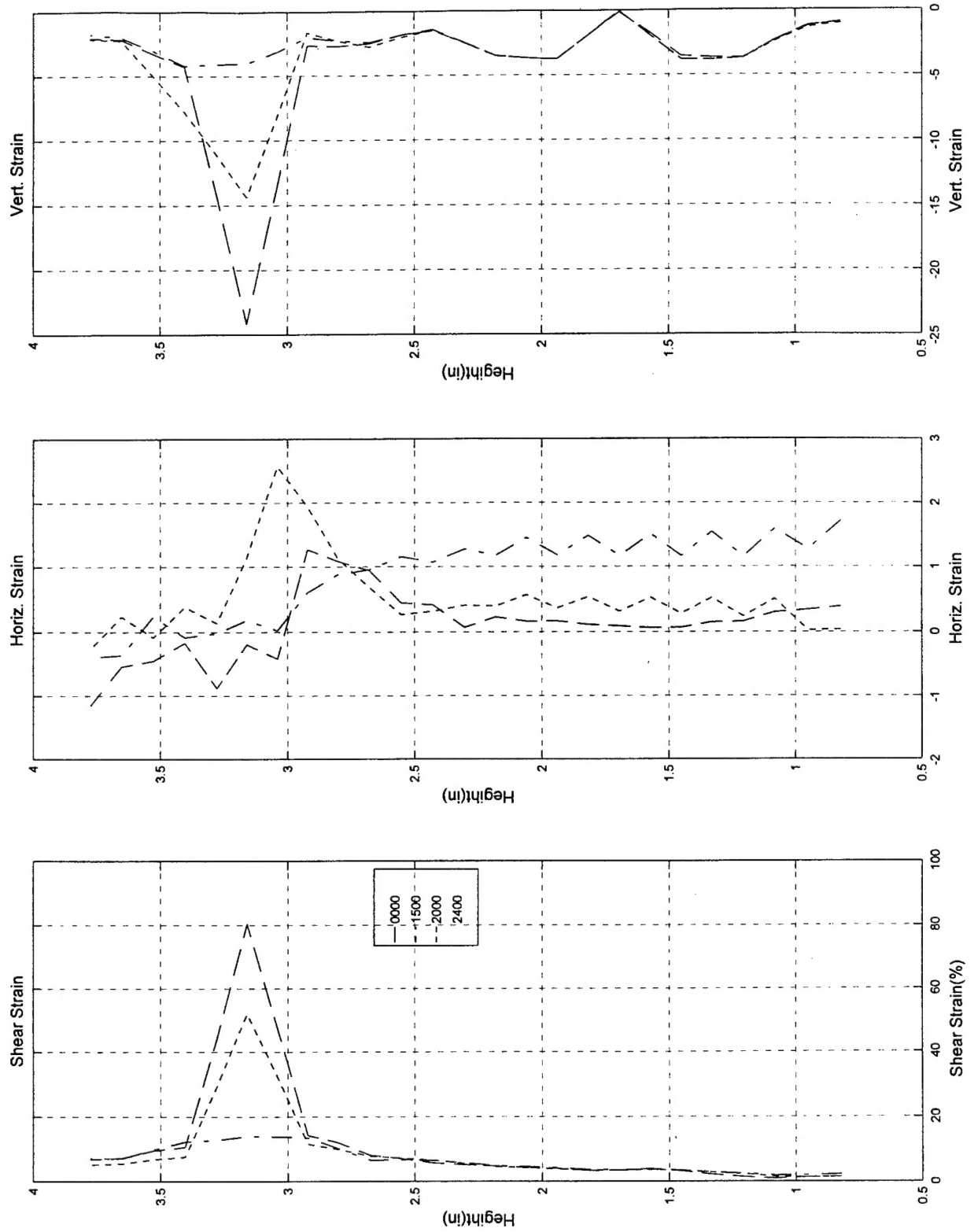Test #79; 4/1/97; Torsion-Extension; ECP=50 psi; Loire, Video d

Test #79, Camera #D, Figure 7